Instituto de Física de Cantabria
(CSIC-Univ. de Cantabria)
y
Departamento de Física Moderna
(Universidad de Cantabria)

# Un Sistema de Alineamiento para el Experimento CMS (Detector Solenoidal de Muones) del Gran Colisionador Hadrónico (LHC)

Memoria presentada por:
**Marcos Fernández García**
para optar al grado de Doctor en Ciencias Físicas
y dirigida por el
**Dr. Antonio Ferrando García**

Santander, Julio 2001

# Index

# Introduction

Almost every human society has its folk tales about how and where it originated. The Masai tribe in East Africa, believes that they originated from an active volcano in their region, a clear link between their origins and the most powerful natural force in their environment. The explanation adduced by the scientific community is that the Universe started with an explosion called *Big Bang* . In this explosion, the Universe expanded from a single point with an infinitely high *energy density*, and infinite temperature.

The first moments of the Universe were of an extraordinary activity: $10^{-43}$ seconds after the explosion, photons, quarks, leptons, gauge bosons and some other nowadays undiscovered particles coexisted in thermal equilibrium, at $10^{32}$ K. At this time, gravity separated from electroweak and strong forces. During the grand unification era ($10^{-35}$ s after the collapse), the strong and electroweak forces became distinguishable in an Universe at $10^{27}$ K. At this early stage, the Universe size is estimated to be about $10^{23}$ m. The temperature was still too high for quarks to join forming neutrons or protons, and so existed in the form of a quark gluon plasma. Only after $10^{-10}$ s and after the temperature reduced down to $10^{15}$ K, the electromagnetic and weak forces could separate. Unstable massive particles disappeared. When the overall temperature was $10^{13}$ K, 0.1 ms after the Bang, the Universe had already grown to the size of our solar system. Quark-antiquark annihilation stopped and the quarks combined to make protons and neutrons. Three minutes later, these recently formed protons and neutrons combined to form helium nuclei in an Universe cooled down to $10^{9}$ K. The temperature had to reduce further to 6000 K to allow electrons to couple with nuclei. This process took 300000 years. The Galaxies formation started after 1000 million years, when the Universe temperature was close to 18 K. Finally, heavy nuclei were synthesized at stars and spread during supernovae explosions.

Nowadays, we begin to wonder what happened 15000 million years ago. The best answer to this question would be given repeating the same conditions that took place at the beginning. Of course, no affordable experiment can reproduce them. However, it is possible to obtain energy densities which are close to those after the explosion, for a short fraction of time. Such high energy densities are obtained in collisions of particles which are accelerated by huge machines called accelerators. Particle accelerators are big scale and very expensive machines. That is the reason why only a small number of powerful accelerators exist in the world, being the Tevatron at Fermilab (Chicago) and the Large Electron Positron (LEP) at CERN (Geneva), the outstanding realizations. At LEP, energy densities reached by collisions are equivalent to the energy density $10^{-10}$ s after the big explosion. During these collisions, the incoming particles give raise to a pleiad of subatomic particles, most of them short-lived particles, which certainly were present right after the explosion. Due to the high energy densities involved, colliding particles act as probes which allow to study the intimate constituents of matter. Thus, the particle substructure can be discovered or, on the contrary, their elementary character can be stated down to the scale searched.

Particle physics or High Energy Physics is the discipline of physics in charge of the study of the basic elements of matter and the forces acting among them. Accelerators and High Energy Physics detectors are the tools employed to study the above phenomena. The number and importance of the achievements in this field during the last century is impressive. Since 1919 when Ernest Rutherford found the first evidence for a proton, till 1995, when the top quark was discovered at Fermilab, the whole spectra of known particles has been discovered.

The theoretical frame used to explain the experimental results was already settled by Glashow, Salam and Weinberg in the middle sixties and it is called the *Standard Model*. This model has been extensively tested with a great success and very high degree of agreement during the last 40 years. With the exception of gravity, it describes all the fundamental forces of nature from a few basic principles and input parameters. There is no experimental result up to date that contradicts the Standard Model. Even though, it is accepted that the picture described by the Standard Model is incomplete and lacks of certain generality. For instance, important questions that are not confirmed yet by this model are the origin of mass, why there are only 3 families of quarks and leptons, what is the origin of matter-antimatter asymmetry, did the quark-gluon plasma exist in the early universe... Among them, the search for the Higgs boson, the particle which confers mass to other particles is favored. The Higgs particle provides the mechanism for electroweak symmetry breaking, that is, it allows the force carriers of the weak interaction (the W and Z bosons) to have mass while the force carrier of electromagnetism, the photon, remains massless. It also allows all other elementary particles to have mass.

In order to answer these questions, a worldwide community of physicists have designed the next generation accelerator machine, called Large Hadron Collider (LHC). The LHC, currently being constructed at CERN, will accelerate bunches of protons using superconducting technology. It will provide four points of collision equipped with large scale compact detectors. Two of them, called CMS − Compact Muon Solenoid − and ATLAS −A Toroidal LHC ApparatuS− are being designed as multipurpose experiments and will work at high collision rate. Other two, LHCb and ALICE (−A Large Ion Collider Experiment−) will be devoted to the study of B physics and lead ions collisions respectively. The energy reached at the center of mass system will allow to explore very high energy physics never studied up to now.

After the collision produces, interactions between the quarks will lead to a chain of events rated by the probability of occurrence and the available energy. Due to this rating, rare channels will be the most interesting ones. The subproducts of each collisions are characterized by reconstructing either the energy of the outgoing particles or its momenta, depending of the kind of particle. The energy of minimum interacting particles (neutrinos) will be measured as the balance of missing energy in the detector, for which it must be very compact. In fact, CMS is designed as a compact detector arranged in layers of subdetectors built around the interaction point.

CMS is the experiment in which this work has been developed, its hardware alignment being the central topic. The overall structure of CMS consists of a tracking system, for the measurement of the momenta of charged particles, composed by inner silicon pixels surrounded by silicon strip modules. Next, an electromagnetic calorimeter made by $PbWO_4$ (lead tungstate) crystals measures the energy of electromagnetic particles (electrons, photons and pions) and will initiate hadronic showers. These showers will be contained by the hadronic calorimeter, formed by copper layers interleaved with scintillator material. The three set of detectors are enclosed within the winding of a solenoid producing a magnetic field intensity of 4 T intensity. The magnetic field provides the bending power needed to curve the trajectories of energetic particles. Those particles which manage to escape the structure of calorimeters and tracking system will be either neutrinos (which hardly interact with matter) or muons. The muons are then measured with 4 layers of drift chambers (in the central part of CMS) or Cathode Strip Chambers (in the endcaps). The chambers are embedded in the return field of the solenoid which is lead through the iron sustaining the chambers in place. Thus, when muons traverse the iron, their trajectories are bent by the action of the magnetic field and their curvature (and therefore their momenta) measured by the chambers. In chapter 1 we give a more detailed approximation to the LHC project and CMS experiment, giving an overview of its components.

Among the particles produced at the LHC energy, muons will carry much of the information from collisions. Therefore measurement of muons in the LHC will be a crucial issue. CMS complements the measurement of muons by combination of the momenta information provided by the Tracker system with the measurements of drift chambers, several meters away from it. In order to achieve a momentum resolution of up to 20% for 1 TeV muons, the relative position among chambers and between chambers and Tracker system must be known with about 150 $\mu$m precision. Otherwise, the momentum resolution will be smeared by the misalignment of the detectors. Due to the combined action of the gravity forces (that will displace the detectors from their nominal positions), the temperature gradients (due to ventilation and power dissipation) and overall, due to the magnetic forces acting on the endcaps of the detector during the power-on process of the magnet, the stability of CMS at the micrometric level can not be guaranteed. This is the reason why highly performance operation of CMS demands an alignment system, monitoring the relative positions among detectors. CMS solves the alignment problem by dividing the detector in three independent parts. Each part (Tracking system, Muon Barrel system and Endcap Muon system) are aligned independently as rigid bodies. Then, these bodies are related by means of the Link System transferring the coordinates of the Tracker (the reference frame) to the rest of detectors. Chapter 2 further develops the description of alignment system of CMS, with special emphasis on the Link system where the activity compiled in this work has been developed.

Aside from the technological challenge set by the alignment of a huge structure as CMS, it is required that the alignment system be easy to integrate in the whole detector layout. In order to increase the compacity of CMS, minimization of dead areas is mandatory. This is why redefinitions of subdetectors in CMS affect directly the layout of the alignment system. The redefinition of the Tracker system obliged to a total new concept of the Link alignment system. If at 1999 there was already the basis for a performance Link system, the $\phi$-system, it had to be changed in favour of a new design which allowed to reach the Tracker region in a more integration-friendly way. As a product of such a redesign, a multipoint alignment system was adopted. The multipoint concept uses a reference light beam intercepted by 2D position sensors mounted on the structures needed to be monitored. The performance of such a design deeply relies in the election of the position sensors. CMS has adopted ALMY sensors (ALMY stands for "ALignment of MYon chambers") for this task. ALMY sensors were developed for the alignment of the ATLAS detector. ALMY sensors mean a new concept of optical detectors, since they are transparent to the light beam that they detect. The novel character of this concept, the complexity it involves and the constant development to which it is being subject have allow the author to participate actively in this project. Part of this work summarizes the contribution to the ALMY development by the CMS group. In particular, we have contributed to the study (chapter 3) and performance tests of many prototypes (chapter 4), geometrical and optical simulations (chapters 4 and 5) of its functioning and radiation endurance tests of ALMY devices (chapter 7). Besides, we have contributed specific solutions for the space-constrained utilization of ALMYs in CMS.

The knowledge of the relative positions among detectors is complemented by distance measurements between alignment elements and by the measurement of the $\phi$ coordinate. The measurement of the $\phi$ coordinate (of central importance for the CMS physics program), is accomplished by means of tiltmeters. This work explains (chapter 6) our geometrical model of the sensor operation and also reports on the tests of these devices. We propose and demonstrate a method which will allow unfolded measurement of the $\phi$ angle in CMS.

After the description of the main components of the Link alignment system, we complete the study of other optical and mechanical components at the ISR hall (CERN) where the first integrated alignment test took place. Chapter 8 summarizes the calibrations carried out at this facility.

# Chapter 1

# The LHC and the CMS experiment

## 1.1 Introduction

After LEP data, all evidence indicates that new physics and answers to some of the most profound questions of our time, lie at energies beyond 1 TeV.
To look for this new physics, the next particle physics research instrument in Europe is the LHC, the *Large Hadron Collider*. In keeping CERN's cost-effective strategy of building on previous investments, it is designed to share the 27-kilometer LEP tunnel, and be fed by existing particle sources and pre-accelerators. This challenging machine will use the most advanced superconducting magnet and accelerator technologies ever employed. In the LHC the energy available in the collisions between the constituents of the protons (the quarks and gluons) will reach the TeV range, that is about 10 times that of LEP and the Fermilab Tevatron.

## 1.2 LHC overview

The LHC is a remarkably versatile accelerator. It can collide proton beams with energies around 7-on-7 TeV at beam crossing points of unsurpassed brightness, providing the experiments with high interaction rates. It can also collide beams of heavy ions such as lead, with a total collision energy in excess of 1250 TeV, about thirty times higher than at the Relativistic Heavy Ion Collider (RHIC) recently completed at the Brookhaven Laboratory in the US.
From the particle physics point of view, two parameters define the performance of a collider: the center of mass energy and the luminosity. The former increases with the energy of the colliding particles, the latter is proportional to the number of collisions per second. In general, for colliding machines, the luminosity is defined as:

$$L = \frac{1}{4\pi} \frac{N_1 N_2 f}{\sigma_x \sigma_y} \tag{1.1}$$

where $N_i$ are the number of particles per bunch in the two colliding beams, $f$ the bunch crossing frequency and $\sigma_{x(y)}$ the RMS of the particle distribution in the direction x(y) transverse to the beam.
The product of the beam-beam interaction cross section $\sigma$ times the luminosity determines the reaction rate $R = \sigma L$. In order to maintain an effective physics program at a high energy $E$ the luminosity of a collider should increase in proportion to $\mathrm{E}^2$. This is because the *De*

*Broglie* wavelength associated to a particle decreases like $1/E$ and hence the cross section of the particle decreases like $1/E^2$. Whereas in past and present colliders the luminosity culminates around L=$10^{32}$cm$^{-2}$s$^{-1}$, in the LHC it will reach L = $10^{34}$cm$^{-2}$s$^{-1}$. This will be achieved by filling each of the two rings with 2835 bunches of $10^{11}$ particles each. The resulting large beam current (0.56 A) is a particular challenge in a machine made of delicate superconducting magnets operating at cryogenic temperatures.

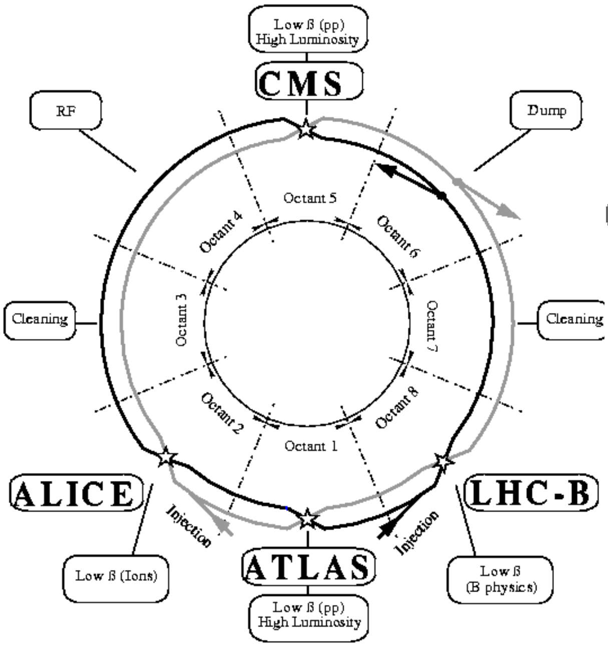


Figure 1.1: *Schematic picture showing the situation of the experimental points at the LHC.*

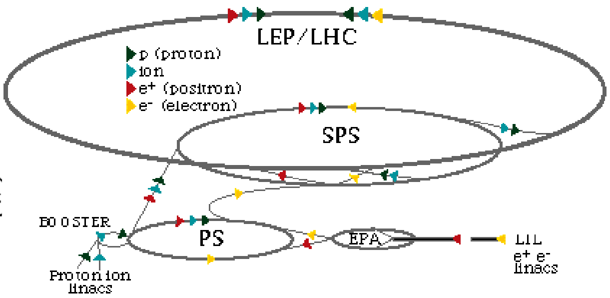


Figure 1.2: *CERN acceleration network. Each type of particle is produced in a different way, but then passes through a similar succession of acceleration stages, moving from one machine to another. The first steps are usually provided by linear accelerators, followed by larger circular machines.*

Nominal parameters of the LHC machine are given in table 1 [1]. Many variables will degrade the final performance of the collider. Among the most important are:

- The electromagnetic repulsion among particles in the bunch will lead to beam-beam interactions. This effect is more important for denser bunches. The maximum beam density should not be exceeded to preserve beam lifetime.

- Bunch to bunch interactions can be minimized by careful control of the electromagnetic

| | | | |
|---|---|---|---|
| Energy at collision | 7 TeV | Bunch separation | 24.95 ns |
| Energy at injection | 450 GeV | Number of particles per bunch | $1.1\times10^{11}$ |
| Dipole field at 7 TeV | 8.33 T | Total crossing angle | 300 $\mu$rad |
| Coil inner diameter | 56 mm | Luminosity lifetime | 10 h |
| Distance between aperture axes (1.9 K) | 194 mm | Energy loss per turn | 7 keV |
| Luminosity | $10^{34}$ cm$^{-2}$s$^{-1}$ | Critical photon energy | 44.1 eV |
| DC beam current | 0.56 A | Total radiated power per beam | 3.8 kW |
| Bunch spacing | 7.48 m | Filling time per ring | 4.3 min |

Table 1: *LHC General Parameters.*

properties of the elements surrounding the beam.

- Quench of the superconducting magnets: a fraction of the particles diffuse towards the beam pipe wall and get lost. In this event the particle energy is converted into heat in the surrounding material and this can induce a quench of the superconducting magnets. Therefore, the particle beam needs to be collimated.

- Energy looses due to synchrotron radiation (less important for protons than for electrons due to their bigger mass) will be about 3.8 kW which will be absorbed by the beam pipe at cryogenic temperature. Some photoelectrons, coming from the interaction of photons with the beam pipe, will be incorporated into the accelerated beam as a result.

The LHC beams will be filled with protons delivered from the SPS and its pre-accelerators at 0.45 TeV. Two superconducting magnetic channels will accelerate the protons to 7-on-7 TeV. After this the beams will counter-rotate for several hours, colliding at the experiments, until they become so degraded that the machine will have to be emptied and refilled. The magnetic channels will be housed in the same yoke and cryostat, a unique configuration that not only saves space but also gives a 25% cost saving over separate rings. To bend 7 TeV protons around the ring, the LHC dipoles must be able to produce fields of 8.36 Tesla, over five times those used a few years ago at the SPS proton-antiproton collider. Superconductivity will make it possible.

### 1.2.1 LHC layout

The basic layout of the machine (see figure 1.1) mirrors that of LEP, with eight straight sections each approximately 528 m long, available for experimental insertions or utilities. The two high-luminosity insertions are located at diametrically opposite straight sections, point 1 (ATLAS) and point 5 (CMS). Two more experimental insertions are located at point 2 (ALICE Pb ions) and point 8 (B physics). These latter straight sections also contain the injection systems. The beams cross from one ring to the other only at these four locations. Increasing the number of simultaneously illuminated collision points would reduce the luminosity in the insertions.
The filling sequence starts (figure 1.2) with three bunch trains injected into the SPS on three successive PS cycles at 3.6 s intervals, filling one third of the SPS circumference. The SPS then accelerates the beam to 450 GeV and transfers each batch (containing 2.4 $10^{13}$ protons) to one or the other of the LHC rings. This is repeated 12 times per ring with a cycle time of 16.8 s. Once both rings are filled the beams are accelerated to nominal collision energy in about 20 min. The acceleration of ions is a well-developed activity at CERN. The first ions were accelerated in the PS in 1976 and in the SPS in 1987. The plans are now to extend the LHC facility in order to support (after a moderate upgrading) lead-ion collisions with a center-of-mass energy of 1148 TeV in the LHC.

## 1.3 The experimental challenge at the LHC

The total cross-section at hadron colliders is very large, about 100 mb at the LHC, resulting in an interaction rate of about $10^9$ Hz at the design luminosity. Figure 1.3 shows (left scale) the expected energy dependence of the total cross section and of some interesting physics processes which have much smaller cross sections [2]. The values at a center of mass energy of 14 TeV are Standard Model predictions extrapolated from data obtained at lower energies in previous experiments. Typical cross sections at $10^{34}\mathrm{cm}^{-2}\mathrm{s}^{-1}$ and event rates expected are (1 pb,$10^{-2}$Hz) for a 500 GeV Higgs boson or (100 $\mu$b,$10^6$Hz) for $b\bar{b}$ pair production.
Many of the foreseen new particles will decay into W and Z bosons, charged leptons or photons. W's and Z's will have to be detected through their leptonic decays (with very small branching ratios) because hadronic decay modes will be overwhelmed by the QCD [3]. The high luminosity will lead to difficult experimental conditions: with an inter-bunch crossing-time of 25 ns at design luminosity, on average 20 interactions ("minimum bias") are expected per crossing. Inner tracking detectors will have to operate in a hostile environment. Besides, the expected $10^9$ inelastic pp events per second will result in a high radiation environment that the detectors and associated electronics will have to withstand.

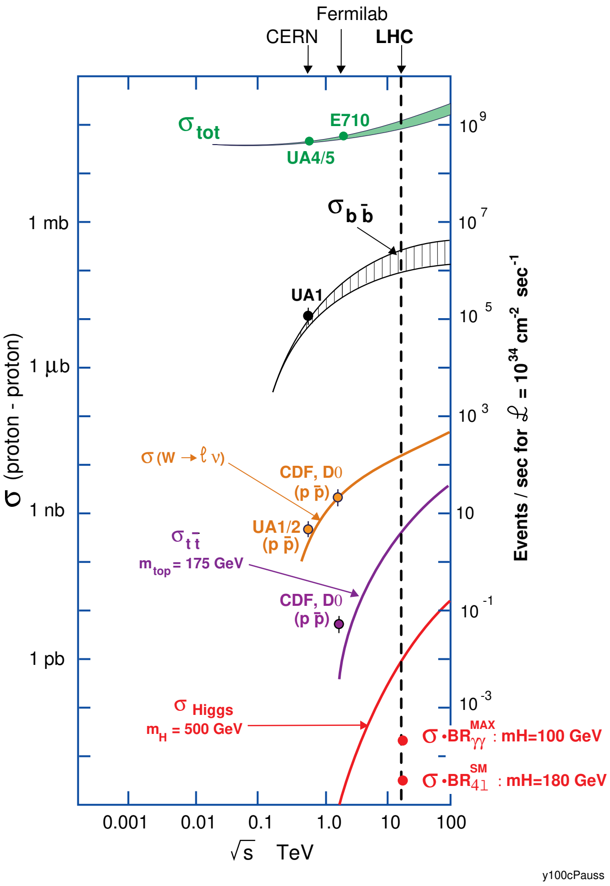


Figure 1.3: *Energy dependence of some characteristic cross-sections at hadron colliders.*

## 1.4 The Compact Muon Solenoid

The Compact Muon Solenoid (CMS) is one of the two general purpose detectors at the LHC. About 150 institutions with almost 2000 scientists take part in the Collaboration. The design concept of CMS was first presented at the LHC Workshop at Aachen, in 1990 [4].
CMS is designed to run at the highest luminosity, although it is also well adapted for studies at the initially lower luminosities. The main design goals of CMS are:

i) A highly performing Muon System

ii) The best possible electromagnetic calorimeter consistent with i)

iii) A high quality central tracking to achieve i) and ii)

iv) A hermetic hadron calorimeter

An overall open view of the CMS detector is shown in figure 1.4. Proton bunches collide in the center of the detector. Around the interaction vertex, layers of subdetectors are arranged avoiding projective cracks. Due to the symmetry of the magnetic field, the central rapidity[1] regions of the Tracker are always arranged in a barrel geometry, while at higher rapidity values the detectors are arranged in disks. Each subdetector is specialized in the measurement of a certain kind of particles. Around the beam pipe, a central tracking system, integrated by silicon detectors, will measure the tracks of charged particles. Those particles with enough momentum will reach the calorimeters. Electrons and photons will be measured in the electromagnetic calorimeter thanks to electromagnetic showers in lead tungstate calorimeters. In turn, charged hadrons may start to shower in the electromagnetic calorimeter and will be contained in the hadron calorimeter, where layers of scintillators are alternate with copper layers. After the calorimeters, only minimum interacting particles will be available (mainly neutrinos and muons). The muons will be accurately measured using a highly redundant muon spectrometer based on gaseous detectors as drift chambers and cathode strip chambers. In what follows, the main figures concerning each subdetector are presented.

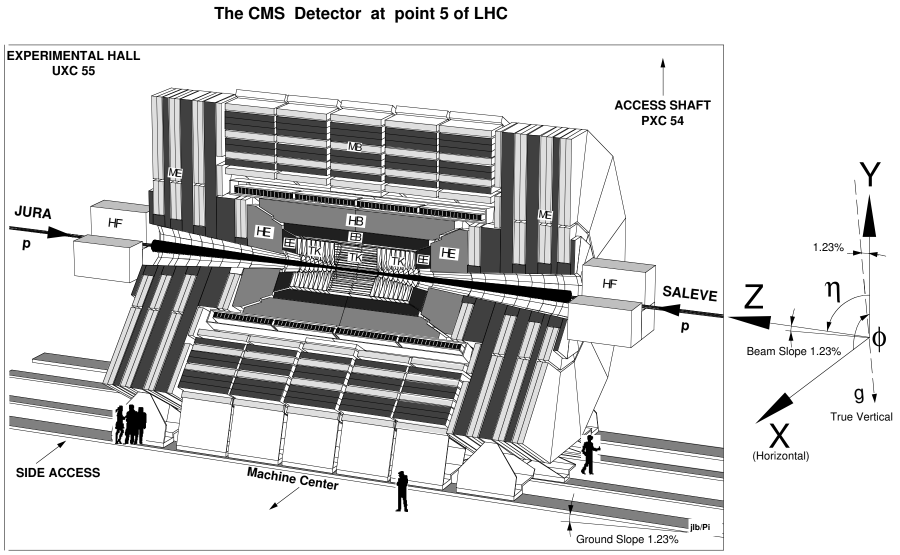


Figure 1.4: *Open view of the CMS experiment. The physical magnitudes are 12500 tonnes weight, 15 m diameter, 21.6 m long and 4 T magnetic field.*

### 1.4.1 The Central Tracker

Robust tracking and detailed vertex reconstruction will play an essential role in the overall performance of CMS. Several physical signatures will benefit from a robust and redundant tracking system. Leptonic decays from W and Z need to be measured at the Tracker to obtain an overall good momentum resolution conjointly with the muon chambers. Also, some of the most interesting events are likely to contain several $b$-jets. In order to get an efficient tagging

[1] The rapidity or pseudorapidity $\eta$ is a geometric variable defined as $\eta = \ln \tan \frac{\theta}{2}$, where $\theta$ is the polar angle contained in the plane $YZ$ of figure 1.4.

of these jets, the tracking must extend as close as possible to the vertex, delivering true space point information. Specially, search for Higgs or SUSY particles will benefit from these features. The Tracker system is divided into two subdetectors.

### The Pixel Detector System

Near to the beam pipe, a Silicon Pixel System will be installed [5]. The barrel part of the Pixel System will have two layers of modular detectors. The modules (see figure 1.5) consist of a thin, 2D squared grid of $n^+$ pixel implants, on an almost fully depleted p-type silicon layer (about 250 $\mu$m thick). In the barrel, due to the Lorentz force on charged particles, the electron-hole pairs will drift with different Lorentz angles (due to their different mobility). The electron drift angle (32°) makes possible a charge sharing process between adjacent pixels, which always improves spatial resolution. The individual pixel is chosen to be a 150 $\mu$m square. Benefiting from the charge sharing, the spatial resolution that can be achieved is about 10-15 $\mu$m for both $R\phi$ and $Z$. In the Endcaps and using the same pixel layout, there will be little charge sharing since the electric and magnetic fields are aligned. Therefore, charge effects are induced by tilting each sensor module by 20 degrees around the CMS $R$ axis. Good resolutions, about 15-20 $\mu$m, are expected for this sensor arrangement. The working conditions of the silicon devices imposes them to be cooled, in order to avoid a strong rise of noise, an increase in power consumption and heat dissipation. The modules will be attached to cooling frames, with the cooling tubes being an integral part of the mechanical structure.

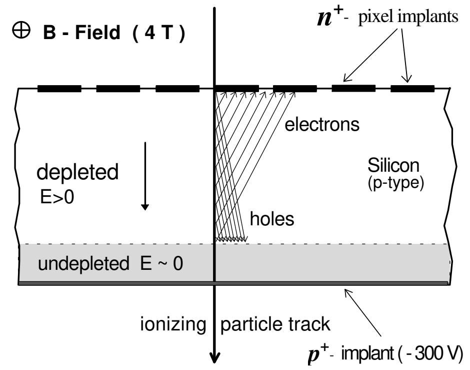


Figure 1.5: *Longitudinal view of a pixel module showing an array of pixels. The figure illustrates the charge collection process. Electrons drift with higher Lorentz angle and distribute their charge among several strips, even for perpendicular tracks. The bottom p doped implant has been actually dropped [5].*

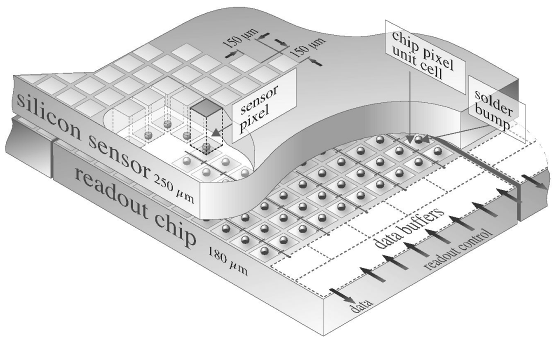


Figure 1.6: *Module showing a 2D grid of pixel elements, bonding layout and readout concept [5].*

Regarding the pixel readout, each pixel is connected, via a solder bump, to a cell unit on a readout chip (see figure 1.6). There the signal is amplified. The hit data are stored on the edge of the chip where they wait for trigger confirmation. The chips are then connected to hybrid

circuits which distribute readout control and clock signals. From the hybrids, kapton cables allow communication with the outer region, from where signals are transmitted optically. The whole process occurs within the 25 ns bunch crossing time.
Due to the hostile radiation environment, those pixels placed at radii smaller than 10 cm will need to be replaced at least once during the lifetime of the experiment. Besides, yearly extraction of the pixel bulk will be required. The pixel system can be shifted in and out and split in two independent right-left halves, avoiding interference with the beam pipe and rest of detectors. During the low luminosity phase, the pixel system will be constituted by two layers at 4 and 7 cm. At design luminosity, the innermost layer will be removed and an extra layer at 11.5 cm will be installed. A 3D view of the whole Pixel System is shown in figure 1.7.

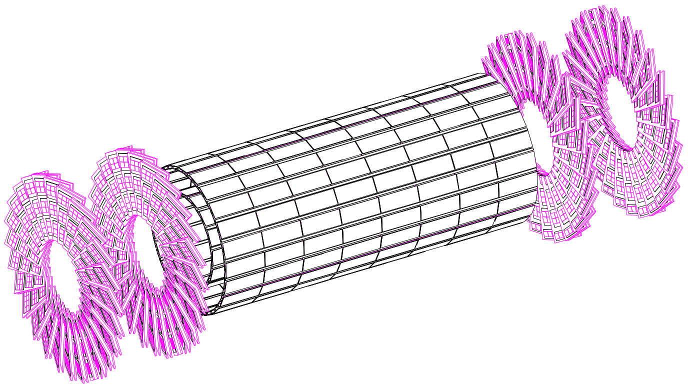

Figure 1.7: *Stereo view of the CMS pixel system (high luminosity configuration) [5].*

**The Silicon Tracker**

The layout of the CMS Tracker has changed since the Tracker TDR [5]. Before December 1999, the Tracker baseline was the election of three detector technologies. In radial increasing order from the beam pipe, these were: a Pixel Detector ($R \lesssim 20$ cm), Silicon Strips ($20 \lesssim R \lesssim 60$ cm) and Micro Strip Gas Chambers, also called MSGCs ($70 \lesssim R \lesssim 210$ cm). In the fall of 1999, the large PSI Milestone resulted in an unambiguous demonstration of the viability of the MSGCs. Also, at that time, an all silicon tracker (AST) alternative was also positively verified. The overall delay for the construction of both the silicon and MSGC trackers raised the consideration of selecting one of the two proposals. The change was put to vote, and the AST solution was endorsed by a minimal majority [6].
The AST system will benefit from the MSGC R&D studies developed so far. First, silicon and MSGCs shared the same front-end electronics chain (just with minor adaptations to match the different pulse shapes of the two detectors). Therefore, no radical changes should be expected in the electronics interface. Second, mechanical studies performed for the MSGC system can also be readapted for the silicon Tracker as an advanced starting point.
The proposed AST layout has now 10 rather than 11 barrel layers and 9 rather than 11 disks in each endcap [7]. The surface reduction is compensated by the faster time response and better resolution of silicon compared to MSGCs, so thus the tracking performance remains unchanged. The current Silicon Tracker layout for a quarter plane is shown in figure 1.8. One of the most

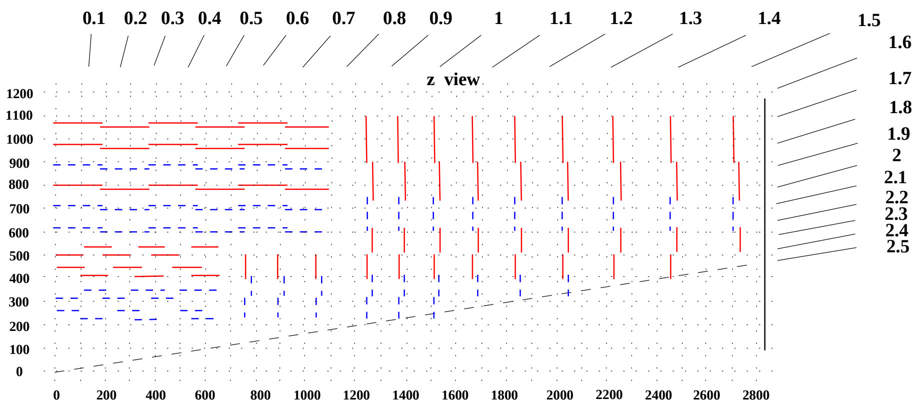


Figure 1.8: *Schematics of the current Silicon Tracker layout (units are mm). Continuous lines are single sided silicon modules. Dashed lines refer to back-to-back (double sided) modules. Inner (Outer) barrel contains double (single) modules and are built with a shell mechanics. Three outer endcap wheels are made of thick detectors and are built with a rod mechanics. [7]*

important differences with respect to the old MSGC layout is the removal of the inner ($R \sim 70$ cm) support tube which acted as a thermal wall, separating the Silicon volume (which must be operated at low temperature) of the MSGC volume which operated at room temperature. With the new layout this restriction does no longer exist. It allows to build hermetic endcaps.

A detector module is the basic functional subunit of the Silicon Tracking system (see figure 1.9). Each module consists of three elements: a set of silicon strip detectors, a readout hybrid and a carbon fiber support. The individual sensors of the Tracker Silicon System are micro-strip silicon devices. Each silicon detector is 320-500 $\mu$m thick (depending on its location), and is readout by front end electronics on a pitch, varying for different layers and disks, between 61 and 183 $\mu$m. The incident particle produces a cloud of carriers. Then the particle impact point is usually given by the center of gravity of the cluster, the weights being given by the charge collected on each strip.

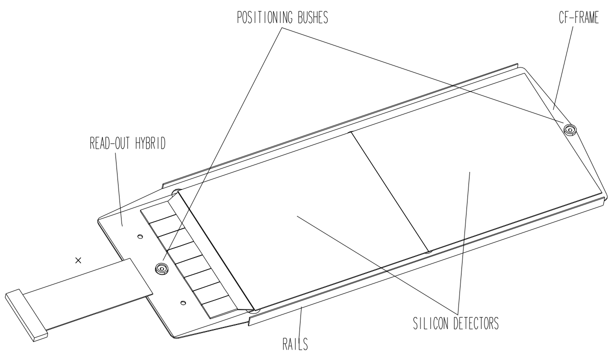


Figure 1.9: *Perspective view of a silicon tracker barrel module [5].*

The radiation of these devices has been proven to be above the expected fluence in CMS. They are relatively simple and low cost devices, since their production is compatible with standard micro-electronics technology.

The operating temperature of the silicon will be -20°C. The foreseen cooling system is based on a heat transfer fluid running through a system of small-diameter pipes embedded in the structure and in good thermal contact with the power dissipating elements (electronics, optical links and service cards, cables and silicon detectors).

The new Tracker layout is subdivided in Inner Barrel (TIB), Outer Barrel (TOB) and endcaps (TE). The TIB comprises 4 layers, from $200 \lesssim R \lesssim 515$ mm. In total, 2808 modules either made

out of two 4" wafers or one 6" wafer. The module active area is 62×120 mm$^2$. The detectors are tilted by 9 degrees to compensate for the Lorentz angle and are arranged to allow $\phi$ and $Z$ overlap. The inner barrel is built around concentric cylindrical structures made on CF and is split into two pieces at $Z = 0$. Each half contains 6 series of detectors. Modules are housed on both sides of the cylindrical structures
The TOB modules will be made out of two 6" wafers each, active area 94×186 mm$^2$. The TOB is built with rod mechanics. The modules are mounted on rods, the rods are inserted along $Z$ inside the TOB structure. The TOB structure will be supported from outside. No Lorentz angle compensation will be setup.
The TEs are built out of 9 big disks and 3 small disks. The detectors are organized on 16 panels per disk, as shown in figure 1.10. Each panel has sensors on both sides, thus providing $R\phi$ overlap. Eight panels face the interaction vertex, the others are placed back to it. The gaps between panels in each side of the disk are employed for insertion and extraction of the panels, rotating each by $\pm 11.25°$ and then shifting it out. All panels can be extracted without the need to uncable the endcap.
In all cases, double sided modules (also called stereo strips) will be faked using two single sided modules placed back-to-back. Instead of patterning strips with a small angle, the whole module will be rotated in plane by 100 mrad. In the front device, radial strip projections point to the beam line ($\phi$ view). In the device on the back, the strips are tilted by 100 mrad (stereo-view), their projections intersecting on a concentric ring around the beam line. In the barrel parts, rectangular single sided modules will provide $R\phi$ information. Stereo modules will allow the measurement of the $Z$ coordinate. In the endcaps, double sided modules will measure both the azimuth $\phi$ and the radial coordinate.
The chosen readout scheme implements a fully analog architecture based on a fast amplifier (the so-called APV series) followed by an analog pipeline and a deconvolution circuit. The analog read-out allows efficient common mode noise subtraction. High speed optical links, based on laser technology, will feature radiation hardness, small size, low power dissipation and high analog transmission quality.

### 1.4.2 The Electromagnetic Calorimeter

In the Higgs intermediate mass range (90 GeV $\leq$ m$_H$ $\leq$ 150 GeV), the H$\rightarrow \gamma\gamma$ decay mode, despite its small branching ratio (BR), provides a distinctive signature for Higgs discovery at the LHC. Since the width of the Higgs signal is entirely dominated by the experimental two-photon mass resolution, it imposes the most stringent performance requirements on the ECAL detector. This experimentally difficult channel has therefore been used as the final goal for optimizing the electromagnetic calorimeter (ECAL) design.
Electrons and photons are measured in dense media, where they initiate an electromagnetic shower, with progressively lower energy, via the processes of bremsstrahlung, pair-production and, at low energies, Compton scattering. The electrons/positrons in the shower may produce either ionization or light (or both), depending on the material in which the shower occurs. The CMS Electromagnetic Calorimeter (ECAL) measures scintillation light produced by crystals of lead tungstate ($PbWO_4$) which is proportional to the energy of the incident particle.
Electromagnetic calorimeters measure the energy of electrons and photons, aid in the particle identification (specifically electron/charged pion separation with the Tracker) and help to measure the energy of high energy hadrons. The barrel electromagnetic calorimeter [8]-[11] is designed to have an inner radius of 1.24 m and a granularity $\Delta\eta \times \Delta\phi$ =0.0175×0.0175 using

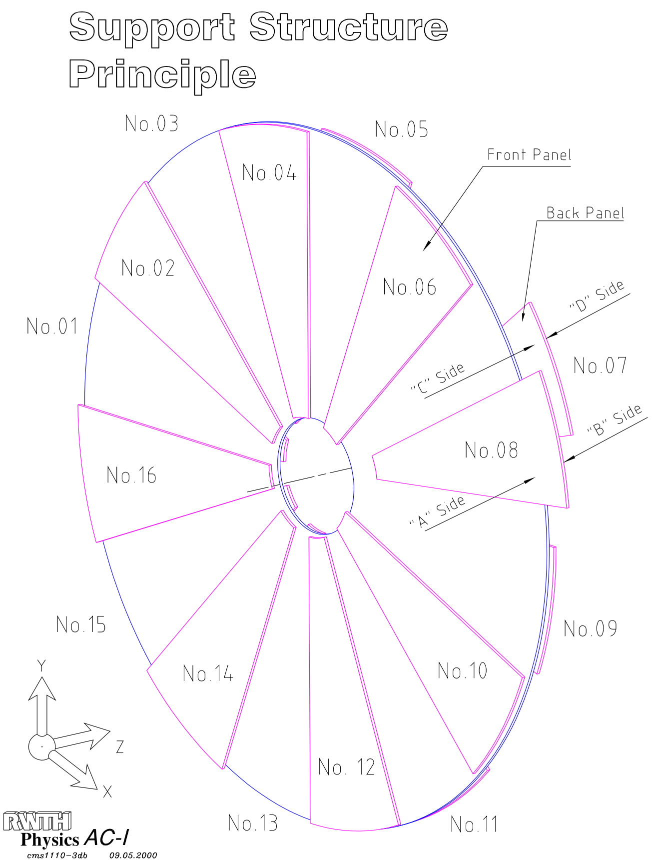


Figure 1.10: *Arrangement of petals in an endcap wheel. Each panel will be equipped with silicon modules at both sides.*

23 cm (26 $\chi_0$) long crystals with a front face of $\sim$22$\times$22 mm$^2$ for a total crystal volume of 8.14 m$^3$ [9].

In the ECAL barrel, an array of 6$\times$2 such crystals is assembled together constituting a submodule. Longitudinal walls of the crystals are covered with reflective coatings. The positions of the crystals within the submodules are fixed with precise plastic pins. A group of 12$\times$4 submodules (tilted 3 degrees to avoid projective gaps) is assembled into a "supermodule" (see figure 1.11). There are 8 supermodules in $\eta$ and 18 in $\phi$.

In the endcap ECAL [8]-[11] the front and rear faces of the crystals are slightly larger than in the barrel, but their length is shorter thanks to the $3\chi_0$ of absorber (endcap preshower). Arrays of 5$\times$5 crystals form supercrystals, arranged in a XY grid to cover the majority of the endcap area (see figure 1.12).

The relatively low light output of the lead tungstate demands photodetectors with internal amplification and low noise. The severe radiation environment in the ECAL (dose rate of 0.18 Gy/h at $\eta = 5$ and 15 Gy/h at $\eta = 3$ at design luminosity; neutron flux 2$\times$ 10$^{13}$ n/cm$^2$ after 10

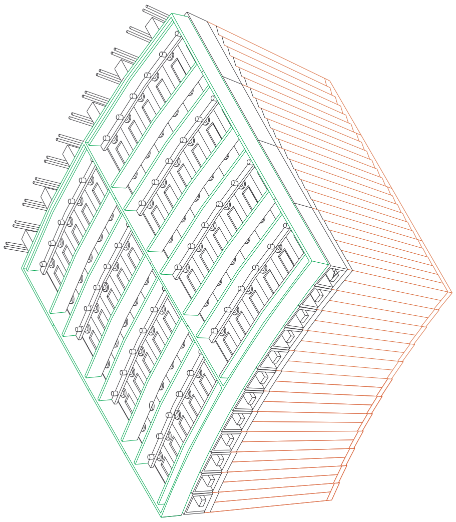

Figure 1.11: *Mechanical structure of a barrel supermodule. Each supermodule weights about 600 kg. The supermodule is made by 12×4 submodules, each submodule being constituted by* $6 \times 2$ *crystals.*

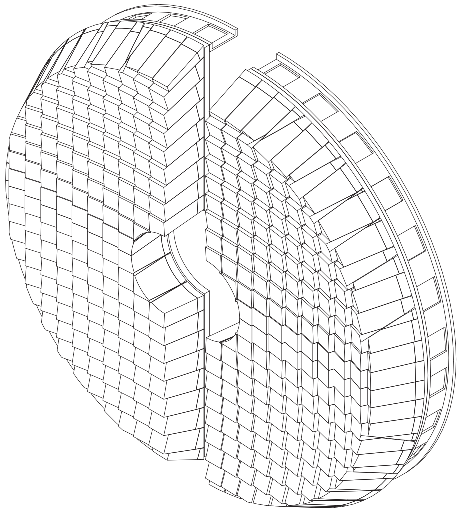

Figure 1.12: *Endcap supercrystal layout.*

years LHC) has allowed to use Avalanche Photodiodes (APDs) in the barrel part but obliged to select Vacuum Phototriodes (VPTs) for the endcaps. Since large area APDs are difficult to manufacture, two such devices per crystal will be used to collect the scintillation photons. APDs are similar to silicon photodiodes, with the exception of a buried *pn* junction reverse biased at a very high electric field, which produces the avalanche. The APD gain is sensitive to variations of voltage and temperature, thus the APD must be operated under stabilized conditions. VPTs have a lower gain than APDs. Their principle of operation is similar to conventional photomultipliers tubes. VPTs have been successfully used in OPAL at LEP. They are insensitive to high magnetic fields [10]. The ECAL VPTs will be constructed by the Research Institute Electron, in Russia. The radiation hardness of the VPTs mainly depends on the window material.

The readout for the CMS ECAL has to work at 40 Mhz in order to match the 25 ns bunch crossing time of the LHC. The readout electronics consists of three parts. A Very Front End (VFE) electronics amplifies the analogue signal from the APD or VPT. Then a Front End Electronics processes pedestal adjustment and zero suppression. It incorporates a 11 bit, 80 Mhz ADC for compression and digitization. Digital signals are transmitted by means of optical fibers to the counting room. Finally, a multichannel DAQ and signal processing module will send data both to the trigger and to the central DAQ system.

Irradiation does not affect the scintillation mechanism and does not affect intrinsic energy resolution. The effect of radiation is the production of color centers, affecting the crystal transmittance, causing thus a loss in the amount of collected energy. A believed cause for the formation of color centers is the presence of Oxygen vacancies [9]. Extensive R&D work has been carried out to improve the crystal radiation hardness through the optimization of stoichiometry and through doping [11].

CMS will utilize a preshower detector in the endcap region (shown in figure 1.13). Its main function is to provide $\gamma - \pi^0$ separation. The preshower detector contains two thin lead converters followed by silicon strip detector planes. Photons incident in the absorber will start to shower, giving signals in the silicon detector. The impact position of the electromagnetic shower is determined by the center of gravity of the deposited energy. The accuracy is typically 300 $\mu$m at 50 GeV. The energy deposited in the absorber must be measured to correct the energy measured by the crystals. In the barrel the rejection of $\pi^0$s in jets which fake two photons can be performed by the crystals due to the relatively large separation between the two photons from the $\pi^0$. In the endcaps the separation is much smaller, necessitating therefore a fine-granularity preshower detector.

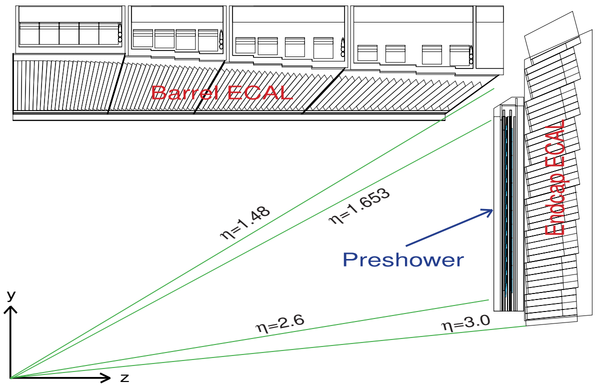


Figure 1.13: *View of a quarter of the electromagnetic calorimeter, showing the position and orientation of crystals and illustrating the position of the endcap preshower [12].*

To maintain the preshower performance during the lifetime of the experiment, the endcap silicon detector has to be operated at $-5°$C, the external surfaces being at ambient temperature of the neighboring detectors.

### 1.4.3 The Hadronic Calorimeter

The Hadronic Calorimeter (HCAL) will play an essential role in the identification and measurement of quarks, gluons and neutrinos by measuring the energy and direction of jets and missing transverse energy flow in events. The hadron calorimeter (HB) [13] barrel will be mounted on rails inside the 4 T field. The barrel has an inside diameter of about 2 m and outside diameter of about 3 m. The $\eta$ and $\phi$ segmentation is $0.087 \times 0.087$ covering $|\eta| < 1.5$. The central barrel consists of 36 wedges. Each wedge is a 20 degree stack, as shown in the longitudinal view in figure 1.14. Shaded areas represent copper layers, hollow areas containing scintillators. The plastic scintillators are 4 mm thick tiles and are grouped in layers each one called megatiles. In turn, the barrel calorimeter still has an extra layer (two layers near $\eta = 0$) of scintillators outside the superconducting magnetic coil and cryostat to sample the energy leakage from the barrel calorimeter. It is called Outer Calorimeter (HOB).

Light emission from each tile is in the blue spectrum ($\lambda = 410 - 425$ nm). The light is collected using a $\sigma$-shaped wavelength shifting fiber embedded in a groove in the tile (see figure 1.15). The fiber is connected to a clear fiber that takes the signal out to a decoder box, where the optical signals from the megatile layers are grouped into towers according to $\eta - \phi$ interval. The tower signals are detected and converted into fast electronic signals by photosensors. For the barrel and endcap detectors, the photosensors are hybrid photodiodes (HPDs). For the very forward detectors (see below), conventional photomultiplier tubes are used [13]. HPDs are capable of operating in high axial magnetic fields and provide a linear response over a large dynamic range from minimum ionizing particles (muons) up to 3 TeV hadron showers. The electronic signals from the HPDs are processed and digitized using special front end integrated circuits called QIE (charge,integration and encode) chips.

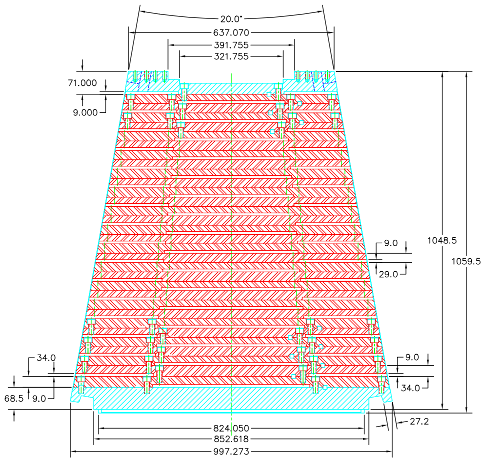


Figure 1.14: *2D view of a 20 degree barrel wedge. Slots held scintillator megatiles. Upper part of the wedge points towards the interaction vertex.*

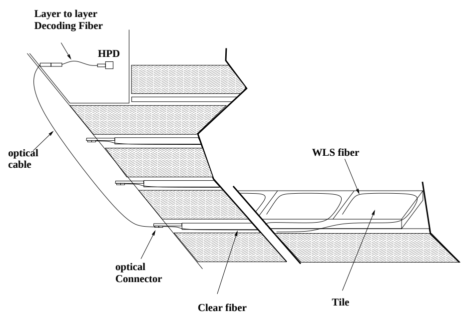


Figure 1.15: *Naive sketch of the optical readout system for the HCAL Barrel and Endcap calorimeters. The tiles are drawn in perspective.*

The endcap hadronic calorimeters (HE) are attached to the muon endcaps and have about 10 interaction lengths. They are about 1.8 m thick, with an inner radius of 40 cm and outer radius of about 3 meters. The $\eta - \phi$ segmentation matches the central barrel, except near the $\eta$ =3 region, where the segment size is 0.17×0.17. There are 19 layers of scintillator megatiles.
Yet another calorimeter at $3 < |\eta| < 5$ is made of iron and quartz fibers, as active media. It resides in a very high radiation area and therefore cannot be constructed of conventional scintillator and waveshifter materials. Hadronic showers are sampled at various depths by the quartz fibers, of selected lengths, which are inserted into the absorber plates. The energy of jets is measured from the Čerenkov light signals produced as charged particles pass through the quartz fibers. These signals result principally from the electromagnetic component of showers, which results in excellent directional information for jet reconstruction. Fiber optics convey the Čerenkov signals to photomultiplier tubes located in radiation shielded zones to the side and behind each calorimeter.

### 1.4.4 The Muon System

The CMS Muon System is formed by two separate parts: the barrel and the endcap system. The Muon System has three purposes: muon identification, muon trigger, and muon momentum measurement.

The Barrel Muon System utilizes drift chambers as tracking detectors, while the Endcap part will use Cathode Strip Chambers (CSC). This election was driven by the low expected background rate (charged particles, hadrons) and by the relatively low intensity of the local magnetic field. Background rates mainly define the detector parameters. The major backgrounds occur at large $\eta$, in the endcaps region. Sources of background are the CMS beam pipe and Forward Hadron Calorimeter [14]. Among the endcaps, the first CSC will be the most affected with total fluences of $10^3$ Hz/cm$^2$ at $\eta = 2.5$. Background rates on the other endcaps are one order of magnitude smaller, while become reduced down to 10 Hz/cm$^2$ in all barrel chambers.
Stray magnetic field will be present in the barrel chambers. The magnetic field in the barrel chambers can be decomposed into two components: axial (along Z) and radial (along R). The axial component reaches a small value (less than 0.4 T) and is constant with Z, except in the dead spaces between wheels (inside the iron). The radial component reaches significant values in MB1 near the Endcaps. On the other hand, the radial component is not constant and may invert its sign near the iron structures.
The trigger capabilities of both brands of detectors will be complemented with the use of gaseous parallel-plate chambers (Resistive Plate Chambers). They combine a moderated spatial resolution with excellent time resolution. Trigger signals coming from the drift tubes, CSCs and the RPCs will proceed in parallel to the Global Trigger in order to perform efficient rejection of background, track identification and applying of $p_t$ cuts.

**Drift Tube Chambers**

The CMS Barrel System is made of four layers of Drift Tube Chambers. The three innermost layers contain 60 drift chambers each while the outer layer contains 70. The muon chamber design is modular: the basic tracking unit is a cell or drift tube (ionization gas detector), made of a wire and electrodes shaping the electric field within the cell. A single array of consecutive cells forms a layer. A group of 4 such layers (staggered by half a cell, thus resolving left/right uncertainty) forms a Super Layer (SL). A drift tube chamber or Muon Chamber is made of three SLs. The two outermost are employed for the measurement of the muon $\phi$ coordinate and have the wires parallel to the beam axis, the inner one measures the Z coordinate with wires perpendicular to the beam axis. In order to create a solid and light frame while increasing the angular resolution, an aluminum honeycomb spacer, 128 mm thick, separates the Z and outer $\phi$ SLs. The chamber design ensures redundancy, since the muon crosses more cells than geometrically needed to define the track [15].
The drift cell functioning is based in the constancy of the drift velocity of electrons for certain gas mixtures, independently of the reduced electric field $E/P$ ($E$ is the magnitude of the electric field, $P$ the gas pressure). If the value of the drift velocity is constant, the drift time of the electron can be measured and thus the passage of a muon is calculated from a linear relationship. Typical drift times are about 400 ns.
The proposed cell has varied since the TDR design [14]. Five electrodes shape the electric field inside the cell. The wire itself, which collects the electrons, two electrodes on the inner sides of the I beams (lateral supports in figure 1.16) and finally two in the inner sides of the aluminum plates. The latter improve the time-position linear relation ship. Both, aluminum plates and I beams are grounded. Therefore, the electrodes are sticked to them, and electrically isolated by Mylar strips. Cell dimensions are 42 mm width by 13 mm height with 50 $\mu$m diameter anode wire. The wire length varies from about 2 to 4 m, from the smallest (inner) to the largest (outer) chambers. As active gas, a mixture of $Ar/CO_2$ 85%/15% will be utilized.

In order to ensure an efficient muon momentum measurement, the target chamber resolution must be 100 $\mu$m in the $R\phi$ plane and 150 $\mu$m in the Z direction. This will be achieved by 8 track points measured in the two $(R, \phi)$ SL, provided the maximum deviation from linearity of the cell space-time relation be less than 100-150 $\mu$m and the wire resolution be better than 250 $\mu$m. In order to reach the cited performance, the position placement precision of the electrodes is 300 $\mu$m. The wire pitch tolerance inside one layer and the misalignment between layers in the same SL has to stay within 100 $\mu$m. Misalignment between SLs of a chamber should be less than 500 $\mu$m and be measured better than 100 $\mu$m.

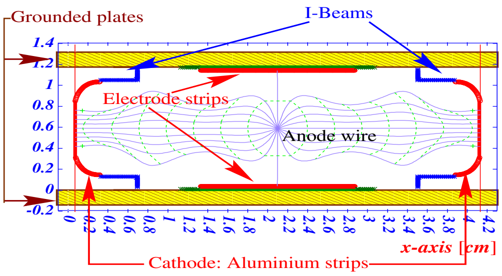


Figure 1.16: *Current cell design showing the geometry of the several components and isochronous lines. Cathodes on the inner sides of the I beams and upper and bottom layers are sticked and isolated with Mylar.*

Front end electronics, placed inside the gas volume, will provide signals grouped by 16 channels [14]. The signals are taken out to Read Out Boards which will have 32-channel TDCs and will receive up to 128 differential signals. The readout boards will receive trigger, timing and control (TTC) signals. After digitization, data are collected by Read Out Servers ROS, one per chamber, and sent to a ROS Master. Each ROS Master receives data from a sector (4 barrels), packs in one data block and sends the data to a Front End Driver.

### Cathode Strip Chambers

CSC chambers are arranged to form three disks, called stations ME1, ME2, ME3 [14]. The station ME1 has three rings of chambers (ME1/1, ME1/2, ME1/3), while the other two stations are composed from two rings of chambers (MEn/1 and MEn/2). All but the ME1/3 chambers overlap in $\phi$. The cracks between chamber rings are not projective, thus coverage defined as at least 3 chambers on a muon path is close to 100%.

CSC are multiwire proportional chambers in which a cathode plane is segmented into strips running across wires. An avalanche developed on a wire induces on the cathode plane a distributed charge of well known shape which is defined by the electrostatics. Their orthogonal segmentation allows the calculation of two coordinates from a single plane.

A typical CSC is shown in figure 1.17. Large chambers cover 10 degrees sectors, and smaller cover 20 degrees. Strips with widths from 3 to 16 mm run radially providing the phi-coordinate of the track. Wires are stretched across strips without intermediate supports and are grouped in bunches from 5 to 16, for readout purposes. For the ME1/1 chambers (endorsed in the 3T $B_z$ field) the wires are strung at 25°.

Seven panels are stacked together to form six gas gaps (see figure 1.18). Six panels have strips milled on one side, the other side being an uninterrupted ground. Wires are wound in three panels onto both sides and grouped into 5 independent HV power supply segments.

Cathode and anode front-end boards are mounted directly in the CSC modules. Data are sent by cables to readout boards also mounted on the chambers. Finally the mother board sends readout and trigger data to the central DAQ and to the trigger system (see section 1.4.5). Trigger, timings and control signals are then fed back.

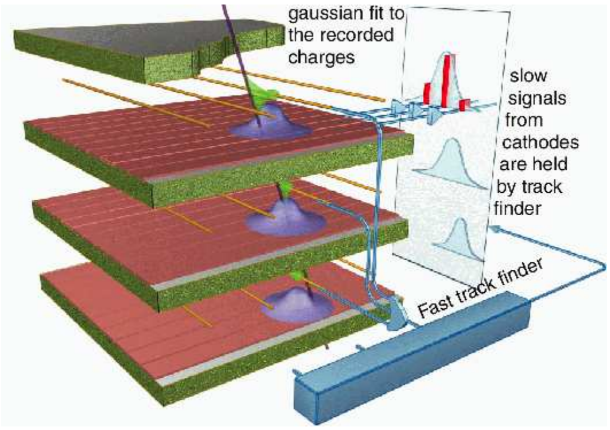


Figure 1.17: *Artistic view of a CSC chamber and the particle detection. An avalanche on a wire induces a charge on several strips of the cathode plane [16].*

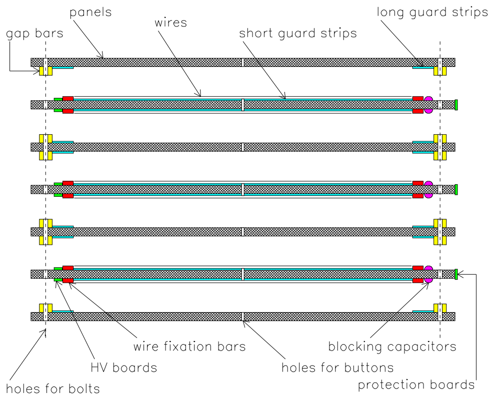


Figure 1.18: *CSC panels. Those with wires are anode panels, the rest cathode panels. Six gas gaps are enclosed by seven panels [14].*

### Resistive Plate Chambers

Resistive Plate Chambers (RPC) are gaseous parallel-plate detectors combining moderated spatial resolution with a time resolution comparable to that of scintillators [17]. They are suited for fast space-time tracking as required for the muon trigger.

When an ionizing particle traverses a RPC (see figure 1.19), a cluster of electrons starts an avalanche multiplication. The drift of the charge towards the anode induces on the pick-up electrode a *fast* charge (that is, charge coming from the first two clusters of the trail [18]), which represents the useful signal of the RPC.

The RPCs (see figure 1.20) are made out of two 2 mm thick bakelite square plates ($100\times100$ mm$^2$) with a resistivity of about $2\times10^{10}$ $\Omega$cm separated by a 2 mm $\pm$ 30 $\mu$m gas gap. The plates separation is provided by insulating spacers about 10 mm in diameter. The outer sides of each plate are coated with conductive graphite paint to form the HV electrodes. The read out is performed by means of aluminum strips separated from the graphite coating by an insulation film.

In normal construction, two such assemblies are placed one on top of the other (double gap RPC), with the readout strips in the center. The entire sandwich is gas tight. The total induced signal will be the sum of the two gaps.

RPCs are operated in avalanche mode: the electric field across the gap is moderate, but the RPC operation gets complemented with a robust front-end signal amplification. In the avalanche region, the drift velocity grows linearly with the applied electric field. RPC operation can be summarized as low gain and high rate. Time tagging capabilities of RPCs is better than 25 ns (LHC bunch crossing time).

A dedicated muon trigger detector, based on RPCs can then identify bunch crossing even in the presence of a high rate and background. The trigger main functions are the identification of

muon track candidates, assignment of bunch crossing and transverse momenta estimation. RPCs are expected to respond with high efficiency and to withstand gamma and neutron background that can reach up to $10^3$Hz/cm$^2$. Therefore, their rate capability should reach 1 kHz/cm$^2$ which demands working gains of $10^7$. At this gain levels, the gas gap width determines the time performance of the detector, while the electrode resistivity will determine the rate capability.
Operation below the 25 ns limit requires a 4-5 ns signal time walk from the strips. The number of contiguous strips giving signal (cluster size) is $\leq 2$, in order to achieve the required momentum resolution.
Each muon station is equipped with one RPC plane except the two innermost barrel stations, containing two RPCs. This is because low momentum muons ($p_t$ <5-6 GeV/c$^2$) cannot reach the outer stations, and therefore a special low $p_t$ trigger has been devised. In the forward direction, the RPCs will have trapezoidal shape with strips running along radial direction. Only one RPC per CSC chamber will be employed.
A front end board (FEB) is connected directly to the RPCs, containing 24 channels of RPC front-end electronics. Inside the FEB, amplification and analog to digital conversion occurs.

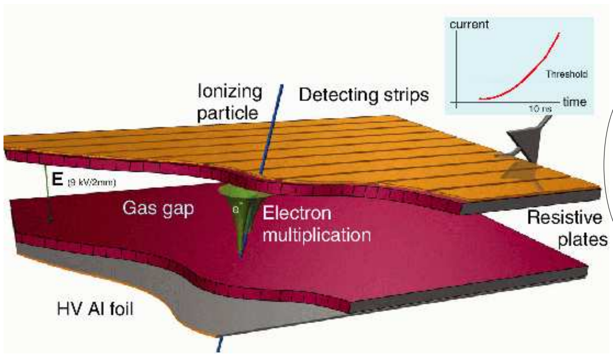


Figure 1.19: *Artistic view of the RPC principle. Two electron clusters avalanches produce signal in the anode strip plane. A proper threshold setting allows the detection of the signal with high resolution [16].*

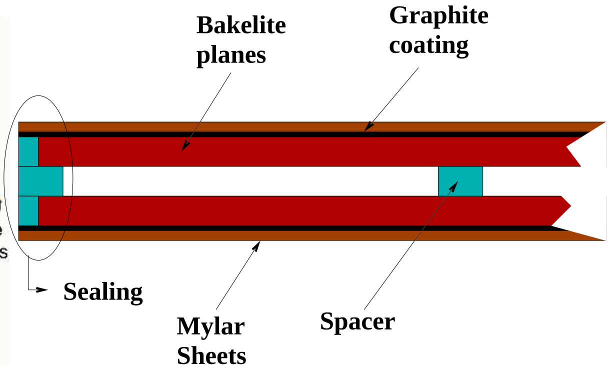


Figure 1.20: *Section of the end of a RPC, showing plates, spacers, frame and seal of one gas gap. Double gap RPCs are composed of two single gap RPC, one on top of the other [14].*

### 1.4.5 The Level-1 Trigger

The purpose of the Trigger system of an experiment is the filtering of interesting events among a stack of overwhelming background. Besides, the Trigger of an experiment can be utilized for other purposes as internal calibrations of detectors employing selected events.
The CMS Trigger system [19, 20] is divided into a hardware implemented Level-1 (L1) Trigger and software higher levels triggers. The Level 1 trigger decision has to be taken after 3.2 $\mu$s, that is, after 128 bunch crossings. In order to avoid any data loss, readings must be buffered in pipelined memories.

Trigger decisions are based on the output of algorithms performed on Trigger objects, namely candidate electrons, jets or muons. In turn, these objects are determined by Calorimeter and Muon specific Triggers. No information from the tracking system is employed, although, if needed, it may be included into the Trigger operation [20].
The final goal of the Trigger system is the reduction of the 40 MHz bunch crossing frequency to a data flow of 100 Hz. This value is set by the capacity of the storage media and computing resources of the Higher Level Trigger systems. The nominal output rate of the Level-1 trigger system will be 100 kHz. In practice, a safe maximum rate of 30 kHz will be adopted, in order to cope with any underestimation of the event cross-sections.

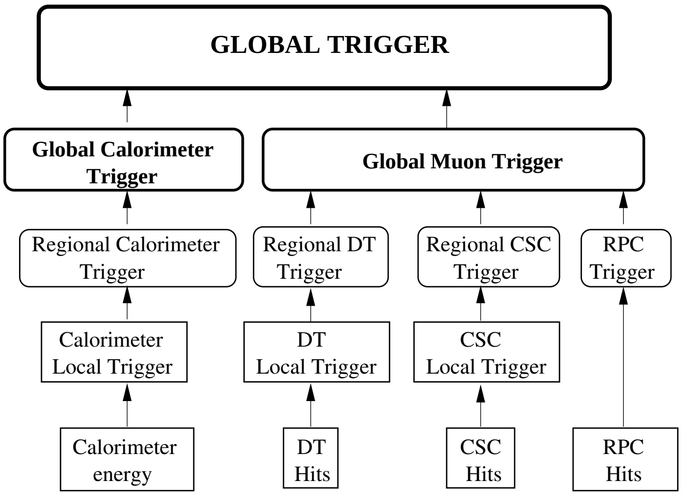


Figure 1.21: *The CMS Level-1 Trigger System [20].*

The L1 trigger system of CMS is realized in several steps (see figure 1.21). On top, the Global Trigger will handle decisions coming from Regional and Global Calorimeter and Muon Triggers. The ultimate goal of the L1 Trigger system will be the production of the L1 Accept or Reject signal (L1A), then transfer it to the Timing, Trigger and Control (TTC) System, which will broadcast it to the different subdetector front-end electronics to gather the data.
Trigger objects are sorted in a ranking determined from transverse energy or momentum and quality information. The highest rank objects are always selected. These objects are then combined in Trigger algorithms. An algorithm is a combination of trigger objects satisfying defined threshold, space (pseudorapidity and azimuth) and quality requirements. For physics runs, 128 parallel algorithms will be performed. The L1A decision will be taken applying a final OR to the 128 algorithms although up to eight final OR's can be made available. The option to record the former and the following events to the L1A selected is foreseen to control pile-up effects or noisy channels.

### Calorimeter Trigger

The Regional Calorimeter Trigger (see figure 1.21) uses energy depositions in the trigger towers of the electromagnetic and hadron calorimeters to find electrons or photons candidates, jets, isolated hadrons (from $\tau$ decays) and to calculate transverse energy sums [20].

The Global Calorimeter Trigger (figure 1.21) sorts these objects and selects the four with highest rank in each category sending them to the Global Trigger.

### Muon Trigger

The muon system of CMS (see section 1.4.4) is based on drift tube chambers with bunch crossing identification capability[2] and CSCs in the forward region. Dedicated Trigger chambers, RPCs, are mounted on both of them. In the DT chambers, the Bunch and Track Identifier (BTI) looks for aligned hits in each superlayer. Then, the Track Correlator combines the track segments in each superlayer and sends the best two track segments in the $R\phi$ plane to the DT Regional Muon Trigger.
For the CSCs, the best three local charged tracks per chamber are transmitted to the CSC Regional Muon Trigger.
The best four DT and CSC muons are sent to the Global Muon Trigger (GMT) which combines them with the top eight patterns of hits found at the RPCs. The GMT performs then a matching and selects the best four muon candidates which are finally sent to the Global Trigger.

## 1.4.6 The Magnet system

In a collider detector, the magnet definition constraints most the subsystems which will be built around it. For CMS, toroidal and solenoidal magnetic fields were studied. Finally, the CMS community chose the solenoid magnet because it provides the same bending power of a toroid with smaller overall size and, besides that, eases the trigger definition since tracks are included in the transverse plane and point to the interaction vertex.
The CMS magnet system [21, 22, 23] will be the largest superconducting system in the world and will become a new step in the development of detector magnets. The CMS magnet system (figure 1.22) is the conjunction of a superconducting coil embedded within a vacuum tank, surrounded by the return iron yoke. The solenoid design parameters are, a 12.5 m long superconducting coil, with a free inner diameter of 5.9 m and an uniform central magnetic field of 4 T. The iron yoke is divided into barrel and endcap parts. The barrel part is formed by 5 vertical rings, 1200 tonnes each. The central one supports the vacuum tank, within which, the coil will be housed. The forward endcap wheels are independent from each other, allowing thus access to CSC chambers. Each wheel weights about 2300 tonnes. The two wheels closer to the vertex will withstand an attraction force of about 85 MN.
Muon, tracking and calorimeter systems are benefited from the election of a 4 T magnetic field [21]:

- In the muon system, the robustness of the muon measurement depends on the independent measurement of the muon direction in the first station after the coil and the combined measurement of the sagita in the four muon stations. Reducing the magnetic field intensity would spoil the momentum measurement resolution.
- In the inner tracking system, a lower magnetic field reduces the sagita and increases the occupancy in the outer barrel and endcaps.

[2] The bunch crossing tagging is performed independently in each of the three SLs by fast pattern recognition circuitry [14]

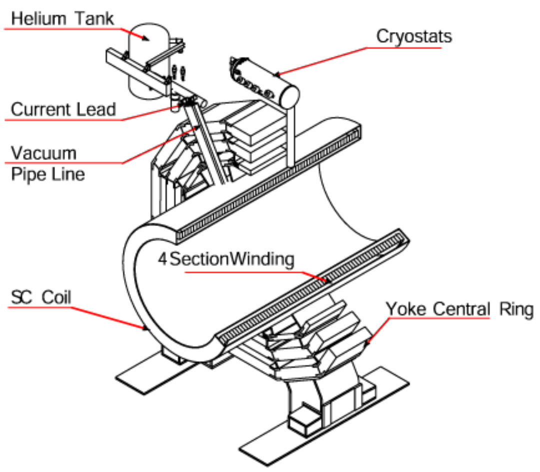


Figure 1.22: *Open view of the superconducting coil inside its vacuum tank. [21].*

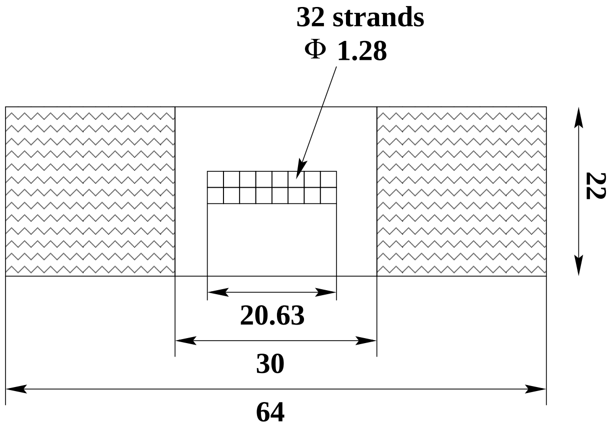


Figure 1.23: *CMS conductor layer cross section (units are mm). A 32 strand superconducting cable is extruded inside the coil. Aluminum alloy are shown patterned [22].*

- On-line calibration of the electromagnetic calorimeter requires a number of precisely measured electrons. The number of electrons needed depends on the ratio of energy measured in the ECAL versus momentum measured in the Tracker. Reducing the magnetic field intensity spoils the momentum measurement in the tracker and doubles the number of electrons needed for the calibration.

A reduction of the magnetic field intensity would generate a worse performance of the overall system, which should be compensated with the time extension of the detector operation, increasing thus the cost of the experiment.
The CMS coil consists of five cylindrical modules mechanically and electrically connected. Each module is wound with four layers of conductor. The conductor has been designed to resist the forces induced by the magnetic and thermal loads. This resistance is achieved reinforcing the aluminum profile which houses the conductor with two sections of aluminum alloy welded using electron beams (see figure 1.23).
Finally, the magnet cryogenization, power supply, vacuum pumping and Slow Control of the System is provided through the ancillaries of the coil (see figure 1.22) from the service cavern (separated from the CMS hall by a 7 m thick wall).

## 1.5 A glimpse on CMS physics potential

The Compact Muon Solenoid, as presented in the former sections, has been designed to give answers on the most important questions in high energy physics nowadays. The different subdetectors have been designed and optimized to best measure the physical signatures of these processes, a typical example being the CMS ECAL, defined to reconstruct the invariant mass of

the two photons coming from an intermediate mass Standard Model (SM) Higgs boson decay to about 10 MeV.
The understanding of the origin of mass will be a central issue but CMS will also cover a much wider high energy physics spectra. If Supersymmetry (SUSY) is a true symmetry of Nature, and it is realized at the TeV scale, it will almost certainly be seen in CMS. The Compact Muon Solenoid will also study subjects as B-physics, heavy ions with interesting phenomena of gluon-plasma production, top physics, search for compositness of quarks and leptons, electro-weak precision tests and measurements of parton distribution functions.

### 1.5.1 SM Higgs search

The introduction of the Higgs boson in the SM allows the masses of all particles to be expressed in terms of their couplings to the Higgs. The theory does not predict the mass of the Higgs, but it does predict its production rate and decay modes for each possible mass. However it is possible to set mass limits attending to current measurements and reasonable arguments. Global fits to electroweak data imply an upper limit on the Standard Model Higgs mass of 236 GeV (95% C.L.) [2]. On the other hand, precise LEP measurements have excluded a Higgs boson bellow 114 GeV. Figure 1.25 summarizes the expected observability of the SM Higgs in CMS assuming an integrated luminosity of 100 fb$^{-1}$. The CMS detector can probe the entire mass range up to m$_{Higgs}$ ~1 TeV with a signal significance well above $5\sigma$.
Depending on the Higgs mass, different experimental signatures will arise. The most promising channels are $H \to \gamma\gamma$, $H \to ZZ^{\star}(Z) \to 4l^{\pm}$, and $H \to W^+W^- \to 4l^+\nu l^-\overline{\nu}$. Figure 1.24 shows the main production processes that will be reachable at the LHC.

$H \to \gamma\gamma$

It is the most promising signature for a SM Higgs with masses between the LEP200 limit and ~150 GeV. The detection of this signal requires an excellent $\gamma\gamma$ mass resolution of $\leq 1\%$ (i.e. $\leq 1$ GeV for $m_H = 100$ GeV) and a very good rejection of $\pi^0$s (coming from jet$-\gamma$ events) where the jet fragments to a leading $\pi^0$, and the $\pi^0$ decays to single photons ($\sim$ 99% branching ratio).
The resolution of the two-photon mass depends on the energy resolution and on the uncertainty on the angle between the two photons. The correct interaction vertex can be inferred using charged tracks and the barrel preshower at any luminosity. For an integrated luminosity of 30 fb$^{-1}$ the signal significance (signal over background square root) for this channel is above $5\sigma$ (see figure 1.25).

$H \to W^+W^- \to l^+\nu l^-\overline{\nu}$

A recent study, carried out after the publication of the Technical Proposal, has demonstrated that the $H \to W^+W^- \to l^+\nu l^-\overline{\nu}$ channel can be used to observe statistically significant signal in the Higgs mass range of 130-200 GeV [25]. The analysis utilizes that the signal events from gluon-gluon scattering (main production process of a SM Higgs) are more central (in the azimuth variable) than the W$^+$W$^-$ background from $q\overline{q}$ scattering. The analysis shows that this channel should allow to discover a SM Higgs with 5 standard deviation for a Higgs mass between 140-200 GeV and integrated luminosities below 5 fb$^{-1}$.

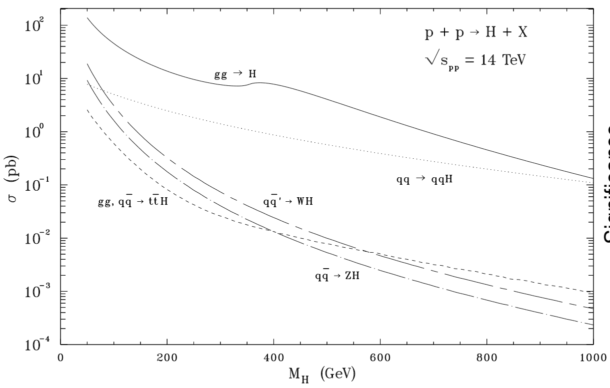


Figure 1.24: *Cross-section (next to leading order) for the Higgs production processes as a function of the Higgs mass.*

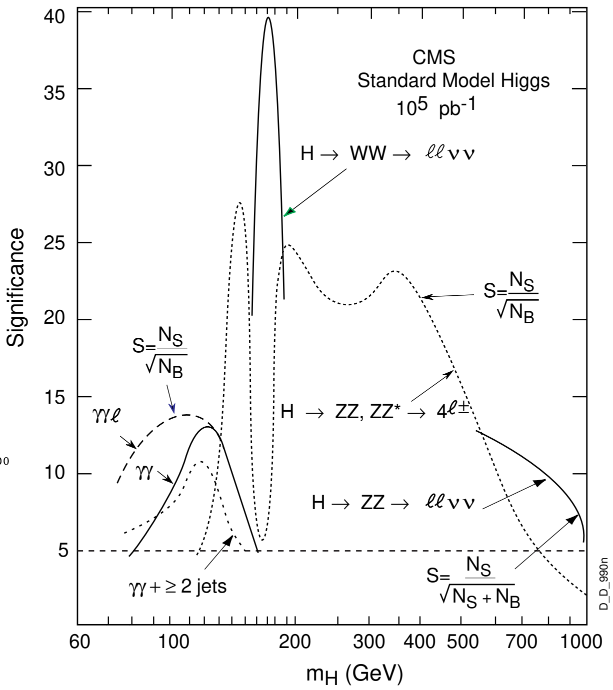


Figure 1.25: *Expected observability of Standard Model Higgs in CMS with $10^5$ $pb^{-1}$. [24]*

$H \rightarrow ZZ^{\star} \rightarrow 4l^{\pm}$, $H \rightarrow ZZ \rightarrow 4l^{\pm}$

In the leptonic channels, the detection relies on the excellent combined performance of the muon chambers, tracker and electromagnetic calorimeter.

Bellow $2\mathrm{m}_Z$, the event rate is small and the background reduction more difficult, as one of the Z's is off mass-shell. The $ZZ^{\star}$ background is irreducible. Detailed simulations [26] of this channel show that a luminosity of $10^5$ $\mathrm{pb}^{-1}$ is needed in order to get a significance above 5 (figure 1.25). The $H \rightarrow ZZ \rightarrow 4l^{\pm}$ channel is sensitive, even with only $10^4$ $\mathrm{pb}^{-1}$, over a wide mass range, from $2\mathrm{m}_Z$ up to about 400 GeV. The main background is non-resonant ZZ production.

### 1.5.2 SUSY searches

Even though the SM describes existing data very precisely, it is known that this model is incomplete. One problem of the SM is the instability of the mass of the Higgs boson under radiative correction in the presence of a high scale like the Planck scale ($\approx 10^{19}$ GeV). This divergence disappear in Supersymmetry, because cancellations between the virtual effects of SM particles and their supersymmetric partners.

Extrapolating the coupling strength of the fundamental forces measured at mass scales of a few 100 GeV to energy scales relevant for cosmology (about $10^{15}$ to $10^{19}$ GeV) does not lead to

unification in the SM. However unification of the electromagnetic, weak and strong forces at the GUT scale ($\approx 10^{15}$GeV) is predicted in SUSY.
In SUSY each fermion (boson) has a superpartner of spin 0 (1/2). The Higgs sector is also extended to at least five Higgs ($h$,$A$,$H^0$,$H^{\pm}$) in the Minimal Supersymmetric Standard Model (MSSM). In SUSY theories there is even room for explaining the dark matter as being due to neutralinos.
As an example for CMS, for the lightest Higgs $h$, the only established signature appears to be the decay $h \rightarrow \gamma\gamma$. If $m_A$ >400 GeV, then SM rates and sensitivity are found. Otherwise the branching ratio is too small to observe a significant signal. Further details are found, for instance, in reference [2].

### 1.5.3 B physics

CP violation implies that there is a small difference in the decay rates of mesons containing the strange quark, $\overline{K^0}$ and $K^0$. One possible explanation is that there exits yet another force in nature that is not matter-antimatter symmetric [16]. Another, more popular explanation is that the weak interaction, through which kaons decay, can actually distinguish between matter and antimatter. If this is true, CMS should be able to observe a large asymmetry in the decay rates of matter versus antimatter mesons that are made of heavy quarks heavier than the $s$.
The decay $B^0$ or $\overline{B^0} \rightarrow J/\psi K^0_S$ presents a very clean experimental signature. The particle content ($B^0$ or $\overline{B^0}$ meson) that gave the decay can be determined from a muon in the event. An asymmetry in the two rates would signal CP violation. This would be the first time that CP violation would be observed outside the neutral kaon system.

# Bibliography


[1] Table 1 and the introductory part of this chapter have been obtained from the LHC web page
http://lhc.web.cern.ch/lhc/

[2] Felicitas Pauss, Michael Dittmar, *Experimental Challenges at the LHC*, CMS CR 1999/008.

[3] J. Stirling, ASI Summer School, St. Croix, 1998

[4] M. Della Negra et al., *Proceedings of the Large Hadron Collider Workshop*, Aachen, Vol. III.

[5] *CMS. The Tracker System Project. Technical Design Report*, CERN/LHCC 98-6, CMS TDR 5, 15 April 1998

[6] *Addendum to the CMS Tracker TDR by the CMS Collaboration*, CERN/LHCC 2000-016, CMS TDR 5 Addendum 1, 21 February 2000

[7] Stefan Schael, *The CMS Tracker*, LHCC meeting, CERN, 16 May 2000.
http://accms04.physik.rwth-aachen.de/~schael/

[8] *The Electromagnetic Calorimeter Project*, Technical Design Report, CERN/LHCC 97-33, 15 December 1997.

[9] F. Nessi-Tedaldi, *The CMS ECAL project – Overview and status report*, CMS CR 1999/028.

[10] D. Barney, *A pedagogical Introduction to the CMS Electromagnetic Calorimeter*, CMS CR 1998/004

[11] H.F.Chen et al, *Radiation Damage Measurements of Undoped Lead Tungstate Crystals for the CMS Electromagnetic Calorimeter at LHC*, Nucl. Instr. Meth. A 414 (1998) 149.

[12] Edwige Tournefier, *The preshower detector of CMS at LHC*CMS CR 2000/010

[13] *CMS. The Hadron Calorimeter Project. Technical Design Report.* The CMS Collaboration, CERN/LHCC 97-31, 20 June 1997

[14] *CMS. The Muon Project Technical Design Report.* The CMS Collaboration, CERN/LHCC 97-32.

[15] Jorge Mocholí Moncholí, *Diseño y estudio de cámaras de deriva para el Detector CMS de LHC*, PhD. thesis, Madrid 1998

[16] Extracted from CMS Posters (TriDAS Gallery) http://cmsdoc.cern.ch/cms/TRIDAS/html/outreach.html

[17] R. Santonico and R. Cardarelli, Nucl. Instr. and Meth. 187 (1981) 377-380.

[18] M. Abbrescia et al., *Properties of $C_2H_2F_4$ based gas mixtures for avalanche mode operation of Resistive Plate Chambers*, CMS Note 97/004.

[19] *CMS. The Trigger and Data Acquisition project, Volume I. The Level-1 Trigger*, CMS TDR 6.1, CERN/LHCC 2000-038, 15 Decemeber 2000.

[20] Claudia-Elisabeth Wulz, *Concept of the First Level Global Trigger for the CMS Experiment at LHC*, CMS Note 2000/052

[21] *CMS. The Magnet Project Technical Design Report*, CERN/LHCC 97-10, CMS TDR 1, 2 May 1997

[22] F. Kircher *et al.*, *Status Report on the CMS Superconducting Solenoid for LHC*, CMS CR 1998/019

[23] Alain Hervé, *The CMS Detector Magnet*. Available in the EDMS web page http://edmsoraweb.cern.ch:8001/cedar/cedarw.site_home

[24] R. Kinnunen and D. Denegri, CMS Note 1997/057

[25] M. Dittmar and H. Dreiner, *Phys. Rev. D 55, 167 (1997)* and hep-ph/9608317.

[26] CMS Collaboration, Technical Proposal, CERN/LHCC 94-38, LHCC/P1, 15 December 1994.

# Chapter 2

# The Alignment System of CMS

## 2.1 Introduction

From the point of view of the muon measurement, CMS behaves as a compact muon spectrometer. The detection of muons in CMS will be favored. Attending to the magnetic field intensity, two different technologies will be employed for their measurement. In the barrel region, surrounding the coil of the solenoid, four layers of drift chambers, interleaved with the return iron yoke, will make a redundant measurement of the muon momenta. A muon chamber is made of three superlayers. Each superlayer is made of four layers of drift cells. The drift cell is the basic unit measuring the drift time of a muon, providing a spatial resolution of 250 $\mu$m. Each superlayer will contribute with a measurement of one coordinate. Two superlayers will measure the $R\phi$ coordinate and one layer will measure the $Z$ coordinate. The mechanical design of a drift chamber is driven by the precision in the determination of a point of the muon track, 100 $\mu$m, which is obtained by fit of the individual hits in each cell.
The muon drift chambers will be subject to variable residual magnetic fields, below 0.4 T for all chambers except for the MB1 chamber near the endcaps. There the magnetic field will raise up to 0.8 T. At the level of the ME1/1 chamber the field will be $B_z \approx 3$T. For such a magnetic field the operation of the muon drift chambers is limited, since the drift cell escapes the linear regime. Other gaseous detectors, called Cathode Strip Chambers (CSCs) can operate in large and non-uniform magnetic field, without significant deterioration of performance. CSCs are multiwire proportional chambers in which one cathode plane is segmented into strips running across wires, both of them instrumented, giving thus 2D information of the particle passage. Due to the intense magnetic field, the trajectory of the muons bend more in the vicinity of the first endcap station where the higher precision requirement is needed (75 $\mu$m). For the rest of the chambers the precision will be 150 $\mu$m.
As already sketched, the measurement of the muon momentum is related with its bending in the transverse plane. The radius of curvature $\rho$ and the momentum component perpendicular to the magnetic field ($p_t$) of a muon are related by [1, 2]:

$$\rho[m] = \frac{p_t[GeV/c]}{0.3B[T]} \tag{2.1}$$

The radius of curvature can be obtained from the measurement of the muon trajectory sagita $s$, after traversing a distance $d$ in the magnetic field, using the approximate expression $\rho \approx d^2/8s$.

An error in the sagita measurement corresponds to an error in the muon measurement. The relative error in the sagita measurement is:

$$\frac{\delta s}{s} = \frac{\delta p}{p} \propto \frac{\sigma_s[mm]p_t[TeV]}{d^2[m^2]B[T]} \tag{2.2}$$

where $\sigma_s$ is the resolution in the sagita measurement. The relative resolution deteriorates with the muon momentum and improves linearly with the magnetic field and quadratically with the traversed distance.
The accuracy required in the position of the muon chambers is determined by the resolution demanded in the reconstruction of the momentum of high energy muons. CMS is designed to achieve a combined (Tracker and Muon System) momentum resolution for the region $|\eta| < 2.4$ of 0.5−1% for p$_t \approx 10GeV$, 1.5−5% for $p_t \approx$ 100GeV and 5−20% for $p_t \approx$1TeV. This design accuracy will require the knowledge of the position of the chambers with an accuracy *comparable* to their resolution. In order to quantify the importance of the chambers misalignment in the momentum resolution, a simulation has been performed [3]. As a result, for the most important coordinate from the physics point of view, ($R\phi$ ), the alignment system should reconstruct the positions of the chambers within 150-350 $\mu$m range (for MB1-MB4, respectively) and within the 75-200 $\mu$m range (for ME1-ME4). The constraints are tighter for ME1 and MB1 since most of the muons reach the maximum curvature near the first muon station. These stations give the main contribution to the momentum measurement precision and therefore lead the requirements of measurement resolution of the chamber and the accuracy on their position knowledge.

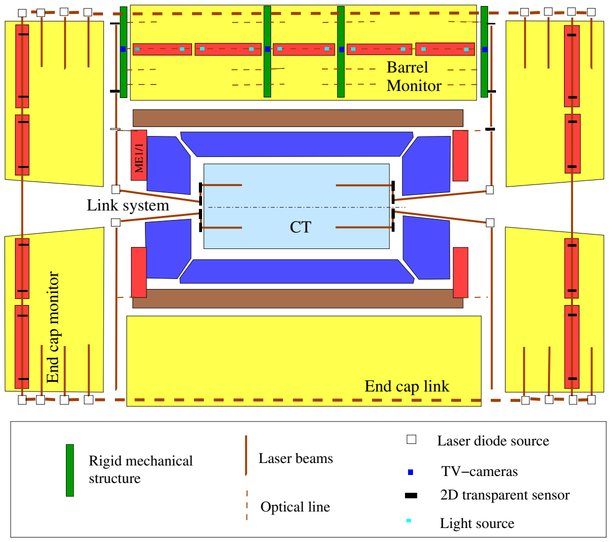


Figure 2.1: *Lateral view of the CMS detector, sketching the Barrel, Endcap and Link alignment systems.*

However, the stability of the muon chambers at the level of the 100 $\mu$m is not guaranteed at all when CMS enters in operation. The expected movements and deflections of the muon spectrometer will exceed this value. To monitor these movements, CMS is instrumented with an optical alignment system that will allow the continuous measurement of the position of the chambers. The information provided by the alignment system can be later on used for off-line correction in the track reconstruction. On the other hand, the best resolution in the muon momentum reconstruction is obtained combining the information given by the tracker and the muon systems on a given trajectory. The alignment system should then provide precise information about the relative position of the muon chambers among them (in the barrel and endcaps), that of the various tracker components and, of course, the position of the muon chambers with respect to the tracker. To cope with all the above, the CMS Alignment System is organized in three blocks:

- The Tracker internal alignment, to measure the positions of the various modules and monitor the eventual internal deformations.
- The Muon Systems (barrel and endcaps) internal alignment, to monitor the relative position among the chambers.
- The Link System, that will allow to relate the position of the various elements of the muon system (barrel and endcaps) with the position of the elements of the tracker and to monitor the eventual movements of elements of both systems.

From these three blocks, the last one is competence of the Spanish groups of Santander (Universidad de Cantabria-IFCA) and Madrid (CIEMAT). The work presented in this thesis has been carried out in the frame of the Link System.
Attending to the azimuthal distribution of the muon system, the CMS alignment system is divided in three $\phi$ planes (active planes for the alignment) to which the three tracking detectors (Tracker, Barrel muon chambers and Endcaps muon chambers) are connected. Figure 2.1 shows the muon alignment scheme for two radial opposite $1/2\phi$ planes. In fact, every $1/2\phi$ plane consists of two independent $1/4$ $\phi$ planes, +Z/-Z mirror image, each one having its own laser light source. All the independent alignment planes are constrained to a common reference using the Tracker.
During detector operation, the system must monitor:

- Large changes from survey positions, due to the magnet forces affecting the return yoke: the expected longitudinal movements (in the sense of the magnetic forces) will go from a few mm to 1-2 cm [4].
- Long-term position stability of the detectors and changes due to thermal effects. With limited gradients ($< 5°$C) across the muon detectors, the thermal expansion of the chambers and their iron supports are expected to be within the submilimeter range.

The range of the movement to be monitored and therefore, the tolerances of the optical paths and dynamic range of the alignment elements, are mainly determined by the deflections produced when the magnet is turned on. During assembly, survey measurements based on photogrametry techniques can provide accurate knowledge of the actual positions of the muon chambers and alignment components. Magnet tests foreseen during the installation period will provide information for detector position offsets. The survey measurements, and the possibility to adjust the key elements of the magnet yoke and alignment system, will allow the efficient use of the full range of the sensors and optical passages of the alignment system.
It should be stressed that the proposed alignment system is not limited to the monitoring of local position changes with time, but provides an absolute measurement of the relative position

of all components. Indeed, the actual measurement does not depend on previous measurements: the alignment system can be switched on and off without loss of precision.

## 2.2 The Tracker alignment system

Before 1999 the CMS Tracker baseline consisted of a pixel detector close to the beam pipe, surrounded by an inner silicon tracker and by an outer MSGC tracker. In 1999, the Tracker Institution Board decided to abandon this design in favor of a tracking system entirely based on silicon detectors. The layout and performance of the new Tracker Layout has been reported on [5] and [6].
The new Tracker is mechanically divided into four sub-detectors: the inner tracker (TIB), the outer tracker (TOB) and the two end-caps (TEC). The thermal screen between MSGCs and Silicon is therefore removed from the old design.
As a consequence of the compacity and higher uniformity of the new design, the former alignment system of the Tracker [7] was changed. The new Tracker alignment system [8] makes use of the Tracker Si-modules themselves (avoiding the error propagation with mechanical transfers) as light detectors and uses tracks for achieving 10 $\mu$m alignment accuracy (the Si-modules resolution is about 20 $\mu$m). Besides, the new design has a lower interference and impact in the Tracker design. As the muon chambers are large scale objects, the muon system can have 6 planes of symmetry. Silicon modules, however, are arranged in rods (Tracker Inner Barrel, Tracker Outer Barrel) and petals (Tracker Endcap Chambers), leading to a sixteen folded symmetry.
The objectives of the Tracker alignment system are:

- Independent alignment of the endcaps, relative alignment of the endcaps and relative alignment of the endcaps with respect to the inner and outer barrel.
- Provide the Link system with $6\times2$ laser beams having well defined position and orientation in the Tracker coordinate frame.

The proposed optical alignment monitor is sketched in figure 2.2.
The alignment of individual endcaps is achieved by laser monitoring of 50% of the TEC petals. The other 50% of the petals are aligned using tracks in the $\phi$ overlap region of the petals. Eight laser beams like “ray 2” and “ray 3” in figure 2.2 will be employed for the optical monitoring.
Another 8 rays of type “ray 4” will be employed for the relative alignment of the TIB and TOB and further relation of the barrel to the Endcaps.
Finally, following the six-folded geometry of the Muon Barrel, six laser beams type “ray 1” and a mechanical disc structure, attached to the outermost wheels of the TEC, will transfer the orientation and position of reference laser beams to the Link system. The $\phi$ coordinate of the Tracker will be inferred from tiltmeters fixed to the mechanical structure, and compared to the measurement of the tiltmeters located in the Muon Barrel region (section 2.5).
Provided the Si-modules are positioned with 50 $\mu$m accuracy within each subdetector (TIB, TOB, TEC) the Tracker alignment system will be able to perform relative alignment better than 100 $\mu$m. This is enough to start the pattern recognition process. After the track fits, the position of the subdetectors will be known with an error of 10 $\mu$m.
The most characteristic features of this subsystem are:

- Usage of laser beams of 1060 nm, suitable for producing measurable signals in the tracker Si-modules.

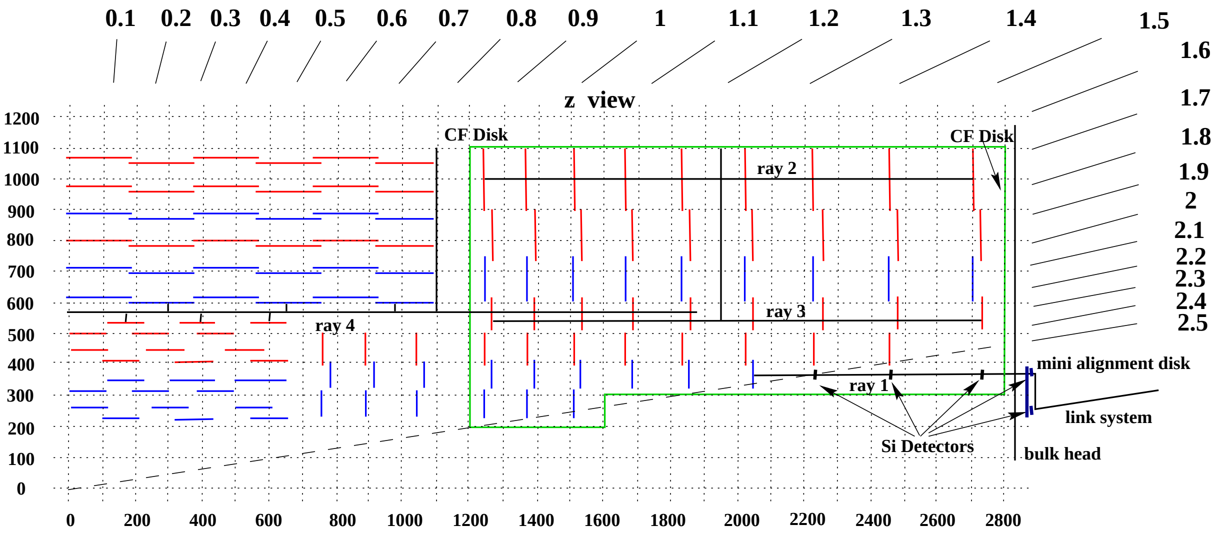


Figure 2.2: *Sketch of the alignment system for the CMS tracker. Ray 1 is used for the link to the muon system, ray 2 and 3 for the internal endcap alignment. Ray 4 connects the two endcaps with the inner and outer barrel [8].*

- Optical monitor hardware is built-in in the tracker structures. All the elements (collimators, tubes and sensors) directly mounted on the tracker elements.
- Combination of optical and tracking data.

The usage of the Silicon HEP detectors as light sensing elements has already been successfully employed in the AMS experiment.

### 2.2.1 Relative alignment

#### Internal alignment of the Endcaps

Laser beams (originated in the counting room) and splitted down in the CMS hall will be injected in the TEC (R≈ 564 ("ray 3") and 1045 mm ("ray 4")) through the same routing as the read-out cables. To provide lines of sight, eight holes of 20 mm diameter are drilled in all end-cap wheels affected. Si-modules in the beam path will have an antireflection coating to increase the transmission reducing the interference and will have a hole in the rear metallization.

#### Endcap-Barrel relative alignment

The ray labelled as 4 (see figure 2.2) is in charge of the relative alignment of TIB and TOB and furthermore of the relative alignment of endcaps (see section 2.2.3). Since it travels inside both endcaps, it is able to relate the endcaps to the barrel simultaneously. As observed in figure 2.2, two laser beams originated in the endcaps are alternatively reflected inside the TOB and TIB. Eight such these rays, distributed in $\phi$, will be employed for this task. Two of them, will hit four times (instead of six times) the inner barrel.
In order to simplify and homogenize the production process of the petals, the three endcap Si-modules located in each petal at R≈564 mm will have holes along $\phi$, although the beam

will pass only through one of them. After leaving the endcaps, the laser beam will be injected within the inner support shell of the TOB. In order to protect the beam propagation and provide adequate splitting of the light beam inside the barrel, the beam will travel along a carbon fiber *alignment tube* embedded within another *protecting* carbon fiber tube. The alignment tube will be equipped with semireflecting mirrors which will distribute the beam inwards and outwards. Sagitas smaller than 10 $\mu$m for an appropriate election of the carbon fiber tubes have been already obtained. The tube will be attached on both ends to two supporting discs of the outer barrel. Since the active elements of the outer barrel are precisely mounted in the same support, it will be possible to accurately relate the measurements of the optical monitors with the position of the Si-modules.

### 2.2.2 Connection to the Link System

After the completion of the internal and relative alignment, a software tracking alignment can determine the position of the Si-modules with 10 $\mu$m accuracy, and as such, it can be aligned as a whole with respect to the rest of CMS. The connection with the Link system demands six rays with known position and angles plus the information of the $\phi$ angle of the Tracker.

Due to the different azimuthal segmentation of the tracker and muon system the interface to the Link system will be done by means of six rays at a distance of 345 mm labelled as “ray 1” in figure 2.2. Three couples (+/-Z) of orthogonal double sided Si-modules (or even 2D ALMY sensors) will measure the orientation of a laser beam of 1060 nm injected from outside the Tracker volume. A single sided module will absorb the Link beam, inside the TEC (see figure 2.2). The installation accuracy for the sensors will be measured with a CMM (Coordinate Measuring Machine) to the level of 20 $\mu$m. The position resolution of the sensors will be 10 $\mu$m (not included external errors as beam pointing instability).

The entrance of the beams, coming at $|\eta| = 3$, inside the TEC will be driven by small periscopes located in the outer side of a support disc structure. This structure is employed for the precise localization of tiltmeters and periscopes in the outermost wheel of the TEC. The disc will be sustained by 6 carbon fiber tubes which will also protect the laser beams “ray 1”. Furthermore, the structure is equipped with 2D Si-module detectors (as those employed inside the Tracker) which will measure the relative orientation of the structure with respect to the Tracker. Since the orientation of the disc structure will be measured by the tiltmeters, the orientation of the Tracker with respect to gravity will be known.

Inside the Tracker, an optical window will allow the Link beam to enter the cooled Tracker area. The optical window is achieved by a tube with a body made on carbon fiber (36 mm wide, 30 mm clearance hole) with two glass window caps made on BK7 G18 or optical grade Fused Silica (see also section 7.3). The design of the tube must avoid moisture condensation on the windows and must avoid optical aberrations of the traversing beam. A prototype has been successfully built and tested. During several runs of 24-36 hours, with a temperature transition between -35°C to 24°C the beam deviated less than 50 mrad (up to 500 mrad tolerance allowed), without condensation of water in the whole measurement period.

Since the 2D tracking sensors mounted on the disc structure are also sensitive to charged particles, the muon halo will be used to improve the alignment accuracy of the 2D sensors with respect to the tracker endcaps.

### 2.2.3 Monte Carlo simulation of the Tracker Alignment System

A Monte Carlo simulation of the Tracker alignment system has been performed [8, 9]. The aim of this simulation was to study the viability and redundancy of the new design.
For any of the intermediate alignment steps the simulation flux is as follows. First, the position and angle placement errors are considered. These include: placement error of the Si-modules, placement error of the support structures, laser beam position resolution of the Si-modules and laser beam stabilities (rounded to 50 $\mu$m error). Then, the positions of the elements are smeared ($\pm 1$ mm, $\pm 3$ mrad typically) and the misalignment parameters calculated making use of the alignment information. Provided the alignment error is below 100 $\mu$m, the track finding procedure can start. A statistics of straight tracks is generated and then reconstructed applying alignment corrections.

- Forward Tracker Simulation: Two forward wheels were used to define a reference system. The remaining seven wheels of an endcap volume were uniformly misaligned and the movements reconstructed to an accuracy of 20-25 $\mu$m for positions and 20 $\mu$rad for rotations. These precisions are well within the 100 $\mu$m limit required to start an efficient track finding procedure. The alignment-corrected resolution of straight tracks was less than 30 $\mu$m using eight "rays 2" and "3" or 40 $\mu$m employing only eight "ray 3", showing the redundancy of this design.

- Forward-Barrel Simulation: The two barrel volumes and endcaps were simulated and linked together by eight "rays 4". By construction of the Tracker support structures, a 50 $\mu$m placement error of the Si-modules in the inner and outer support structures will be achieved. After alignment corrections of the tracks, the placement accuracy are 49 $\mu$m for the inner barrel, 85 $\mu$m for the outer.

  Since "ray 4" joins both endcaps, the endcap to endcap relative alignment was performed better than 20-40 $\mu$m.

- Link Connection simulation: With a placement accuracy of 20 $\mu$m for the 2D sensors on the end-cap petals and their laser position resolution of 10 $\mu$m the "ray 1" coordinates and rotations will be known with an accuracy of 14 $\mu$m and 45 $\mu$rad respectively. The disc structure parameters will be known as well as 10 $\mu$m for its position and 30 $\mu$rad for its rotations.

All the above ensures that the hardware alignment of the Tracker system will be possible at the 100 $\mu$m level and that with the accumulation of tracking data statistics, the former numbers will be further improved down to 10 $\mu$m.

## 2.3 The Barrel alignment system

The position monitoring system for the barrel part [10] is designed to measure the positions of the barrel chambers with respect to each other (internal monitoring). The position of the whole barrel muon system is related to that of the Central Tracker and the Endcap muon system via the Link System.
Monte Carlo studies were employed [11] to calculate the maximum alignment error for an efficient reconstruction of the muon momenta. The precision for a good matching between the interaction

point, Tracker and muon chambers in order to obtain a momentum resolution below 20% for 1 TeV muons is about 100 $\mu$m for MB1, 300 $\mu$m for MB2 and MB3 and 500 $\mu$m for MB4.
The scheme of the barrel position monitor system is shown in figure 2.3. It is based on the monitoring of the muon chamber positions with respect to a network of 36 rigid mechanical reference structures called MABs (Module for Alignment of Barrel). The MABs are fixed to the barrel yoke forming 12 RZ half planes parallel to the beam and distributed in $\phi$. Six of them (called active planes) are connected to the link system. The other six planes (called passive planes) are connected to the active ones via diagonal connections.

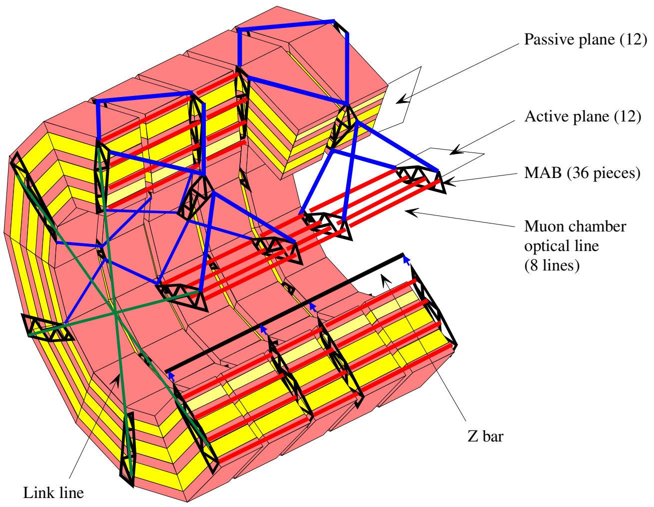


Figure 2.3: *Schematics of the barrel alignment system. The system relies on rigid mechanical structures (36 MABs and 6 bars for the Z measurement) optically connected among them and also connections between MABs and muon chambers. Afterwards, the position of the barrel with respect to Tracker is determined via 6 beam lines produced by the Link system [12].*

The chambers are equipped with light sources looking at opposite directions. These light sources are mounted on frames rigidly attached to the chambers (see figure 2.4). The position transfer between the wires and the light sources is made by the measurement of the wire positions with respect to the outside fiducials during manufacturing and by the knowledge of the behavior of the chambers due to temperature changes. The transfer of the position from the outside fiducials to the light source will be made by precalibration of each chamber.
Each of the 36 MABs contains (see figure 2.5) camera-boxes made of a video camera and a lens which observe light sources mounted on the muon chambers. The MABs also contain 4 light sources (on the active planes) or 4 camera-boxes (on the passive planes) providing the diagonal connections. In addition, all 24 MABs of the 6 active planes are also equipped with cameras measuring the $Z$ positions by observing carbon-fiber bars called Z-bars installed on the vacuum tank of the CMS magnet. All the 12 MABs that are connected to the link system (i.e. the outer MABs of the active planes) contain also elements belonging to the link and endcap systems.
The MABs with all the elements mounted on them are considered to be rigid bodies with calibrated geometries having 6 degrees of freedom. The fixation of the MABs on the barrel yoke

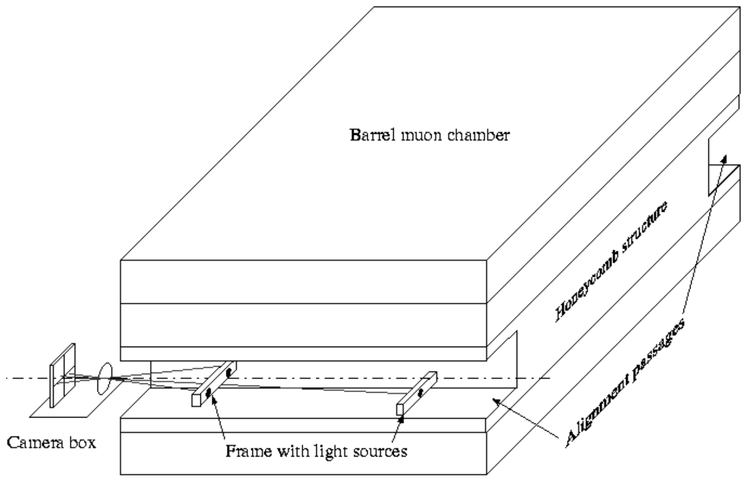


Figure 2.4: *Illustrating the measurement of the chamber position with respect to the MAB [12].*

must ensure that this condition is fulfilled. The stability and rigidity conditions demanded for the MAB are stringent: 50 $\mu$m for position and about 50 $\mu$rad for the rotations.

In addition to the 6 degrees of freedom of the MAB, the frames with the light sources are each considered to be one independent point-like object with 3 degrees of freedom. The Z-bars with the light sources mounted on them are also considered to be objects with 1 degree of freedom (movement along the z-axis). The total number of independent degrees of freedom in the stand-alone barrel position monitoring system is around 3000, while the number of independent observations is more than 4000 giving the desired redundancy to the system.

### 2.3.1 Measurement of the chamber positions with respect to the MABs

The principle of chamber position measurement with respect to the MABs was shown in figure 2.4. The frames with the light sources are mounted on the rigid honeycomb structures (used to separate $\phi$ and $Z$ superlayers, providing internal rigidity to the structure) in the alignment passages (two on each side, 0.5 m from the corner). The position of a light source is determined by the calculation of the centroid of the light intensity distribution falling on the CCD matrix. The $R$ and $\phi$ positions are measured directly by the camera-box by measuring the corresponding light sources positions. The $Z$ positions (only for the chamber corners close to the camera-boxes) are measured by triangulation, measuring the relative positions of two light sources mounted on the same frame 20 mm from each other.

There are up to 3 light sources per frame and up to 10 light sources per muon chamber. The R and $\phi$ coordinates are measured for all four corners of the chambers. The $Z$ measurement is provided for two corners.

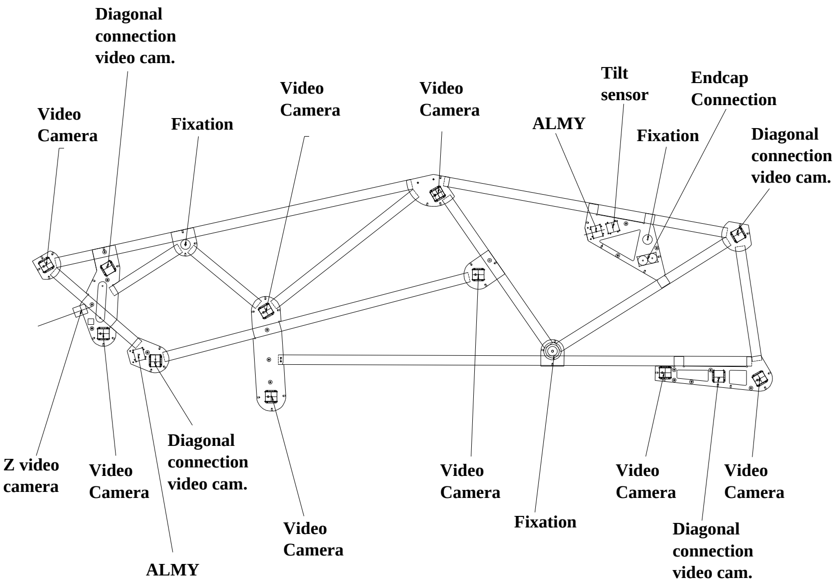


Figure 2.5: *MAB design showing positions for video-cameras and Link sensors [12].*

### 2.3.2 Calibration of the muon chambers and installation

The position of the different elements in the MABs (cameras, Link sensors ...) will be measured in a laboratory setup, prior to the fixation on the barrel yoke. The calibration makes use of a survey network, as the one used for the ISR test (see chapter 8). The calibration error plus the deformation errors should not exceed 50 $\mu$m in displacement and 50 $\mu$rad in rotation.
The position transfer between the frames and the anode wires is a two steps process. First, during the chamber production process, the position of the wires is measured with respect to outside fiducials called reference blocks. Then, the position of the alignment light sources will be measured with respect to the outside blocks, with a precision of 60 $\mu$m in r$\phi$ and 300 $\mu$m in $Z$ direction, placing the chambers in a calibration bench equipped with 4 reference videocameras [13].
Finally, the Barrel monitor design will allow to mount the MAB with a tolerance of 5 mm and the barrel wheels with 100 mm, with respect to the nominal positions. Once everything is positioned, the expected accuracy in the measurement of the relative position of the chambers in a barrel sector is $\sigma_{R\phi} < 146$ $\mu$m, while the relative position between barrel sectors will be $\sigma_{R\phi} < 210$ $\mu$m.

## 2.4 The Endcap alignment system

The endcap alignment system aims to measure the position of each of the 360 endcap cathode strip chambers (CSC) with respect to the Tracking system. The Endcap Muon (EMU) Alignment will use 2-D light sensing position detectors, wire extension potentiometers and proximity sensors. The $\phi$, $R$ and $Z$ alignment will rely on the rigidity of the MABs. Since the MABs are referenced via the Link System, the positions of the Endcap system will be defined relative to the tracker.

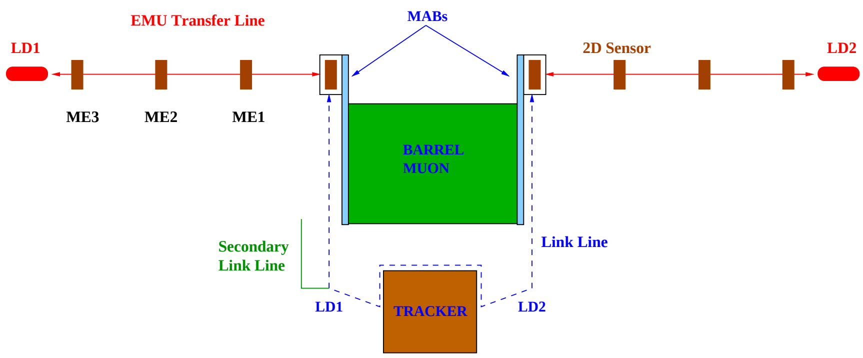


Figure 2.6: *Tracker to Endcap coordinate transference via the Link System [15].*

Early Monte Carlo studies [3] showed that the alignment error can be larger than the CSC resolution at momenta below 100 GeV. For higher momenta, the CSC contribution becomes decisive for the momentum fit and therefore the alignment error must be comparable to the CSC resolution. The CSC resolution was simulated in detail [14] and upper values for the alignment errors were extracted:

- The R$\phi$ resolution of the CSCs was determined by the multiple scattering of muons with $p_t < 100$ GeV to be 75 $\mu$m for the ME1/2 chambers and 150 $\mu$m for the rest. Therefore, the alignment errors must be better than these values.

- The actual $R$ position of the strips is not determined by the CSC $R$ resolution but it is determined by the $\phi$ alignment requirements [15]. The $R$ coordinate must be known better than 430 $\mu$m for the ME1 and ME2,3/1 stations and better than 860 for ME2,3/2.

- A 1000 $\mu$m error in $Z$ will have a negligible effect on $\phi$. The $Z$ position of the CSCs will be monitored to better than 0.5 mm.

### $\phi$ transfer

The endcap muon position monitor transfers the $R\phi$ coordinate from the active plane MABs via light lines that run along Z and along the outer perimeter of CMS. The laser beam defines a direction in the space which is measured with respect to the $\phi$ orientation of the MAB. These lines are called *Transfer lines*. Each transfer line (see figure 2.6) is made of:

- Two laser sources facing each other (LD1 and LD2 in figure 2.6) and located each at the farthest iron plates

- Eight two dimensional position sensors (one in each CSC and one in the outermost MABs of the active planes)

- Six base plates (also called *transfer plates*) supporting the 2D sensors.

The 2D sensor position is fiducialized better than 25 $\mu$m in the $R\phi$ direction and better than 0.2 mm in the other coordinates (see section 8.2). The plates transfer the Tracker reference coordinates onto the surface of the CSC stations.

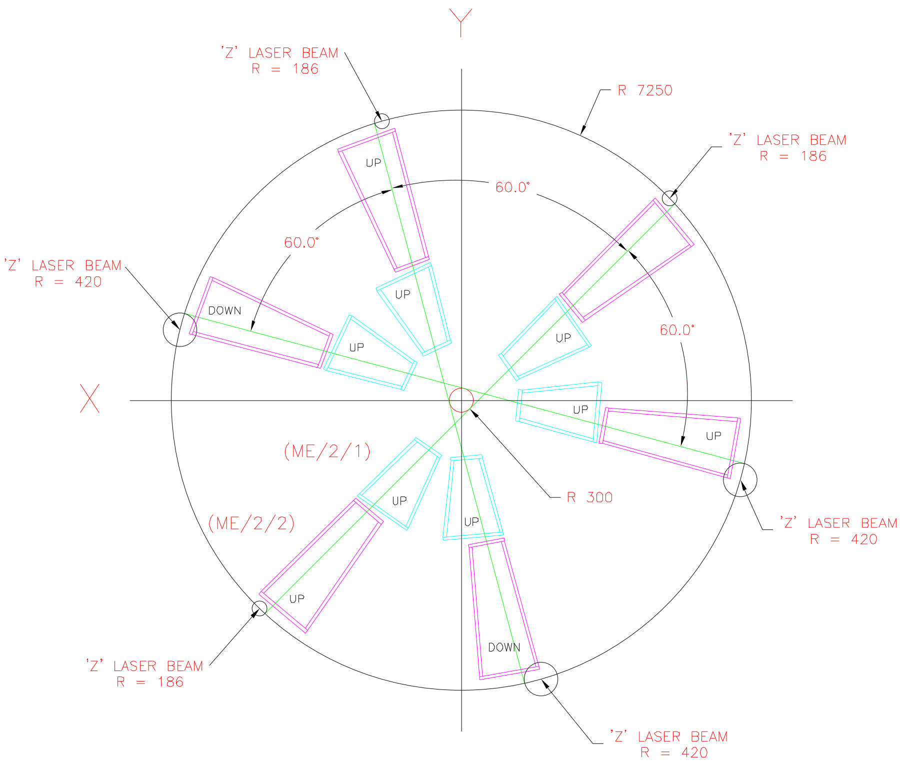


Figure 2.7: *Definition of the SLMs orientation on station ME2. Only CSCs fitted with 2D sensors are shown. The six circles contain the interception of the Transfer lines and the location of the SLM lasers [15].*

Besides the 2D sensor for the $R\phi$ measurement, each transfer plate attached to the muon stations carries an extra 2D sensor and a laser source mounted perpendicularly to the Transfer line. The laser travels across a vertical plane of CSCs and joins two diametrically opposed Transfer lines. Two 2D sensors on each CSC along that laser direction will give the $\phi$ orientation and Z position of the chambers. These lines are called straight line monitors arrays or *SLM lines* [15]. Due to the CMS geometry and due to budget reasons, only three of such lines per plane of CSCs will be employed. Figure 2.7 shows the SLM orientation on station MEm/2. The remaining chambers will be aligned in $\phi$ through their overlap with their neighbours. This method will rely on a precise knowledge of the R position of the CSC strips, as well as in the precise machining and referencing of the strips themselves.

### Z transfer

The $Z$ coordinate of each station will be concatenated from the MAB to each transfer plate. Carbon fiber tubes with proximity sensors in both extremes will take care of the $Z$ transfer. The connection with the MABs will be done with large range proximity sensors, while shorter range sensors will be employed between transfer plates. The $Z$ transference along the Transfer line is shown in figure 2.8. Since two dimensional sensors are employed in the SLM lines, the Z coordinate is directly transferred to those chambers equipped with sensors. The $Z$ position

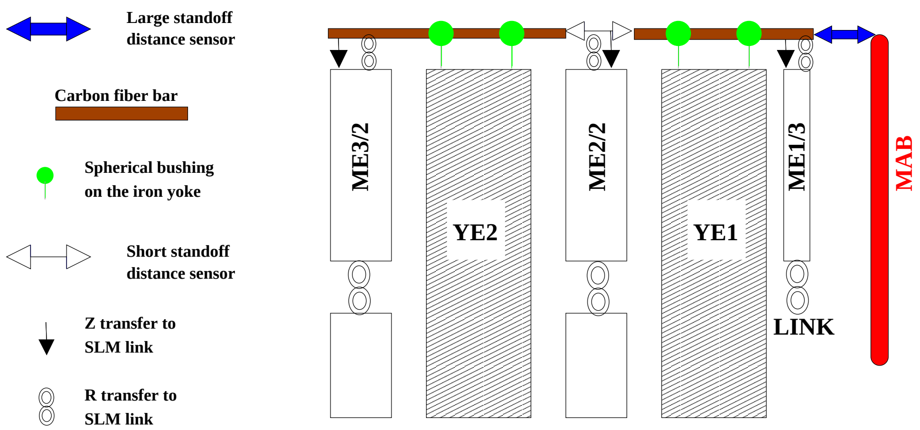


Figure 2.8: *(Z,R) transfer*

of the remaining chambers will be interpolated from the measured chambers and from modeled deflections for the iron under magnetic field.

#### R transfer

The EMU alignment system measures the distance along $R$ between the Transfer plate (of known $R$ value) and the precision end frame of the CSC by using simple cable extension linear potentiometers. The following chamber is referred to the outer one with another linear potentiometer (figure 2.8). This procedure relies on the precise knowledge and stability of the physical dimensions of the CSCs.

All the remaining chambers can be aligned using charged particle tracks. Simulation studies must still validate this assumption.

### 2.4.1 ME1 alignment

The ME1 station is the only one having three rings of chambers. The ME1/1 and ME1/2 rings will be aligned by the Link system (see section 2.5). The ME1/3 ring will have Straight Line Monitors starting from six outer Endcap Transfer-line points and six inner reference sensors mounted on the ME1/2 CSCs, measured by the Link System. $R$ measurements from the ME1/3 to the Transfer plates and to the ME1/2 chambers will be possible. Since there is no overlap for the ME1/3 ring, the R$\phi$ measurement requires proximity sensors at each end of one radial edge of the CSCs.

### 2.4.2 Strip knowledge

The Transfer and SLM plates will reference the position of the sensing strips to the actual sensor position.

### The Transfer plate

After assembly, and prior to installation, Transfer plates will be measured with a Coordinate Measuring Machine (CMM). This offset coordinate measurement together with the information from a dual inclinometer (see section 6.8) will define the transfer plane position relative to the SLM.
Proximity sensors will be attached to the Transfer plates for the $Z$ measurement. Its position will be established by computer numerical control (CNC) machine tolerances on mounting brackets and measured in the CMM machine. The position can be calibrated to an accuracy of 100 $\mu$m. For the transfer plates, this measurement defines the local $Z$ position of the SLM reference sensor.

### The SLM plate

Two 2D sensors per CSC chamber will be installed on standard sensor brackets, mechanically pinned-attached to mounting plates. The inner plate is precisely referenced to the CSC strips (the active elements) via a transfer fixture using two pins in the top panel. The holes for the pins can be defined relative to the CSC strip ends with 25 $\mu$m, using survey techniques.
R sensors can be calibrated relative to the holes of the top CSC panel and strips to an accuracy of 100 $\mu$m.

## 2.5 The Link alignment System

The Link system is designed to relate the position monitoring systems of the Tracker and the Muon Chambers [16]. The system connects tracker and muon detectors creating twelve (+/-Z) light paths accessible from both alignment references: tracker alignment discs and MABs (to which barrel and endcap detectors are related). The Link system provides a set of points out of the Tracker volume, whose coordinates are known with respect to the Tracker reference system. This is achieved comparing the position of a common laser beam in the Muon system and in Tracker.

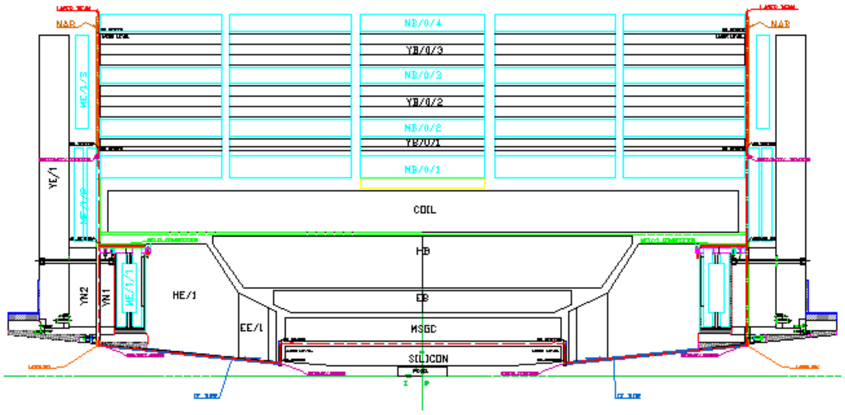


Figure 2.9: *Longitudinal section a 1/2Φ plane, showing the light path for the Link System. The figure refers to previous version of the CMS Tracker including MSGCs and the Link line traveling through the Tracker.*

Following the $\phi$ segmentation of the Muon system, the light paths define half planes in $\phi$, every 60 degrees, as shown in figure 2.3. This segmentation, although redundant, allows a direct reference of each barrel muon sector with the tracker detector and provides direct tracker references to the endcap monitoring system. Figure 2.9 shows schematically a longitudinal section of the CMS detector with the layout of the alignment lines.
To minimize the interference with other subdetectors, the light path follows the inner detector boundaries as shown in the figure and reaches the muon region through radial light channels in the endcap iron disks. The locations of the link points along the path are indicated in detail in the figure 2.10 for a $\phi$ plane. Two primary points on each MAB structure are used to reference the barrel and endcap alignment systems in this plane with respect to the Link line. Because of the special location of the ME1/1 and ME1/2 stations, extra link points will be used to align these chambers, as also seen in figure 2.10.

### 2.5.1 The light path

The performance of the system depends mainly on the precise definition and stability of the light path. Light beams are generated by two independent floating laser sources (at $Z \approx \pm 6630$ mm, $R \approx \pm 660$ mm) attached, at YN1, to the endcap return yoke. Each source produces three laser beams: two of them are parallel and run outwards to the Barrel region, the third one at a fixed angle of about 95.7 arcdeg from the plane defined by the former two. Due to the high magnetic forces induced by the solenoid [4] the yoke iron disc that supports the source will deform and shift in position. Since the expected motion may exceed the range of the alignment active elements, the laser source platform will incorporate a precision remote control block to adjust the location and orientation of the laser beams. The expected distortions of the iron are $(\Delta X, \Delta Y, \Delta Z) \approx (1, 1, 14)$ mm and $\leq 2.5$ mrad rotations. The required source re-positioning accuracy will be about $(1, 1, 14)$ mm for the placement of the source and $\leq 1$ mrad for its angular position.
Once the light is within the range of the sensors, the position and orientation of the rays are irrelevant for the monitoring method. Six radial light channels of $70 \times 110$ mm$^2$, including clearance, are machined in the yoke plates of the iron noses at both ends of the detector to allow the laser beams to reach the muon region. The required tolerances due to the shifts and distortions of the return iron under the magnetic forces determine the position and dimension of the channels.
Carbon fiber (or aluminum) light protecting tubes coupled to short range distancemeter, attached to the source platform, will be used for radial distance measurements between the source and the muon link points that are housed on the external MAB structures (see figures 2.5 and 2.10), at the two ends of the barrel detector.
At $R \approx 2630$ mm the ME1/1 stations will receive a splitted light beam from the Link system. Six lines of sight at $2630 < R < 2700$ mm, parallel to the CMS Z-axis, will allow to refer these chambers to the muon alignment system.
At the inner detector part, along the endcap detector boundaries, the optical lines from the light source are parallel to $\eta = 3$ and reach the tracker at $R \approx 300$ mm. On the tracker alignment discs, periscopes will insert (and shift in the $\phi$ coordinate) the laser beam, allowing optical measurements inside the tracker volume. As already explained before, the Tracker system will measure the position and angular orientation of these twelve laser beams. All the other systems will use this knowledge to align relative to the Tracker.

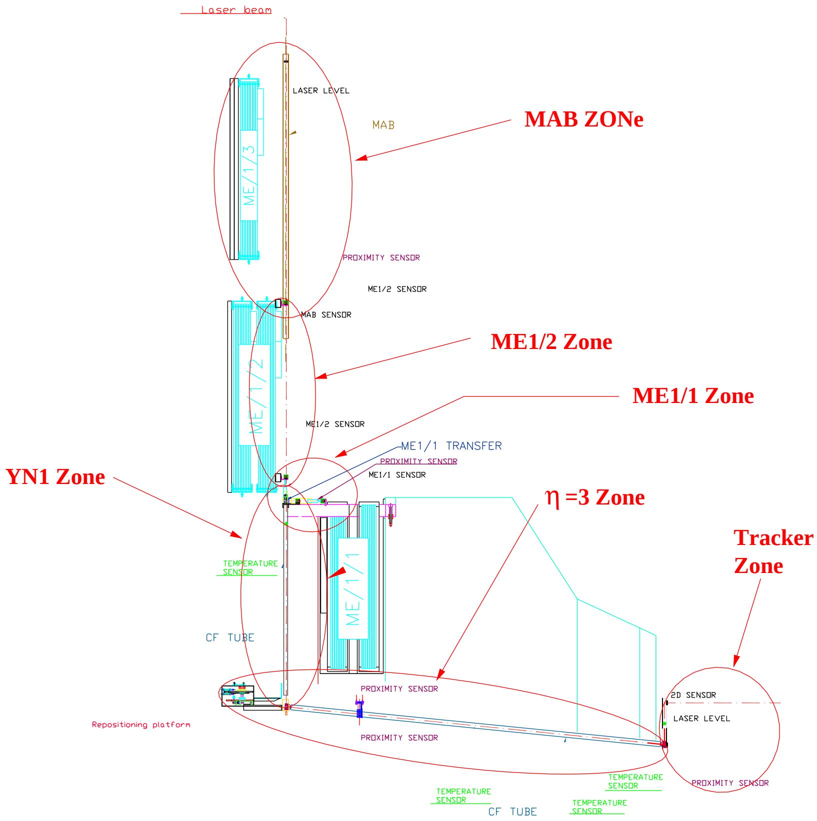


Figure 2.10: *Detailed view of a quarter Φ plane, with a highlight of the main tasks concerning the Link system.*

While the ability to monitor the position across the tracker volume is crucial, the final radial position of the alignment passages is not relevant for the performance of the system. In fact, the achievable accuracy of the system depends on unexpected variations of the light path shape introduced by the periscope. This imposes serious constraints on the calibration and stability of the periscope elements. Fortunately, the calibration of a periscope prototype presented in chapter 8 shows that these requirements can be achieved.

The requirements on the angular position stability of the periscope mirrors are set to limit the error contribution to position measurements at $< 40$ $\mu$m. The angular position of the periscopes on the tracker wheel should be known to within 100 $\mu$rad, while the stability of the mirror orientation must stay below 5 $\mu$rad [17].

### 2.5.2 The working principle

#### Linking the tracker to the barrel and endcap monitoring systems

The measurement of the MAB positions with respect to the tracker alignment wheels uses a total of four linking points along each light path: two placed at the tracker periscope and two at the MAB structures. The measurement of the position of the ME1/1 chambers uses three

position sensors and ME1/2 uses another two.
The localization of the MAB structure with respect to the Tracker involves:

- The definition of the laser beam with respect to the tracker discs: its position (X, Y co-ordinates) is obtained as the intersection of the light ray with the 2D sensors located at the tracker disc structure, at $|\eta|$ =3. The origin of the beam from the tracker (Z co-ordinate) is obtained by distance measurements along $|\eta| = 3$.
- The definition of the MAB relative to the radial beam: 2D position sensing detectors, located at the two link points defined on the MAB structure, measure the relative position and orientation between laser beam-MAB. A radial distance measurement from the origin of the laser beam to the MAB give the $R$ co-ordinate of the link points.
- The $\phi$ orientation MAB-Tracker cannot be directly obtained with this geometry, so it is measured independently by laser levels (laser and tilt sensors) placed on the MAB and tracker discs.

### Position monitoring of the ME1/1 rings

At $R \approx 2630$ mm the ME1/2 laser line (see figure 2.11), coming from the laser box, reaches a Link transfer platform. The platform is mounted with three sensors: two of them perpendicular to the radial beams, the third one perpendicular to a satellite beam produced with the help of a pentaprism. The satellite beam, traveling to the ME1/1 chamber is measured by two position sensors. In this way, the angle of the satellite beam around $R$ can be monitored. The simulated precision achieved with this method is 100 $\mu$m for the $R$ and $\phi$ coordinate [18]. The $Z$ position of the ME1/1 chamber with respect to the Tracker can be obtained by measuring the longitudinal distance from the Transfer platform, by means of proximity sensors. The expected error in this coordinate, with respect to the Tracker $Z$ position is about 130 $\mu$m.
Only twelve ME1/1 chambers (+/-Z) will be connected to the Link system using this procedure. All the remaining chambers will be relative aligned using tracks, benefiting from the $\phi$ overlap [19]. The precision obtained for the relative alignment of two overlapping ME1 chambers, with a single track, is about 300 $\mu$m. After one day of LHC operation this error can be reduced to almost 10 $\mu$m. After the relative alignment and provided a known point in six chambers, the three coordinates $(R, \phi, Z)$ of the ring will be obtained.

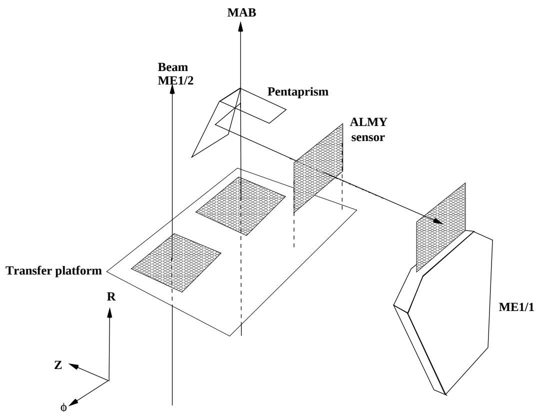


Figure 2.11: *Sketch of the ME1/1 monitor. One of the radial beams is splitted by using a pentaprism and its angular rotation around R is measured with two vertical position sensors.*

### Position monitoring of the ME1/2 rings

Once the beam light crosses the pentaprism of the ME1/1 transfer platform in the $R$ direction, it crosses two 2D position detectors located on the ME1/2 structure (see figure 2.10). These two references allow to link the ME1/2 chambers to the muon alignment system.

### 2.5.3 Elements of the system

The elements of the Link System belong to four categories:

- Sensors
  - 2D position sensing detectors (transparent amorphous-silicon sensors) to measure coordinates transverse to the light beams. ALMY sensors (see following chapters) are the current election.
  - Tiltmeters as part of the Laser Levels, for angular measurements
  - proximity sensors, for short distance measurements (long distances will be measured using aluminum or carbon fibre tubes).
  - temperature sensors (will allow to correct, when needed, the angular and distance measurements)
- Optomechanical components
  - light sources (also called laser boxes)
  - periscopes
  - ME1/1 transfer plate
- Mechanics
  - light source repositioning platform
  - tracker wheel
- Associated electronics

## 2.6 Expected performance

The influence of the errors of every free parameter of the Link system (basically positional and angular placement precision of individual and composed objects) has been simulated [17]. From this simulation, the transference of the (Z,R) coordinates between the two MABs has been also calculated.
Table 1 [17] shows the calculated contribution of each parameter (on the left column) to either the placement errors or the angular errors of the MAB, ME1/1 and ME1/2 chambers.
No angular information is provided for the ME1/1 chamber, since only one point per chamber is monitored by the Link System. No information on rotation around the $R$ coordinate is given neither for the MAB nor for the ME1/2 chamber, since the position sensor readings are not sensitive to moderate rotations around R.
We can see that the main contributions to the total error budget are the errors in the Tracker region. A misplacement error of 15 $\mu$m in the Tracker endcap sensors sharing "ray 1" (see figure 2.2) propagates through the rest of parameters (definition of the Link ray in the splitter and mirror of the periscope, uncertainty in the radial traveling beams) as an error of 100 $\mu$m in the $\phi$ coordinate of the MAB. The errors in the position of the sensors in the silicon wheels of the Endcap Tracker and the alignment Tracker disc (former minidisc version) contribute

by themselves around 3/4 of the total error in the $\phi$ coordinate of the MAB and the ME1/2 chamber. The error in the rotation angle around $Z$ of the Tracker minidisc and the periscope have also an important contribution to the total error. For the periscope, however, this rotation can be monitored with the tiltmeters situated in the Tracker minidisc.
Along this document we will test the most critical components of the Link System.

| | | | MAB | | | | | ME1/2 | | | | | ME1/1 | | |
|---|---|---|---|---|---|---|---|---|---|---|---|---|---|---|---|
| | | | Centre | | | Angle | | Centre | | | Angle | | Centre | | |
| **Object** | **Parameter** | **Value** | **R** | $\phi$ | **Z** | @$\phi$ | **@Z** | **R** | $\phi$ | **Z** | @$\phi$ | @Z | **R** | $\phi$ | Z |
| MAB sensors | Position(1) | 40 $\mu$m | - | 40 | 40 | 22 | 22 | - | - | - | - | - | - | - | - |
| MAB laser level | Position(2) | - | - | - | - | - | - | - | - | - | - | - | - | - | - |
| | Angle(2) | - | - | - | - | - | - | - | - | - | - | - | - | - | - |
| | Angle @ Z tiltmeter-laser | 10 $\mu$rad | - | 38 | - | - | - | - | 22 | - | - | - | - | 20 | - |
| ME1/2 sensors | Position(1) | 40 mm | - | - | - | - | - | - | 40 | 40 | 34 | 34 | - | - | - |
| ME1/1 Transfer | Position(2) | - | - | - | - | - | - | - | - | - | - | - | - | - | - |
| | Angle(2) | - | - | - | - | - | - | - | - | - | - | - | - | - | - |
| | Internal calibration | | | | | | | | | | | | 150 | 80 | 150 |
| ME1/1 | Position(1) | 40 $\mu$m | - | - | - | - | - | - | - | - | - | - | 40 | 40 | - |
| Tube $\eta = 3$ | Position | 20$\mu$m | - | - | - | - | - | - | - | - | - | - | - | - | - |
| | Angles | 1000 $\mu$rad | 10 | - | 90 | - | - | 10 | - | 90 | - | - | 10 | - | 90 |
| Laserbox(1) | \|\| beams shift out plane | 10 $\mu$m | - | - | - | - | - | - | 8 | - | - | 1 | - | (8) | - |
| | \|\| beams deviation out plane | 5 $\mu$rad | - | - | - | - | - | - | - | 9 | - | 4 | - | (8) | - |
| | \|\| beams deviation in plane | 5 $\mu$rad | - | - | - | - | - | - | - | 11 | - | - | - | (8) | - |
| | Angle between 95° beams(3) | 10 $\mu$rad | - | - | 38 | 10 | - | - | - | 22 | 10 | - | (8) | - | (8) |
| | Angle \|\| between 95° beams(3) | 100 $\mu$rad | - | - | - | - | - | - | - | 2 | - | - | - | (8) | - |
| Periscope | Position | - | - | - | - | - | - | - | - | - | - | - | - | - | - |
| | Angle @R(5) | 100 $\mu$rad | 20 | 4 | 23 | 6 | - | 20 | 4 | 13 | 6 | - | 17 | 3 | 13 |
| | Angle @ $\phi$(5) | 100 $\mu$rad | 2 | 14 | 3 | 1 | - | 2 | 14 | 2 | 1 | - | 2 | 13 | 1 |
| | Angle @ Z(5) | 100 $\mu$rad | 3 | 53 | 5 | 1 | - | 3 | 53 | 3 | 1 | - | 2 | 47 | 3 |
| Periscope splitter | Position(3) | 100 $\mu$m | 5 | 5 | 7 | 2 | - | 5 | 5 | 4 | 2 | - | 4 | 4 | 4 |
| | Angle @R(3) | 5 $\mu$rad | 7 | 22 | 8 | 2 | - | 7 | 22 | 5 | 2 | - | 6 | 20 | 4 |
| | Angle @ $\phi$(3) | 5 $\mu$rad | 36 | 6 | 39 | 9 | - | 35 | 6 | 25 | 9 | - | 32 | 6 | 22 |
| | Angle @ Z(3) | 5 $\mu$rad | 7 | 20 | 8 | 2 | - | 7 | 20 | 5 | 2 | - | 6 | 18 | 4 |
| Periscope mirror | Position(3) | 100 $\mu$m | 8 | 1 | 12 | 3 | - | 8 | 1 | 7 | 3 | - | 7 | 1 | 7 |
| | Angle @R(3) | 5 $\mu$rad | 7 | 22 | 9 | 2 | - | 8 | 22 | 6 | 2 | - | 7 | 20 | 5 |
| | Angle @$\phi$(3) | 5 $\mu$rad | 35 | 6 | 39 | 9 | - | 35 | 6 | 24 | 9 | - | 32 | 5 | 22 |
| | Angle @Z(3) | 5 $\mu$rad | 7 | 18 | 8 | 2 | - | 7 | 18 | 5 | 2 | - | 6 | 15 | 4 |
| Tracker wheels sensors | Position(6) | 15 $\mu$m | 101 | 103 | 102 | 24 | - | 101 | 103 | 65 | 24 | - | 92 | 94 | 59 |
| Minidisc | Angle @ Z(7) | 20 $\mu$rad | - | 76 | - | - | - | - | 45 | - | - | - | - | 42 | - |
| Minidisc sensors | Position(6) | 30 $\mu$m | 78 | 78 | 72 | 17 | - | 77 | 78 | 46 | 17 | - | 71 | 72 | 42 |
| Thermal window | Beam shift | 20 $\mu$m | 20 | 20 | - | - | - | 20 | 20 | - | - | - | 20 | 20 | - |
| | Beam deviation | 10 $\mu$rad | 38 | 38 | 4 | 10 | - | 38 | 38 | 4 | 10 | - | 2 | 2 | - |
| 2D sensors | Meas. precision | 5 $\mu$m | 29 | 33 | 31 | 8 | 3 | 29 | 30 | 20 | 8 | 6 | (8) | (8) | (8) |
| Tiltmeter MAB | Meas. precision | 20 $\mu$rad | - | 75 | - | - | 20 | - | 44 | - | - | 20 | (8) | (8) | (8) |
| Distancemeters | Meas. precision | 80 $\mu$m | 139 | - | 112 | - | - | 114 | - | 112 | - | - | 80 | - | 80(8) |
| | **TOTAL** | | **189** | **168** | **158** | **40** | **28** | **171** | **156** | **126** | **45** | **42** | **165** | **179** | **140** |

Table 1: *Contribution of parameters (left column) to placement and angular errors, for the MAB, ME1/1 and ME1/2 chambers. Footnotes: (1) Expected mechanical precision, (2) Parameters measured by the Link System, (3) Errors from calibration (CIDA, Santander, ISR), (4) Laser box parameters defined as in the calibration of the ISR, (5) Expected mechanical stability of the minidisc, (6) Expected position errors obtained with tracks, (7) Calibration of verticality of minidisc plus errors in tiltmeters on minidisc, (8) Error included in internal calibration, (after [17]).*

# Bibliography


[1] Jorge Mocholí Mocholí, *Diseño y estudio de cámaras de deriva para el Detector CMS de LHC*, Ph.D. thesis, Madrid 1998

[2] V. Karimäki, Nucl. Instr. and Meth. in Phys. Res. A 410 (1998) 284-292

[3] *Requirements on the alignment errors of MS based on muon $P_T$ resolutions.* F. Matorras, A. Meneguzzo, CMS TN/95-069 and V. Karimäki, G. Wrochna, CMS TN/94-199

[4] *CMS. The Magnet Project Technical Design Report.* The CMS Collaboration, CERN/LHCC 97-10.

[5] *Addendum to the CMS Tracker TDR*, The CMS Collaboration, CERN/LHCC 2000-016, CMS TDR 5 Addendum 1, 21 February 2000

[6] Stefan Schael, *The CMS Tracker*, LHCC meeting, CERN May 2000
http://accms04.physik.rwth-aachen.de/~schael

[7] *A novel straightness measurement system applied o the position monitoring of large Particle Physics Detectors*, R. Goudard, M. J. Price, R. Ribeiro and F. Klumb, CMS CR 1999/034

[8] *An Alignment System for the CMS Tracker*, A. Ostapchuk, S. Schael, R. Siedling, B. Wittmer, S. Hameed Khan
http://accms04.physik.rwth-aachen.de/~schael

[9] A. Ostapchuck, CMS Tracker Week CERN, 26 Oct 2000. Available at:
http://accms04.physik.rwth-aachen.de/~schael

[10] L. Brunel, *Muon Barrel Alignment.* CMS TN/94-239
J.C. Gayde et al., *Muon Barrel Alignment system*, CMS TN/94-250.

[11] F. Matorras, T. Rodrigo and I. Vila, *Influence of intrinsic and alignment errors of MS on muon $p_t$ measurement*, CMS TN/95-069

[12] Courtesy of Laurent Brunel
http://cmsdoc.cern.ch/~lbrunel/website/cms/COMMUNIC/RAPPORTS/Rapports.htm

[13] L. Brunel et al., *A calibration bench to measure the positioning elements of the barrel muon chambers for the CMS experiment*, CMS IN-1998/005

[14] *CMS. The Muon Project Technical Design Report.* The CMS Collaboration, CERN/LHCC 97-32.

[15] Endcap Muon Alignment Project. June 23, 1999
http://home.fnal.gov/~maeshima/alignment/alignment.html

[16] The Muon Collaboration, *Engineering Design Review of MUON, MUON_EDR-03 for Muon Alignment* , held at CERN 30 November & 1 December 2000-

[17] P. Arce et al. *Engineering Design Review of MUON, MUON_EDR-03 for Muon Alignment*, Chapter 6.

[18] P. Arce et al. *Study of the alignment of the CMS ME1/1 stations*, CMS IN 1999/048

[19] P. Arce et al. *Internal alignment of the ME1/1 stations with tracks*, CMS IN 2000/009

# Chapter 3

# ALMYs as solid state devices

## 3.1 Introduction

ALMY sensors are solid state devices. Their production process is identical to that of the amorphous silicon solar cells. Both use transparent thin film layers which are piled in a stack. Since ALMY sensors are operated as photoconductors, they need to be supplied with current from an external power source. However a photovoltaic cell acts itself as a source of e.m.f when it is illuminated. Both kind of devices implement semiconductors as active or sensitive materials. This election, far from being arbitrary, is favored by the energy gap of the absorbing material (amorphous silicon). Semiconductor gap energies match the wavelength of visible radiation.
An in-depth study of an ALMY sensor requires the characterization of the sensor from at least three fields: semiconductor physics (at the light detection stage), electronics (handling of photocurrent signal) and optics (study of transmission through the multilayer). This chapter serves as a reminder of the two first topics. The optical characterization of the ALMY device is provided in chapters 4 and 5 of this work.
Thus, next section presents a brief review of the most important semiconductors physics concepts needed. It introduces $n$-type and $p$-type semiconductors, $pn$ junctions and Schottky junctions. The section provides the figures of merit needed to explain the sensors from the solid state physics side. Although all the layers involved in the ALMY design play a role, perhaps the most interesting one is the a-Si:H, since all the relevant physics processes involve it. Due to its importance we describe its properties in section 3.3, where amorphous materials are introduced stressing their main differences with respect to their crystalline counterparts. An extensive discussion of the so called Staebler Wronsky effect in amorphous silicon is given in section 3.4. This effect will be recalled during the characterization tests of the sensors (chapter 4) and the radiation tests presented in chapter 7. After this theoretical summary, the ALMY sensor structure is finally introduced in section 3.5 and its electrical functioning explained.

## 3.2 Semiconductors background

As said above, one of the ALMY sensor layers is a semiconductor: amorphous silicon. Semiconductors are electronic conductors with values of the electrical resistivity at room temperature in the range $\sim 10^{-2}$ to $\sim 10^{9}$ $\Omega$cm, intermediate between good conductors and insulators.
The band scheme of a typical semiconductor at room temperature is shown in figure 3.1. The partially filled conduction band allows the material to exhibit moderated electrical conductivity.

At zero temperature all the states in the valence band would be filled and the conduction band empty, thus the semiconductor would become an insulator. The thermal excitation is responsible for the *intrinsic conductivity* of the semiconductor. Both, the thermally excited electrons in the conduction band and the vacant states or holes left behind in the valence band will contribute to the electrical conductivity, as shown in figure 3.2. The discontinuous line in figure 3.1 represents the Fermi energy level[1] $E_F$. As an important result, the Fermi levels must be equal for elements in contact [1]. The last statement is equivalent to say that in equilibrium net electron and hole currents must be zero [2]. The electron energy is conventionally defined to be positive when measured upward, and the hole energy is positive when measured downward.

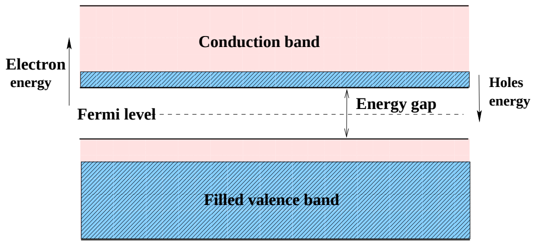


Figure 3.1: *Band scheme for a semiconductor at room temperature. The shaded area shows energy levels filled with electrons.*

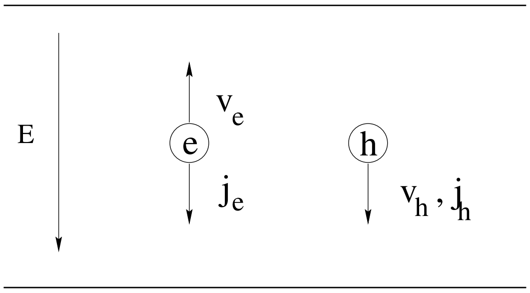


Figure 3.2: *Motion of electrons (e) and holes (h) in presence of an electric field E. By convention, the sense of the velocity and the current flow is opposite.*

### 3.2.1 $n$ and $p$ type semiconductors

Certain types of impurities and imperfections may affect drastically the electrical properties of a semiconductor. For example, the addition of boron to silicon in the proportion of 1 boron atom to $10^5$ silicon atoms increases the conductivity of the silicon by a factor of $10^3$.

In particular, silicon (valence four) may be doped with atoms of valence five (P, As, Sb). If one of the valence four atoms is substituted by one pentavalent atom, there will be one valence electron left over after the impurity atom has been accommodated in the structure. The structure will have an excess (local) positive charge from the impurity atom which has lost one electron, and also the excess electron (the semiconductor, as a whole, remains neutral). The ionization energy of the electron is about 0.05 eV, but at room temperature a substantial proportion of the impurity atoms will have lost their excess electron through thermal ionization. A pentavalent atom doping a semiconductor is called a donor atom, because it can give one electron to the conduction band. The material is said to be $n$ type, its conductivity being due to negative charges. The excess electrons lower the energy level of the doped material. The Fermi level for $n$ type materials lies closer to the conduction band edge.

If the impurity is a trivalent atom (Boron, for instance) it is called an acceptor because the

[1] At absolute zero it has the significance of a cut-off energy: all states with energy less than $E_F$ are completely filled, with $E > E_F$ are vacant

impurity can take an electron from the valence band, leaving a hole there. The conductivity of the material is then associated with holes and the material is said to be $p$ type. For $p$ doped materials, the Fermi energy level lies closer to the valence band edge.

### 3.2.2 $pn$ junction

If a $n$ type semiconductor is brought into contact with a $p$ type sample, then the higher concentration of electrons in the $n$ type material will result in electrons crossing from the $n$ to the $p$ type material, and, in a similar way, holes would cross from the $p$ to the $n$ type material (see figure 3.3 left). As the current flow continues, the $n$ type material becomes positively charged with respect to the $p$ type, due to the ions close to the junction that have sacrificed a charge carrier. The result of such a charge motion is that a potential difference builds up between both materials, from the $n$ type material to the $p$ type. The polarity is clearly such as to oppose the charge flow that is responsible for it, so that eventually the system reaches equilibrium with no net movement of charge across the junction. The electric field produces a region near the junction which is *depleted* of majority charge carriers (figure 3.3 top right). As there are comparatively few charge carriers in the depletion layer, there will be a net charge density due to the ionized impurity atoms firmly bound in the lattice (figure 3.3 bottom right). Increasing the doping densities results in an increase in layer field strength and in a reduction in depletion layer width. Qualitatively if the doping is low, the electron and hole travel from far behind and the depletion region gets wider. In practice the active part of a device comprises the depletion layer and the regions about a diffusion length wide on either side.
Although the total currents are zero, individual hole and electron currents exist in the depletion layer [3]. In equilibrium, carrier generation (for instance by thermal vibrations) is balanced by carrier recombination.
When there is no applied voltage across the semiconductors the junction is said to be operated in short-circuit mode. If a negative voltage is applied to the $n$ region and positive to the $p$ region (this is called forward biasing), there will be a large current flow from the donor $n$ type semiconductor and the junction will act as a conducting material. If the voltage is reversed (reverse bias operation), the potential difference will inhibit the charge motion. It is said that the junction has rectified the current, since conduction only happens in one sense.

### 3.2.3 The addition of an intrinsic layer

Intrinsic semiconducting layers introduce further versatility to the $pn$ junction. Placed between the $p$ and $n$ type semiconductors, an intrinsic $i$-layer will introduce a phase delay in current response due to the finite drift velocity of the carriers crossing it. As the charge densities within the intrinsic layer are small compared with those within the $p$ and $n$ regions, the whole width of the intrinsic region acts as a very wide depletion layer with an uniform field distribution.
The first practical point about the *pin* diode is that given voltages are associated with much lower internal field strengths. Thus, *pin* diodes are used in high-voltage applications.

### 3.2.4 The Schottky diode

A metal−semiconductor junction separated by an insulating film is called a Schottky diode. As carriers must tunnel through this film, it is kept as thin as possible. In practice, the inevitable oxide film on the semiconductor surface is suitable as the insulator. The metallic coating is then

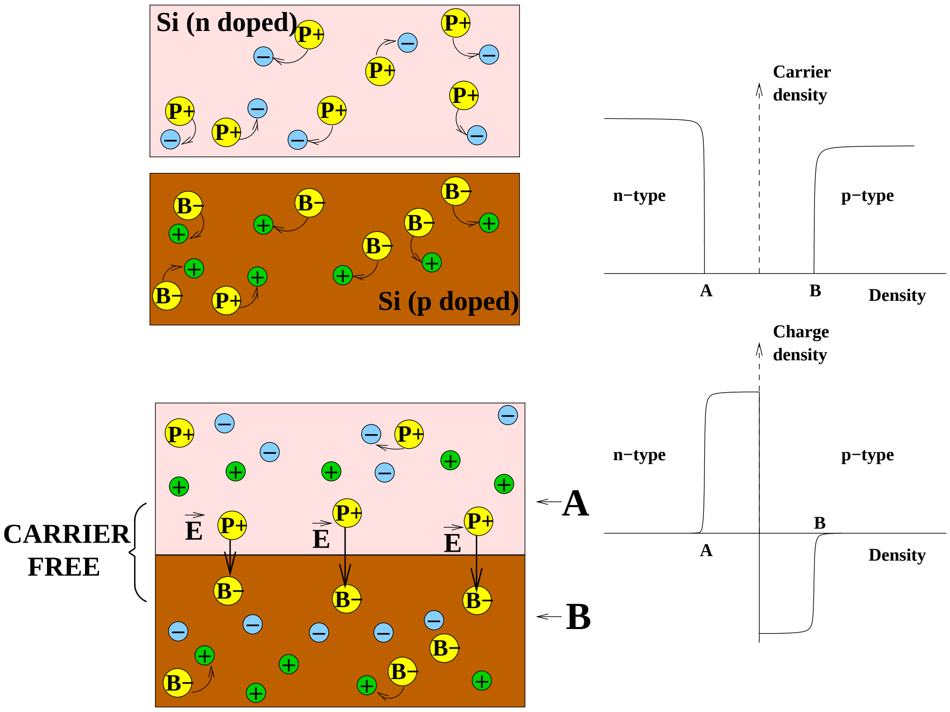


Figure 3.3: *Top Left: A semiconductor n type (donor) and p type are brought together. As the p type semiconductor lacks electrons there is a diffusion towards it. Bottom left: A region depleted of carriers comes up. The ions left by the charge carriers of each material lead to a built-in electrical field. Overall electric field and charge are zero. Top right: Carrier densities in a pn junction. Bottom right: Depletion layer at a pn junction: charge profile (due to the ions, not due to the charge carriers).*

simply deposited on top. The function of the insulating is to act as a barrier for the electron flow.

Let us suppose that the semiconductor ($n$ type) has lower work function[2] than the metal. Then there will be a net flow of electrons from the semiconductor to the metal since they have higher energy. The semiconductor energy levels will sink, since it gets rid of electrons. These electrons contribute to the conduction band of the metal. Equilibrium is reached when the negative electric potential of the metallic conductor is sufficient to prevent further accumulation of electrons. The electrons that flow from the semiconductor to the metal leave behind positively charged donor ions in a depleted region near to the surface. As a result of the electron flow, the region near the Fermi level moves deeper into the semiconductor, leading to upward bending of the energy bands (figure 3.4 left).

In the steady state, electrons are continually crossing and re-crossing the junction, and in absence of external current flow the current from the semiconductor and the current from the metal must equate. If now the semiconductor is made negative (reverse biased) its energy levels will raise and the current from the semiconductor to the metal will increase rapidly (figure 3.4 middle). Biasing the semiconductor positively with respect to the metal will lower its energy levels and

[2]Energy needed to remove to infinity an electron from the lowest free electron state.

the current from the semiconductor to the metal will decrease (figures 3.4 right). Qualitatively, the behavior resembles that of the *pn* junction, and the d.c. characteristic reflects that similarity. With both, positive and negative bias, the current from the metal is unaffected.
The particular merit of the Schottky diode is its very short turn-off time, because the conduction is by electron flow. In the majority of cases the depleted zone extends the whole semiconductor. Another type of metal−semiconductor contact widely used is the *ohmic contact*. Ohmic contacts have a negligible contact resistance relative to the bulk of the semiconductor and supplies current with a voltage drop that is sufficiently small compared to the drop across the active region of the device. High doping concentration, low barrier height, or both must be used to obtain low values of the contact resistance.

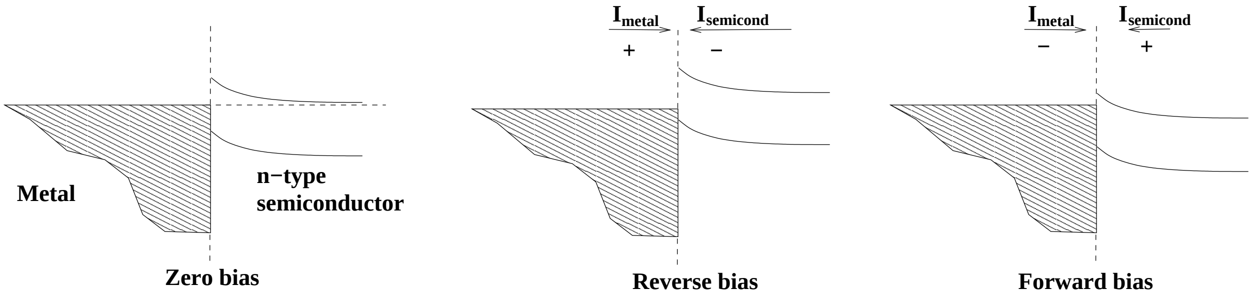


Figure 3.4: *The effect of bias on the Schottky diode: a) Zero bias; b) metal positive. Current from the semiconductor increases c) metal negative. Current from the semiconductor decreases.*

### 3.2.5 Photodiodes

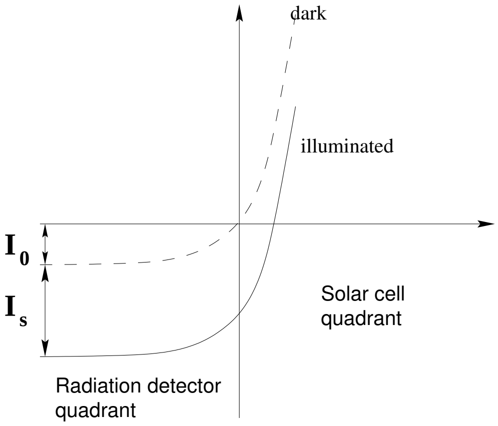


Figure 3.5: *Current-voltage characteristic for a photodiode in dark environment and under illumination.*

Photodiodes are special kinds of diodes which are designed to operate in a narrow wavelength range. The photodiode family includes the *pn* junction diode, *pin* diode and metal semiconductor diode (Schottky barrier). Photodiodes have a depleted semiconductor region with a high electric field that serves to separate photogenerated electron-hole pairs.
Let us now consider the current-voltage characteristics of a diode under illumination and in the dark. The behavior is shown in figure 3.5. If the series resistance of the diode is ignored, the dark current is given by [3]:

$$I = I_0 \left[\exp\left(\frac{eV}{kT}\right) - 1\right] \tag{3.1}$$

where $eV$ is the electron energy, and $kT$ the thermal energy. It is supposed that, upon illumination, there is an additional photocurrent $-I_s$, with negative sign since it flows in opposite direction to the forward current of the diode. The current on illumination is thus $I - I_s$. If the diode is to be used as a sensitive radiation photodiode, it is advantageous to supply a reverse bias voltage so that the bottom left-hand quadrant of the current voltage characteristic becomes relevant. If $P$ is the flux of photons and $\eta$ the quantum efficiency (that is, number of carriers generated per incident photon), $I_s = \eta e P$. Therefore, the current supplied by the external circuit to the photodiode *increases linearly* with the intensity of the incoming light. This feature will be employed for the detection of the laser beam by ALMY sensors.

## 3.3 Crystalline and amorphous materials

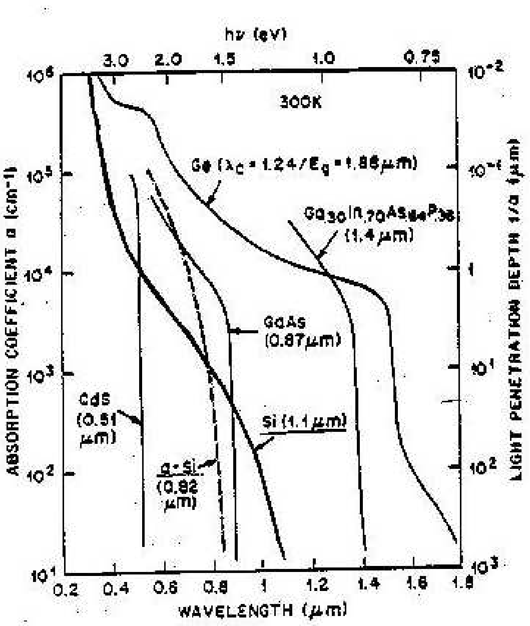


Figure 3.6: *Absorption coefficient for several photodetector materials.*

The unprecedented impact of silicon on the electronic industry and on solid-state research in particular started with the invention of the bipolar transistor at Bell Laboratories in 1947 [2]. Prior to 1947, semiconductors were only used as thermistors, photodiodes and rectifiers. On the other hand, hydrogenated amorphous silicon (a-Si:H) was a late arrival to the research on amorphous semiconductors. a-Si:H was first made in the late 1960s, while the development of a photovoltaic device had to wait until 1976, at RCA Laboratories. Other applications for a-Si:H have been liquid crystal displays, optical scanners and radiation imagers. Whereas crystalline Si (c-Si) is in use in applications in which its high cost is not a problem amorphous Si (a-Si) is the choice for large area devices. Figure 3.6 reveals that the optical absorption of c-Si is much lower than that of the a-Si in the visible region. Because of this difference, thin films (1 $\mu$m or less in thickness) of a-Si can be used in solar-cell applications, while much thicker films (50 $\mu m$ or more) are needed to adequately absorb the sun photons in the case of c-Si. On the other hand, c-Si conversion efficiency is bigger than the a-Si one. However, this need for less material in the a-Si case is a significant advantage for large-scale applications. Another very attractive features of a-Si are the low temperature technological process and the possibility of deposition on inexpensive substrates such as glass, metal or plastic.

The strict selection rules that govern crystalline solids forbid direct first order light-induced transitions (transitions between states mediated only by photons) [4]. Only second-order electron excitation processes by photon absorption, involving the simultaneous creation or destruction of a crystal phonon are permitted. Such second-order processes are orders of magnitude weaker than direct-transition processes, which amounts for the weak absorption exhibited by c-Si. In amorphous solids, no such restrictions apply. Therefore a-Si behaves like a solid with a direct bandgap and absorbs light at photon energies starting just above its optical bandgap.

The disorder of the atomic structure is the main feature which distinguishes amorphous from crystalline materials. Amorphous materials have the same short range order as the crystalline ones, but lack the long range order [5]. The disorder is exhibited by deviations in the bond lengths

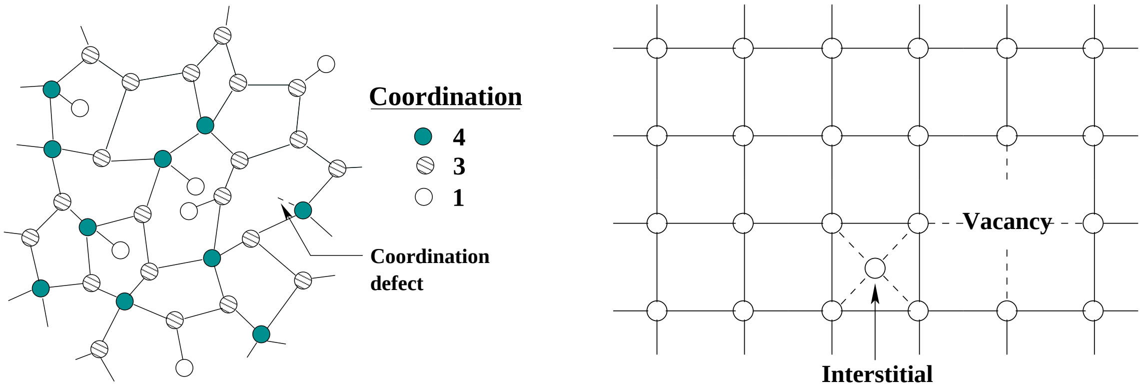


Figure 3.7: *Left: An example of amorphous network (silicon). This scheme is also called continuous random network. The coordination number counts the number of neighbors to which the silicon atom is bonded. Right: Crystalline network of silicon showing two kind of defects: vacancies and interstitials bonding [5].*

and deviations in bond angles. A pictorial comparison between crystalline and amorphous materials is shown in figure 3.7.

When the atoms combine to form a solid, the electron interaction splits the valence states into bonding and anti-bonding levels. Chemical bonds are formed such that the maximum number of electrons are paired in bonding orbitals, the remaining electrons are paired in non-bonding states (bonding states with lone electrons) and the anti-bonding states are empty. According to the free electron theory, the band gap is a consequence of the periodicity of the crystalline lattice. Subsequent work explained that the band gap is a consequence of the splitting of the bonding and anti-bonding states of the covalent bond. In the case of amorphous materials it is not always possible to arrange all the valence electrons in bonding orbitals (atoms in figure 3.7 left with less than four neighbors), and levels with lone electrons arise. The energy of these levels lays within the recently created band gap and act as traps for carriers. When many electrons are added together to form a solid, the bonding states generate the valence band, the antibonding states produce the conduction band and the non-bonding levels in between become the defects states, which will be placed in the middle of the gap as it will be shown later. The difference in energy between the bonding and anti-bonding states amounts the gap energy.

The preservation of the short range order results in a similar overall electronic structure of an amorphous material compared to the equivalent crystal. The abrupt band edges of a crystal are replaced by a broadened tail of states (see figure 3.8) extending into the forbidden gap, which originates from the deviations of the bond length and angle arising from the long range structural disorder. Electronic states deep within the band gap arise from departures from the ideal network, such as coordination defects.

The addition of a large concentration of hydrogen impurities has the effect of cleaning out the bulk of the band gap states. The beneficial action of H in $Si_{1-x}H_x$ is attributed to the strength of the Si-H covalent bond. Hydrogen terminates the dangling bonds occurring in a-Si by bonding to them, thus removing the gap states. In addition, the hydrogen atoms open up the weak reconstructed bonds associated with long Si-Si bonds, replacing them by two Si-H bonds. Since the Si-H bond is very strong and its bonding-antibonding splitting is larger than that of Si-Si, the states introduced by the Si-H bonds lie at energies which are outside the bandgap region of

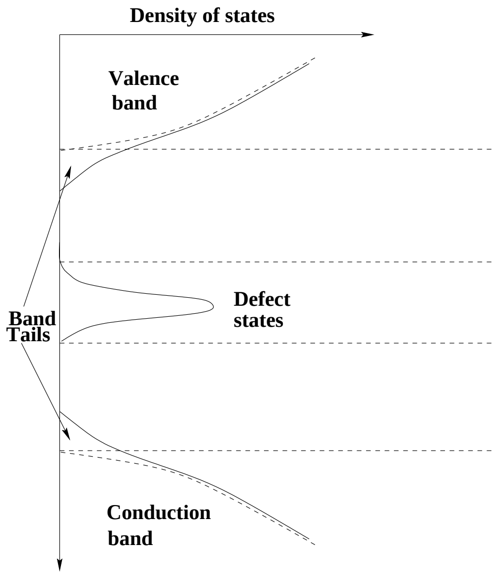


Figure 3.8: *Schematic density of states distribution for an amorphous semiconductor showing the bands, the band tails, and the defect states in the band gap. The dashed curves are the equivalent density of states in a crystal.*

the a-Si. The effect of this is to wipe out most of the electron states in the gap.

Hydrogenated a-Si, sometimes called silicon-hydrogen alloys and written a-Si:H (although $Si_{1-x}H_x$ would be more appropriate, where x is typically 0.1 to 0.2) is of technological interest. $Si_{1-x}H_x$, with x≈0.1, reveals its electronic superiority to elemental a-Si in its high electrical resistivity and in exhibiting clear photoconductivity. Most importantly, the semiconductor properties can be controlled by doping the material either $n$ or $p$ type.

## 3.4 The Staebler Wronsky effect (ageing)

The photoactive material of ALMY sensors is hydrogenated amorphous silicon. Since 1977, it is known that properties of a−Si:H are susceptible to change upon prolonged illumination. When Staebler and Wronsky [6] discovered that the dark conductivity and photoconductivity of glow-discharge-deposited amorphous silicon could be reduced by prolonged illumination with intense light, they attributed this change to a reversible increase of the density of gap states. Since then, this effect is known as Staebler Wronsky Effect (SWE). In 1985 Stutzmann *et al.* [7] performed a systematic study using electron-spin resonance (ESR) and photoconductivity measurements, monitoring changes in a set of samples. The conclusions of the work from Stutzmann *et al* are shown here as an introduction to the SWE.

This section is intended to give a basic approach to the also called *ageing phenomena*. We will display the dependences of the photoconductivity (PC) with the illumination time and power of the source employed. For further information on this topic, refer to [7].

### 3.4.1 Metastable defects

The amorphous phase of a material is characterized by the existence of a finite number of local potential energy minima separated by potential barriers (see figure 3.9). If an externally applied excitation $E_{ex} \geq \Delta E + V_0$ is applied, stimulated transitions between levels $q_0$ and $q_1$ ($q_i$ some suitably chosen variable) will occur. A state like $q_1$ which remains populated after the excitation is switched off is called a metastable defect. When laser light is the excitation source, some generated carriers will be trapped in these defects and the photocurrent will decrease.

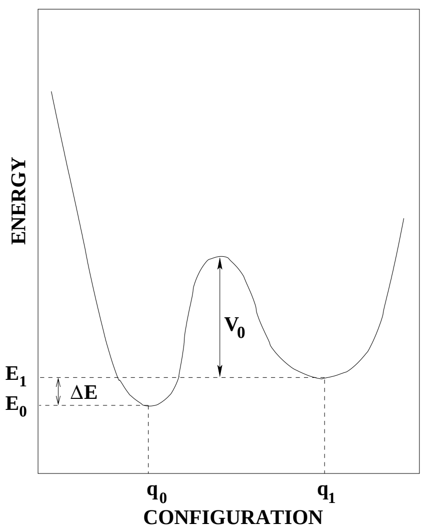


Figure 3.9: *Energy-configuration diagram used for a system with a minimum potential energy and a metastable level $\Delta E$ above.*

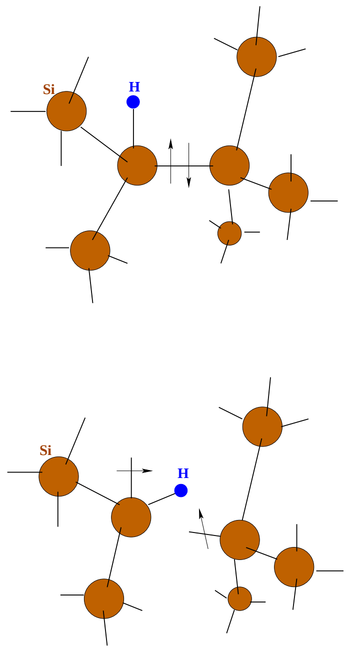


Figure 3.10: *The upper picture shows a network of a-Si:H, with a weak Si–Si bond. After a phonon (coming from a non radiative tail-to-tail recombination between optically excited electron and hole) splits the bond (bottom picture) a rearrangement of the hydrogen leads to a metastable configuration (after [7]). In this case, a dangling bond plus a Si–H–Si hybrid state.*

The SWE is an effect inherent to amorphous silicon. Light soaking of samples with N and O impurity concentrations from $10^{16}$ to $10^{20}$ cm$^{-3}$ show that the SWE is independent of the impurity concentration. Only at high impurity concentrations ($> 10^{20}$ cm$^{-3}$), the density of metastable defects increases. Besides, the SWE increases proportional to the sample thickness up to about $d = 0.5 - 0.6$ $\mu$m (independently of the wavelength), and then stabilizes. This fact indicates that there is both a surface and a bulk contribution to the SWE.

### 3.4.2 Microscopical description of the SWE

The breaking of weak Si−Si bondings (figure 3.10 up), for instance due to the absorption of a phonon, into one or two Si *dangling bonds*, together with a possible rearrangement of hydrogen in a−Si:H (figure 3.10 bottom) is considered to be the microscopical description of the SWE. The model from Stutzmann *et al* is based on the assumption that new metastable dangling bonds are created by the fraction of **nonradiative, direct tail-to-tail recombination transitions**. In figure 3.11 these transitions are labelled as $A_t$. The factor $C_{SW}$ represents the efficiency of the transitions $A_t$ for the creation of new dangling bonds.

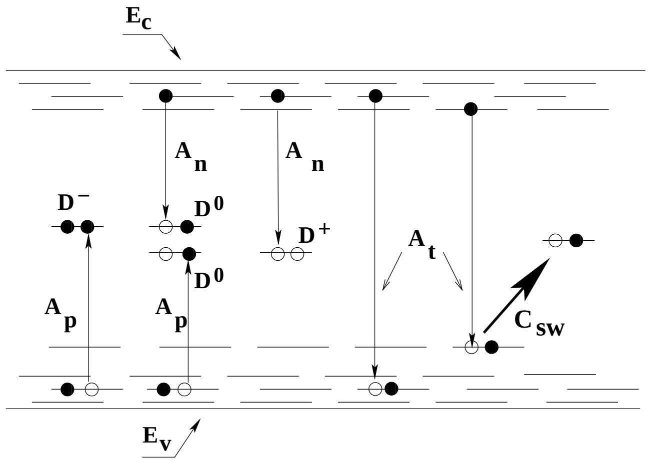


Figure 3.11: *Generation and recombination diagrams of excess electrons and holes. The rightmost process shows a recombination electron−hole. The mediating phonon leads to the creation of the metastable defect (in the middle of the gap).*

The three possible charge states of the generated Si dangling bond, which will become recombination centers, are called $D^+$ or $D^-$ when occupied by two holes or two electrons and $D^0$ if the dangling bond is singly occupied. The density of dangling bonds in a−Si:H may be calculated as:

$$N_r = N^+ + N^0 + N^- \tag{3.2}$$

where $N^+$ and $N^-$ are the densities of the configurations of charged dangling bonds and $N^0$ is the density of neutral dangling bonds.
In the model proposed by Stutzmann *et al*, the creation of metastable defects occurs by nonradiative recombination between optically excited electrons and holes. The lattice vibration produces the splitting of a weak bond thus leading to a variable number of dangling bonds $N_r = N_r(t_{ill})$ depending of the illumination time $t_{ill}$.

### 3.4.3 Influence of the photon energy and temperature

The efficiency for creating metastable dangling bonds is independent of the photon energy in the range $h\nu = 590-1033$ nm. This suggests that the defect creation step occurs after thermalization of the optically excited carriers.

Regarding the role of the temperature, the steady state is reached more quickly when the experiment is performed at elevated temperatures. The rate of defect creation is insensitive to the temperature.

### 3.4.4 Density of metastable defects

Radiative generation processes of excess electrons and holes occur with a constant generation rate G (proportional to the incoming light power). The charges generated contribute to the photoconductivity (PC) during a mean lifetime $\tau$. This lifetime *is limited* by the recombination of the carriers. A recombination is any event that removes an electron or hole from the integral populations $n$ or $p$ (band energy tails included). This is possible by sequential deep trapping of a hole by a doubly occupied $D^-$ or singly occupied $D^0$ dangling bond inside the gap, and of an electron by a positively charged $D^+$ dangling bond. Direct tail-to-tail transitions between excess electrons and holes are possible. At room temperature or above, the transitions are predominantly nonradiative, that is, mediated by a multiphonon process.
It can be demonstrated that the rate of creation of new dangling bonds, $dN_r/dt_{ill}$, decreases with the square of the density of already existing dangling bonds. The physical reason for this decrease is that the tail-to-tail transitions leading to the creation of metastable dangling bonds are inhibited by the existing stable or metastable dangling bonds. In this sense, the SWE is a self-limiting effect.
The explicit number of dangling bonds created after the illumination time $t_{ill}$ can be calculated as [7]:

$$N_r^3(t_{ill}) = N_r^3(0) + C(A_t)G^2 t_{ill} \tag{3.3}$$

where $C$ is a constant independent of G an $t_{ill}$.

### 3.4.5 Photoconductivity dependencies

Assuming low illumination intensities, and following [7], the photoconductivity can be calculated as:

$$\sigma_{ph} \quad = \quad B(G/N_r) \tag{3.4}$$

where B is a constant independent of G. Displaying the dependence on external parameters G and $t_{ill}$:

$$[\sigma_{ph}(t_{ill})]^{-3} - [\sigma_{ph}(0)]^{-3} = 3c_{SW}kt_{ill}/G \qquad \text{long time limit}$$

$$[1/\sigma_{ph}(0)](1/[\sigma_{ph}(t_{ill})] - 1/[\sigma_{ph}(0)]) = c_{SW}k't_{ill}/N_r(0) \qquad \text{short } t_{ill} \text{ and/or small generation rates}$$

The absolute level of the PC decreases both with decreasing illumination intensity and increasing illumination time. The decrease in the PC occurs parallel to the increase of the dangling-bond density.

### 3.4.6 Annealing of a–Si:H

In the early work from Staebler and Wronsky [6] they also found that the observed changes were reversible by annealing at elevated temperatures ($\geq$150°C). The accepted theoretical model establishes that the annealing rate $dN_{ind}/dt$ is proportional to the number of existing metastable defects, $N_{ind}(t)$. This leads to an exponential decay of the number of metastable dangling bonds:

$$N_{ind}(t) = N_{ind}(0)\exp[-\nu t] \tag{3.5}$$

where $\nu$ is not a constant but a distribution that depends directly on the activation energy and inversely on the temperature. The formula above states that the number of dangling bonds anneals in an exponential way. The fact that the metastable defects are distributed in energy (not an unique value of $V_0$ in figure 3.9) implies the undefinition of the decay frequency [7].
According to equation 3.5 a low temperature annealing followed by another at higher temperature is less efficient than one at higher temperature.

## 3.5 The ALMY sensor

ALMY sensors are transparent two dimensional position strip sensors. A position sensor allows to calculate the position (in a certain reference system) of a suitable signal acting on it. The basic structure of an ALMY is presented in figure 3.12, and its main design parameters are given in table 1. ALMY sensors are made by a multilayer structure built on top of a glass sheet. The stack is formed by a continuous layer of amorphous silicon in between a double layer of perpendicular Indium Tin Oxide (ITO) strip electrodes. A thin layer of passivant material is deposited over the top electrode (not drawn in figure 3.12), providing thus electrical isolation of the device.

| | |
|---|---|
| Sensor type | a-Si |
| Active area | 20 × 20 mm$^2$ |
| Number of strips | 64 × 64 |
| Strip pitch | 312.5 $\mu$m |
| Strip width | 302.5 $\mu$m |
| Substrate thickness | 0.5 - 1 mm |
| Bias Voltage | 1 - 5 V |
| $\mu_p^{Hall}$ | $10^{-4}$ cm$^2$/Vs |
| $\mu_n^{Hall}$ | $10^{-2}$-$10^{-3}$ cm$^2$/Vs |
| Effective band gap | 0.82 $\mu$m |

Table 1: General properties of the amorphous (a-Si) silicon strip sensors

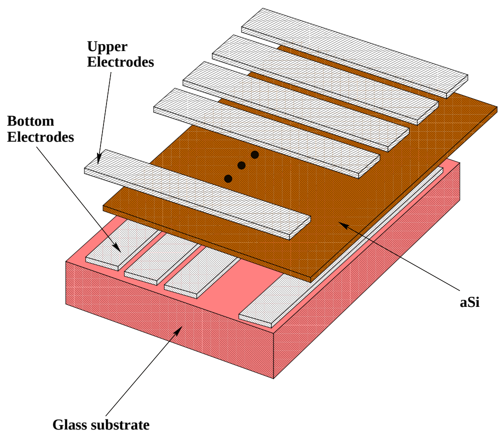


Figure 3.12: *Three layer stack of ITO and a-Si:H on glass: the ALMY sensor.*

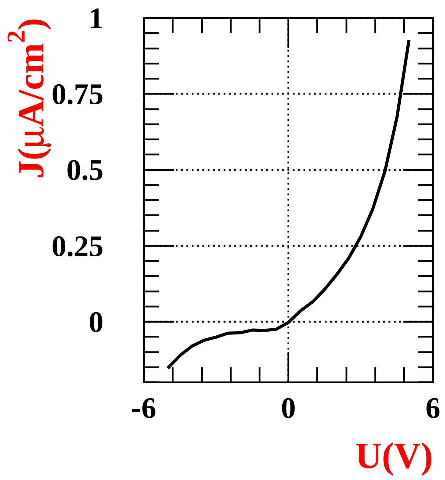


Figure 3.13: *IV characteristic of an ALMY sensor photodiode, measuring an individual photodiode from a strip crossing [8]*

If only one layer of a-Si:H is employed, the device results a Schottky structure (metal−semiconductor junction), or a *pin* when three layers ($p$ doped, intrinsic and $n$ doped) are used. Optical properties (transmittance and reflectance of the stack) are affected by the choice. In order to illustrate the electrical functioning of ALMY sensors, we will assume now that we are dealing with Schottky ALMY structures. In this case, the upper electrode forms a Schottky diode with the a-Si:H layer, while the bottom electrode simply acts as an ohmic contact.

As already explained in subsection 3.2.5, reverse biased photodiodes produce signal proportional to their illumination. Provided the reverse bias keeps under certain values, the proportionality can be chosen to be linear. The orthogonal arrangement of upper and lower ITO metal contacts, produces a 2D matrix of (64 × 64) Schottky photodiodes, as the ones shown in figure 3.13 [9]. Each volume of a-Si:H enclosed by the intersection of one upper and one bottom electrodes defines a Schottky photodiode. The position of a light spot on the sensor surface can be calculated as the center of gravity of the photocharge distribution collected by the 2D network of photodiodes. The accessing of the photodiodes in the ALMY sensor is characteristic of the sensor. If we call $N_{x(y)}$ the number of photodiodes along the $X$ $(Y)$ coordinate, the ALMY sensor contains $N_x \times N_y$ photodiodes but they are accessed as a set of $N_x + Ny$ rows and columns of photodiodes.

During ALMY operation, upper and lower electrodes are read out independently. The readout scheme of ALMY sensors is illustrated in figures 3.14 and 3.15. Figure 3.15 is an aerial representation of figure 3.14 for a better understanding. Both figures show a simplified ALMY sensor, reduced to 4+4 strips, defining 4×4 photodiodes. Each photodiode has been labelled with a matrix-like nomenclature D$rc$, being $r$ the row number (rows are in the bottom layer) and $c$ the column number. Polarization is provided by the $+V$ voltage applied to upper electrodes. $R_{cy}$ is the polarization resistor for the column $c$ and $R_{rX}$ the resistor for row $r$. Lower electrodes are

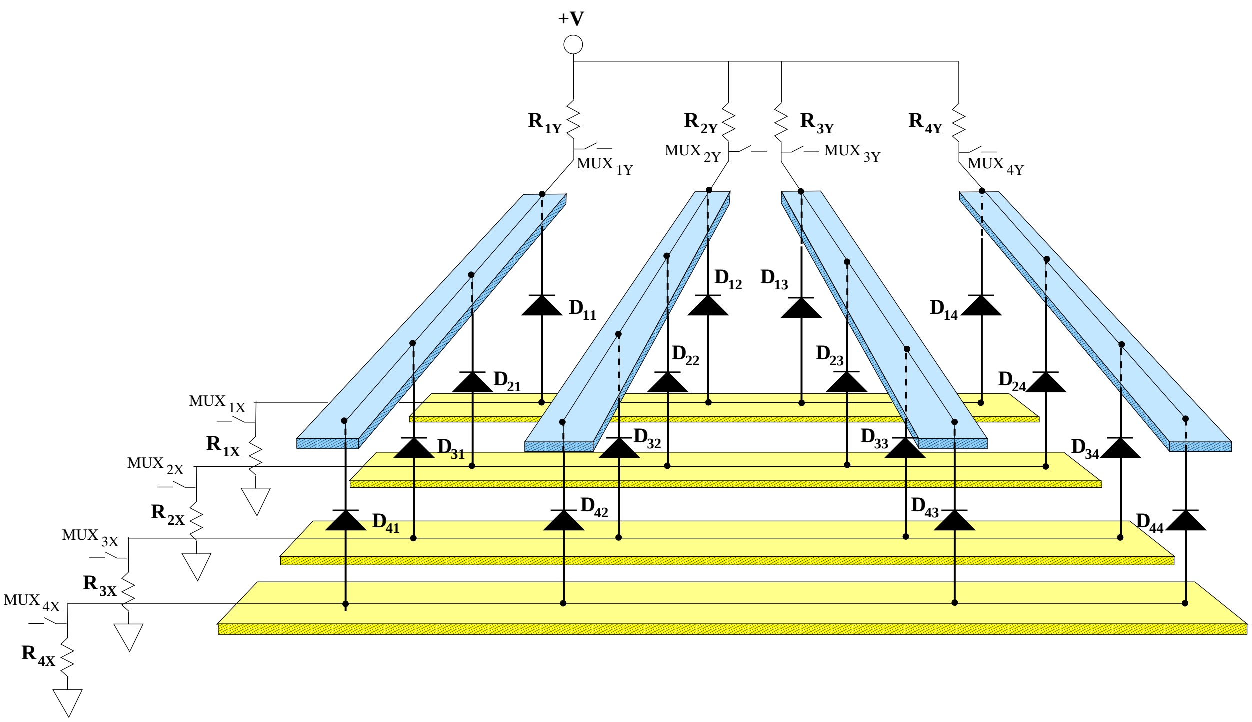


Figure 3.14: *ALMY sensor (simplified to 4 upper and 4 lower electrodes) as a 2D matrix of photodiodes. Each time a strip is accessed, the diodes along the strip are set in parallel and the charge collected by each strip is then extracted. Upper electrodes are biased at $+V$, while lower electrodes are grounded. Each strip is selected via a multiplexer channel. Dots in the figure represent electrical connections. [9]*

grounded.

In the commercial version of the electronics, ALMY strips are accessed using four (16:1) multiplexer per strip layer. The multiplexers ($MUX_{rX}$ and $MUX_{cY}$ in figure 3.14) switch 4 neighboring channels for the bottom and top electrode respectively in 16 consecutive addressing steps.

Let us imagine that we could illuminate strip 1Y only (upper leftmost strip). Then photodiodes $D_{11}$,$D_{21}$,$D_{31}$,$D_{41}$ would produce photocharges. By closing multiplexer $MUX_{1Y}$, all the charge produced by these four photodiodes can be collected. A 2D representation of this process is shown in figure 3.16. In this way, the charge collected by a strip results the *addition* of individual signals of each photodiode crossed by the strip. Sources with symmetrical intensity distribution, when being slice-by-slice integrated, will produce a symmetrical photocharge distribution. If asymmetrical distributions are utilized, then the shape of collected photocharge distribution and the beam shape of the beam intensity will not match. Laser beams with Gaussian intensity profiles, as provided by HeNe tubes or semiconductor lasers, are thus preferred to be utilized with ALMY sensors.

The transparency is the second characteristic feature of ALMY sensor. ALMY sensors are transparent sensors because the active material (a-Si:H) is able to absorb a small fraction of the incoming photons while leaving the bulk of them to traverse it. Besides, the detector is built on top of a transparent substrate, allowing the light to propagate across it.

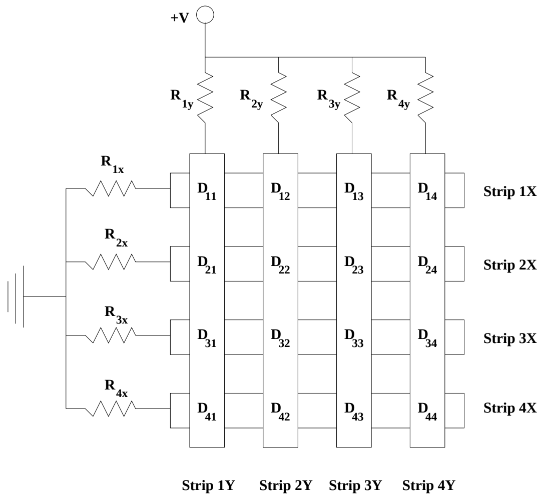


Figure 3.15: *2D ALMY photodiode network (see also figure 3.14)*

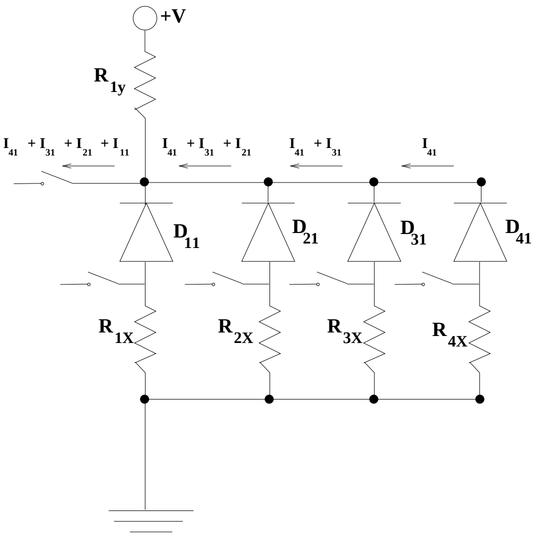


Figure 3.16: *Charge collected by strip 1Y is obtained setting diodes $D_{11}$ to $D_{41}$ in parallel. Diodes are reversely polarized. Electrons travel to the anode and escape through the multiplexor, because the resistance along this path is lower.*

### 3.5.1 Description of the ALMY electronics

As it will be explained in chapter 4, different ALMY versions studied during this work had different electronics. However, all of them shared common elements as the multiplexing of signals or current to voltage conversion. This section describes the commercial version of electronics [10].
Commercial ALMY sensors are equipped with a front end electronics (housed in the sensor carrier) and an electronics box with: a signal processing board, an interface board and a microcontroller board.
Elements attached to the sensor carrier are 2×64 polarization resistors (packaged into 2+8 resistor networks) and 2×4 multiplexers. Each strip of the bottom and top electrode is connected to one input of a 16:1 multiplexer and a parallel 47 kΩ resistor. The top electrode of the sensor is connected to the analog bias voltage and the bottom electrode to analog ground. Multiplexers are addressed simultaneously switching 4 neighboring channels for the bottom and top electrodes in 16 consecutive addressing steps. The sensor carrier is connected with the electronic box through a flexible printed circuit board (PCB).
The eight (top and bottom) photocurrent signals of the sensor are converted to voltage signals (feedback resistor 1 MΩ) on the signal processing board. This board provides the analog bias and analog ground for the top and bottom electrodes. By switching off input photocurrents, the electronics is able to measure the offset voltages of each current voltage converter, storing them for further signal correction. The amplified signals are passed to a four-fold sample&hold. Its output signals are transferred to the A/D converter.

At the interface board, voltage supplies for the microcontroller and the sensor carrier are supplied. An in-board 2-color LED can be utilized for a fast intensity adjustment without additional measurement equipment.
Finally the controller with an integrated ADC of 10 bits and an A/D conversion time of 20 $\mu$s is located in the microcontroller board. Ten different programs stored in an EPROM can be selected. The main functions of the programs are sending the raw signals of each strip or perform calculations of the centroid positions.
The electronic box needs a DC power supply (connected to the interface board) of +9 V. The data are sent out by a serial line, allowing baud rates from 9600 to 115200 bps. One electronic box can operate up to 4 sensors.

## 3.6 Summary

We have reviewed the main concepts needed to explain the structure and operation of ALMY devices. An ALMY sensor is a transparent position sensor, acting as a large 2D network of photodiodes working in parallel. Due to its importance for the current design of the CMS alignment system, these sensors will be the subject of chapters 4 and 5. Special attention has been payed to the amorphous silicon material, being the active layer of the ALMY sensor. We have introduced the energy bands structure of the a-Si:H and have summarized the ageing effect, which affects the long term performance of ALMY sensors. We explained the operation of a Schottky type sensor, from the absorption of light to the collection of photocarriers by the strips. The electrical operation has been illustrated explaining the conversion of these photocharges to digital signals performed by the electronics version of commercial ALMY sensors.

# Bibliography


[1] Charles Kittel, *Introduction to Solid State Physics*, John Wiley & Sons (1953)

[2] S.M. Sze (1981), *Physics of Semiconductor Devices* John Wiley & Sons

[3] T.H. Beeforth and H.J. Goldsmid, *Physics of Solid State Devices*, Pion Limited, 207 Brondesbury Park, London NW2 (1970).

[4] Taken from Lecture "MSE 570 - Introduction to the Physics of Solids", handed in at the $21^{st}$ of December 1994, University of Pennsylvania
http://staff.ub.tu-berlin.de/ harloff/index.html

[5] R.A. Street *Hydrogenated amorphous silicon* , Cambridge Solid state, Science Series.

[6] D.L. Staebler and C. R. Wronski, Appl. Phys. Lett. 31, 292 (1977)

[7] M. Stutzmann, W.B. Jackson, and C.C. Tsai, *Light-induced metastable defects in hydrogenated amorphous silicon: A systematic study* , Phys. Rev. B 32, 1 23-46.

[8] Sandra Horvat, *Status of ALMY sensors* , Presentation at MPI, $30^{th}$ May 2001

[9] Private communication with Dr. Antonio Molinero, responsible person for the Link electronics team. CIEMAT, Avda. Complutense 22, P.O. 28040, Madrid (Spain).

[10] DPSD 2064, EG&G Optoelectronics. 45 William Street, Wellesley, Massachusetts, 02181. U.S.A.

# Chapter 4

# ALMY sensors characterization

## 4.1 Introduction

This chapter summarizes the results of tests performed on a number of ALMY sensors, belonging to different production processes. The most relevant features are studied, namely: light detection, beam deviation, collected charge and transmittance. An overview of the ageing phenomena (degradation of the photocurrent generated by the a-Si:H layer after intense illumination) is also presented.
First section is a historical review of the development of transparent sensors. The current ALMY layout and common features to all kinds of ALMY sensors are explained in subsection 4.2.2. In section 4.3 we define the two different algorithms employed to obtain the position of the spot from the signals of the strips. Subsection 4.3.3 shows a comparative study on the performance of different reconstruction methods for the displacement of the spot on the sensor making a decision favoring one of them.
In section 4.4 the propagation of the light through an ALMY sensor is studied accounting for multiple reflections inside it. The whole deflection process is simulated retrieving the typical deflection patterns measured in the laboratory. The relation of the deflection with the glass shape, interdistance between sensors and indexes of the materials is also displayed. In chapter 5, a complementary optical simulation can be found. There, the sensors are studied as infinite multilayers and the aim is to calculate the energy ratios between incoming and outgoing energy. Here we consider Gaussian beams which propagate inside shaped media and are deviated. The magnitude of the deviation is the goal of the study.
Sections 4.6 through 4.8 summarize the most important results of our calibrations. In section 4.10, results of ageing measurements done at different laboratories are presented.

## 4.2 Development of Transparent Position Sensors

### 4.2.1 Crystalline silicon position sensors

The predecessor of the current ALMY sensor is the crystalline silicon strip position sensor, devised by W. Blum *et al.* [1]. Its origin dates to 1993 [2]. These sensors were produced by CSEM [3] at Neuchâtel. Crystalline silicon (c-Si) was used as active material.
Crystalline silicon sensors operate on the principle of silicon strip photodiodes. It consists of 67 $p^+$ strips implanted in a $n$-type silicon substrate (see figure 4.1). Aluminum strip contacts are

located at both extremes. The bulk contact is made in the front surface, using a ring-shaped $n^+$ implant surrounding the strips. A layer of silicon nitride, 30 nm thick, on top of 90 nm of silicon dioxide coats both surfaces of the substrate, reducing the internal reflections to a negligible extent. The main design parameters are summarized in table 1.

The position of the spot perpendicular to the strips direction is obtained as the center of gravity of the signal of the strips. Taking into account the saturation current (5 $\mu$A/strip), the dark current and electronic noise (<1nA/strip), the intrinsic position resolution is better than 1 $\mu$m (see equation (4.2)). The position of the spot along the strips direction is obtained by current division: reading the strips on both sides and measuring the asymmetry in the current. The intrinsic resolution of this method is about 60 $\mu$m [4].

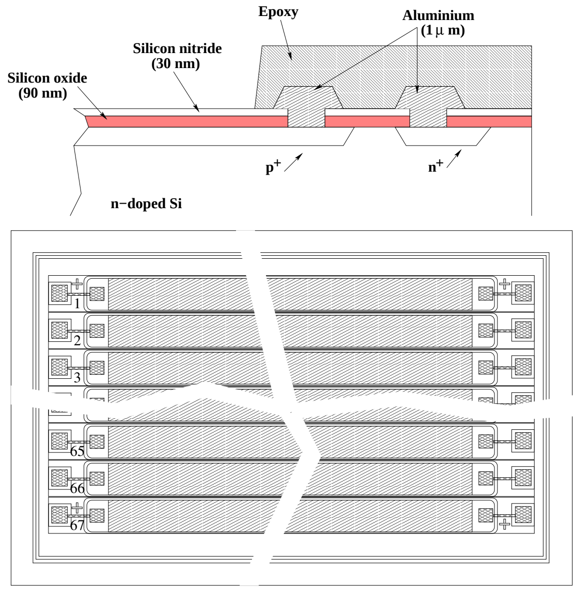


Figure 4.1: *Upper: Cross section of c-Si sensors. Bottom: Upper view of the sensor. The sensor has strips along one direction.*

However, the position resolution (across the strips) over the whole surface is limited to 10−30 $\mu$m (depending on the sensor) due to non uniformity of the strips response. According to simulations [4], the effect corresponds to sensitivity variations of about 5%. Since the position calculated errors are reproducible for each sensor, they may be corrected by precalibration of the sensor. The corrected spatial resolution decreases thus down to 2-3 $\mu$m. The origin of the heterogeneous response are interferences in the several layers. Although this device is coated, the performance of the coating on silicon is not as good as it can be for coatings on glass (see section 4.7.3).

Spreads in the beam deflection (after traversing a sensor) between 10 and 25 $\mu$rad for maxima absolute deflection of about 200 $\mu$rad were observed. Again, using the same precalibration method (see also section 4.4) as before, the beam deflection could be corrected to 1−1.5 $\mu$rad.

Transmittance values of 71% have been obtained at 1064 nm for 300 $\mu$m thick c-Si sensors.

| Sensor type | c-Si | a-Si |
|---|---|---|
| Active area | 20 × 20 $mm^2$ | 20 × 20 $mm^2$ |
| Number of strips | 67 | 64 × 64 |
| Strip pitch | 298.5 $\mu$m | 312.5 $\mu$m |
| Strip width | 280 $\mu$m | 302.5 $\mu$m |
| Substrate thickness | 300 $\mu$m | 0.5 - 1 mm |
| Bias Voltage | No | 1 - 5 V |
| $\mu_p^{Hall}$ | 310 $cm^2/Vs$ | $10^{-4}$ $cm^2/Vs$ |
| $\mu_n^{Hall}$ | 1650 $cm^2/Vs$ | $10^{-2}$-$10^{-3}$ $cm^2/Vs$ |
| Effective band gap | 1.1 $\mu$m | 0.82 $\mu$m |

Table 1: General properties of crystalline (c-Si) and amorphous (a-Si) silicon strip sensors

### 4.2.2 The ALMY design

The heterogeneous response of the crystalline devices, the further degradation of the performance near the edges and the expected higher radiation damage of crystalline silicon, led to discard the crystalline technology favoring the amorphous silicon development. The amorphous silicon sensor (already presented in chapter 3) consists of a multilayer structure built on top of a glass sheet. The stack is formed by amorphous silicon in between a double layer of perpendicular Indium Tin Oxide (ITO) strip electrodes. When one layer of a-Si:H is employed, the device results a Schottky structure (metal-semiconductor junction, with a thin layer of insulator), or a *pin* when three layers (p-doped, intrinsic and n-doped) are used. Optical properties are deeply affected by this choice. A 3D view of the sensor is shown in figure 3.12. A thin layer of passivant material is deposited on top of the top electrode (not drawn in figure, providing thus electrical isolation of the device. The design parameters are summarized in table 1.

The operation of these devices relies in the carrier (electron and holes) creation under illumination. The external bias contributes further to the charge separation. Electrons are driven to upper electrodes while holes contribute to the current in the lower electrodes. The voltage applied depends on the ALMY version, the number and thickness of the layers.

Since only the electrodes are segmented, the 64 × 64 crossings produce 64 + 64 signals. The incoming beam spot is then reduced to two 1D intensity distributions. The magnitude of the response given by each strip is discussed immediately.

The protocol followed to read the strips is implementation dependent. Different procedures are available for different version of electronics. Commercial sensors, read four upper and four lower strips simultaneously. Sixteen multiplexer cycles are needed to readout the whole sensor collected photocharge.

Since electrodes are segmented into strips, the readout photocharge can be originated all along the strip extension. In this sense, the ALMY does not produce a true 2D shot of the beam, as if it were a 64×64 video camera. Instead, the charge readout by each strip is the charge *integrated* along this strip.

## 4.3 Position reconstruction

The original and most remarkable characteristic of the ALMY sensors is that they allow to measure the position of the light beam that traverses them. This feature eases the solution of alignment problems and reduces the amount of volume spent by other concepts based on non-transparent devices.
During the design phase, the sensor parameters were optimized for typical laser beam diameters 2-3 mm (which can be maintained along distances of several meters), around the red wavelength. Collimated single mode laser beams are preferred since they have a clear Gaussian intensity distribution. The orthogonal segmentation of the electrodes allows to obtain a pair of 1D images of the incoming beam. Vertical electrodes integrate all the signal collected along them reconstructing a well defined Gaussian signal. The orthogonal distribution is obtained collecting all the charge induced in the horizontal strips.
Although the strip pitch is 312.5 $\mu$m the position resolution is greatly improved if the information of several strips is used simultaneously. This improvement may be achieved using, for instance, a Gaussian fit of the signal or calculating the intensity centroid.

### 4.3.1 Beam position estimator: Gaussian mean or centroid?

Provided a good stability of the light source, the position of the light spot on the sensor can be determined by different reconstruction algorithms. We have studied two different candidates: weighted centroid and Gaussian mean. The expression for the first one is:

$$x_C = \frac{\sum_{i=0}^{63} x_i I_i}{\sum_{i=0}^{63} I_i} \tag{4.1}$$

where $x_i$ are taken as the position of the center of the strips, and $I_i$ the photocurrent read by each strip. An analogue formula applies for the Y coordinate.
In order to avoid random fluctuations of the intensity, the signal may be averaged (typically 10-20 times, taking each measurement fractions of second). Therefore a set of intensities $I_{ij}$ ($i$ is the strip number and $j$ the number of measurement) for each strip is obtained. The centroid algorithm can not introduce this statistical effect into the calculation. Instead of this, the mean value of the photocurrent $\overline{I_i}$ provided by each strip is utilized in equation 4.1 as constant and the statistic is introduced calculating the error of equation (4.1), which is:

$$\sigma_{x_C} = \sqrt{\sum_{i=0}^{63} (x_i - x_C)^2 (\frac{\sigma_{I_i}}{I_T})^2} \tag{4.2}$$

where $I_T = \sum_{i=0}^{63} \overline{I_i}$ and $\sigma_{I_i}$ is the standard deviation on $\overline{I_i}$. The Gaussian fit can account for these fluctuations in a straightforward manner, weighting $\overline{I_i}$ by the standard deviation of each set. The parameters of the Gaussian are then estimated having the fluctuations into account. Attending to symmetry arguments, the centroid and the Gaussian mean coincide if the intensity distribution is a Gaussian. In this work we have employed the Gaussian mean as position estimator of the light spot. Only when the light intensity distribution was not a clear Gaussian, the centroid was used.

### 4.3.2 Inhomogeneity of the sensor and displacement error

ALMY sensors are 2D position sensors. Electrodes integrate the signal intensity falling on the sensor surface. Upper electrodes integrate along a direction perpendicular to the lower electrodes. Thus, two 1D images from the incoming spot are reproduced. By calculating the center of gravity of each distribution we can associate a 2D position to the light intensity distribution. Utilization of these devices as position sensors requires to study the skills of the sensor reproducing a displacement of the light spot over its surface. This displacement can be obtained mounting the sensor on a two axis stepping motor. A light beam impinging on the sensor can sweep its surface by moving the platforms in a sequence. Then, the spot position is calculated and the displacement on the sensor compared to the displacement of the platform. Figure 4.2 shows a horizontal scan of the laser beam over the sensor. The platform step was constant and equal to 400 $\mu$m. A linear relationship between calculated position on the sensor and the platform displacement is observed. The difference between the calculated positions and a straight line fit to figure 4.2 (residuals of the fit) shows the quality of the movement reproduced by the sensor. The residuals from a straight line fit to figure 4.2 are shown in figure 4.3.

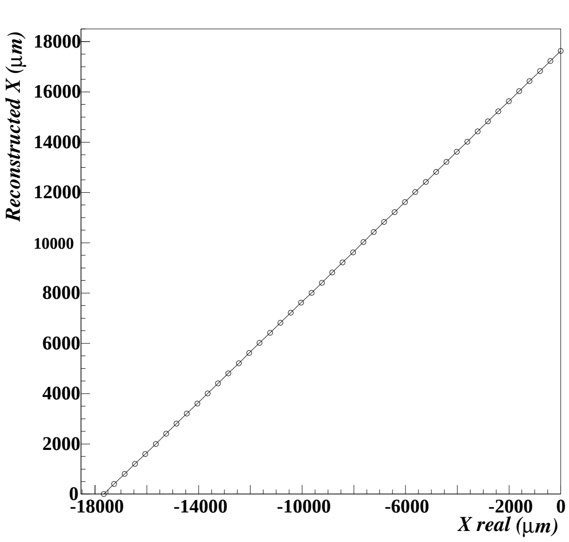


Figure 4.2: *Vertical axis: Position of the spot, as reproduced by an ALMY sensor during a horizontal scan. Horizontal axis: Displacement of stepping motor.*

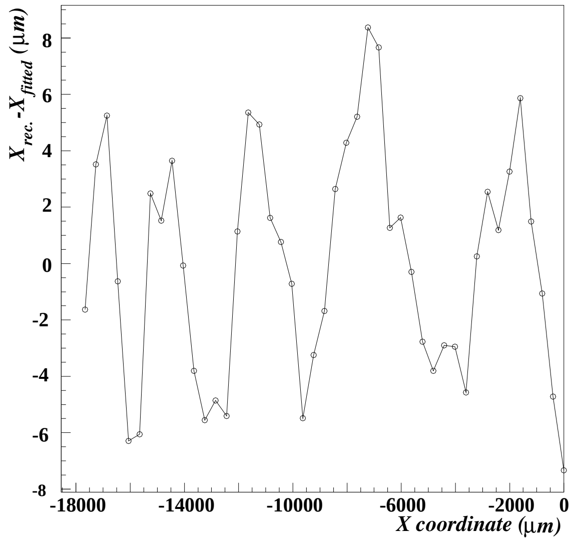


Figure 4.3: *Residuals of the fit of figure 4.2 to a straight line.*

As it can be observed in figure 4.3 the reconstruction of the spot position shows a systematic component, clearly seen as oscillations around the zero value of the residuals. Repeating the scan on different horizontal lines on the sensor produced always systematic contributions (different from line to line scanned).

We observed that the oscillation pattern was independent of the platform employed and independent of the step [5]. The observed effect was inherent to the sensor. Different sensors showed different patterns. A scan of the sensor extended to all its surface calculating the residuals along independent lines reveals the shape of the systematic pattern. Since the pattern indicates a lack of uniformity in the position reconstruction, we call this pattern the inhomogeneity pattern of the sensor.

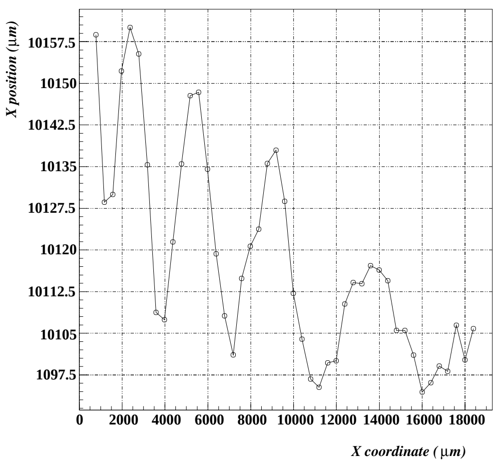


Figure 4.4: *X position measured after the beam traversed an ALMY sensor. The position is measured by another ALMY sensor.*

As ALMY sensors are transparent position sensors, we may wonder whether patterns arise in the reconstruction of the transmitted beam position. The measurement of the beam position downstream the first sensor can be performed with a CCD camera, or another ALMY sensor. The calculated position of the beam as measured by an ALMY sensor behind the sensor under study is shown in figure 4.4 as a function of the spot coordinates in the first sensor. Figure 4.4 shows a clear oscillating pattern for the calculated position on top of a linear change. Again, the pattern depends on the scanned line on the first sensor. Extending the scan to the whole surface, a 2D pattern appears. The pattern is characteristic of each sensor, independent of the platform and platform step.

It seems reasonable that if both, the inhomogeneity and transmitted light patterns were different realizations of the same effect they should be correlated. We studied the correlations point to point of both patterns, but did not find any straightforward relation between both.

The origin of the oscillating patterns and shape of the transmitted beam position distributions has been subject of controversy in the past. As it will be explained in chapter 5, the multilayer structure of the ALMY sensor leads to interference between reflected and transmitted beams in the several layers. Within a sensor, the intensity distribution of the incoming beam is slightly changed due to the light coming back from inner internal reflections. The interference produced is then observed as a measurable shift on the position of the spot on the sensor, leading to the observed patterns. Two variables contribute to the stability of these interferential patterns: the geometrical shape of the sensor and the wavelength stability of the laser. The former defines the shape of the systematic beam shifts obtained after scanning the surface with a laser spot. The latter modifies the thickness at which the interferential condition is fulfilled. The importance of the systematic contributions in the calculation of the position depends on the magnitude of the shifts. We advance that resolutions below 5 $\mu$m are easily achieved. For an explanation of the physical process leading to the observed behavior in the transmitted beam see section 4.4.

As already said, the standard procedure to calculate the map of systematic shifts (inhomogeneity pattern) is to sweep the sensor surface with a laser beam, comparing the displacement reproduced by the sensor with the real displacement of the laser beam. Taking advantage of the transparency of the ALMY, another position sensing device may be placed behind it. This allows to measure the deviation of the beam induced by the target sensor[1].

Although the grid of the sensor may be patterned with submicrometer precision, the mounting of the sensor in the electronics board, and the position of the board on the sensor support can induce an angle of the horizontal strips with respect to the vertical line of sight. Besides, if the

[1] This deviation is unavoidable due to the presence of media of different indexes

horizontal strips are taken as reference, any scan of the sensor will subtend an angle between the longitudinal direction of the scan and the vertical (in general, called the misalignment angle). For instance, a misalignment angle of 0.2 deg will move the spot 50 $\mu$m above its starting position (see figure 4.5).

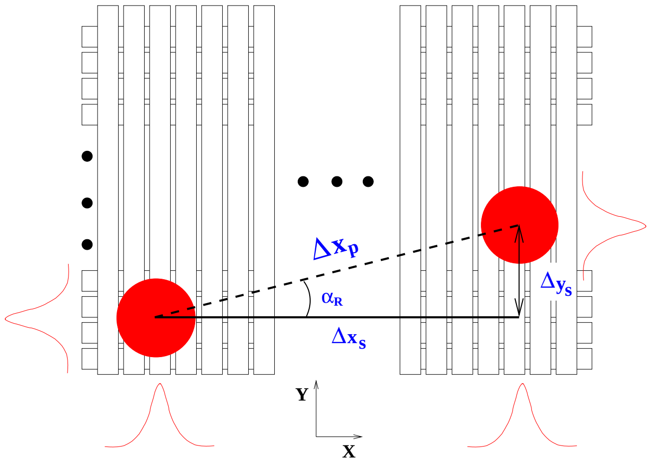


Figure 4.5: *Due to a misalignment between the scan direction of the platform and the horizontal strips, the light spot moves along a diagonal. The distance moved by the platform is $\Delta x_p$, the displacement reproduced by the sensor is $\Delta x_s$, and $\Delta y_s$ is the vertical displacement.*

Even though the performance of the sensor is independent of the mounting angle, the method employed to calculate the sensor inhomogeneity must consider it. Otherwise, errors as big as 50 $\mu$m would be wrongly associated to the sensor. Here we will present two common methods used to extract the systematic contribution from the sensor.

### 4.3.3 Position reconstruction error

One of the aims of the 2D scan is the calculation of the inhomogeneity pattern. As we have just mentioned, the inhomogeneity leads to a systematic error in the estimation of the beam position on the sensor. We call this the study of the linearity of the sensor, since the ability of the sensor reproducing a displacement over its surface is found. The instrument providing an accurate movement is a 2D stepping motor. We have employed two different stepping motor systems [6, 7] controlled by computer. Stepping precisions better than 2 $\mu$m are reported by the manufacturers.

The following analyzes the problem of the linearity. We concentrate in any of the $N_y$ horizontal scans performed over the sensor. Let $x_i$ $(i = 0, .., N_x - 1)$ be the position of the spot in an ideal sensor. The scan moves $N_x - 1$ times the position of the spot. Due to the presence of the sensor inhomogeneity, the calculated positions are affected by an error. Let $x'_i = x_i + h_i$ be positions calculated by a real sensor, where $h_i$ are the unknowns. Finally, we define $xp_i$ the successive positions of the platform step. Attending to the scanning scheme depicted in figure 4.5, the ideal sensor would reproduce:

$$x_0 = x_0$$

$$\begin{aligned} x_1 &= x_0 + (xp_1 - xp_0)\cos\alpha_R && (4.3)\\ x_2 &= x_1 + (xp_2 - xp_1)\cos\alpha_R \\ &= x_0 + (xp_2 - xp_0)\cos\alpha_R && (4.4)\\ &\vdots \\ x_{N_x-1} &= x_0 + (xp_{N_x-1} - xp_0)\cos\alpha_R && (4.5) \end{aligned}$$

but the real sensor is affected by the inhomogeneity, and the reconstructed positions are:

$$\begin{aligned} x'_0 &= x_0 + h_0 \\ x'_1 &= x_1 + h_1 = x_0 + (xp_1 - xp_0)\cos\alpha_R + h_1 \\ x'_2 &= x_2 + h_2 = x_0 + (xp_2 - xp_0)\cos\alpha_R + h_2 \\ &\vdots \\ x'_{N_x-1} &= x_{N_x-1} + h_{N_x-1} = x_0 + (xp_{N_x-1} - xp_0)\cos\alpha_R + h_{N_x-1} \end{aligned} \qquad (4.6)$$

These are $N_x$ equations and $N_x + 2$ unknowns (because $\alpha_R$ and $x_0$ are unknown). Equations for the Y coordinate are obtained substituting:

$$\begin{aligned} x'_i &\longrightarrow y'_i \\ x_i &\longrightarrow y_i \\ h_i &\longrightarrow g_i \\ \cos\alpha_R &\longrightarrow \sin\alpha_R \end{aligned}$$

The inhomogeneity $h_i$ is not the same for the Y coordinate. The explanation for this fact is that the interference of the light (which is at the origin of the inhomogeneity patterns) is different for X and Y coordinates. Then, in general the $h_i$ refers to X patterns, $g_i$ to Y patterns.
We present few methods which may be devised to compute the inhomogeneity patterns.

### 4.3.4 Method of the equations

The simplest way to solve the inhomogeneity $h_i$ pattern from equations (4.6) would be to have an extra measurement of the misalignment angle and to know one position of the sensor with no error ($x_0$). The angle $\alpha_R$ is very difficult to be measured experimentally, so an estimation of its value is obtained from the equations themselves. The calculation of angle $\alpha_R$ can not be performed from two consecutive steps, due to the magnitude of the inhomogeneity. A good estimation would be obtained from a long displacement, provided the error in both extremes be small.
We fit the $Y$ position of the spot on the sensor to a straight line, the position of the platform being the independent variable. The slope of the fit is taken as the sinus of the misalignment angle. This relation is easily understood with the following example. Let us consider the two extreme points of the scan ($xp_0$,$y'_0$) and ($xp_{N_x-1}$,$y'_{N_x-1}$). The straight line that joins both points is $y'_i = a \cdot xp_i + b$, where:

$$b = y_0 + g_0 - xp_0 \left( \sin \alpha_R + \frac{g_{N_x - 1} - g_0}{xp_{N_x - 1} - xp_0} \right) \quad (4.7)$$

$$a = \frac{g_{N_x - 1} - g_0}{(xp_{N_x - 1} - xp_0)} + \sin \alpha_R \quad (4.8)$$

The approximation consists on taking $\sin \alpha_R \approx a$. Then, the X and Y inhomogeneity patterns are calculated from 4.6:

$$h_i = x'_i - x_0 - (xp_i - xp_0) \cos \alpha_R \quad (4.9)$$

$$g_i = y'_i - y_0 - (xp_i - xp_0) \sin \alpha_R \quad (4.10)$$

Since $(x_0, y_0)$ are unknown, *values* $(x'_0, y'_0)$ *are used.*

### 4.3.5 Method of the residuals

The performance of the ALMY sensors reconstructing linear displacements over its active area is limited by the sensor inhomogeneity. An ideal sensor would be that where $(h_i, g_i) = (0, 0)$ for all $i$ values. In the ideal sensor, the relationship between the space moved by the platform and the distance reconstructed by the sensor should be 1 (after considering the misalignment angle). If there was a certain angle between the strips and the scanning direction, the slope would not be 1 anymore. The method of the residuals relies on considering that the values $h_i$ $(g_i)$ spoil the linear law. By fitting the displacement reproduced by the sensor to a straight line (the slope is left free), the residuals of the fit may be interpreted as the sensor inhomogeneity.
As the slope is attributed to the misalignment angle, this method should be independent from $\alpha_R$. The coordinate perpendicular to the scanning direction is also fitted to a straight line, and the residuals $g_i$ are obtained in the same way.

### 4.3.6 Method of the increments

This method focuses in obtaining the error in the displacement between two points of the sensor, more than finding the inhomogeneity itself. After each step of the platform, the displacement reproduced by the sensor is compared to that of the platform and the difference is the error. From equations (4.6):

$$x'_i - x'_{i-1} = (xp_i - xp_{i-1}) \cos \alpha_R + h_i - h_{i-1} \quad (4.11)$$

If the angle $\alpha_R$ is estimated as in section 4.3.4, the difference between the displacement on the sensor and the real displacement is:

$$\Delta sp = x'_i - x'_{i-1} - (xp_i - xp_{i-1}) \cos \alpha_R \quad (4.12)$$

$$= h_i - h_{i-1} \quad (4.13)$$

Therefore, the relative error between consecutive locations of the sensor is calculated.

Based on the set of equations described above, a geometrical simulation of the measurement process has been carried out. The aim of the simulation is to ease the decision of which is the method that produces 2D inhomogeneity patterns closest to the real ones. In this simulation, two independent stepping motors (2 $\mu$m precision each) shift a laser spot[2] over a sensor which has random X and Y inhomogeneity patterns. The patterns are simulated as Gaussian distributions $N(0,5)$. The longitudinal axis of the platform is allowed to form an angle $\alpha_R$ with the horizontal strips, which is also unknown. The vertical platform is assumed to be perfectly perpendicular to the horizontal. We have calculated the inhomogeneity patterns for both X and Y projections and studied how the misalignment angle influences the performance of each method. The scan is not limited to a single line of the sensor, but to all its surface.
The decision on the method is helped with the use of auxiliary functions. For each angle, we compare 2 functions of the calculated $h_{ij}$ values to the real inhomogeneity values. The following functions study the evolution of the mean values of the calculated $h_{ij}$. They give an idea of the precision of the method:

- Difference between mean input inhomogeneity pattern and calculated (method of equations) or fitted (method of the residuals) inhomogeneity.

$$f_1 = \overline{h^{input}} - \overline{h^{fitted}} \tag{4.14}$$
$$f_2 = \overline{h^{input}} - \overline{h^{equations}} \tag{4.15}$$

We also compare the calculated distributions bin by bin, since two 2D distributions may have the same mean but be very different when compared. The following functions quantify how different calculated and parent distribution are.

- When $h_i^{calc}$ comes from methods of equations or the method of the residuals

$$f_1 = \frac{1}{N_{xy}} \sum_{i=0}^{N_x-1} \sum_{j=0}^{N_y-1} (|h_{ij}| - |h_{ij}^{calc}|) \tag{4.16}$$

- When the inhomogeneity is calculated for the method of the increments

$$f_2 = \frac{1}{N_{xy}} \sum_{i=0}^{N_x-1} \sum_{j=0}^{N_y-1} (|h_{ij}| - |\Delta x p_{ij} - \Delta x'_{ij}|) \tag{4.17}$$

In the above equations $N_{xy} = (Nx-1)(Ny-1)$. The performance of the several methods is shown in figures 4.6 through 4.9. The misalignment angle is varied in a pessimistic scale ($\alpha_R \in [0,7]$ deg).
Figure 4.6 shows that the residuals method has a precision of about 0.1 $\mu$m. The residuals method is independent of the misalignment angle because it is fitted. The precision observed for

[2] As this is a geometrical simulation we approximate the spot by its center.

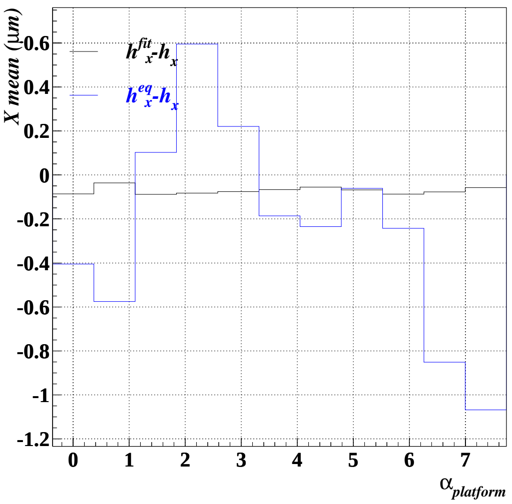


Figure 4.6: *Precision in the reconstruction of the position along the motion direction as a function of the misalignment angle. Methods involving fit or direct solution of equations are compared.*

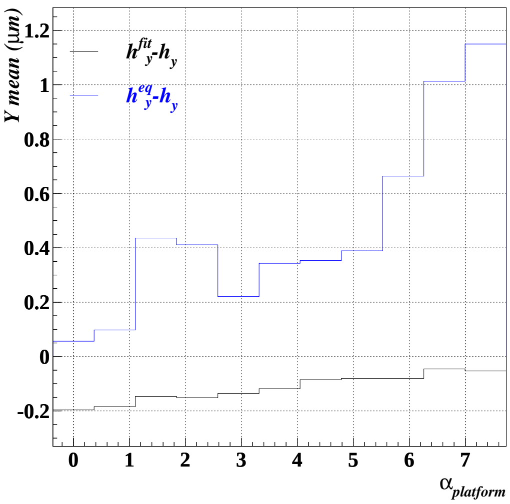


Figure 4.7: *Comparison of precision of two methods used to estimate the input inhomogeneity pattern. Comparison is performed perpendicular to the platform movement. The method involving fit slightly depends on the angle.*

the method of the equations is affected by the incomplete knowledge of two parameters $(x_0, \alpha_R)$. The slope comes from the error in the calculation of the misalignment angle.
Figure 4.7 shows again that the residuals method performance is equivalent to the sensor precision and that it is hardly affected by the misalignment. Ignorance of $\alpha_R$ is more important than the ignorance of $y_0$, most probably because the error is proportional to the sinus error.
Figures 4.8 and 4.9 compare *bin by bin* calculated $h_{ij}$ distributions with respect to the parent $h_{ij}$. They quantify how different their shapes are. For comparison purposes we also show the error induced if the increments are taken as the inhomogeneity distribution. In average, the inhomogeneity obtained from the method of the fit is $2\mu$m away from the input distribution. It may be shown that the offset introduced in the equations method is produced by the ignorance of $(x_0, y_0)$.
In this work, we will use the method of the residuals.

## 4.4 Propagation of a light beam through an ALMY

ALMY sensors are often called semitransparent sensors. It means that only a small fraction of the incoming energy is used to measure the position of the spot, the rest exiting through the rear surface. However, although the different sensor layers might be shaped perfectly planeparallel

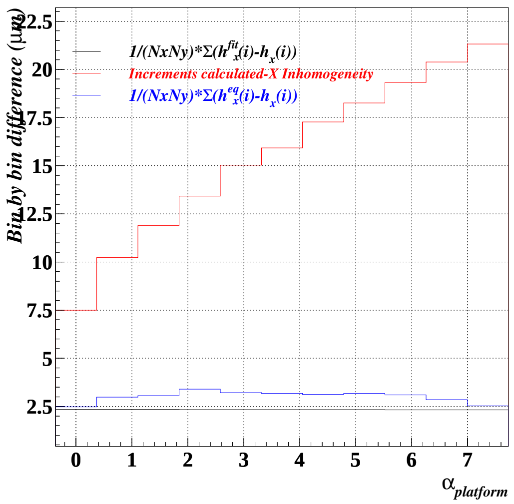


Figure 4.8: *Bin by bin comparison of the three methods devised to calculate the inhomogeneity pattern of the sensor. In the best case (fitting), the calculated $h_{ij}$ distribution is $\approx$ 2 $\mu$m away from the input distribution.*

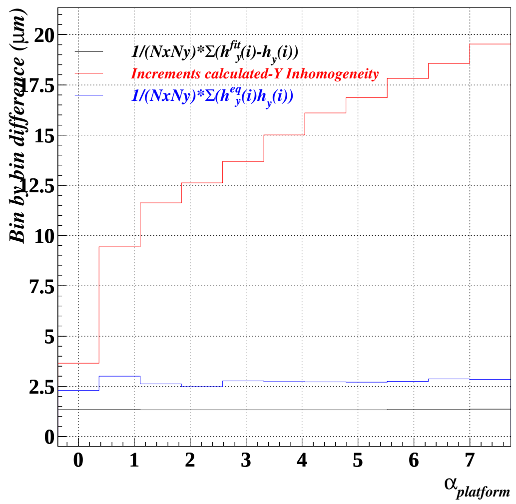


Figure 4.9: *Bin by bin comparison analogue to figure 4.9, but for the perpendicular coordinate.*

and the indexes of the materials were consciously chosen, the light will suffer a refraction. The magnitude of this refraction will be studied in this section.

From Gaussian optics, it is known that two different effects will disturb the straight propagation of a light ray. They are illustrated in figure 4.10. An incoming beam under an angle $\theta$ changes its direction by $\Delta\theta$ when the crossed medium is delimited by non planeparallel surfaces. If the beam now enters a planeparallel plate, the light will still shift by $\delta x$ with respect to the incoming beam. Setting aside environmental disturbances, both effects avoid the linear propagation of light. Depending on the refraction indexes, planeparallelism and thicknesses of the crossed materials, the deviation of the beam may be important. The large distance between sensors in current alignment systems and the dimensions of these devices makes us to expect beam deviations of order $\mu$rad.

Besides the former geometrical effect, internal reflections in the interface between layers lead to interferential effects. A distribution of overlapping waves exit the multilayer structure, shifting the center of gravity of the incident beam as measured in a second prompt sensor or CCD receiving the beam.

The above effects combined altogether contribute to the change in the beam centroid after traversing an ALMY. We will refer this change as the *beam deviation* and sometimes *beam deflection*. The implications of the beam deflection are important for alignment sensors. The reduced active area of the sensors and the alignment working range establish constraints the

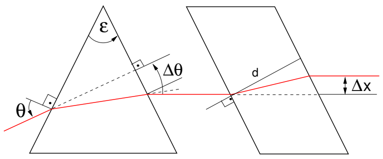


Figure 4.10: *A light ray passing through a material suffers a deviation and a shift with respect to its incoming direction. Both contribute to the equivalent beam deflection.*

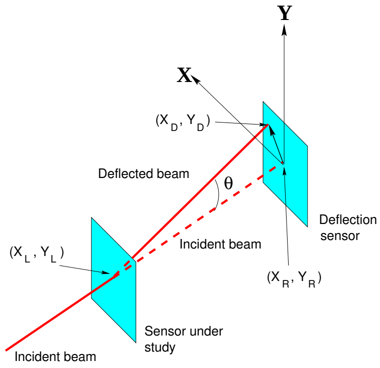


Figure 4.11: *The laser beam defines three points in the sensors, which are used to calculate the deflected angle.*

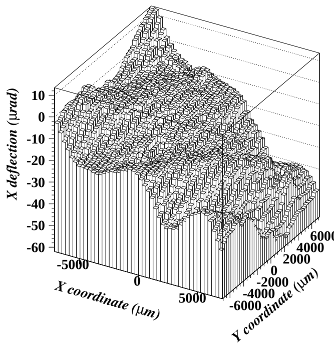


Figure 4.12: *Lego plot showing the beam deviation interpreted as a deflection. The deflection is calculated for each position of the laser spot in the first sensor.*

maximum distances and allowed deviations. Unexpected beam deviations would misleadingly be associated to movements or tilts in the monitored items. Some actions might be considered to improve the straight propagation of the laser beam inside the sensors. The different layers should be deposited/machined avoiding either wedges or curvature radius which might refract the light beam. The thickness of the layers and the refraction indexes may be chosen to favor minimum reflectance inside the stack.

A typical scan of an ALMY sensor can be used to measure the beam deviation by placing another position sensing detector behind (see figure 4.11). Prior to the start of the calibration, the target sensor is extracted out of the light path. A sample of the undeflected *reference* beam $(X_R, Y_R)$ is recorded. Then the target sensor is placed back and scanned. The position of the deflected beam in the second sensor $(X_D, Y_D)$ is compared with the previously measured reference. As expected, the new position of the beam differs from the reference value. Even though we already know that the beam deviation is a combination of refraction and interference, we will compute the deviation as a deflection angle dividing the shift in the rear sensor by the distance $D$:

$$\tan\theta_x = \theta_x = \frac{X_D - X_R}{D} \tag{4.18}$$

$$\tan\theta_y = \theta_y = \frac{Y_D - Y_R}{D} \tag{4.19}$$

for the $X$ and $Y$ coordinates, respectively. For the magnitude of the deflected beam ($\mu$rad), we can safely replace $\tan\theta \approx \theta$.

Figure 4.12 shows a lego plot of the measured beam deviation, according to above equations, for an ALMY sensor. The X deflection (vertical axis) is calculated for each position $(X_L, Y_L)$ of the laser spot in the first sensor. In this way, we can associate a deflection pattern map to the sensor under study.

## 4.5 Simulation of the beam deviation

Repeated measurements of different sensors show common trends in all the deviation patterns. The distributions of measurements in the second sensor are tilted and modulated by a wavy pattern (see figure 4.4). In this section we will show that the tilt of the distribution is produced by the curvature of the layers while the wavy pattern is a consequence of the interference in the films.
The hypothesis drawn above are verified with a physical simulation of the passage of light through an ALMY sensor. In order to keep calculations as simple as possible, we have reduced the problem to a single layer of material (the glass substrate), since it is at least two orders magnitude thicker than any of the other layers and presumably will contribute more to the beam refraction. This study is inspired in a previous work [8]. There, the substrate is considered as a 1D wedge of negligible thickness. We have simulated slightly more realistic scenarios:

- The substrate is a 3D double wedge of 20 mm$^2$ area and $\approx$500 $\mu$m thick. As coordinates X and Y can be treated independently, we have simulated a substrate with a double wedge angle (see figure 4.13). The wedge amounts 1 $\mu$m in 20 mm both along X and Y.
- The substrate is not a wedge but has certain curvature (figure 4.14)

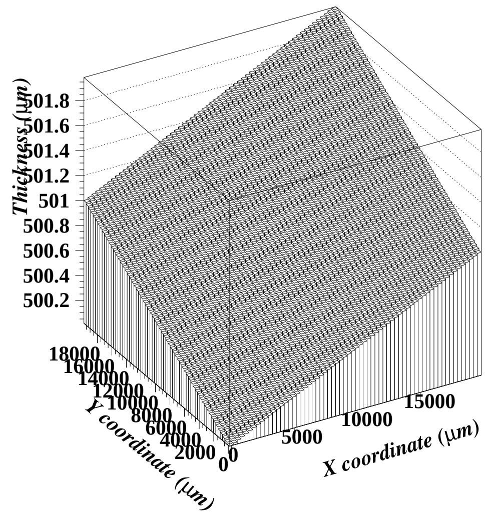


Figure 4.13: *Modeling of a double wedge substrate.*

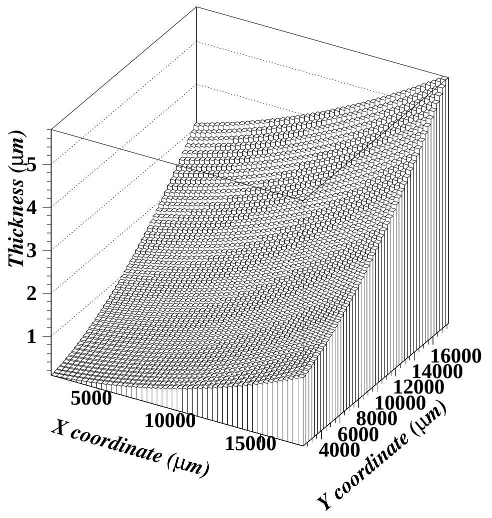


Figure 4.14: *Modeling of a curved substrate.*

Depending on the reflectivity of the material, a wave entering a film in the form of a wedge suffers multiple reflections inside [9]. The exiting wave will be a superposition of, let's say, $p$ waves (see figure 4.15).

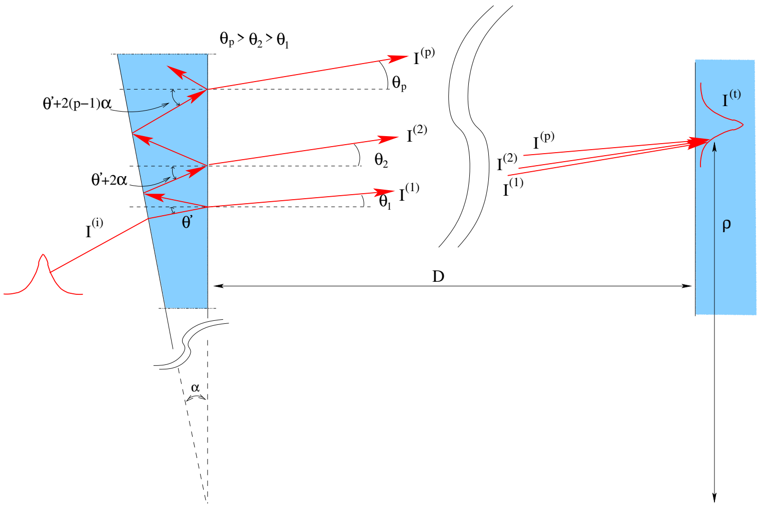


Figure 4.15: *Fifteen incoming rays as $I^{(i)}$ enter a thin wedge of angle $\alpha$ and are reflected back and forth repeatedly. For each $I^{(i)}$, a train of less energetic waves $I^{(1)} \ldots I^{(p)}$ comes out, at different angles (after [9]).*

We have taken in the calculation, the incoming wave as a Gaussian beam extended over a distance equivalent to 15 consecutive strips. Each one of these 15 signals is interpreted as a single wave of intensity $\mathrm{I}^{(i)}$, superscript $i$ meaning incident. Then, the wave is reflected many times inside the wedge. As a result from the multiple reflections, each $\mathrm{I}^{(i)}$ yields $p$ waves. The interference of these waves inside the wedge produces the image $\mathrm{I}^{(t)}$ in the second sensor. Provided $I^{(t)} \neq I^{(i)}$, the shape of the output light distribution will differ from the original one. The wedge, therefore, modifies the center of gravity of the spot in the second sensor.
If, as explained above, $I^{(i)}$ is any of the input rays (which follow a Gaussian intensity distribution), then the intensity on exit, for each $I^{(i)}$, is [9]:

$$I^{(t)} = I^{(i)}\mathcal{T}^2 |\sum_{i=1}^{p} \mathcal{R}^{p-1} \exp^{i\delta_p}|^2 \tag{4.20}$$

with:

$$\mathcal{T} = (4n_{air}n_{glass}(n_{air} + n_{glass}))^2 \tag{4.21}$$
$$\mathcal{R} = ((n_{glass} - n_{air})/(n_{glass} + n_{air}))^2 \tag{4.22}$$
$$\delta_p = \frac{2\pi}{\lambda_0}(n_{glass}\rho\{\sin[\theta' + 2(p-1)\alpha] - \sin\theta'\} + n_{air}D(\frac{1}{\cos\theta'} - \frac{1}{\cos\theta_1})) \tag{4.23}$$

$\mathcal{T}$ and $\mathcal{R}$ are the square of transmitivity of the film and the square of the reflectivity, respectively. Several magnitudes involved in the phase calculation $\delta_p$ are easily identified in figure 4.15. The vector $\rho$ addresses the distance from the wedge apex at which the interference is calculated. The first term in equation (4.23) is the phase change calculated in the rear surface of the wedge. The second term accounts for the phase change from the wedge to the second sensor.

### 4.5.1 The substrate as a wedge

A wedge of non-negligible thickness may be simulated by moving the incident ray away from the wedge apex. The beam was simulated by a Gaussian of 500 $\mu$m width falling perpendicularly to the tilted surface. The wavelength chosen was $\lambda = 785$ nm. The thickness of the wedge crossed by the refracted ray increases as $\rho \tan\alpha$, being $\rho$ the distance from the apex. Along both coordinates, see figure 4.13, the substrate is formed by a succession of wedges of constant angle and increasing thickness. As the phase difference is proportional to the amount of traversed material, the interference will change with the position in the wedge. The interference spoils the Gaussian shape of the exiting beam producing a systematic shift in the position with respect to the undistorted beam. The calculated angle in the second sensor is shown in figure 4.16. We take the undisturbed beam as reference to calculate the magnitude of the average deflection angle of the $p$ rays.

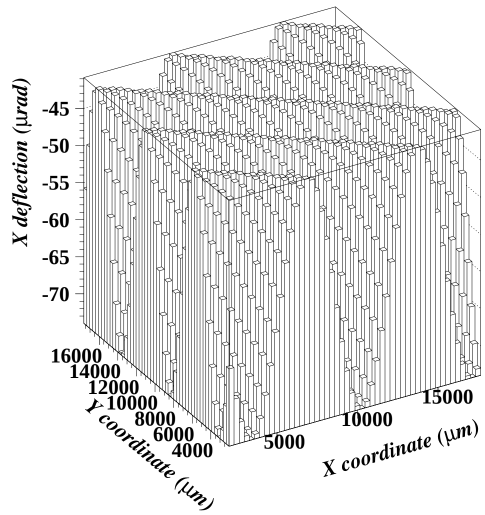


Figure 4.16: *Calculated X deflection angle as a result of a double wedge shaped substrate (see figure 4.13). The interference spoils the initial Gaussian distribution of the exiting beam producing a systematic shift in the position with respect to the undistorted beam.*

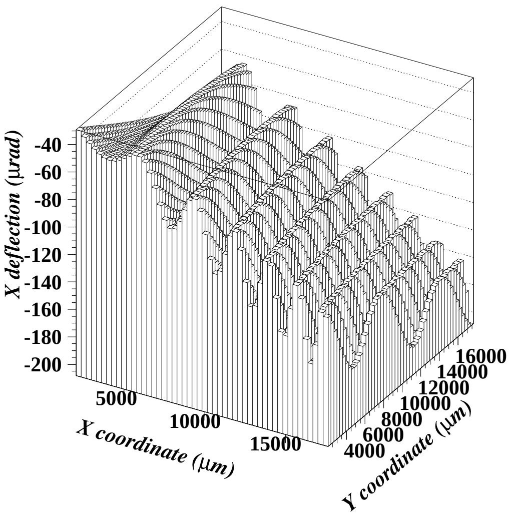


Figure 4.17: *Deflection angle (X projection) for a curved substrate. The absolute value is just illustrative, since the thickness can not be included (see text) in the calculation.*

### 4.5.2 The substrate as a curved surface

Although deflection patterns obtained from a wedge clearly show the effects of the interference, they do not resemble the patterns obtained experimentally. As it may be observed in figure 4.4, real distributions do not fluctuate about a constant value of the deflection angle, but along a tilted plane. While a wedge deviates an incoming beam a certain fixed angle, a curved surface will deviate the beam linearly. This may be easily realized if the curved surface is considered as made by linearly increasing wedges. If the ALMY surface is curved, the beam deviation introduced by it, is equivalent to a lens. As the deviation angle is of order $\mu$rad, it will behave as a very large focal length lens.

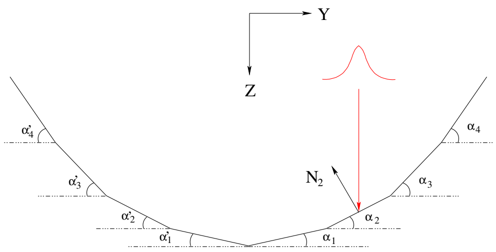


Figure 4.18: *A curved substrate is modeled as a succession of slightly varying wedges.*

In order to incorporate the curvature in the tedious interferential calculation we have done an approximation. Since we exactly know the contribution for a wedge like substrate, the curved substrate is simulated as a succession of linearly increasing wedges (see figure 4.18). Unfortunately, the thickness of the substrate can not be obtained by moving away from the apex (as we did in section 4.5.1). This argument is only valid for one wedge. Considering that we only pretend to make a qualitative study of the deflection process, the results remain still valid.

The simulated deflection angle produced by a substrate as the one shown in figure 4.14 is presented in figure 4.17. This figure clearly shows the two contributions to the deflection angle, as outlined in section 4.3.2. The deflected angles distribute with an oscillating pattern on top of a linear change. From equation 4.23 it is deduced that the phase difference between the traveling waves is only a function of the wedge thickness, the distance traveled (outside of the wedge) and the refraction indexes. In figures 4.19 and 4.20 we calculate the relative dependence of the deflected angle with the distance and the refraction indexes. Figure 4.19 shows that the effect of the interference is less important at larger distances from the sensor. The amplitude of oscillations at three meters is considerably smaller than the amplitude at one meter. This argument may be employed to attempt cross-corrections between different configurations. A cross-correction is a correction of the deflection pattern in one configuration of two sensors by the pattern extracted from a different configuration. If the geometrical contribution to the deflection angle is more important than the interferential part, then corrections may be achieved (see section 4.8.1 for an example). The cross corrections are easily tested within our naive modelization of the sensor. The result agrees with what is expected from figure 4.19. Deflection patterns at distances bigger than 1 meter are corrected by each other. For distances smaller than 1 m, the correction does not work.

It is also possible to study the dependence of the interferential patterns with the refraction index. The more different the refraction indexes of the surrounding medium and the substrate are, the higher amplitude of the interferential waves. This is produced by the increase in the reflectance coefficient, therefore more light is reflected and the interference is better observed.

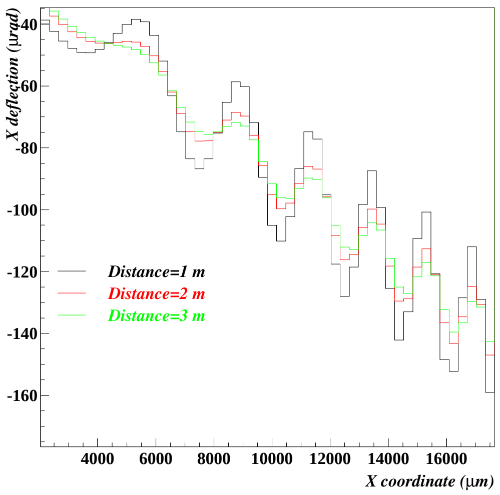


Figure 4.19: *Comparison of the X deflection angle for three different interdistances*

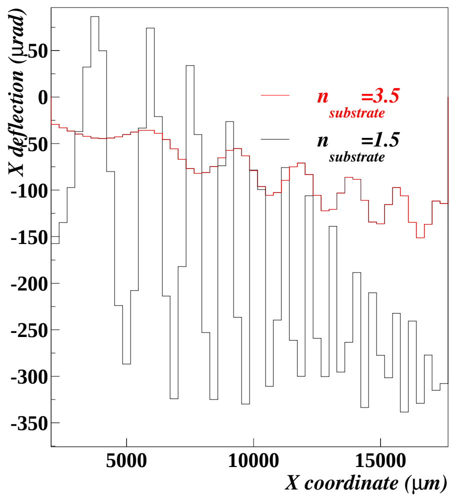


Figure 4.20: *Comparison of the X deflection angle for two different indexes of the material*

## 4.6 Tests of ALMY sensors

In this section, a summary of results on ALMY calibrations is presented. The amount of sensors studied is relatively large. The tests were carried out in different laboratories. In chronological order, a set of 7 commercial sensors [10] (set I) were extensively tested in the CMS Laboratory of High Energy Physics at the University of Cantabria (UC), Santander (Spain). Two groups of 13 and 15 sensors (sets II and III) were studied for a period of 6 months in the ATLAS Laboratory at the Max Planck Institute (MPI) of Munich[3]. Finally a set of 10 extra sensors (set IV) has been studied and characterized at the UC to be used in the first large scale alignment test of CMS [12]. The results from each specific set will be presented separately, since they belong to different ALMY generations.

### 4.6.1 Experimental facilities

#### The UC CMS Laboratory

Sets I and IV, studied at the UC, have been tested making use of a two branch granite bench, being 6 and 3.4 m large respectively. Each branch is independent of the other. The branches are perpendicular, simulating the CMS Link geometry at $|\eta| = 3$. The bench is isolated from the building floor by means of its own grounding. The sagita of the bench was measured in all its extension to be better than 5 $\mu$m [13]. The laboratory is also equipped with an optical

[3]More than one hundred sensors were previously characterized at MPI. We will only refer here to those studied by CMS and ATLAS together

table, allowing more complicated and flexible configurations employed for some calibrations of components. During calibrations, the laboratory is darkened and all the computers are operated from a contiguous room. Thus, the disturbance produced by human activity or parasite light is reduced to the minimal. The temperature stability has been measured to be 0.1°C during few hours [14]. A picture of part of the laboratory during an ALMY calibration is shown in figure 4.21.

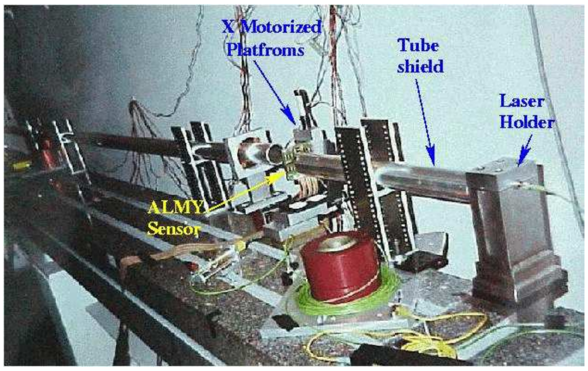


Figure 4.21: *Picture of the CMS laboratory during the calibration of an ALMY sensor.*


Figure 4.22: *Image of the MPI test setup.*

The data taking process is PC based. For the sensor calibrations, three motorized platforms [6] (range 20 mm) were utilized. Two of them were used to remove the sensor from the light path in horizontal direction. The third one moves the sensor along the vertical line. Characteristics of the motorized platforms are summarized in the first row of table 2.

| | Travel Range mm | Accuracy ($\mu$m) | Repeatibility ($\mu$m) | Hysteresis ($\mu$m) | Speed mm/s |
|---|---|---|---|---|---|
| Newport Model | 25 | $\sim$2 | 0.2 | 5 | 0.7 |
| Spindler & Hoyer | 100 | $\sim$1 | 1 | 3 | NA |

Table 2: Specifications of the different stepping motors employed. The repeatibility is taken as unidirectional, while the hysteresis is measured in a roundtrip travel. (NA means not available)

Sensors utilized by CMS used the electronic boxes provided by the manufacturers. Up to four sensors may be addressed by each box. The sensors and the electronics are joined by a common bus in such a way that the signal from the last sensor has to travel through the rest in order to reach the electronics. The sensor is mounted in a frame with multiplexers and resistors embedded. The link to the common bus and the bus itself uses a 34 channels flat PCB cable. The identity of the sensors is easily configured via jumpers. Inside the electronics box there are 3 boards. In the signal processing board the amplified photocurrent signals of the sensor are converted to voltage signals. In the interface board, the voltage supplies for the microcontroller and for the sensor carrier are generated. Finally, in the microcontroller board, the signals are digitized with 10 bits (resolution is 5 nA/bit).
As explained above, commercial sensors were employed for tests of set I. The baseline for commercial versions is supposed to be a Schottky structure: Protection/ITO/a-Si:H/ITO/glass ($< 0.1/0.1/1/0.1/500$) $\mu$m thick. There is a strong evidence [15] of the existence of a very thin layer of protection material on top of the sensor multilayer. The 10 sensors from set IV were delivered on bare substrates. They were purchased to colleagues from HERAB. Although they were provided without any specifications, it seems likely to be 100/1000/100 after their performance was simulated by the technique described in chapter 5. These sensors belonged to a much newer ALMY generation and were coated with an antireflection coating. The *Electronic and Automatic Division* from CIEMAT [16] made a new design of the electronic frames (following the model from EG&G) in order to reuse the electronic boxes previously purchased. The bonding was done at SIMESA [17]. Some spare sensors were employed for new "3D" versions of the sensor layout which will be presented later on.
The communication between the electronic box and the PC was via serial line. We used ADAM modules as interface between the computer and the hardware [18], which are characterized by their ability to handle different combinations of input types and ranges: temperature probes, currents (mA) and voltages (V, mV) into one module. The data taking software was entirely written using LabView [19].
The laser sources employed are summarized in table 3.

| | |
|---|---|
| Source 1 (HeNe 1) | 3mW $\lambda$ =632.8 nm |
| Source 2 (D.L. InGaAIP) | 10 mW $\lambda$ =686 nm with monomode fiber |
| Source 3 (HeNe 2) | 5mW $\lambda$ =632.8 nm |

Table 3: *Laser Sources*

### The ATLAS Laboratory

It has already been mentioned that the development of the sensors originated in the Max Planck Institute of Munich [1]. Although the commercial sensors were produced based in these prototypes, the MPI ALMYs evolved independently from their commercial counterparts. The electronic sticked to the sensors was designed to be modular. The bare substrates were bounded to a ceramic board where the internal pitch of the sensors is fanned out and lead together. The transition to the nearby electronic frame, localized in an independent board, was made by means of two gold strips which join the substrate with the upper board. The electronic frame implements multiplexers, ADC converters and interface to VME bus. Besides, the readout electronics

of the ALMY detector relies on two Application Specific Integrated Circuits (ASIC). The VME card is read out using a server program running on a LYNX OS machine sitting in the VME crate. Then, the data are transferred to a local machine over the network [20]. A maximum number of 128 sensors could be handled by the VME crate (by means of 8 boards allowing 16 addresses each). The speed supplied by the VME crate is, by far, much higher than needed. It was intended to be used in the laboratory. This is the reason why new, more affordable, versions of the readout electronics were built. One was based in the serial line (see [21], for instance) and following the advice of the LHC Detector Control Systems (DCS) the final models will implement the CANbus [22].
The motorized platform employed was a 10 cm range XY table [7]. Its performance is also summarized in table 2.
Regarding the MPI setup bench, a single massive granite bench was used. The bench rests in the cellar of the building. The temperature of the laboratory was very stable. Although the room could be darkened, the measurements were done with daylight conditions. To protect the sensors from stray light and external disturbances, aluminum tubes shielding the light path were employed (see figure 4.22). This solution was adopted after intensive tests on beam propagation [23]. Beam stabilities of order 1 $\mu$m are easily obtained in this configuration.

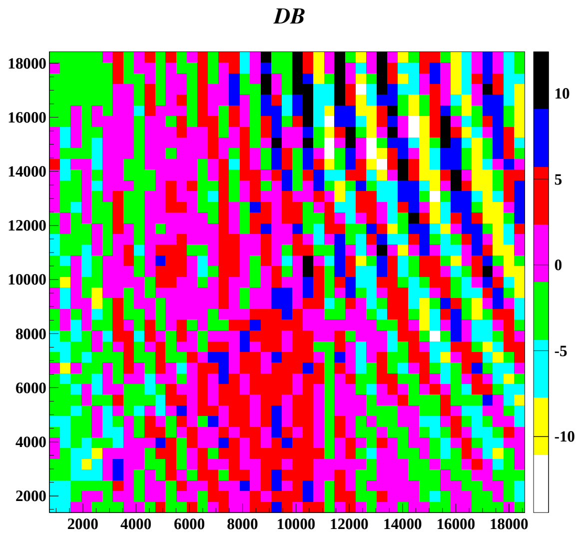


Figure 4.23: *2D distribution of the linearity residuals for sensor named D belonging to the first set of tested ALMYs.*

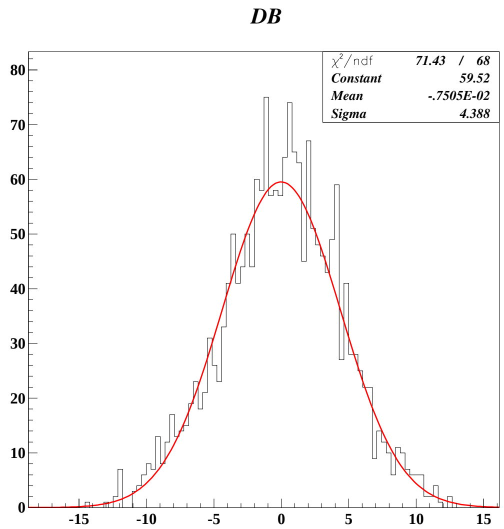


Figure 4.24: *Residuals distribution for the sensor D. The spatial resolution calculated as the Gaussian width is 4.4 $\mu$m.*

## 4.7 Linearity tests

The different approaches for the linearity analysis have been presented in sections 4.3.4 through 4.3.6. As said before, we use the method of the residuals to extract the inhomogeneity pattern from the

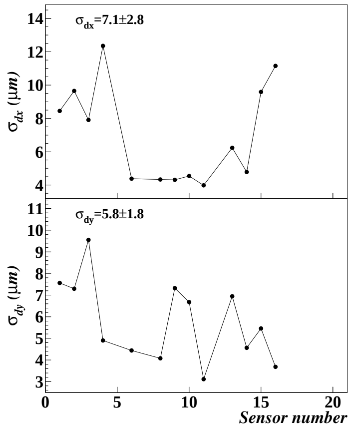


Figure 4.25: *Spatial resolution (in $\mu$m) for X and Y coordinates. Sensors shown belong to set II.*

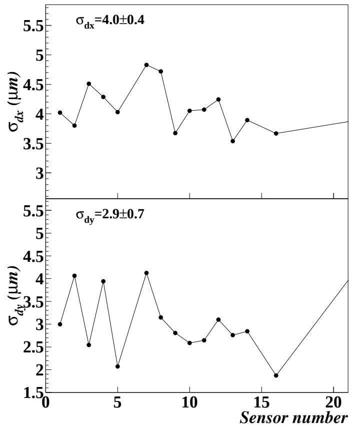


Figure 4.26: *X and Y spatial resolution (in $\mu$m) for the coated ALMY sensors (set III).*

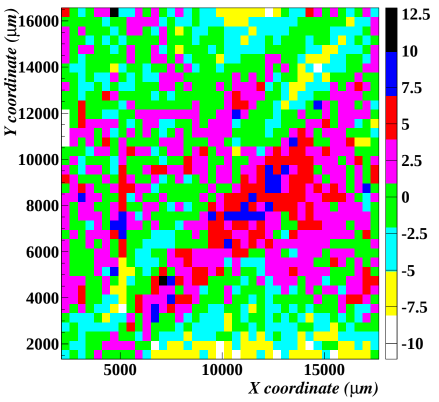


Figure 4.27: *Spatial resolution for a coated ALMY sensor (set III). This figure should be compared with figure 4.23.*

measurements. The calibration procedure was explained in section 4.3.2. Here we will present the result of the individual calibrations with remarks on some systematics effects, when needed. In what follows we will define the spatial resolution of the sensor as the standard deviation of the residuals distribution and the reconstruction error as the mean value of the distribution. The resolution corresponds, in average, to the minimum displacement the sensor can resolve.

| | Set I | Set II | Set III | Set IV |
|---|---|---|---|---|
| $\sigma_x$ ($\mu$m) | 4.1 | 7.1 ± 3.0 | 4.0 ± 0.4 | 4.4 ± 1.0 |
| $\sigma_y$ ($\mu$m) | 4.6 | 5.8 ± 1.8 | 2.9 ± 0.7 | 13.7 ± 7. |

Table 4: Spatial resolution of repeated measurements of ALMY sensors belonging to different sets. Standard deviation within each sample is also shown.

### 4.7.1 Linearity set I

Typical spatial distributions found with these ALMYs of the first generation are shown in figure 4.23. Clear interferential patterns are observed. Even though the systematic effect is evident, the spatial resolution is better than 5 $\mu$m for both coordinates and all sensors. Average spatial resolution in X and Y coordinates are given in table 4, summarizing the seven sensors studied.

The distributions of the residuals are Gaussians. The residuals distribution for the linearity pattern showed in figure 4.23 is shown in figure 4.24.

### 4.7.2 Linearity sets II and III

Sensors from set II are similar to those of the set I. However, this set of sensors uses a different electronics allowing interface to VME and operation of the sensors at reduced laser power. Again interferential patterns appear in the reconstruction of the position of the spot. The spatial resolution of 13 of such sensors tested is summarized in figure 4.25. In these two plots, the RMS of the residuals distributions (spatial resolution) for X and Y coordinates are shown. The reconstruction error (not shown) is equivalent to zero.

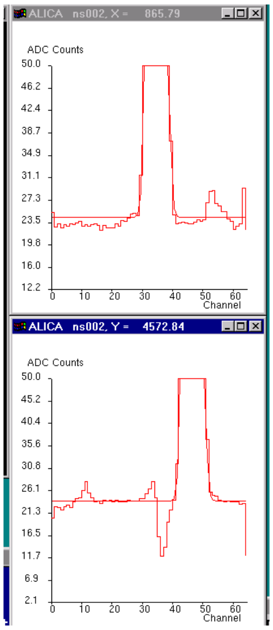


Figure 4.28: *X and Y window-shots taken during an ALMY measurement. Upper plot shows the tails of the Gaussian beam (note maximum ADC value is limited to 50 ADC counts) as seen by the X electrodes. Lower plot has a rebound signal to the left of the Y beam projection.*

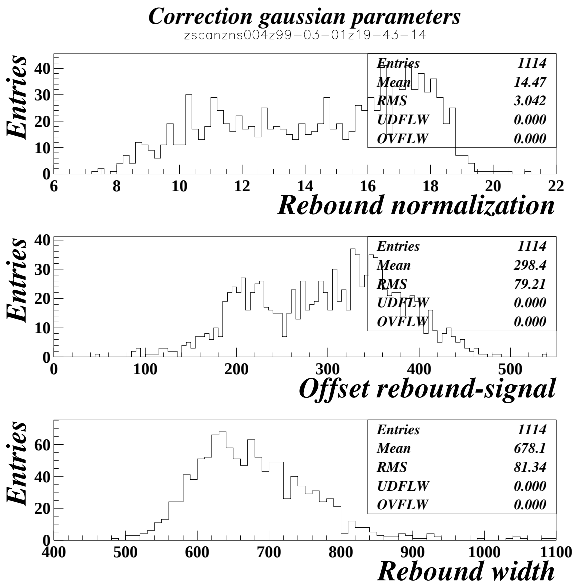


Figure 4.29: *Calculation of average rebound parameters. Upper plot histograms the average rebound depth. Middle plot shows the offset (in $\mu$m) between Y rebound and $X_{beam}$. Bottom plot shows the average rebound width.*

Sensors from set III were, at that time, the best ALMY sensors ever produced. They had antireflection coatings and no systematic patterns neither in the position reconstruction nor in deflection characteristics. Their performing X and Y spatial resolution plots are shown in figure 4.26. A scan of the sensor surface, as the one shown in figure 4.27 shows the lack of oscillating patterns. Average values of the spatial resolution for both sets are shown in table 4. The absence of oscillations uncovered an extra systematic contribution to the spatial inhomo-

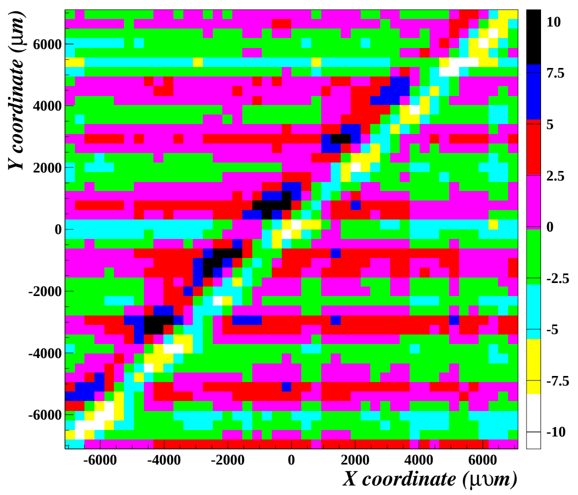


Figure 4.30: *Scan inhomogeneity pattern showing a clear systematic pattern along X≈Y.*

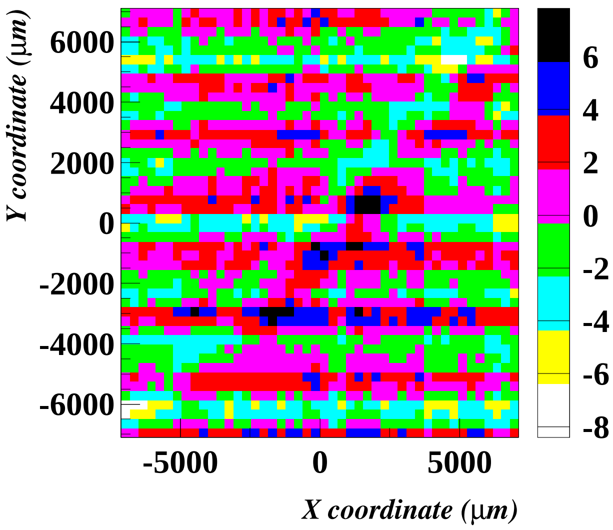


Figure 4.31: *Correction of the systematic shown in figure 4.30 by the rebound method (see text).*

geneity. Figure 4.27 (and perhaps 4.23) show a blurred contribution along the region $X = Y$ of the plot. The origin of this effect could be identified during the data taking process. Figure 4.28 shows a zoom of the X and Y projections of the laser beam as obtained during a measurement. It can be clearly observed that the X signal (upper distribution) induces a mirrored signal in the Y distribution (rebound between channels 30−40). The subtraction of signal produced by this rebound is only important when $X_{beam} \approx Y_{beam}$. Outside of this region, the rebound is too far from the maximum of the distribution, and it is not included in the Gaussian fit. We found that there was a direct correlation between the position of the X position of the Gaussian beam and the position of the "mirror" or "rebound" signal. However the depth of the rebound did not correlate with the intensity of the X signal. We developed an offline correction of this effect, by defining an "average rebound" within each scan. Once the scan of the sensor is completed we can calculate the average depth of the rebound (upper plot in figure 4.29), distance between ordinate of the rebound and ordinate of the Gaussian beam (figure 4.29 middle) and finally the rebound average width (figure 4.29 bottom). The average rebound is then added to all beam positions where the rebound spoiled the Y intensity distribution. Finally, the new inhomogeneity pattern is calculated. We show in figure 4.30 the Y inhomogeneity as obtained from a scan where this effect is clearly remarkable. The correction by the average rebound method introduced above is shown in figure 4.31. The spatial resolution for the raw scan was 2.8 $\mu$m, and 2.3 $\mu$m for the corrected one. The importance of the correction does not come from the average residuals reduction. The correction is important locally, in the zone where the systematic appears, since the error is reduced by several microns.

After the electronics of the sensor were revised, it was found that the origin of the rebound was an electronics *cross-talk* from the X layers of the electronic board to the Y layers. After this problem was fixed, the electronics cross-talk disappeared.

### 4.7.3 Linearity set IV

A total number of 20 bare sensors with backside coating composes set IV. Ten of these sensors were employed in the ISR tests. The remaining sensors have been utilized for different tasks. Among others, four sensors were used for the 3D ALMY configuration which will be presented in section 4.9.
The optical characteristics of these sensors are similar to those of set III. The sensors were operated with electronics frames designed at CIEMAT, imitating the commercial ones. This allowed to reuse the electronic boxes previously acquired from EG&G. The sensors were reverse biased at 3V and read using the serial line.

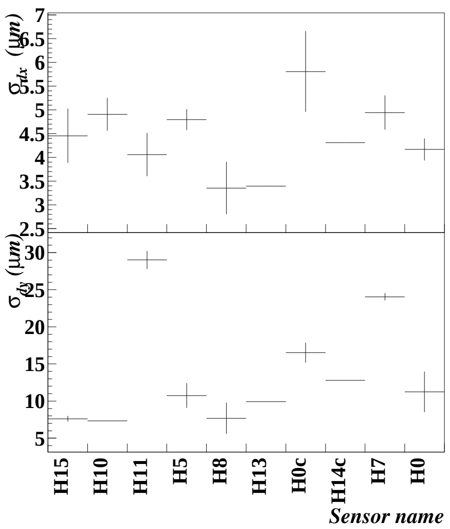


Figure 4.32: *X and Y spatial resolution (in μm) for sensors of set IV. Sensors are Schottky-type and backside coated (see text).*

Characterization of these devices was carried out in the CMS UC Laboratory and then were moved to the ISR installation (see chapter 8). Again, no systematic effects and no cross-talk were observed in X or Y coordinates. The performance summary is shown in figure 4.32 and table 4 for the X and Y coordinates. Measurements were repeated few times. Vertical error bars represent the RMS of the measurements. Horizontal bars are meaningless. The high values observed in the Y coordinate of set IV were identified to come from an unavoidable beam drift in this direction.

## 4.8 Beam transmission tests

In this section we will refer to all the tests dealing with transmitted light, namely: beam deviation and transmittance. We preserve the same notation as used in section 4.7.

The procedure employed to measure the beam deflection was already introduced in section 4.4 and figure 4.11. Besides, an explanation for the several effects involved in the deflection measurement was also given there.
The transmittance is calculated as the ratio of the signal collected in the second sensor when the first (target) sensor is in front of the beam to the signal collected when it is not.

### 4.8.1 Deflection Set I

Spatial distributions of the deflection angles show interferential patterns. The mean values measured are spread but always below 175 $\mu$rad. It was shown in section 4.5.2 that the mean values depend on the incident angle, the substrate thickness and the curvature. The dispersion of the deflection angles around the mean could be as high as 20 $\mu$rad. These values are too far from the required 5 $\mu$rad maximum deviation intended for the CMS and ATLAS operation.

| | $D = 3$ m | $D = 2$ m | $D = 1$ m | $D = 3$ m, $\Delta t = 1$ month |
|---|---|---|---|---|
| $D = 3$ m | 51.25<br>9.36<br><br>-0.03<br>1.09 | 48.72<br>10.05<br><br>-1.12<br>3.15 | 49.86<br>17.10<br><br>0.27<br>13.22 | 49.29<br>9.16<br><br>-1.99<br>2.70 |
| $D = 2$ m | 50.67<br>9.12<br><br>2.00<br>4.54 | 48.72<br>10.05<br><br>0.01<br>1.09 | 49.86<br>17.10<br><br>0.89<br>9.79 | 49.29<br>9.16<br><br>-1.00<br>4.38 |
| $D = 1$ m | 50.67<br>9.12<br><br>0.27<br>11.83 | 48.72<br>10.05<br><br>-1.63<br>9.26 | 49.86<br>17.10<br><br>0.09<br>2.70 | 49.29<br>9.16<br><br>-2.27<br>13.61 |
| $D = 3$ m $\Delta t = 1$ month | 51.45<br>9.05<br><br>1.87<br>2.76 | 49.11<br>9.92<br><br>0.77<br>4.69 | 50.29<br>17.26<br><br>2.84<br>14.26 | 49.89<br>9.46<br><br>-0.06<br>1.33 |

Table 5: *Scalability test (see subsection 4.8.1). All numbers in $\mu$rad.*

An offline correction of the deflection angle is then needed if the sensors have to be operated under these conditions. The method employed for the correction was already outlined in section 4.5.2. A 2D scan of the beam deviation is taken as a calibration of the deflection angle of the sensor. Then, this matrix with deflection values and coordinates is subtracted to actual measurements, interpolating between positions case it were needed. The performance of this technique was already studied in [11, 24]. We measured a sensor in three different spatial configurations, with interdistances of 1, 2 and 3 m. Some measurements were taken with a month time difference between them. The test was performed using a HeNe laser source. Every single configuration is alternatively considered to be the calibration of the deflection angle. The remaining measurements are then corrected by it. If the calibration is able to correct the current measurement, then both the mean deflection angle and the spread of the deflection values decrease. The results, after sequential application of the former method, are summarized in table 5. The table is read as follows: the first left column is the calibration measurement. The upper row shows the measurements to be corrected. Within each cell there are four rows of numbers: the first one is the uncorrected deflection, the second one is the spread with respect to the uncorrected value. Third row is the corrected deflection and finally the forth row is the new dispersion with respect to the mean value. The mean diagonal represents a self correction using a grid where each individual cell is twice a normal cell (mainly for completion purposes). All the numbers refer to the global deflection:

$$\tan\theta_{global} = \theta \quad = \quad \frac{\sqrt{(X - X_R)^2 + (Y - Y_R)^2}}{D} \tag{4.24}$$

where subscripts refer to measurements on the reference sensor and $D$ is the interdistance. As observed in the table, the cross-correction performs well at interdistances bigger than 1 m. This agrees with the conclusion extracted from section 4.5.2 and figure 4.19 where we showed that interferences depend on the traveled path outside the sensor. As we calculated there, the interference at distances bigger than 1 m had similar magnitude among them, and therefore corrections perform well in these cases.
At the HeNe wavelength the mean transmittance was $\overline{\tau} \pm \sigma_\tau = (21.9 \pm 1.1)\%$. At 686 nm the transmittance raised up to $(57.2 \pm 1.6)\%$. Although interferential patterns were also observed in the transmittance, there is not a strong correlation with the deflection patterns (varying between 0 and 0.5).

### 4.8.2 Deflection sets II and III

Deflection patterns in sets II and III are very similar. Since the deflection may be parametrized as a tilted surface (see section 4.5.2), we performed fits of the deflection distributions to quadratic functions:

$$\theta = a\,x^2 + b\,y^2 + c\,xy + d\,x + e\,y + f \tag{4.25}$$

and subtract them to the deflection angles. After the fit, just the interferential component of the deflection remains. Provided the amplitude of the oscillations is small, the 5 $\mu$rad threshold will be conserved.
Although a plane fit would be sufficient, the quadratic fit achieves better precision. Thus, instead of a matrix of about 1600 points required in the procedure of section 4.8.1, only $6+6$ parameters are needed for both coordinates. The spreads around the mean for sensors in set II are shown in figure 4.33.
The sensors belonging to set III had an antireflection coating in the backside of the substrate which eliminates the interferential problem. Only the geometrical effect of the curved substrate remains. The parameterization of the deflection as a continuous smooth function performs even

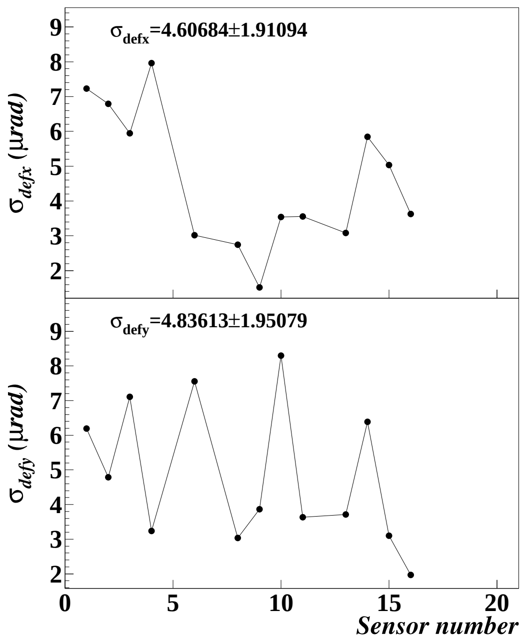


Figure 4.33: *Deflection spread for sensors belonging to set II.*

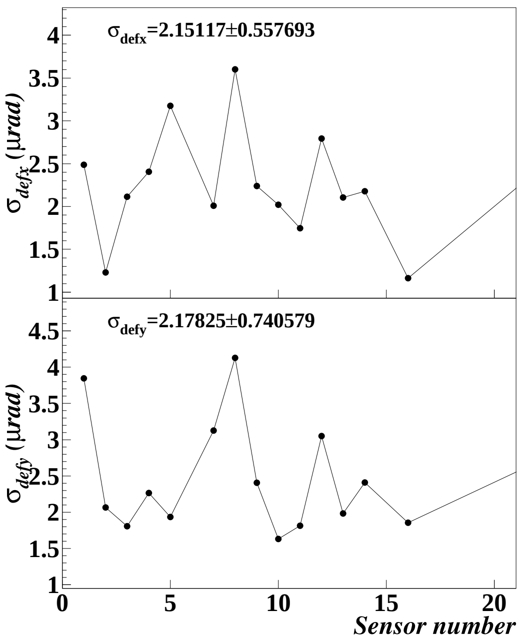


Figure 4.34: *Deflection spread for sensors belonging to set III.*

better than for sensors of sets I and II. Figure 4.34 summarizes the deflection performance after a fit to a quadratic surface. Figure 4.35 shows a typical deflection distribution of a coated sensor. The absence of systematic patterns is clear (to be compared to figure 4.12)

### 4.8.3 Deflection Set IV

Although sensors from sets III and IV are equipped with different kinds of electronics, their optical properties are very similar. Their performance is summarized in figure 4.36 (after fit to a surface).

## 4.9 3D ALMY sensors

Space inside any experiment in High Energy Physics is absolutely constrained. In CMS, narrow light passages have to be reserved in order to allow light to travel inside inner detectors while producing the minimum disturbance. The high radiation dose that some electronic components will undergo led to remove critical electronics part out of the influence region. Foreseeing the absence of radiation hard multiplexers, and constrained by the lack of free space in the Tracker region, a condensed and modular version of the sensor was developed. The prototypes presented in this section were not the first sensors of this kind (see [25]). Colleagues from MPI Munich

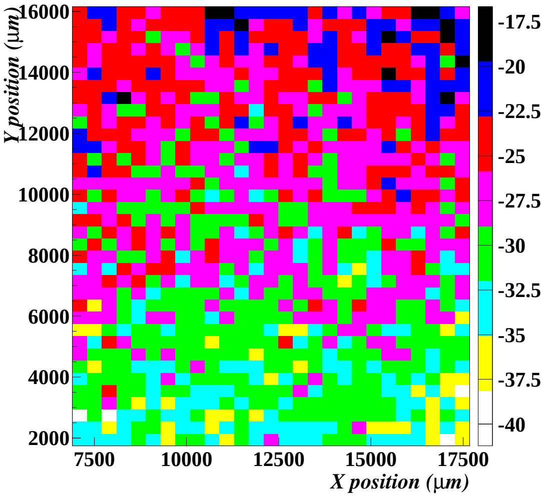


Figure 4.35: *Plot of the deflection angle as measured by a second ALMY sensor 3 m behind. The raw deflection has been corrected. The width of the corrected distribution is less than 4 μrad.*

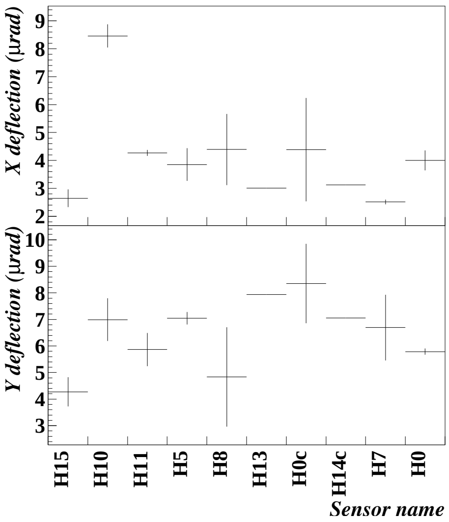


Figure 4.36: *Deflection spread for sensors belonging to set IV.*

developed the model shown in figure 4.37. However, both developments have been parallel and have proved their normal operation. The CMS prototype used bare sensors from set IV. The electronics was entirely developed at CIEMAT and the bonding was done by at SIMESA[17]. A picture of the prototype is shown in figure 4.38. The name 3D refers to the fact that the electronics is not sticked in the same plane as the sensor sheet, but it is located perpendicular to it. The performance of these sensors is similar to those of set III and IV. In the future, this development will be employed in selected parts of CMS.

## 4.10 Evaluation of the SWE in ALMY sensors

The photoconductivity degradation upon prolongated illumination of a−Si:H devices has also been observed in ALMY sensors. It is measured as a local decrease in the sensitivity of the sensor. As it happened in the study of linearity and deflection, any asymmetry in the photoresponse of the sensor reverts in a systematic effect on the position reconstruction. The implications of the SWE (see section 3.4) are even deeper if the photoresponse degradation develops with time.
Figures 4.39 and 4.40 show a map of the photoresponse (charge collected, expressed as ADC counts) and transmission of an ALMY sensor of set II, respectively. A clear reduction of the photoresponse with a round shape indicates the place where the laser was hitting. Observing the transmittance map we realize there is no degradation of the transmittance associated to

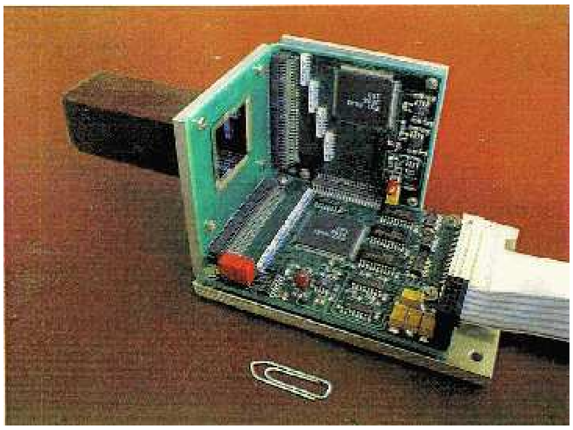

Figure 4.37: *Compact ALMY sensor developed at MPI (after [25])*

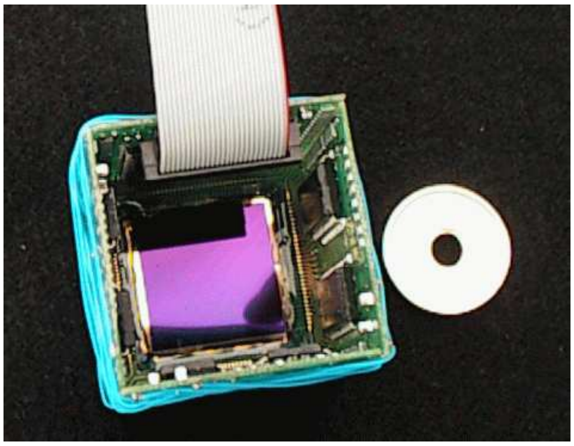

Figure 4.38: *3D CIEMAT sensor. The flat cable is connected to commercial electronics. The diameter of the coin is 2 cm.*

this region. It demonstrates that the ageing affects to carriers produced by the interaction of a photon in the silicon layer, but not to the fraction of photons that traverse the sensor without interaction (since they do not produce carriers susceptible of being trapped). Among those producing a pair electron-hole in the semiconductor, a fraction is trapped by defects. This fraction contributes to the ageing phenomena observed.
As the sources employed are not extended, ageing in ALMY sensors is a local effect. The size of the aged region is comparable to the size of the light spot. The distortion of the photocurrent collected in the *aged* region of the sensor induces a noticeable error in the calculation of the position of the spot, with respect to the non aged sensor. When the beam falls on an aged region, several strips collect less photocurrent than they should, an the overall effect is a shift of the beam centroid. We reproduce in figure 4.41 the result of the study performed in [26]. The figure shows the reconstruction error along the X coordinate, parametrized as a function of the photoresponse degradation, for an aged region centered around zero. In order to obtain a contribution to the error lower than 5 $\mu$m a maximum 2% photoresponse degradation has to be reached.
The ageing of ALMY sensors, and specially the ageing rate, has been subject of controversy in the past. Some tests were performed with different versions of ALMY sensors and with different results.

1) We presented an ageing test of a set I sensor, lasting 84 hours in [27]. Using a laser irradiance of 0.05 mW (HeNe source, $\lambda \sim 632$ nm) and $\sim 1$ mm diameter no degradation was observed.

2) Kroha *et al.* [28] cite several ageing experiments. Tests performed at MPI, using a $\lambda = 780$ nm laser of 2.5 mW and 1 mm diameter (or $\approx$318 mW/cm$^2$), show a degradation of 10% after 20 hours burn-in.

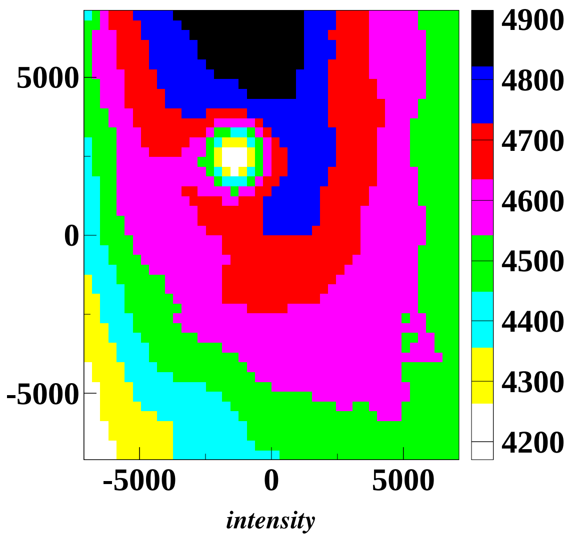


Figure 4.39: *Photoresponse (integrated signal on the sensor). The area aged by the laser illumination is clearly shown as a depression on the ADC level.*

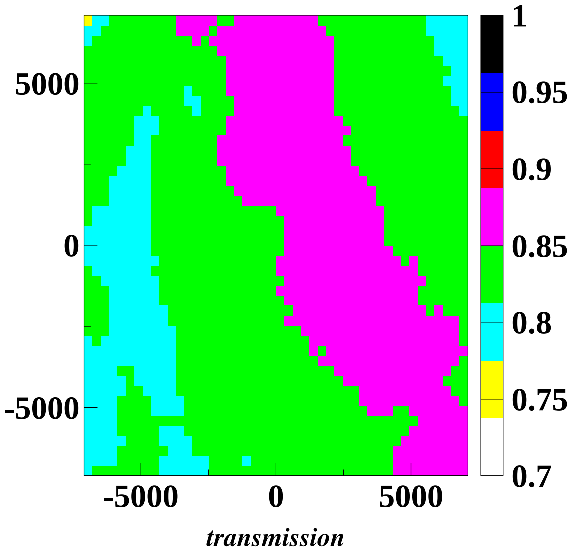


Figure 4.40: *Plot of the transmission as a function of the laser spot position in a scan of the sensor. Photons absorbed in the a-Si layer may or not lead to charge collected by the electrodes. Non absorbed photons traverse the sensor, and thus are not affected by the ageing effect.*

3) In reference [29] large photocurrent variations are reported. Using a laser of 670 nm and power of 57 mW/cm$^2$ during 35 days, they observed 25% degradation in the photocurrent. After 48 hours of white light soaking over fresh sensors, using a source 300 mW/cm$^2$, a degradation of 25% was found.

As explained in section 3.4, the photocurrent degradation depends on the laser power and illumination time (through equation 3.4). Therefore the reduction of the laser power will lead to a reduction of the photodegradation rate. Regarding the scheduled operation of ALMY sensors, the maximum time they will be illuminated during ten years of CMS or ATLAS operation is about 500 hours. With these arguments in mind we performed, in 1999, a systematic ageing study of ALMY sensors. The tests extended 500 hours. Four sensors belonging to set III (see section 4.7) were tested at MPI. A picture of the setup is shown in figure 4.42. The sensors had an optical coating on the backside of the substrate. Besides, the amplifier and electronics nearby allowed a great reduction of the laser power without spoiling the signal to noise ratio. This allowed reduction of the working laser power(irradiance) down to 0.9 mW(115 mW/cm$^2$). The laser source was a 780 nm laser diode coupled to a fiber splitter. The sensors were scanned repeatedly: a first scan before the test started, and then, a new one every 24 hours. The sensors were rigidly attached to the optical bench, thus ensuring the same area of the sensor was illuminated each time. The sensors were powered during the whole test.

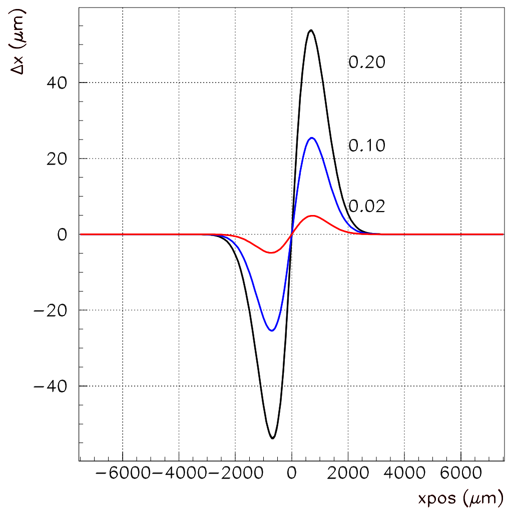


Figure 4.41: *Reconstruction error along the displacement direction for a sensor in three different steps of ageing [26].*

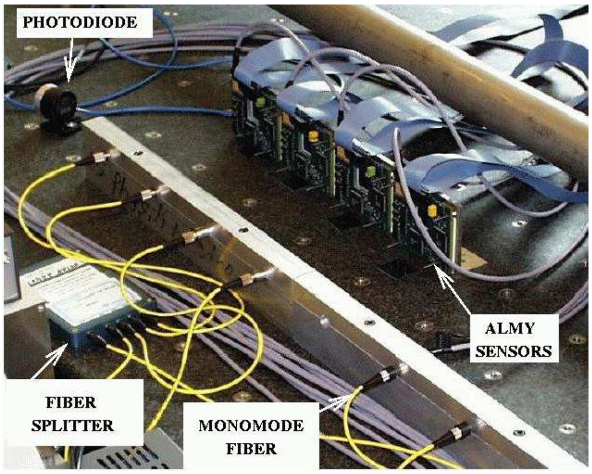


Figure 4.42: *Sensors are attached to a rigid bench and continuously aged. The power is monitored by the photodiode.*

Figure 4.43 shows a plot of the ageing development for a total time of about 500 hours. In vertical axis we show, for the four sensors tested, the intensity collected by the strip which has the spot centered on it. The photocurrent degradation amounts 2−3% for all sensors (5 $\mu$m reconstruction error). Overimposed to the plot is the fit to equation (3.4) plus equation (3.3). To ease comparison between sensors we may use a simple linear fit to the distributions showed. The values of the slopes of the four sensors are:

$$\sigma_{ph}(ADU/h) = \quad (-4.7 \pm 0.5, -4.3 \pm 0.5, -2.6 \pm 0.2, -4.0 \pm 0.4) \times 10^{-5}$$

Although the laser was hitting the surface of the sensor, the whole setup was in a dark environment. This was done so to avoid the action of external sources of light. However, these will not be real operating conditions in almost any experiment. Consequently we studied the ageing rate when the sensors were exposed to the combined action of the laser and the daylight. The result is shown in figure 4.44. It is clearly seen that the effect has speeded. The ageing rate is almost 5 times faster than before. Attending to the theoretical model exposed in section 3.4.3, the SWE is not wavelength dependent. Therefore we interpret the speed-up as a combined effect of all wavelengths hitting the surface of the sensor.

No attempt to anneal the ageing defects created has been carried out during this work.

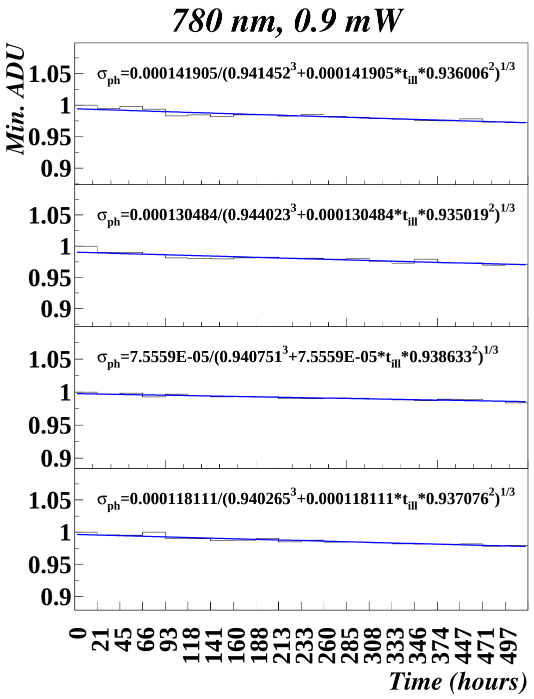


Figure 4.43: *Reduction of the photocurrent monitored in the strip where the spot is centered. Overimposed (see text) is the fit to the theoretical function.*

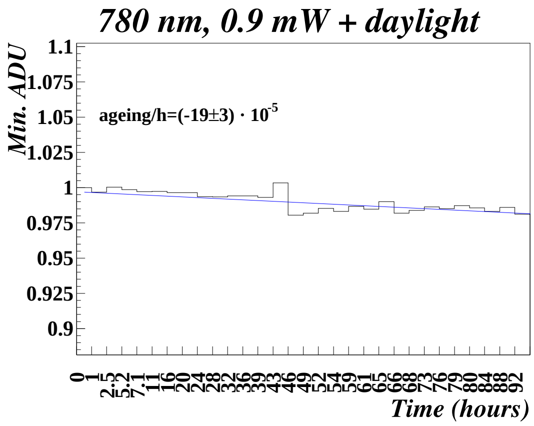


Figure 4.44: *Combined action of laser ageing and daylight contributes to the increase of the ageing rate.*

## 4.11 Alternative PSD sensors

ALMY sensors are not the only position sensing detectors able to locate the position of an incident light beam. Not even the first ones using amorphous silicon as the resistive layer. This section summarizes some of the available alternatives to ALMY sensors that are or have been commercially available. For another interesting projects under investigation see for instance [30].
The majority of the photodetectors use Silicon (either crystalline or amorphous) as sensitive/active material. Crystalline silicon has a typical response from 350 to 1100 nm, peaking between 700 and 900 nm (although some ultraviolet enhanced models may exhibit response down to 200 nm and lower [31]. This response characteristic make silicon photodetectors optimum for use with a variety of common light sources including He-Ne lasers, laser diodes, light emitting diodes (LED), infrared emitting diodes (IRED), and incandescent or fluorescent lamps. Hydrogenated amorphous silicon films are accepted as one of the common materials for low cost, large area devices such as high-efficiency solar cells [32].
The use of silicon photodetectors for making quantitative light measurements has been long established. However, silicon photodetectors have shown performance measurement capabilities in applications such as measurement of movement, angles, straightness, height, centering ...

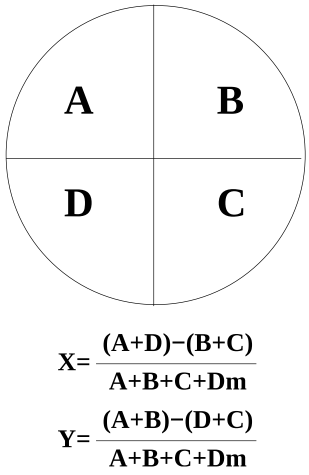


Figure 4.45: *Quadrant detector and formulas. Ideal for centering or nulling applications. Exceptional signal to noise ratio.*

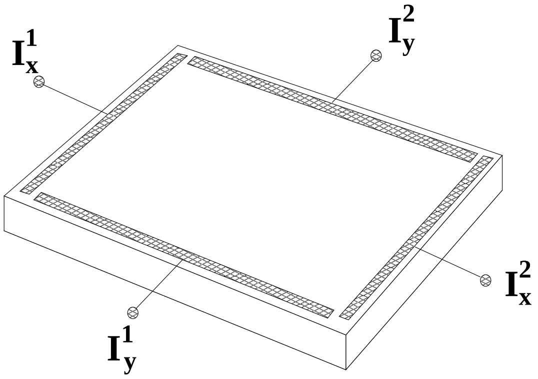


Figure 4.46: *Tetra-lateral PSD extracts current collected by one resistive layer dividing it into 4 parts. Low current and fast response time as main features.*

An ALMY sensor belongs to the family of the Digital Position Sensing Detectors −DPSDs−, for short. PSDs are single substrate photodiodes capable of locating a beam within a defined sensing area. Many techniques for fabricating them are employed, however, for high resolution positioning devices, planar diffused (pin) and Schottky barrier constructions prove most effective.

Photodetectors made in crystalline silicon often exhibit an exceptional sensitivity to changes in incident light. It is common to find photodetectors with a noise equivalent power of less than 0.1 nanowatt, and a maximum power density of few tens of mW. These unparalleled features allow unsegmented photodetectors to be used even for pattern and edge recognition [33].

Bi-cell and quadrant photodetectors have two or four separate photodiode elements separated by a small gap (with widths of few micrometers). A sketch of a quadrant detector and the formulas to derive beam position on it are given in figure 4.45. The ratio between the photocurrent outputs from the elements determines the relative position of the spot on the surface. Their main limitation is their short measuring range (the detector provides position information over a distance twice the spot diameter). Besides that, the transfer function for a circular spot is not linear. It has been proposed the use of an homogeneous square shape LED light to extend the linearity range of the sensor [34]. These disadvantages have lead to use these quadrant and bi-cell detectors as centering devices (favored by the excellent signal to noise ratio) where resolutions of 0.1 $\mu$m are easily obtained.

When position sensing applications require measurement over a wide spatial range, continuous detectors are a common choice. There is no gap between cells. Continuous sensing detectors derive position by dividing photo-generated electrons within their substrate and not by taking an intensity profile of the beam, as segmented detectors do. The former is achieved by applying multiple ohmic contacts on the device. Their working principle was devised by Schottky in 1930 [35] who observed that a nonuniform illumination of a photodiode not only causes a

photovoltage between the two sides of the junction, but also because *the lateral photoeffect* leads to a photovoltage parallel to the junction.
Continuous PSD extend the dynamic range of segmented photodetectors. The sensors are independent of the spot shape and the overall spot intensity distribution. Two contacts are made at opposite ends of the sensor for single axis versions, while dual axis units utilize four contacts coinciding with the extremes of the cartesian axes (tetra-lateral type). An example is shown in figure 4.46. Several authors have reported formulas to calculate the spot position in these kind of devices [36]. Although the intrinsic resolution of continuous sensors is of order of 1 $\mu$m, their linearity (accuracy of the measured position compared to the real position of the spot) is not extremely good. In fact, lateral effect diodes are not perfectly linear. Most devices exhibit typical $\pm 0.5\%$ linearity over the central 25% of their area, $\pm 3.0\%$ out to 75%, and $\pm 5.0\%$ out to the periphery. The major contributor to this nonuniformity is the sheet resistance of the device. At the center of the detector, where the light spot is equidistant from all contacts, these nonuniformities will tend to average to a greater extent than at outlying areas on the detector. The position detector error is a fraction of the lateral size, so bigger sensor have worse linearity. To aid the comparison with ALMY sensors in absolute numbers, model S1881 from Hamamatsu has a typical position detector error of $\pm 400$ $\mu$m (maximum is 600 $\mu$m) over an active area of $22 \times 22$ mm$^2$ [37].
Finally, duo-lateral sensors working in transparent mode might be found in the bibliography [38]. They take advantage of the semitransparent nature of the thin amorphous silicon films on a glass substrate. Performance is equivalent to their opaque partners.

# Bibliography


[1] W. Blum , H. Kroha and P. Widmann, *A novel laser alignment system for tracking detectors using transparent silicon strip sensors.* Nucl. Instrum. and Methods A367 (1995) 413417.

[2] W. Blum , C. Eimer, H. Kroha, P. Widmann, *An optical alignment System for the ATLAS Muon Spectrometer* ATLAS Internal Note, MUON-NO 028, 20 October 1993.

[3] CSEM SA, Centre Suisse d'Electronique et de Microtechnique, Rue Jaquet-Droz 1 P.O. Box CH-2007 Neuchâtel
http://www.csem.ch/

[4] W. Blum , C. Eimer, H. Kroha, P. Widmann, *Development of an Optical Alignment Monitoring System for the ATLAS Muon Spectrometer – Update–* ATLAS Internal Note, MUON-NO 047, 12 July 1994.

[5] J. Berdugo, M.G. Fernández, A. Ferrando, M.I. Josa, A. Molinero, J.C. Oller, P. Arce, E. Calvo, C.F. Figueroa, N. García, T. Rodrigo, I. Vila, *First test results of semitransparent amorphous silicon sensors for the link system of the CMS alignment*, Nucl. Instr. and Methods A425 (1999) 469-479.

[6] Physik Instruments, M125.10. Polytec-Platz 1-7 D-76337 Waldbronn, Germany

[7] Linos Photonics, XY stages x.act XY with Stepping Motor 100 ST.

[8] S. Horvat, *ALMY: Opto-elektronički senzori u laserkom sustavu za odred ivanje položaja mionskih komora u sklopu detektora ATLAS* , Diplomski Rad, Sveučiliste u Zagrebu, PMF-Fizika, 1999

[9] Born M and Wolf E 1975 *Principles of Optics* 5th edn (Oxford: Pergamon)

[10] EG&G Optoelectronics. 45 William Street, Wellesley, Massachusetts, 02181 U.S.A.

[11] M.G. Fernández, *Sensores Matriciales transparentes de silicio amorfo para el sistema de alineamiento de CMS*, Graduation thesis, University of Cantabria, October 1998
http://wwwae.ciemat.es/~mfg

[12] A.L.Virto *et al.*, *Results of the first real scale CMS alignment test*, CMS Note in preparation.

[13] *Diseño, construcción y pruebas de prototipo para el alineamiento de CMS: el monitor* $\phi$ . Ivan Vila, Graduation thesis.

[14] A.L.Virto *et al. Testing tiltmeters for the alignment system of the CMS experiment*, CIEMAT 2000-930

[15] R.M. Almazán, G. Pérez, M.T. Rodrigo, M.C. Torquemada, G. Vergara, *Informe sobre la caracterización del detector "ALMY" solicitado por el Instituto de Física de Cantabria*, CIDA, C/. Arturo Soria, 289 28033 Madrid

[16] CIEMAT Electronics and Automatics division, Avda. Complutense 22, 28015 Madrid (Spain).

[17] SIMESA (Grupo BERU), C/. Uritiasolo, N°14 Vitoria (Spain)

[18] See for instance:
http://www.esis.com.au/Adam/Adam0_4000.htm

[19] LabVIEW, National Instruments Corporation. 6504 Bridge Point Parkway Austin, TX 78730-5039

[20] James Tickner, *Guide to using the Transparent Silicon Position sensors*, j.tickner1@physics.ox.ac.uk. See also: S. Schael *ALICA: The ALMY client* , Stefan.Schael@cern.ch

[21] M.F.García, *ALMYs Current Status & ALMY simulation*, MPI Munich, July 13$^{th}$, 1999. http://wwwae.ciemat.es/~mfg

[22] Varuzhan Danielyan, Stefan Schael *Proposal for a new Readout for MPI-ALMY Detectors*, ATLAS ATL-COM-MUON-98-028, 09 November 1998.

[23] Volker Bartheld *Experience and progress with alignment lasers*,Workshop on Transparent Sensors, MPI München, 6 April 1998

[24] M.G. Fernández, A. Ferrando, M.I.Josa, A. Molinero, J.C. Oller, P.Arce, E.Calvo, C.F.Figueroa, N.García, T.Rodrigo, I.Vila, A.L. Virto, *Semitransparent amorphous silicon sensors for the CMS alignment: an in-depth study*, Nucl. Instrm. and Methods A 440(2000) 372-387.

[25] J. Fent, *Readout Electronics for MPA-ALMY Sensors and Sensor Module Development at MPI* , Workshop on Transparent Sensors, MPI München, 6 April 1998

[26] Stefan Schael, *Alignment Sensors. Design and Performance*, LHCC referee meeting, CERN, May 1998

[27] M.G. Fernández, *CMS Test results of MPA-ALMY EG&G sensors*, Workshop on Transparent Sensors, MPI Munich, 6-8 April 1998.

[28] H. Kroha, *Summary of Ageing Tests of Amorphous Silicon sensors*, Workshop on Transparent Sensors, MPI Munich, 6-8 April 1998.

[29] K.S. Hashemi, J.R. Besinger *ALMY stability* , ATLAS Note, Muon-No-221 (1998)

[30] SATRAPS, Proceedings of the International Workshop on Acclerator Alignment, Grenoble 1999.

[31] UDT Sensors, Inc
12525 Chadron Avenue. Hawthorne, CA 90250.

[32] Preparation and Characterization of Amorphous-silicon Photovoltaic Devices Having Mycrocrystalline Emitters, J. Cárabe, J.J. Gandía, M.T. Guitiérrez, CIEMAT Technical Reports ISSN: 1135-9420

[33] Non-contact optical position sensing using silicon photodetectors.
UDT Application Note, No. 13, April 1982

[34] J. Alberdi et al.; Nucl. Instr. and Meth. A 408 (1998) 591-593

[35] W. Schottky, Phys. Z. 31, 913 (1930)

[36] W. Morawek, U. Gollerthan and W.Schwab, Nucl. INstr. and Meth. A 258 (1987) 82

[37] Hamamatsu Photonics K.K.
See on-line catalog, under Products→Opto-semiconductors→PSDs

[38] Satoshi Arimoto, Hidekazu Yamamoto, Hideo Ohno and Hideki Hasegawa. J. Appl. Phys. 57(10), 15 May 1985

# Chapter 5

# ALMY simulation Calculating transmittance and reflectance

## 5.1 Early history

The earliest of what may be called modern thin-film optics was the discovery, independently, by Robert Boyle and Robert Hooke of the phenomenon known as "Newton's rings". Then, on 1801, Thomas Young enunciated the principle of the interference of light and produced the first satisfactory explanation of this effect as due to the interference in a single film of varying thickness.

Recognition came slowly and depended much on the work of Augustin Jean Fresnel [1]. Fresnel's laws, governing the amplitude and phase of light reflected and transmitted at a single boundary, are of major importance.

In 1873, the work of James Clerk Maxwell, *A Treatise on Electricity and Magnetism* [2], was published, and in his system of equations we have all the basic theory for the analysis of thin-film optical problems.

It was Fresnel who first summed an infinite series of rays to determine the transmittance of a thick sheet of glass, and Denis Poisson, in correspondence with Fresnel, who included interference effects in the summations.

This classical treatment of optical multiple reflections in the layers involves extremely complex calculations and an alternative, and more effective, approach has been found in the development of entirely new forms of solution of Maxwell's equations. The solution of the thin-film problems appears as a very elegant product of $2 \times 2$ matrices, each matrix representing a single film.

The basis of this method is presented in the next section. Its main purpose is to give the physics background needed to perform the calculation of the transmittance and reflectance of a multilayer system. In section 5.3 we declare the goals of the simulation, as a guidance for the rest of the chapter. Then, section 5.4 presents the method we have developed to calculate the unknown optical constants of single layers. This method is applied in order to reproduce a Schottky ALMY sensor in section 5.5. Section 5.6 deals with the optimization of the several layers for maximum transmittance. Finally a brief comparison with other methods found in the bibliography is exposed.

## 5.2 Theoretical background

The first step to attack thin-film problems is to solve Maxwell's equations together with the appropriate material equations. We look for solutions in the form of plane-polarised harmonic waves, choosing the complex form of this wave, the physical meaning being associated with the real part of the expression.

$$\mathbf{E} = \mathcal{E} \exp[i\omega(t - x/v)] \tag{5.1}$$

This represents such a wave propagating along the $x$ axis with velocity $v$. $\omega$ is the angular frequency of this wave and $\mathcal{E}$ the vector amplitude. The vectorial character of the fields is assumed in this discussion. For equation (5.1) to be a solution of Maxwell's equations it is necessary that:

$$\omega^2/v^2 = \omega^2\varepsilon\mu - i\omega\mu\sigma \tag{5.2}$$

where $\varepsilon$, $\mu$ and $\sigma$ are the dielectric constant, magnetic permeability and electric conductivity of the medium, respectively. In vacuum we have:

$$\begin{array}{ll} \sigma = 0 & v = c \\ \varepsilon_0 = 8.8541853 \times 10^{-12}\ \mathrm{Fm}^{-1} & \mu_0 = 4\pi \times 10^{-7}\ \mathrm{Hm}^{-1} \end{array}$$

Using $\varepsilon_0 = 1/(\mu_0 c^2)$ and dividing (5.2) by $\omega^2$ we obtain:

$$\frac{\mathbf{c^2}}{\mathbf{v^2}} = N^2 = \frac{\varepsilon\mu}{\varepsilon_0\mu_0} - i\frac{\mu\sigma}{\omega\varepsilon_0\mu_0} \tag{5.3}$$

N is a dimensionless parameter known as the complex refractive index. There are two possible values of N from equation (5.3), but for physical reasons we choose the one that gives a positive real part. Then:

$$N = n - ik \tag{5.4}$$

$n$ is simply known as the refractive index and $k$ is the extinction coefficient. The distance $\lambda/2\pi k$ is that in which the amplitude of the wave falls to $1/e$ of its initial value.
Multilayers consist of a number of boundaries between various homogeneous media and it is the effect these boundaries will have on an incident wave which we wish to calculate. The figures of merit are the transmittance (reflectance) representing the amount of energy which leaves (is reflected by) the multilayer structure, in unit time, relative to the incoming energy. For the present, we will obtain the transmittance and reflectance of a single boundary in order to illustrate the physics involved in this calculations.

### 5.2.1 The single boundary

Although we will be dealing with absorbing media in thin-films assemblies, our incident media will never be heavily absorbing and it will not be a serious lack of generality if we assume that our incident media are absorption-free.

Any incident wave of arbitrary polarization can be split into two components: a wave with the electric vector in the plane of incidence (XZ in figure 5.1) which is known as p-polarised or as TM (transverse magnetic) and another with the electric vector normal to the plane of incidence known as s-polarised or TE (transverse electric). Any result relating to TM waves may be deduced from the corresponding result for TE waves interchanging **E** and **B** and simultaneously $\varepsilon$ and $-\mu$. Therefore we will only study TE waves in detail.
Since we will be emphasizing the electric vector, the most convenient sign convention is to choose the positive direction of **E** along the x axis for all the beams involved. The sign convention chosen is displayed in figure 5.2.

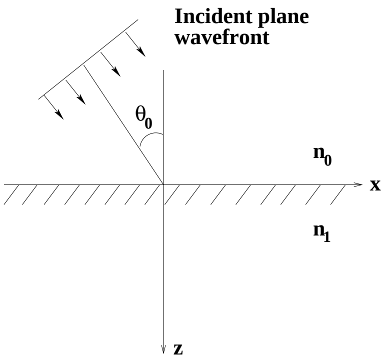


Figure 5.1: *Plane wavefront incident on a single surface.*

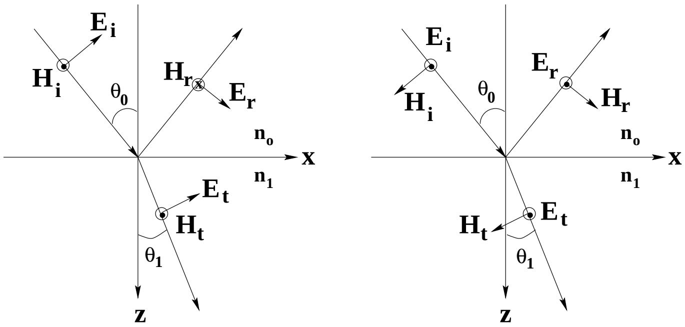


Figure 5.2: *a) Convention defining the positive directions of the electric field and magnetic vectors for p-polarised light (TM waves). b) Convention defining the positive directions of the electric and magnetic vectors for s-polarised light (TE waves).*

Let the direction of propagation of the wave be given by unit vector $\hat{s}$ where

$$\hat{s} = \alpha\mathbf{i} + \beta\mathbf{j} + \gamma\mathbf{k}$$

Then, the phase factor of the incident, reflected and transmitted waves will be, accordingly to (5.1)

$$\text{Incident} \quad \exp\{i[wt - (2\pi n_0/\lambda)(x\sin\theta_0 + z\cos\theta_0)]\} \tag{5.5}$$

$$\text{Reflected} \quad \exp\{i[wt - (2\pi n_0/\lambda)(x\sin\theta_0 - z\cos\theta_0)]\} \tag{5.6}$$

$$\text{Transmitted} \quad \exp\{i[wt - (2\pi(n_1 - ik_1)/\lambda)(\alpha x + \gamma z)]\} \tag{5.7}$$

The expression $(\alpha x + \gamma z)$ is simply the distance along the direction of propagation of the transmitted wave. As the phase factors in the boundary must be identically equal for all $x$ and $t$ it implies:

$$\alpha = \frac{n_0\sin\theta_0}{(n_1 - ik_1)} \tag{5.8}$$

$$\gamma = (1 - \alpha^2)^{1/2} \tag{5.9}$$

Among the two solutions of last equation, we choose the root that lies in the fourth quadrant, which leads to an exponential fall-off of the amplitude with $z$. The expression for $\gamma$ is therefore:

$$\gamma = \frac{(n_1^2 - k_1^2 - n_0^2 \sin^2\theta_0 - i2n_1k_1)^{1/2}}{(n_1 - ik_1)} \tag{5.10}$$

Substituting the values of $\alpha$ and $\gamma$ from equations. (5.8) and (5.10) into (5.7)

$$\exp(-2\pi bz/\lambda)\ \exp\{i[wt - (2\pi n_0 \sin\theta_0 x)/\lambda - 2\pi az/\lambda]\} \tag{5.11}$$

which is the transmission phase factor for the transmitted wave. In the last equation we have equated $a - ib = (n_1^2 - k_1^2 - n_0^2\sin^2\theta_0 - i2n_1k_1)^{1/2}$. A wave like this is called inhomogeneous since the surfaces of constant amplitude do not coincide with the surfaces of constant phase.
A particularly attractive mathematical feature of the Maxwell equations is that the existence of absorption may be taken into account simply by introducing a complex dielectric constant (or complex index of refraction), instead of a real one [3]. By analogy with the law of refraction for non-absorbing materials we include the possibility of complex angles, to extend the Snell law to absorbing media:

$$(n_1 - ik_1)\sin\theta_1 \quad = \quad n_0 \sin\theta_0$$

where $\theta_1$ no longer has the simple significance of an angle of refraction. Using Snell law in equation (5.8) produces $\alpha = \sin\theta_1$.
A direct consequence from Maxwell equations is the perpendicularity between the magnetic and electric fields [4], expressed here as:

$$\frac{N}{c\mu}(\hat{s} \times \mathbf{E}) = \mathbf{H} \tag{5.12}$$

It is usual to define some extra quantities to reduce the notation of the reflectance and transmittance expressions. Instead of the complex refraction index, it is common to use the quantity $\mathrm{y} = N/(c\mu)$ (ratio of magnetic field to electric field strengths) known as the characteristic optical admittance of the *medium* . In free space, the optical admittance is:

$$\mathcal{Y} = (\frac{\epsilon_0}{\mu_0})^{1/2} = 2.6544 \times 10^{-3}S$$

and since $\epsilon_0 = 1/(\mu_0 c^2)$ and at optical frequencies $\mu = \mu_0$, we can write:

$$\mathrm{y} = N\mathcal{Y}$$

The modified optical admittance $\eta$ is the ratio of the components tangential to the boundary of the electric and magnetic fields, namely:

$$\eta_p \quad = \frac{\mathrm{y}}{\cos\theta} \quad = \frac{N\mathcal{Y}}{\cos\theta} \tag{5.13}$$

$$\eta_s \quad = \mathrm{y}\cos\theta \quad = N\mathcal{Y}\cos\theta \tag{5.14}$$

Qualitatively, the modified optical admittance behaves as the characteristic optical admittance but modified by the incidence angle. This quantity is important when the incidence is not normal.
Equation (5.12) allows the calculation of the modified optical admittances for both s- and p-polarization for the inhomogeneous wave which results [4]:

$$\begin{aligned} \eta_p &= \mathrm{y}/\gamma \\ \eta_s &= \mathrm{y}\gamma \end{aligned}$$

Now $\gamma$ can be identified with $\cos\theta_1$, which agrees with the angular definitions in figure 5.2.

$$\begin{aligned} \alpha &= \sin\theta_1 \\ \gamma &= \cos\theta_1 \end{aligned}$$

We will apply now the boundary conditions to the vector amplitudes, since with the above, we have already ensured that the phase factors will be correct.
The boundary conditions at a surface of discontinuity state that the tangential component of the electric vector is continuous across the surface of discontinuity. This leads us to calculate energy flows normal to the boundary.

### s-polarised light

*(a)* Electric component parallel to the boundary continuous across it.

$$\mathcal{E}_i + \mathcal{E}_r = \mathcal{E}_t$$

*(b)* Magnetic component parallel to the boundary continuous across it

$$\begin{aligned} \mathcal{H}_i \cos\theta_0 + \mathcal{H}_r \cos\theta_0 &= \mathcal{H}_t \cos\theta_1 \Longrightarrow \\ \Longrightarrow \mathrm{y}_0 \cos\theta_0 \mathcal{E}_i - \mathrm{y}_0 \cos\theta_0 \mathcal{E}_r &= \mathrm{y}_1 \cos\theta_1 \mathcal{E}_t \end{aligned}$$

where we have used equation (5.12) in the last expression.
The reflectance R is defined as the ratio of the reflected and incident intensities and the transmittance as the ratio of the transmitted and incident intensities. The intensity of a harmonic electromagnetic wave is calculated by means of its Poynting vector:

$$I = \frac{1}{2} Re(\mathbf{E} \times \mathbf{H}^*)$$

and is found to be:

$$I = \frac{1}{2} n\mathcal{Y}(amplitude)^2 \quad \text{or} \quad I = \frac{1}{2} n\mathcal{Y}(amplitude)(amplitude)^* \tag{5.15}$$

This expression is a better form than the more usual $I \propto (amplitude)^2$. The refraction index factor is important when comparing intensities of two waves propagating in media of different index. Then the transmittance and reflectance formulas will be (using equation (5.15)):

$$T_s = \frac{n_1}{n_0}\frac{\mathcal{E}_t\mathcal{E}_t^*}{\mathcal{E}_i\mathcal{E}_i^*} = \frac{n_1}{n_0}\tau_s\tau_s^* = \frac{4\mathrm{y}_0\cos\theta_0\mathrm{y}_1\cos\theta_1}{(\mathrm{y}_0\cos\theta_0 + \mathrm{y}_1\cos\theta_1)^2} \tag{5.16}$$

$$R_s = \rho_s\rho_s^* = \left(\frac{\mathrm{y}_0\cos\theta_0 - \mathrm{y}_1\cos\theta_1}{\mathrm{y}_0\cos\theta_0 + \mathrm{y}_1\cos\theta_1}\right)^2 \tag{5.17}$$

where $\rho_s$ and $\tau_s$ are called the Fresnel amplitude reflection and transmission coefficients and are given by:

$$\rho = \frac{\mathcal{E}_r}{\mathcal{E}_i} \tag{5.18}$$

$$\tau = \frac{\mathcal{E}_t}{\mathcal{E}_i} \tag{5.19}$$

Equation (5.16) shows the importance of considering the refractive indexes in the intensity definition.
For the p-polarised light a similar process must be followed. By using the definitions of modified optical admittances a general expression for the transmittance and reflection can be written:

$$\rho = \frac{\epsilon_0 - \eta_1}{\epsilon_0 + \eta_1} \qquad \tau = \frac{2\epsilon_0}{\epsilon_0 + \eta_1} \tag{5.20}$$

$$T = \frac{n_1}{n_0}\tau\tau^* = \frac{4Re(\eta_0)Re(\eta_1)}{(\eta_0 - \eta_1)(\eta_0 + \eta_1)^*} \qquad R = \rho\rho^* = \left(\frac{\eta_0 - \eta_1}{\eta_0 + \eta_1}\right)\left(\frac{\eta_0 - \eta_1}{\eta_0 + \eta_1}\right)^* \tag{5.21}$$

where $\eta$ can be $\eta_p$ or $\eta_s$ (defined in equations (5.13) and (5.14)). These expressions are valid for non-absorbing materials (by equating the complex part of the refraction index to zero) and for normal incidence ($\theta_0 = 0$).
In the former equations we find a justification for the definitions of the modified optical admittances. These equations are identical to the Fresnel formulae, having first been derived in a slightly less general form by Fresnel in 1823, on the basis of his elastic theory of light.

### 5.2.2 Wave propagation in a thin film

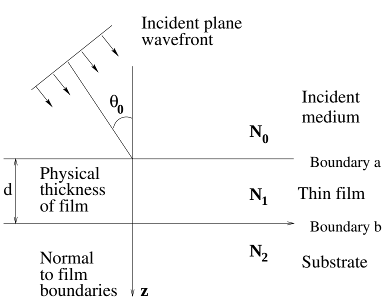


Figure 5.3: *Plane wave incident on a thin film*

A single thin film is delimited by two interfaces, the second one shared with the substrate. The presence of these two interfaces means that a number of beams will be produced by successive reflections and the properties of the film will be determined by the summation of all these beams.
A film is called thin when interference effects can be detected in the reflected or transmitted light, that is, when the path difference between the beams is less than the coherence length of the light[1], and thick if the path difference is greater. Normally, films on substrates can be treated as thin while the substrates supporting the films can be considered thick. In subsection 5.2.4 it is explained how to include the effect of thick substrates in the transmittance and reflectance calculations.

[1] Coherence length $= \overline{\lambda}^2/\Delta\lambda$, with $\lambda$ the laser wavelength and $\Delta\lambda$ the wavelength stability.

We will denote waves in the direction of incidence by the symbol + and waves in the opposite direction by $-$. The following discussion is illustrated by figure 5.3. Maxwell equations establish that tangential components have to be continuous across the boundary. As the substrate is considered as infinite, there is no negative-going wave in the substrate. The resultants of all the traveling waves at interface "b" can be written as:

$$\begin{aligned}\mathcal{E}_b &= \mathcal{E}_b^+ + \mathcal{E}_b^- \\ \mathcal{H}_b &= \eta_1\mathcal{E}_b^+ - \eta_1\mathcal{E}_b^-\end{aligned}$$

From both equations, we can obtain the expressions for the traveling waves:

$$\mathcal{E}_b^+ = \frac{1}{2}(\mathcal{H}_b/\eta_1 + \mathcal{E}_b) \tag{5.22}$$

$$\mathcal{E}_b^- = \frac{1}{2}(-\mathcal{H}_b/\eta_1 + \mathcal{E}_b) \tag{5.23}$$

Hence:

$$\mathcal{H}_b^+ = \eta_1\mathcal{E}_b^+ = \frac{1}{2}(\mathcal{H}_b + \eta_1\mathcal{E}_b) \tag{5.24}$$

$$\mathcal{H}_b^- = -\eta_1\mathcal{E}_b^- = \frac{1}{2}(\mathcal{H}_b - \eta_1\mathcal{E}_b) \tag{5.25}$$

These are the amplitude terms for the fields at the interface "b". A wave traveling inside an absorbing material experiments an exponential fall-off in amplitude, as described by equation (5.11). Therefore the expression of the fields at interface "a" are the same as at "b" but affected by the appropriate phase factors. The phase factor of the positive-going wave will be multiplied by $\exp(i\delta)$ where

$$\delta = \frac{2\pi N_1 d\cos\theta_1}{\lambda}$$

while the negative-going wave will be multiplied by exp(-i$\delta$). Using the values from equations (5.22) to (5.25):

$$\begin{aligned}\mathcal{E}_a^+ &= \tfrac{1}{2}(\mathcal{H}_b/\eta_1 + \mathcal{E}_b)e^{i\delta} \\ \mathcal{E}_a^- &= \tfrac{1}{2}(-\mathcal{H}_b/\eta_1 + \mathcal{E}_b)e^{-i\delta} \\ \mathcal{H}_a^+ &= \eta_1\mathcal{E}_b^+ = \frac{1}{2}(\mathcal{H}_b + \eta_1\mathcal{E}_b)e^{i\delta} \\ \mathcal{H}_a^- &= -\eta_1\mathcal{E}_b^- = \frac{1}{2}(\mathcal{H}_b - \eta_1\mathcal{E}_b)e^{-i\delta}\end{aligned}$$

The resultant fields in "a" are:

$$\begin{aligned}\mathcal{E}_a^+ &= \mathcal{E}_a^+ + \mathcal{E}_a^- = \mathcal{E}_b\cos\delta + \mathcal{H}_b\frac{i\sin\delta}{\eta_1} \\ \mathcal{E}_b^+ &= \mathcal{E}_b^+ + \mathcal{E}_b^- = \mathcal{E}_b i\eta_1\sin\delta + \mathcal{H}_b\cos\delta\end{aligned}$$

These equations can be written in matrix notation as

$$\begin{bmatrix} E_a \\ H_a \end{bmatrix} = \begin{bmatrix} \cos\delta & (i\sin\delta)/\eta_1 \\ i\eta_1\sin\delta & \cos\delta \end{bmatrix} \begin{bmatrix} E_b \\ H_b \end{bmatrix} \tag{5.26}$$

Therefore the former equation relates the $x$ and $y$ (or s- and p-polarised) components of the electric and magnetic vectors which are known for one plane ($z = a$) to the components in an arbitrary plane $z =$ d transmitted through the final interface. For the purposes of determining the propagation of a plane monochromatic wave through a stratified medium, the medium only need be specified by an appropriate two by two unimodular matrix, which is called characteristic matrix. It is completely specified by the material properties.

### 5.2.3 Wave propagation in an assembly of thin films

Let another film be added to the single film on the previous example (figure 5.4). Equation (5.26) allows to calculate the fields at the boundary "b", starting from the interface "c", in the same manner exactly as we have just done above. Then, the problem is reduced again to that of a single thin film.

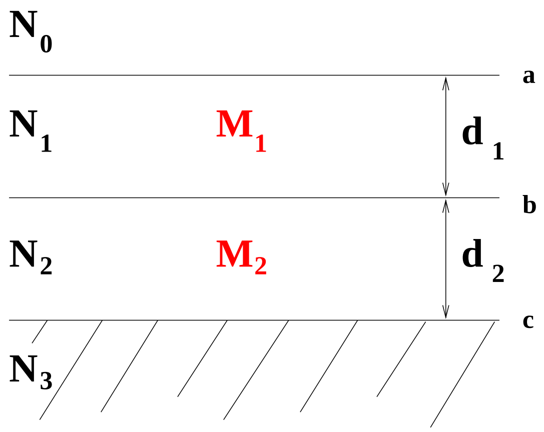


Figure 5.4: *Notation for refraction indexes, layer thicknesses (for δ phase factors) and boundary names.*

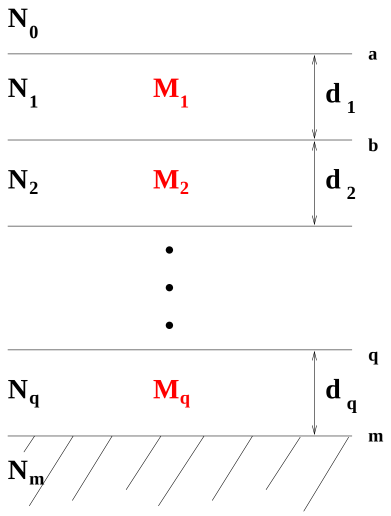


Figure 5.5: *Notation adopted for a multilayer structure. The substrate is assumed to be semi-infinite.*

For an arbitrary number of films (see figure 5.5) it can be easily shown that this argument can be applied recursively. The resultant calibration matrix is the (ordered) product of the individual calibration matrixes:

$$\begin{bmatrix} \mathcal{E}_1 \\ \mathcal{H}_1 \end{bmatrix} = \left( \prod_{i=1}^{q} \begin{bmatrix} \cos\delta & (i\ \sin\delta)/\eta_1 \\ i\eta_1\ \sin\delta & \cos\delta \end{bmatrix} \right) \begin{bmatrix} \mathcal{E}_m \\ \mathcal{H}_m \end{bmatrix} \tag{5.27}$$

or in a slightly different manner:

$$\begin{bmatrix} B \\ C \end{bmatrix} = \left( \prod_{i=1}^{q} \begin{bmatrix} \cos\delta & (i\ \sin\delta)/\eta_1 \\ i\eta_1\ \sin\delta & \cos\delta \end{bmatrix} \right) \begin{bmatrix} 1 \\ \eta_m \end{bmatrix} \tag{5.28}$$

The subindex "m" references the substrate. The quotient $\mathtt{Y} = C/B$ is called optical admittance of the surface (or the multilayer), since we replace the multilayer by a single surface which has an input admittance Y. As in the case of the single boundary, the reflectance and transmittance coefficients can be calculated by using the Fresnel coefficients (5.18) and (5.19). The best forms (from a computational point of view) for these expressions are:

$$R = \left(\frac{\eta_0 B - C}{\eta_0 B + C}\right)\left(\frac{\eta_0 B - C}{\eta_0 B + C}\right)^* \tag{5.29}$$

$$T = \frac{4\eta_0 \mathrm{Re}(\eta_\mathrm{m})}{(\eta_0 B + C)(\eta_0 B + C)^*} \tag{5.30}$$

$$A = 1 - (R + T) \tag{5.31}$$

The former calculated transmittance is the *transmittance inside the substrate* rather than the transmittance across it, since in section 5.2.2 we have assumed an infinite substrate.

### 5.2.4 The effect of the substrate second surface

It is a common trend in many books dealing with thin films to extract the expressions for the transmittance and reflectance discarding the effect of the back surface of the glass. But, in fact this is an important contribution if we want to match calculated and measured data.

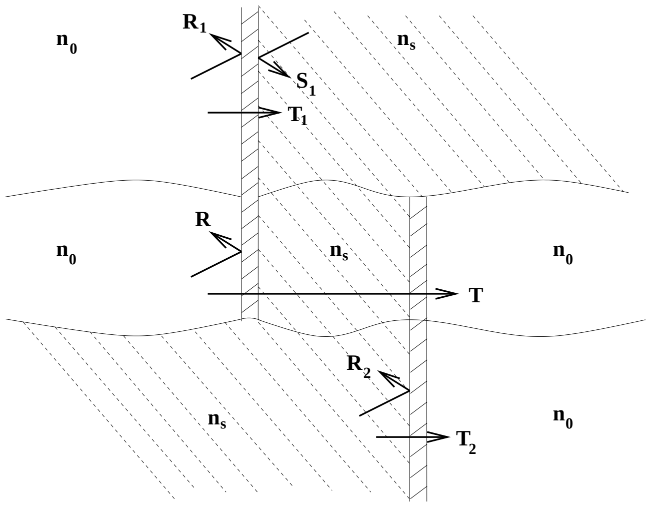


Figure 5.6: *Diagram illustrating the definition of the several quantities defined for transmittance and reflectance calculations in equations (5.33) and (5.32).*

The thickness of the substrate introduces serious average effects in the reflectance and the transmittance, so that the substrate does not behave as a wavelength-dependent element of the multilayer. The influence of a non absorbing substrate can readily be evaluated in the following way [5]. Figure 5.6 shows a very general situation where the substrate is coated on the two sides by multilayer films, either or both of which may be assumed to contain absorbing elements. Let the intensity reflectance and transmittance of the left-hand combination be $R_1$ and $T_1$ for light incident from the left, assuming the substrate to be massive, and let $S_1$ be the reflectance for light incident from the substrate, again assumed massive. Similarly, let $R_2$ and $T_2$ be the corresponding intensities for the right-hand combination assuming light incident from the massive substrate. Then formulas for the overall reflectance $R$ and transmittance $T$ are given by:

$$R = \frac{R_1 - R_1 S_1 R_2 + T_1^2 R_2}{1 - S_1 R_2} \tag{5.32}$$

$$T = \frac{T_1 T_2}{1 - S_1 R_2} \tag{5.33}$$

These formulas apply to oblique as well as to normal incidence, for each polarization separately.

## 5.3 Goals of the ALMY simulation

The ALMY simulation was born as an attempt to have a physical and quantitative description of ALMY parameters. Since the beginning of the ALMY project several kinds of sensors were produced. The baseline for the production adopted by the optolectronic division of EG&G was the Schottky-type sensors. Due to a company redistribution, production of ALMY sensors moved from CSEM [6] in Switzerland to a production plant in the US. This change implied a new production line, based in *pin* diodes. Although EG&G mastered all the technology needed to deposit the ALMY thin layers and make the photolitography of the ITO electrodes, it was not possible for them to measure the quality of the produced devices. The ALMY simulation is a software tool which allows a direct quality control of the samples produced. By studying the transmittance and reflectance curves of a sensor, we may calculate the key properties of the multilayers from the optics approach: complex refraction indexes and layer thickness. A comparison of the relevant parameters within a single sensor allows to study the homogeneity of the deposition process. The repeatability and reproducibility of the fabrication method is studied by comparison of parameters for different sensors.
Once we will have verified the goodness of our mathematical model we will attempt to find an extreme configuration optimizing the transmittance of the device, by means of proper selection of the different layer thicknesses. This is a general method which can be applied to any kind of multilayer. As it will be remarked later on, the optimization tries to perform such a calculation from the multilayer point of view. There are other aspects as the quantum efficiency and sensitivity of the layer of a-Si:H which should be fixed at proper values in advance, in order to obtain a measurable signal afterwards.
The central body of the simulation deals with the obtention of the thin film parameters, as are the complex refraction index and the layer thickness. As it was explained before, these parameters determine the characteristic matrix of the layer, which is the only input needed to calculate transmittance and reflectance of the sample.
The strategy adopted was a minimization of the difference between calculated reflectance and/or transmittance with respect to the measured data. A summary of some alternative methods will be given in the last section of this chapter.

### T and R calculation preamble

The input data used in this simulation were:

i) Four values of the complex refraction index at selected wavelengths, for each layer of a *pin* ALMY sensor. These values are reproduced in table 1. Besides that, plots for the transmittance of the a-Si:H, ITO and glass layers, for the *pin* sensor.

ii) Two detailed measurements of the refraction index of the a-Si:H in the wavelength range $[690, 900]$ nm, every 10 nm [7]. One of the measurements taken in the center of the sensor, the other in one extreme.

iii) A measurement of the transmittance and the reflectance of a Schottky-type ALMY sensor, measured at CIDA [8]. Reproduction of these two measurements is the final goal of the simulation.

iv) Nominal values of the layer thicknesses are $d_{ITO1} = d_{ITO2} = 100$ nm, and $\mathrm{d}_{a-Si:H} = 1000$ nm, although the real thicknesses of the ALMY are unknown.

v) A plot of $(n, k)$ for a-Si:H taken from the *Handbook of optical constants* [9] which gives an idea of the variation of the indexes with the wavelength.

| ITO | $\lambda$ =650 nm | $\lambda$ =700 nm | $\lambda$ =750 nm | $\lambda$ =800 nm |
|---|---|---|---|---|
| n | 1.84 | 1.81 | 1.78 | 1.74 |
| k | 0.028 | 0.036 | 0.044 | 0.055 |
| a-Si:H | $\lambda$ =700 nm | $\lambda$ =750 nm | $\lambda$ =800 nm | $\lambda$ =850 nm |
| n | 3.6387 | 3.5543 | 3.4950 | 3.4495 |
| k | 0.00602 | 0.00184 | 0.00095 | 0.00061 |
| Glass | $\lambda$ =546 nm | $\lambda$ =589 nm | $\lambda$ =644 nm | $\lambda$ =656 nm |
| n | 1.5354 | 1.5333 | 1.5311 | 1.5306 |

Table 1: *Starting values for the complex refraction indexes of the several layers of the ALMY system.*

Instead of trying to reproduce directly the T and R measurements of the ALMY system, we will calculate each layer separately and then will combine all the information to reproduce the T and R of the whole sensor.

## 5.4 Calculation of the complex refraction index of a single layer

When all the parameters of a layer are known, the calculation of the transmittance and reflectance are quite straightforward, by substitution in equations (5.26), (5.32) and (5.33). Finding the $(n, k, d)$ values of a layer is not an easy to solve problem. As it can be deduced from the expressions in section 5.2.2, the dependence of the transmittance and reflectance on these parameters is not linear. Furthermore, the solutions $(n, k, d)$ that satisfy the equations of transmittance and reflectance are periodical. This periodicity is evident in the case of a single layer on a substrate. The condition for interference fringes sets:

$$2nd = m\lambda \tag{5.34}$$

where $n$ is the real part of the refraction index, $d$ is the layer thickness and $m$ is an integer for constructive interference (local maximum in the transmittance curve) and half integer for destructive interference (local minimum in transmittance). For a defined value of $\lambda$, there are infinite $nd$ values verifying equation (5.34), only one of them producing the measured curves.
Let us explicitly write the dependencies of T and R with the layer parameters. For a single layer, on a substrate:

$$T = T(n_1, k_1, d_1) \tag{5.35}$$
$$R = R(n_1, k_1, d_1) \tag{5.36}$$

where the enter and exit mediums and data of the substrate are supposed to be known. We have 2 equations and 3 unknowns. Although equation (5.34) can reduce in one the number of unknowns, it can only be applied in case there are interference fringes. In order to have maxima and minima in the transmittance and reflectance curves it is therefore needed to have a layer thick enough for equation (5.34) exists for a few "m" values. As this is not always the case (see figure 5.10 top), we consider the layer thickness as unknown.

The true values $(n, k, d)$ which satisfy equations (5.35) and/or (5.36) are such that:

$$\chi_T \equiv T_{measured} - T(n, k, d) = 0 \tag{5.37}$$
$$\chi_R \equiv R_{measured} - R(n, k, d) = 0 \tag{5.38}$$

In order to reduce the number of allowed solutions, we can use the four values of the refraction indexes given in table 1 as bound conditions for the $(n, k)$ values. In what follows, we assume the dispersion functions ($n = n(\lambda)$ and $k = k(\lambda)$) to be continuous and monotonous functions of the wavelength in the regions delimited by the constraints. This is specified stating that the derivative of the refraction index has to be greater than zero or smaller than zero:

$$\chi_{\frac{\delta n}{\delta \lambda}} \equiv sign[\frac{n_i - n_{i-1}}{\lambda_i - \lambda_{i-1}}] = \text{ constant} \tag{5.39}$$
$$\chi_{\frac{\delta k}{\delta \lambda}} \equiv sign[\frac{k_i - k_{i-1}}{\lambda_i - \lambda_{i-1}}] = \text{ constant} \tag{5.40}$$

In equations (5.39) and (5.40) an iterative process is already assumed (since the searching process is a numerical method). Some other common-sense constraints may help. For instance :

1) Consecutive values of the indexes not very different:

$$\chi_{\delta n} \equiv n_i - n_{i-1} \approx 0 \tag{5.41}$$
$$\chi_{\delta k} \equiv k_i - k_{i-1} \approx 0 \tag{5.42}$$

2) Maximum and minimum values the indexes are constrained:

$$n \in [1, 6], \quad k \in [k_{inf}, k_{sup}] \tag{5.43}$$

$k_{inf}$ and $k_{sup}$ depend on the interval where the search is done.

Each of these constraints may be combined together in the form of a function that has to be minimized, that is a function which satisfies all the above conditions. It is a common $\chi^2$ minimization problem. When all these terms are added in quadrature we end up with a function like:

$$\begin{aligned} \chi^2 &= w_1\chi_T^2 + [w_2\chi_R^2] + w_3\chi^2_{\frac{\delta n}{\delta\lambda}} + w_4\chi^2_{\frac{\delta k}{\delta\lambda}} + \\ & w_5\chi_{\delta n} + w_6\chi_{\delta k} + w_7(6-n)^2 + w_8(1-n)^2 + w_9(1-k)^2 + w_{10}k^2 \end{aligned} \tag{5.44}$$

with $w_i$ $i = 1, ..., 10$ weights that are tuned by hand. The relative magnitude of these weights may favor some of the above constraints and degrade the others. The importance of each weight has to be set by hand for the different layers.
The core of the calculation (minimization of function (5.44)) is done using the standard CERN library MINUIT [10] (the internal processor used being MIGRAD).

### 5.4.1 Determination of thickness and optical constants of a-Si:H

The first step for the calculation of the transmittance and reflectance of the ALMY system will be the calculation of the optical constants of a thin layer of a-Si:H on glass. It corresponds with the measurement at the center of the sensor reported in section 5.3.iii). The layer thickness ($d_{a-Si:H}$=1448.96 nm) was measured with a profilemeter Talystep (Rank-Taylor-Hobson [11]). Following the process described in section 5.4 we can obtain $(n, k)$ for the system. The calculated indexes are shown in the middle and bottom plots of figure 5.7. The obtained $(n, k)$ indexes are then used, together with the layer thickness to obtain the calculated transmittance, which is shown in the top plot of figure 5.7. The maxima and minima displayed appear because the layer is thick enough for interference condition (equation 5.34) to be fulfilled.
We may compare these results with the indexes measured by JENOPTIK for the same sample. Thus, in figure 5.8 we show several plots of the refraction index $n_{a-Si:H}$. The dotted and the continuous line (fit) on top corresponds to the values reported in the literature [9]. Then, we have a group of three overlapping lines. Upward arrow-heads are measurements of $n$ at the extreme of the sensor. Downward arrow-heads are measured at the center. On top of them, the calculated values. As it may be seen there is a remarkable agreement. Figure 5.9 shows the corresponding $k$ indexes. Again dotted line for reported values of extinction coefficient. The values *measured* by JENOPTIK at the center and at the extreme are now clearly differenced. The simulated values lie on top of the indexes measured at the center, which was our goal.
The measured difference in the extinction coefficients leads to different values of the transmittance in the center of the sensor and in the extreme. It happens that maxima and minima appear shifted for measurements in different points of the same sample. It is due to the different optical constants and thicknesses, which affects the interference condition (5.34). The explanation for these differences is found in the deposition process [12]. The optical properties of amorphous silicon are sensitive to preparation conditions and doping with hydrogen, are affected by the amount of disorder in the samples and also by surface conditions and oxide films on the surface. The difference in the $k$ indexes therefore reveals certain inhomogeneity in the deposition process, and might point that more effort in obtaining better layers should be made in the manufacturers side. campo

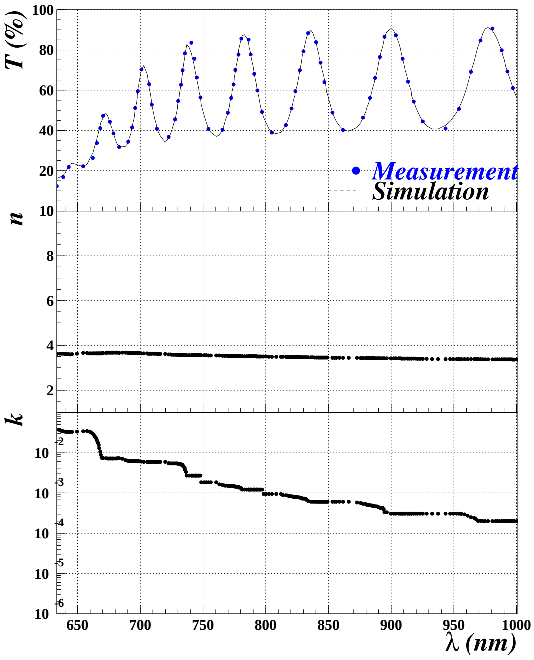


Figure 5.7: *Top: Calculated and measured transmittance for a-Si:H of ≈ 1449 nm + glass system. Middle: refraction index obtained from the calculation. Bottom: absorption coefficient.*

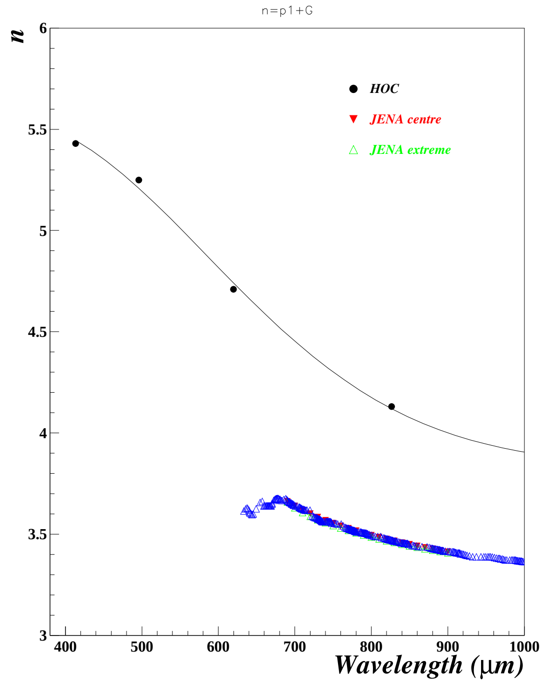


Figure 5.8: *Tabulated values of the a-Si:H refraction index (continuous dotted line). Measured values for the current sample and calculated ones overlap (arrow-heads)*

### 5.4.2 Determination of thickness and optical constants of ITO

In order to obtain the optical constants of the ITO layer, a similar process to that of the a-Si:H is followed. However, there are certain differences with respect to that case. In the ALMY layout, the ITO is a thin layer of ≈ 100 nm with half the value of the refraction index of amorphous silicon (table 1). In order to see at least one maximum at $\lambda$ =500 nm a thickness of ≈ 140 nm is needed. Otherwise there is no room for interference maximums to occur, and the transmittance curve is flat, as it can be observed from figure 5.10 top. As in the latter example, the upper curve shows the computed values (continuous line) for the transmittance, calculated by means of the $(n, k)$ indexes obtained from the measured T values (dots). The indexes are shown in the middle and bottom plots. As there were no external measurements of the ITO indexes, the only cross-check is the calculation of the transmittance itself. The small gaps in some $(n, k)$ are related with the bound conditions, where optical constants are fixed from the beginning.

In the case of the ITO layer the thickness is unknown. An estimation of its value was obtained applying the $\chi^2$ method to the four values of $(n, k, \lambda)$ given in table 1. The value obtained was fixed as the thickness of the ITO layer and the transmittance plus the refraction indexes were calculated. Afterwards, we used this information as input data to recalculate the thickness. The final value obtained was 47.2 nm.

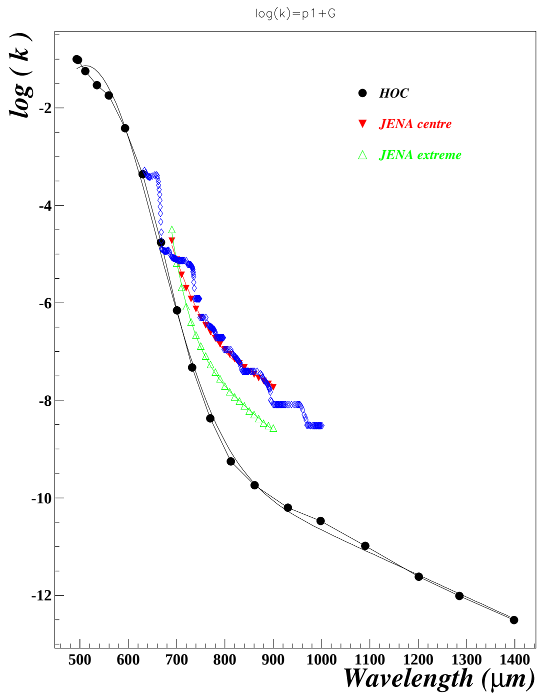


Figure 5.9: *Same as figure 5.8, but relative to the absorption coefficient.*

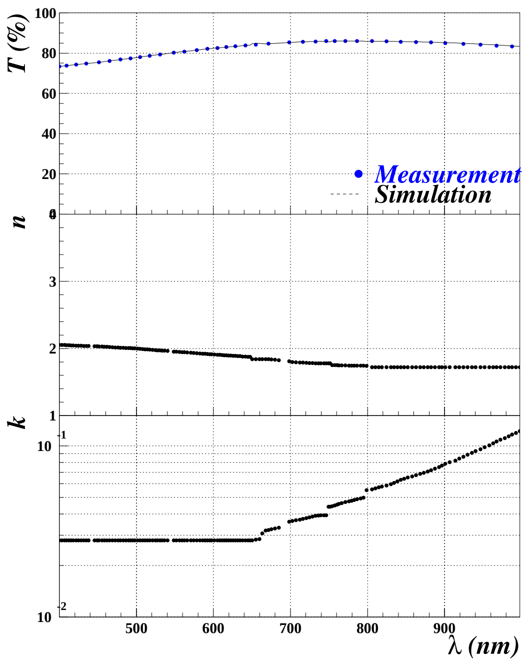


Figure 5.10: *Top: Calculated and measured transmittance for an ITO layer of ≈ 47 nm on glass. Middle: refraction index obtained from the calculation. Bottom: absorption coefficient.*

### 5.4.3 Modeling ITO and a-Si:H indexes

It would be desirable to have dispersion functions describing the already obtained refraction indexes, at least in the region of interest. We have tried to describe the $(n, k)$ indexes in figures 5.8 and 5.9 (and the corresponding ones for ITO −not shown−) in terms of known and simple functions.

Our election has been always to use a straight line fit plus a Gaussian curve, the parameters of these functions being obtained by fits to the calculated indexes. The only exception was the absorption coefficient of a-Si:H which was more accurately described as:

$$\ln k_{a-Si:H} \quad = \quad P_1 + P_2\lambda + G(P_3, P_4, P_5) \tag{5.45}$$

where $P_i$ are the parameters and $G(N, \mu, \sigma)$ is a Gaussian of mean $\mu$, width $\sigma$ and height peak $N$. As an example of the fits, we show in figure 5.11 that used for a-Si:H.

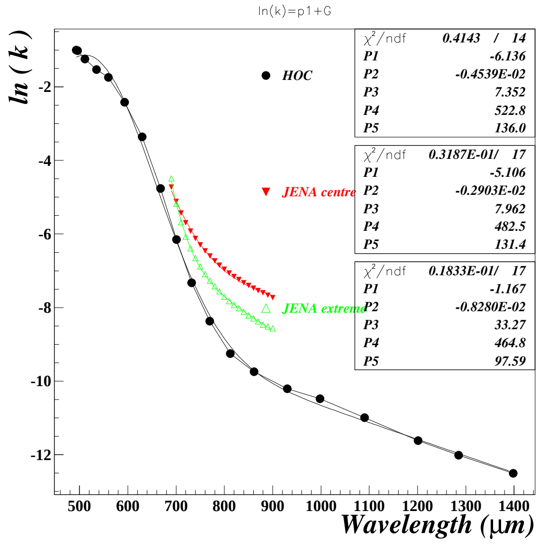


Figure 5.11: *Fits (with values) of the several parameterizations for the $k_{a-Si:H}$ absorption coefficient.*

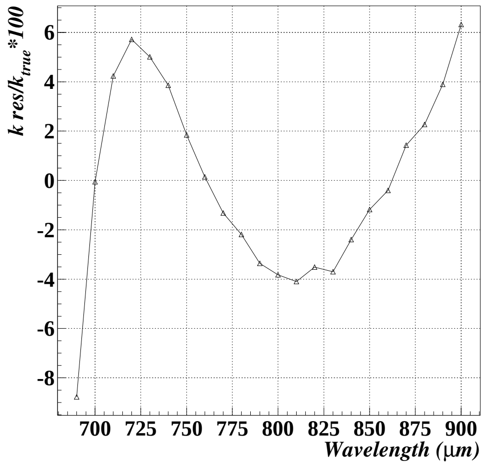


Figure 5.12: *Residuals of the fit shown in figure 5.11 for the measurements taken at the center.*

In fact, this fit is the most limiting one. We show in figure 5.12 the percentage residuals of the fit. It is evident from this plot that the fit performs bad for values of $\lambda \leq 700$ nm. This is not a real drawback for the simulation, since the working wavelength value was 780 nm. From now on we will focus on the region $\lambda \in [700, 900]$ nm.

Some authors choose a different way to solve the problem of finding the optical parameters of a thin film: they postulate a specific function which can describe the refraction indexes and then fit the parameters of the function to account for the measured data [13, 14]. One of these techniques has been applied for the case of the a-Si:H layer (see section 5.7).

## 5.5 T and R for an ALMY sensor

The calculation of the transmittance and reflectance of a multilayer is accomplished by means of equations (5.32) and (5.33). Refraction indexes (wavelength dependent) and the layer thickness are the only parameters of the thin films needed to compute these magnitudes. Unfortunately, these parameters are difficult to obtain, and very often transmittance and reflectance are directly measured and $(n, k, d)$ calculated from them.

In the previous section we have calculated dispersion functions for the refraction indexes of a couple of representative thin film samples. We also obtained functional forms that describe quite accurately those indexes in the wavelength range $[700, 900]$ nm. All this information concerns prompt samples of *pin* devices. Our aim is to reproduce a few measurements of transmittance and/or reflectance of *Schottky-type* sensors.

We have employed the knowledge on individual layers to reproduce the measurements of the whole device. The refraction indexes are introduced in the simulation as functions of the wave-

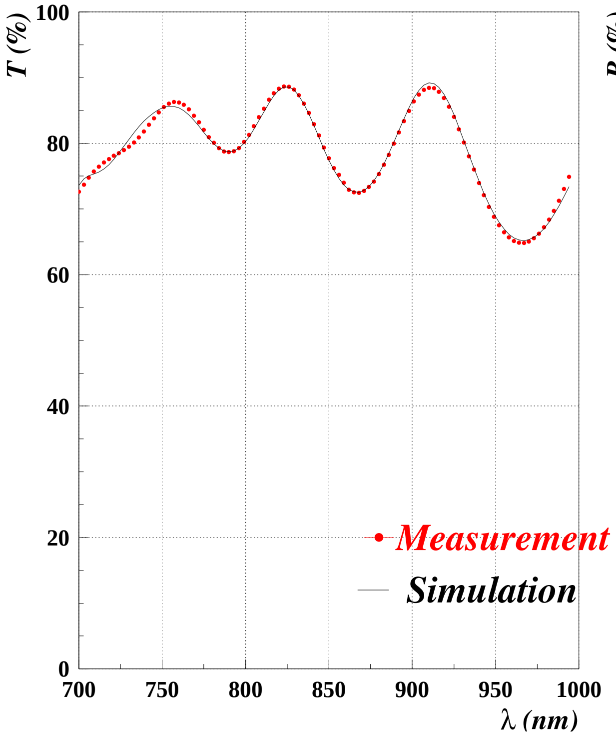


Figure 5.13: *Measured (dots) and calculated (line) transmittance for a Schottky-type sensor.*

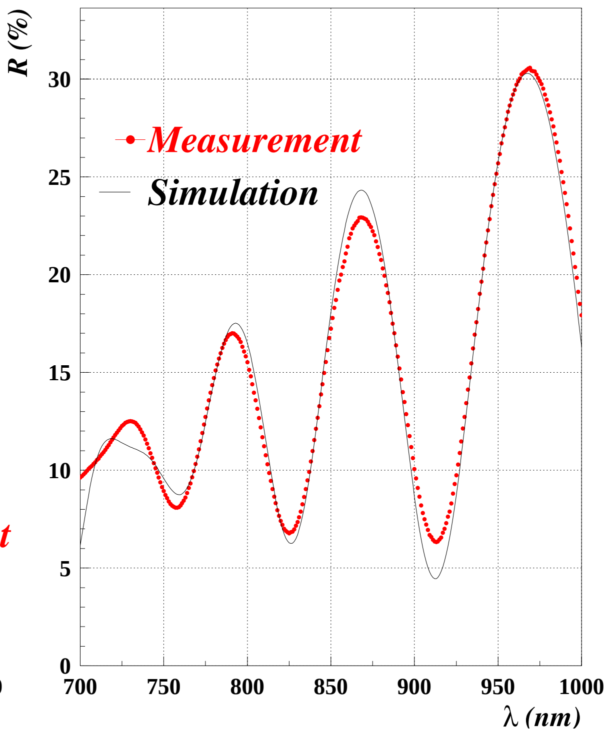


Figure 5.14: *Measured (dotted) and calculated (line) reflectance for a Schottky-type sensor.*

length with their coefficients $P_i$ (see section 5.4.3) as free parameters. Also thicknesses of the several layers are left free. The theoretical function of these variables is minimized with respect to the real data, as in equation (5.44). The values of the parameters calculated for single layers and the nominal thicknesses (100,1000,100) nm are used as starting values for the minimization. In this way, the simulation also produces the refraction indexes which lead to the measured T and R values.

In figure 5.13 we show a transmittance measurement of a Schottky-type sensor drawn with continuous graph, while measured values are shown with full dots. The measured values overlap the curve for almost all wavelengths. A measurement of the reflectance for the same sensor is shown in figure 5.14. The agreement between calculated and measured reflectance is slightly worse. These differences might arise from spatial differences in the transmittance and reflectance measurement regions. In fact, it is not possible to ensure that *exactly* the same part of the sample is measured in transmittance and reflectance, since the spectrophotometers used for these measurements need special accessories for reflectance measurements (see [15] for a review of different measurement methods). The instrument employed for the current measurement was a Perkin-Elmer [16] spectrophotometer.

The dispersion functions of the refraction indexes are shown in figure 5.15. The plot shows from left to right, top to bottom, the refraction indexes and absorption coefficients. The asterisks represent those values used as bound conditions for the single layers. As it happened with the calculated indexes of the a-Si:H, the real part of the refraction indexes is nicely reproduced. However, there is a measurable disagreement between $k$ indexes. As it was explained in section 5.4.1, these differences are expected since the sensors come from different deposition processes. This interpretation is reinforced by the fact that even a measurement of the absorption coefficient in two regions of the same sensor are as different as shown in figure 5.9 or 5.11. The calculated thicknesses for the several layers are ($d_{ITO1}$,$d_{a-Si:H}$,$d_{ITO2}$) $\approx$ (103,1056,73) nm.

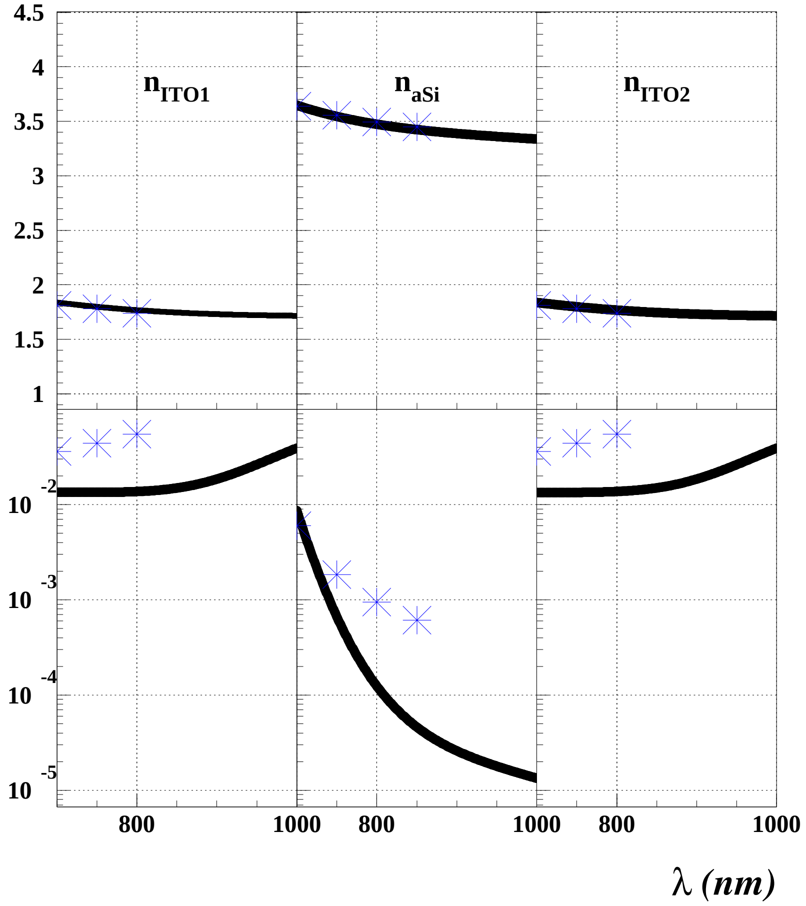


Figure 5.15: *Upper row: refraction index of $ITO_1$, a-Si:H, $ITO_2$. Bottom row: absorption coefficients in the same sequence. Asterisks are single layer indexes.*

As a byproduct of this simulation, we have here a clear evidence that *interferences rule the optical behavior of the sensor* . As it happens with solar cells, an antireflection coating will improve the performance of the device. For solar cells, anti-reflection coatings are deposited to reduce the amount of light lost by undesired reflections. An antireflection coating on the ALMY sensor will improve its performance by eliminating a fraction of the waves traveling back inside the sensor. As shown in chapter 4, implications of the antireflection coating are observed as an improvement of the spatial uniformity and smoothing of the beam transmission figures of the sensor.

## 5.6 ALMY optical optimization

Since the optical path of visible lasers inside the a-Si:H thin layer is comparable to the thickness, the wave interferes with itself. This interference is responsible for the maxima and minima observed in the transmittance curve. The performance of the device shown in figure 5.13 is not specially dramatic: all wavelengths lower than $\approx$ 950 nm have transmittance higher than 70%. An arbitrary or uncontrolled election of the layer thicknesses may lead to differences in transmittance between sensors as high as 35%. Furthermore, in applications where transmittance is a key point an order within the sensor set must be established, leaving sensors with lower transmittance behind those being more transparent. It would be desirable then to optimize the sensor layout in order to homogenize the signal and the transmittance. In fact, there is always a tradeoff between signal collected in the sensor and transmittance.
It is not difficult to attach to the sensor an electronics able to handle currents in the order of $\mu$A. For fine utilization of these devices the thickness of the a-Si:H layer should be chosen to meet the requirement [17]:

$$QE(\lambda) \approx 1/N \tag{5.46}$$

where $QE(\lambda)$ is the quantum efficiency (number of charge carriers collected per incident photon at wavelength $\lambda$) and N is the number of sensors to intercept the same laser beam. This would contribute to get signals balanced among all sensors.

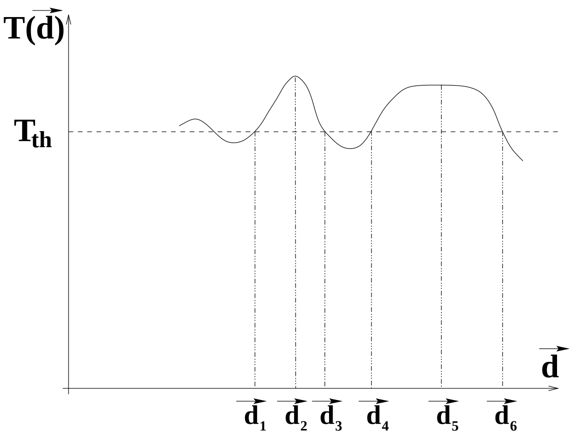


Figure 5.16: *Illustrating the concept of the optimization method. For certain values of the multilayer thickness $\vec{d}$ (see text) we can select wide and flat maxima.*

Once the thickness of the active layer is fixed, those of the remaining layers must be chosen in order to maximize the transmittance. Further refinements, as antireflection coatings, are not studied here since they are not inherent to the basic design of the sensor. Anyway, as it is shown in chapter 4, its utilization improves the performance of the sensor as well as increases its transmittance. If we take into account that all the deposition processes have a certain associated error, the sensor design needs to be specified with certain levels of tolerance in order to keep a constant value of the transmittance for small changes in the layer thicknesses. We have searched for a configuration that produces the maximum transmittance within a moderate wavelength range despite the thickness change. The variables involved in this calculation are the three layer thicknesses and the wavelength range.
Although the thickness of the a-Si:H layer is fixed, we have decided to include it as a free parameter in order to calculate the thickness tolerance of this layer too. As a matter of fact it has been found that the transmittance of the device depends overall on the thickness of the first ITO layer and that of the a-Si:H layer.
The method to find tolerant configurations is illustrated in figure 5.16. The figure shows possible maxima configurations depending on the value of the thicknesses chosen, represented as $\vec{d} = (d_{ITO_1}, d_{a-Si:H}, d_{ITO_2})$. Election of tolerant configurations must sacrifice sometimes high and

narrow maxima ($\vec{d_2} \in [\vec{d_1}, \vec{d_3}]$) against broad and lower ones ($\vec{d_5} \in [\vec{d_4}, \vec{d_6}]$). In this sense, the right maximum in figure 5.16 is preferred instead of the left one. Note that for the case of a single layer the width of the consecutive maxima does not depend strongly on the thickness. In order to locate these flat maxima in a computer program, we impose conditions on the derivative of the maxima searched. The *addition* of the derivatives extended to the requested interval is lower for a flat maximum than for a steeper one. The expression of the derivative of the transmittance with respect to the thickness is:

$$dT = \sum_{i=1}^{3} \left| \frac{\delta T}{\delta d_i} \right| \Delta_i \tag{5.47}$$

with $\Delta_i$ the value of the pursued thickness tolerance. Absolute values of the partial derivatives are taken to avoid a reduction of the derivative with negative slopes. For these kind of multi-variable analysis we use a $\chi^2$ minimization. Proceeding similarly to the case of the $(n, k, d)$ search we will try to minimize the following function:

$$\chi^2 = \sum_{\lambda} [w_1(T(\lambda, d_i) - 1)^2 + w_1 R(\lambda, d_i)^2 + w_2 (\sum_{d_i - \Delta_i}^{d_i + \Delta_i} dT)^2] \tag{5.48}$$

The first two terms are the maximization and minimization of the transmittance and the reflectance, respectively. Third term favors flat maxima, since derivatives are lower for them. The three terms are added in the wavelength range $\lambda \in [770, 790]$, since $\lambda = 780$ nm was the operation wavelength chosen. The optimization starts from the set of thicknesses $\vec{d} = (d_{ITO1}, d_{a-Si:H}, d_{ITO2}) \approx$ (103,1056,73) nm, and searches for tolerant configurations. The resulting set of thicknesses obtained from this process is $(d^{opt}_{ITO1}, d^{opt}_{a-Si:H}, d^{opt}_{ITO2}) \approx$ (109,1113,106) nm. A remark should be set at this stage. Of course, the resultant optimized thicknesses depend on the starting values given. We are always working around the nominal values of the thicknesses (100,1000,100) nm.

### 5.6.1 Calculation of the tolerance

Let us suppose we have a single layer problem. One feasible definition of the tolerance would be the change in thickness leading to a transmittance value below a threshold. In one dimension, the tolerance can be specified as one range of thicknesses. When several variables are added to the problem the definition of the thickness tolerance gets complicated. For instance in figure 5.17 we show level curves where the transmittance of a two layer system takes constant values. The space region where $T \geq 0.79$ is a tolerant region with respect to the thicknesses $d_1$ and $d_2$. Any combination of these two indexes leads to a transmittance value above 0.79.
Our definition of tolerance for multi variable problems will be a rectangular region centered in the starting configuration (drawn with a cross in figure 5.17, where the transmittance value is always above a certain value. In the case of the ALMY system we have arbitrarily selected transmittance to stay above 0.79. It corresponds to the second rectangular area in figure 5.17 (a rectangular-like volume in 3D). In the best case, the calculated area coincides with the tolerant region. Otherwise is a subestimation of the real tolerance region.
The computation of the volume is done by calculation of all the transmittance values resulting after changing the thickness values in one unit. From the central configuration, the volume expands until the limit transmittance for one variable is reached. The overflowing variable is

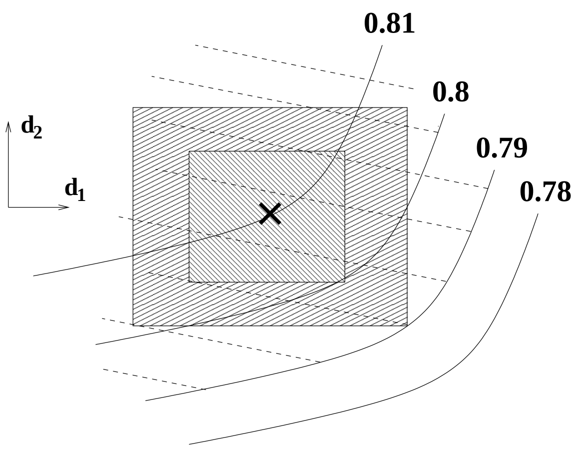


Figure 5.17: *Level curves for a hypothetic 2 variable problem. Shaded area (not enclosed in a box) is a thickness tolerant region. Outer box is our estimation of the real tolerance.*

then constrained to vary within this region while the others are still left free. The search process terminates when there are limits for all variables. Proceeding this way, the following values are found:

$$\begin{aligned} d_{ITO1} &= 109 \pm 12 \text{ nm } (11\%) \\ d_{a-Si:H} &= 1113 \pm 12 \text{ nm } (1.1\%) \\ d_{ITO2} &= 106 \pm 13 \text{ nm } (12\%) \end{aligned}$$

Tolerances like this are easily achieved by normal deposition processes. Any sensor with thicknesses as those defined above has a transmittance greater than 0.79 in the wavelength range $\lambda \in [770, 780]$ nm provided the optical constants of the several materials match those we have used in the simulation. The performance of the central configuration as well as the two extrema is shown in figure 5.18.

## 5.7 Quality check with the envelopes method

Determination of optical constants is an important step in the characterization of absorbing thin films. Besides ruling the propagation in a medium, they are related to the dielectric constant of the material through the expression [3]:

$$N = \sqrt{\mu\epsilon} \tag{5.49}$$

being $\epsilon$ a complex number. Many methods have been developed to determine the optical properties of semiconductor thin films. Some of them use the transmittance T at normal incidence, others the transmittance and reflectance or combinations of them. All of them restrict to the study of a single thin film on a substrate.
The work from Swanepoel *et al* [18] and Tomlin*et al* [19] is pointed out here since they represent very different approaches to the one shown in this chapter. We have performed a comparison with the first of them, since it was specially devised for thin layers ($\approx 1$ $\mu$m) of a-Si:H on glass

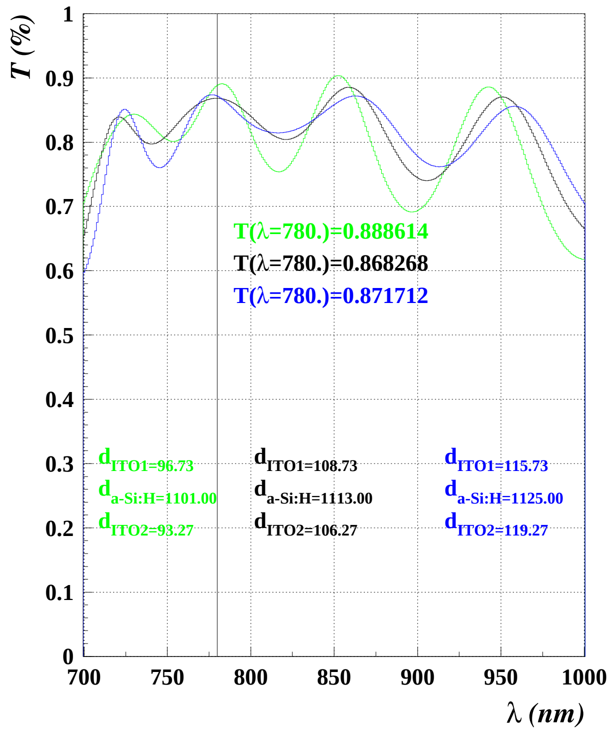


Figure 5.18: *Central and extreme tolerant configurations for the ALMY system. Transmittance is always higher than 0.79 for* $\lambda = 780 \pm 10$ *nm.*

(although the method also works for any thin film showing enough fringes in the transmittance spectra). This work handles information regarding the transmittance of the sample. The upper and lower envelopes rather than the full spectra itself (figure 5.19) are used for calculations. In this method, wavelengths where condition (5.34) is fulfilled have a main role in order to compute the layer thickness, since the aforementioned constraint complements the measured data. Once the $(n, k)$ values are known, an iterative procedure is applied in order to calculate the layer thickness

Following the criteria given by the author, the spectra is divided into three regions. Theoretically, in a layer of a-Si:H of $d_{a-Si:H} \approx 1\mu$m the region of high wavelengths ($\lambda >$ 800 nm for films, roughly), where the value of maxima is constant is called the transparent region. The region for very low wavelengths ($\lambda <$600 nm), where the transmittance reduces significantly is called the region of strong absorption. In between, the medium-weak absorption region stands. Attending to this criteria, we show in figure 5.19 a tentative classification of the spectra.

The author simplifies the expressions of the transmittance assuming very low absorption of the sample for all wavelengths and derives expressions for the refraction index and extinction coefficient in the transparent and medium-weak parts of the spectrum. The region of high absorption is calculated by extrapolation on the latter region, with the subsequent loose of accuracy. In the referred paper, the performance of the method is shown by reproducing the optical constants and thickness of a *simulated* sample. We have programmed this method and trained with the same example. Although we managed to retrieve the same result we failed reproducing our *measured* data.

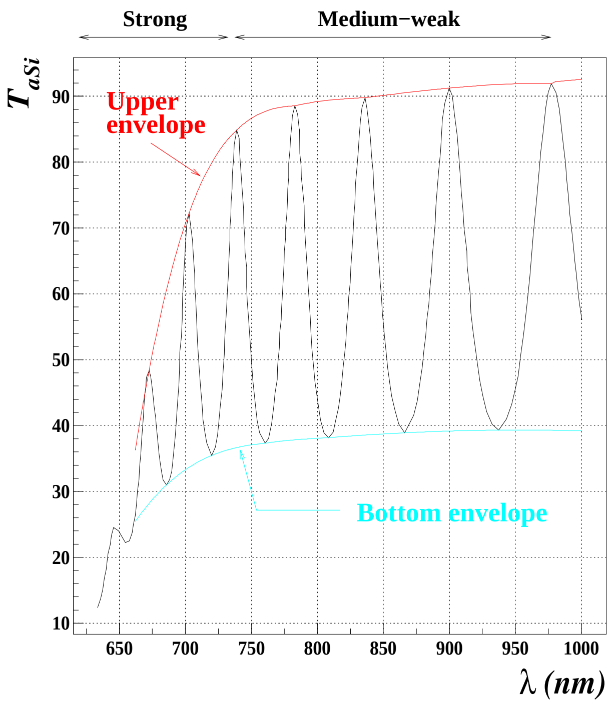


Figure 5.19: *Transmittance spectrum of a sample of a-Si:H of 1448.96 nm on glass. Envelopes of upper and bottom maxima have been calculated. A tentative division of the regions of the spectra (regarding the absorption) has been drawn.*

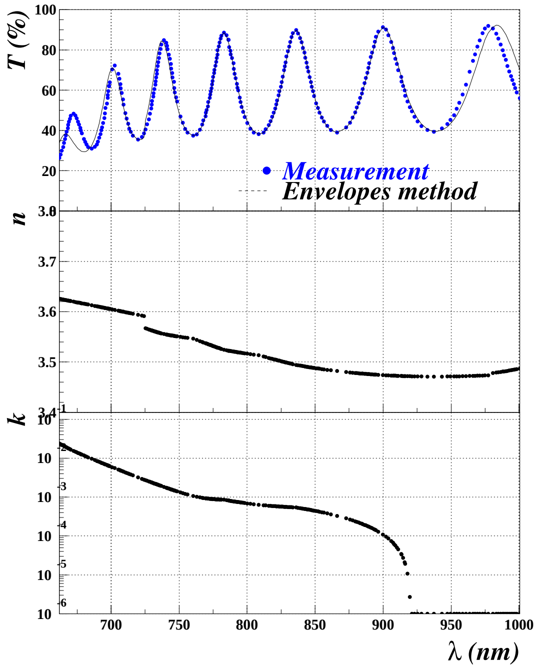


Figure 5.20: *Transmittance (upper plot) measured and reproduced using the envelopes method. Middle: Reproduced refraction index. Bottom: Extinction coefficient.*

Figure 5.20 shows the transmittance, refraction index and extinction coefficient of the sample of a-Si:H measured at the center (introduced in section 5.3). The calculated layer thickness is ≈1555 nm, meaning more than 100 $\mu$m error. In the strong absorption region, the transmittance is badly reproduced due to the error in $n$. The extrapolation has been performed by means of a Cauchy dispersion relation of three parameters, as recommended by the author. For high wavelengths (above 950 nm) the method fails, because of the inefficient reconstruction of the envelope, as shown in figure 5.19. Another maximum above 1000 nm would help to improve the calculated transmittance in this region. The hypothesis of small absorption coefficient is too premature for high wavelengths, and the calculated extinction coefficient drops very fast to zero as may be seen in figure 5.20 bottom.

The goal pursued by this cross-check was to compare the results obtained following the envelopes method [18] with the results obtained applying our method. The expertise and understanding of our $\chi^2$ method is, by far, deeper than the understanding of this method. It is very likely that our computer model of the envelopes method lacks of some fine tuning. Some authors claim that inhomogeneities and surface roughness of thick samples smear the accuracy obtained from the interference extrema [20]. This might be behind the lower accuracy we have found.

# Bibliography


[1] L. Fresnel, H. de Senarmont H and E. Verdet 1866-70, *Oeuvres completes d'Augustin Fresnel (Paris: Imperiale)*

[2] Maxwell JC 1873, *A treatise on Electricity and Magnetism* . First edition published in 1873. The third edition, originally published by the Clarendin Press in 1891, was republished in unabridged form in 1954 (New York: Dover)

[3] Born M and Wolf E 1975 ,*Principles of Optics*, 5th edn (Oxford: Pergamon)

[4] H. A. Macleod, *Thin-film optical filters* , Second edition, Adam Hilger Ltd., Bristol

[5] Reproduced from Peter H. Berning, *Theory and Calculations of Optical Thin Films*, Physics of Thin Films, Academic Press (New York and London)

[6] CSEM SA, Centre Suisse d'Electronique et de Microtechnique, Rue Jaquet-Droz 1 P.O. Box CH-2007 Neuchâtel
http://www.csem.ch/

[7] JENOPTIK Laser, Optik, Systeme GmbH, Göschwitzer Straße 25
D-07745 Jena (Germany)

[8] Centro de Investigación y Desarrollo de la Armada (CIDA), C/. Arturo Soria, 289 28033 Madrid

[9] D. Palik, *Handbook of Optical Constants of Solids*, Edited by Edward Naval Research Laboratory, Washington, D.C. Academic Press, Inc (1985)

[10] MINUIT, Function Minimization and Error Analysis, Version 94.1, F. James. CERN Geneva, Switzerland
(http://wwwinfo.cern.ch/asdoc/minuit/minmain.html)

[11] Taylor Hobson Ltd
http://www.taylor-hobson.com

[12] H. Piller, Department of Physics and Astronomy, Louisiana state University, Baton Rouge, Lousiana. See contribution to [9].

[13] H. W. Veleur, *J. Opt. Soc. Am., 58* (1968) 1356

[14] J. Rivory, *Opt. Commun., 1* (1970) 334

[15] H.E. Bennett, Jean M. Bennett , *Precision measurements in Thin Film Optics*, contributed paper in Physics of Thin Films, Vol. 4 Academic Press (1967)

[16] PerkinElmer Lambda 9. PerkinElmer Analytical Instruments, 761 Main Avenue Norwalk, CT 06859, USA
(http://instruments.perkinelmer.com)

[17] Private communication: J. Cárabe and J.Javier Gandía, CIEMAT. Avda. Complutense, 22. Ed 42, E-28040 Madrid - Spain

[18] R. Swanepoel *Determination of the thickness and optical constants of amorphous silicon*, J. Phys. E 16, 1214-1222 (1983)

[19] R.W.Denton, R.D. Campbell and S.G. Tomlin, *The determination of the optical constants of thin films from measurements of reflectance and transmittance at normal incidence*, J. Phys. D 5, 847-863 (1972)

[20] J.L Hernández-Rojas, M.L. Lucía, I Mártil, G. González-Díaz, J. Santamaría and F. Sánchez-Quesada, *Optical analysis of absorbing thin films: application to ternary chalcopyrite semiconductors*, Applied Optics. Vol. 31, No. 10, 1 April 1992

# Chapter 6

# Measuring the $\phi$ angle in the alignment system of CMS

## 6.1 Introduction

In this chapter we present the devices called tiltmeters. These devices measure an angle with respect to the gravity. In CMS, tiltmeters will appear taking part of a slightly more complex structure, called Laser Level, being the junction of a laser beam, two tiltmeters and one transparent sensor. In the current alignment scheme for the CMS experiment the $\phi$ coordinate will be monitored using Laser Level boxes [1].
Since Laser Levels are composed objects, a calibration of one unit involves a previous calibration of each device independently. The main body of this chapter will be devoted to the tiltmeter calibration. For a study of the associated position sensor, refer to chapter 4.
The tiltmeters will measure the $\phi$ angle with respect to the gravity and will allow to connect the measurements between the Tracker [2] and Muon Chambers Systems [1]. Since Tracker and muon detectors must be aligned with a precision better than 20 $\mu$rad in the bending plane, the angular movements will have to be measured with a resolution better than *15* $\mu$rad.
The tiltmeters investigated in the present work belong to two different firms: Applied Geomechanics Incorporated (AGI) [3] and Advanced Orientation Systems (AOSI) [4]. We have calibrated the output response of tiltmeter sensors against longitudinal tilts and studied the variables affecting their operation. We also show that, an arrangement of two tiltmeters under a certain (measured) angle aids the determination of the angle moved by the structure.
The chapter is organized as follows. Sections 6.2 and 6.3 introduce the tiltmeter principle and the experimental facilities for its calibration. In section 6.4 we present geometrical variables which will influence the behavior of these devices. The calibration of electrolytic tilt sensors is presented in following sections (6.5 through 6.7). Finally the working procedure and first tests on the Laser Level device is presented in section 6.9.

## 6.2 Tiltmeter principle

Tiltmeters or tilt sensors measure tilts with respect to the most stable reference: the vertical *gravity vector*. They measure angular position and rotational movement of the elements to which they are attached.

The highest precision is obtained by electrolytic tilt sensors. Their operation is based on the fundamental principle that an enclosed bubble, suspended in a liquid, will always orient itself perpendicular to the gravity vector. The bubble (see figure 6.1) is allocated in a liquid-filled case, with three electrodes. When an AC voltage is applied across the two excitation electrodes, the AC output measured at the central pick-up electrode changes as a function of the tilt angle. In the case of the AGI sensors, the conversion of AC output current to DC current is obtained by means of Signal Conditioning Units (SCU). An adequate SCU can be purchased together with each equipment. The SCU from AGI is capable of handling a couple of tiltmeters while measuring the electronics temperature. The sensors are shipped with a 4.5 m long connection cable although we have successfully used the sensors with 50 m long cables. The manufacturer reports operation of the sensors with cables up to 100 m.
AOSI sensors, however, come with a much smaller but nearby electronics module. Each module addresses one sensor. Temperature value and remote operation of the sensors is available upon request.
Table 1 summarizes nominal features of both brands of sensors.

| | Working Range (degrees) | Resolution ($\mu$rad) | Repeatibility ($\mu$rad) | Linearity ($\mu$rad)@1deg | Temperature change |
|---|---|---|---|---|---|
| AGI | $\pm 2$ | 1 | 5 | N/A | +0.05%/C |
| AOSI | $\pm 3$ | 2 | <5 | 88 | NR |

Table 1: Nominal characteristics reported by AGI and AOSI manufactures. N/A means not available. NR not reported.

## 6.3 Calibration setups

Sensors from two different manufacturers were tested. AGI sensors were calibrated twice, each time with different setups. The time difference between both calibrations was three years (measurements taken during 1997 and 2000). AOSI sensors were scanned once (2000).
The first scan of AGI sensors took place at CIEMAT (Madrid). A picture of the setup employed may be seen in figure 6.2. A mechanism providing rotations of the order of the microradian is necessary to cope with the accuracy of the tiltmeters in test. We used a 450 mm long arm tripod which can be moved (by one of its ends) in steps of 0.5 $\mu$m (that is $\approx 1\mu$rad). The tripod sustains on three knobs that can be moved independently. A sketch of this structure is shown in figure 6.3. While studying longitudinal tilts, the sensors are placed along the longest arm. For transversal tilts the sensors are placed orthogonal to the longest arm. In any case, the knob called 'A' (see figure 6.3), will be the only one manipulated. The sensors (see figure 6.4) are screwed on a platform, which is the interface with the tripod. The knob 'A' tilts the tripod along the Z axis (axis definition is in figure 6.3). The Z displacement is measured by a length gauge Heidenhain [5] with a resolution of 0.5 $\mu$m. The theoretical angular resolution under this configuration is 1 $\mu$rad.
The tripod, platform and sensors were placed on a stable bench in the basement of a building in order to minimize any disturbing motion. To avoid any scratch of the bench, the knob sits on commercial Kennametal [6] 'pills'. These basis are smooth at the $\mu$m scale, but the bottom

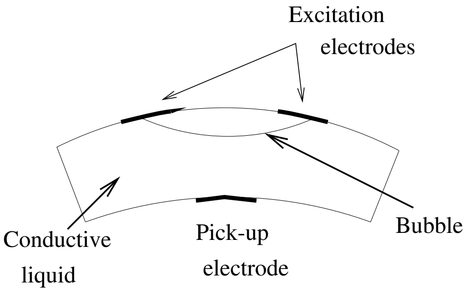


Figure 6.1: *Schematic structure of a tiltmeter.*

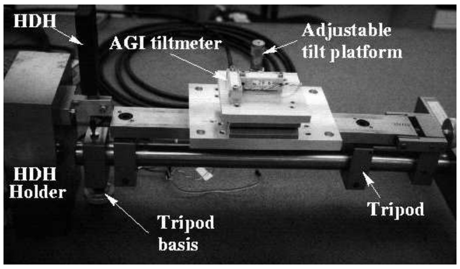


Figure 6.2: *Picture of the AGI calibration setup. A couple of independent tiltmeters are orthogonally screwed to a tilt platform on top of the tripod. The angle moved is measured by means of a length meter gauge, rigidly attached to a massive holder.*

and upper sides are not necessarily parallel. The temperature of the laboratory was kept around 20±2°Celsius (air conditioned room).
The second calibration of AGI sensors, and the calibration of AOSI devices was carried out in the HEP laboratory at Cantabria University. Instead of using a tripod, the sensors were screwed on a two degrees of freedom platform. This platform produces tilts along two perpendicular directions. The platform was fixed on top of a massive granite bench. The angle tilted by the platform was measured by means of an ALMY sensor (chapter 3). In order to avoid corrections of the deflection angle, the sensor was alternatively shifted between two sockets. The angular resolution obtained amounts $\approx 5\mu$rad.

## 6.4 Definition of the tilts

Tiltmeters are 1D sensors. This means that they are intended to measure tilts along one direction. In an external frame (the vertical axis defined by the gravity vector −see figure 6.6.a−) one measures tilts *around* the Y axis, or equivalently, *along* the X axis. The calibration of a tiltmeter consists in finding the relationship between the angle moved in the ZX plane (see figure 6.6.b) and the voltage measured by its electronics.
In practice it is almost impossible to achieve in the laboratory a pure rotation around the Y axis. Instead, the orientation of the real rotation axis may even be out of the XY plane. Let us first consider the most propitious case: the direction of the tilt axis belongs to the XY plane but it slightly differs from the Y axis.

### 6.4.1 In plane Rotation axis

As the gravity only defines the vertical axis, we can always rotate the XY frame in order Y axis and the rotation axis overlap. In such a coordinate system the tiltmeter will not be located along the X axis anymore, but will be misaligned. The misalignment $\epsilon$ is measured from the rotation

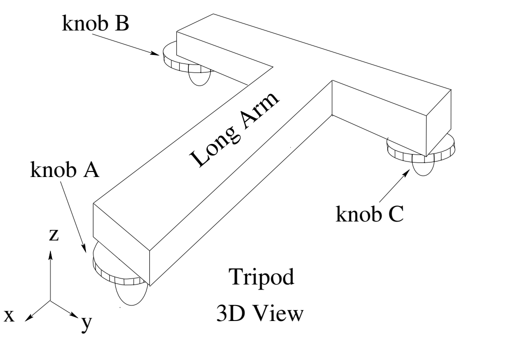


Figure 6.3: *Notation employed for the tripod elements and tripod axis frame.*

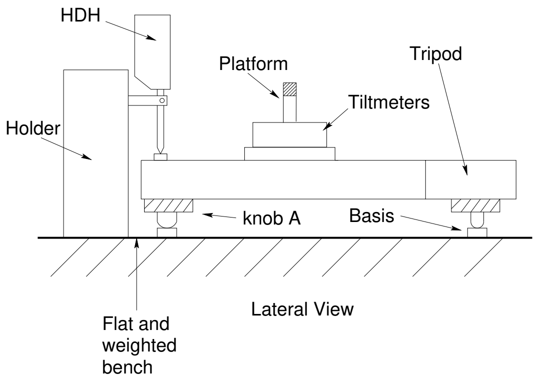


Figure 6.4: *Lateral view of the bench, tripod, tiltmeters and Heidenhain setup. The Heidenhain is supported by a heavy holder, to ensure it does not move when the tripod tilts.*

axis. The angle $\epsilon$ is depicted in figure 6.7, as the angle between -Y axis and the tiltmeter, represented by the vector $\vec{v}$. In this figure, the platform is represented by a tilted plane $X'Y'$, the tilt angle being $\theta$. In figure 6.7, primed axis are defined in the platform system, tilted an angle $\theta$ away from the frame referred to gravity (XYZ).
Sometimes, the sensor may be consciously lifted in order to get a non-negligible signal. This is useful to study the effect of a transversal tilt on the sensor response. The lifted angle is represented in figure 6.7 by $\gamma$ (implicitly assuming that $\alpha$ and $\gamma$ are both in the $Zv$ plane). The angle of the tiltmeter with respect to the gravity is the angle between the Z axis and vector $\vec{v}$ (assuming $\gamma = 0$). In what follows, the complementary angle $\alpha$ will be employed as the *angle measured by the tiltmeter*. Figure 6.7 indicates that the angle measured by the tiltmeter just coincides with *the real angle moved by the structure* (angle $\theta$), for $\epsilon = \pi/2$. For a fixed $\theta$, the angle measured by the tiltmeter varies between $\alpha = 0$ arc degrees (for $\epsilon = 0$) and $\alpha = \theta$ ($\epsilon = \pi/2$). The magnitude of the difference $\alpha - \theta$ will define the precision of the measurement. In figure 6.8 we show the difference between both angles, as a function of the misalignment. It is clear that, in order to get an error lower than 15 $\mu$rad in the calculation of angle $\theta$, we should know the misalignment better than $\approx$4 arcdeg. Reciprocally, provided the misalignment is smaller than 4 arcdeg, the contribution to the measurement error keeps bellow 15 $\mu$rad (without considering internal error contributions from the tiltmeter itself).
The angle measured by the tiltmeter may be calculated from figure 6.7 to be:

$$\alpha' = \alpha + \gamma = \arcsin(\cos\gamma \cdot \sin\epsilon \cdot \sin\theta + \sin\gamma \cdot \cos\theta) \tag{6.1}$$

A tiltmeter calibration consists in finding the relationship between output voltage and angle moved. The response of the sensor will be fitted to a polynomial in $\alpha$ (or $\alpha'$). When using the above expression for the angle, there is no need to sort tilts as longitudinal or transversal. Instead they may be considered as tilts with bigger or smaller misalignment. Anyway, when the

Figure 6.5: *Second setup employed for calibrations of tiltmeters. ALMY sensors equipped with special mechanics for reference network, receive the beam from the tiltmeter support structure (in the background).*

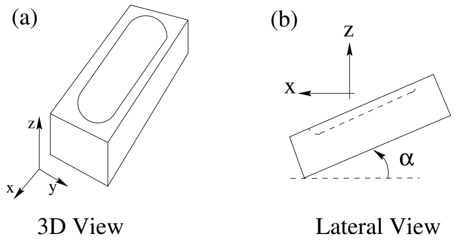


Figure 6.6: *In a tiltmeter: a) Axis definition for the tiltmeter. b) Lateral view for a pure longitudinal tilt.*

sensor is perpendicular to the tilting axis ($\epsilon \approx \pi/2$) we will refer to a longitudinal calibration. If the sensor lays along the tilt axis we will call it transverse calibration.

### 6.4.2 Off plane Rotation axis

In the above discussion, the rotating axis is assumed to be contained in a plane perpendicular to the gravity vector. In the most general situation, the rotation axis will not coincide with this direction but will be located out of the XY plane, that is it will be off-plane. In this case, the election of Euler angles aids the parametrization of the tilts involved. In figure 6.9, we represent the XYZ frame (Z is parallel to the gravity vector) with respect to which the tiltmeter response is measured. A generic rotating axis $X'$ is drawn. It is consciously made to coincide with the X axis of a system characterized by its Euler angles ($\phi$,$\psi$,$\chi$). The tiltmeter is again substituted by a vector $\vec{v}$, deviated $\epsilon$ with respect to the rotation axis and lifted $\gamma$ above the $X'Y'$ plane (not drawn for the sake of simplicity). Expressing $\vec{v}$ and the director cosines $\hat{x}'\hat{y}'\hat{z}'$ in the $XYZ$ frame, and calculating the scalar product $\vec{v}\hat{z}$ we obtain the expression of the angle $\alpha$ for the off-plane rotation axis.

$$\alpha' = \arcsin(\cos\gamma \cdot \sin(\epsilon + \psi) \cdot \sin(\chi + \theta) + \sin\gamma \cdot \cos(\chi + \theta)) \tag{6.2}$$

The expression above does not depend on the $\phi$ angle, which means that a rotation around Z, keeping the other angles fixed, will not change the angle between $\vec{v}$ and Z.
As a particular case of equation (6.2), the configuration ($\phi = 0$,$\psi = 0$,$\chi = \theta$) produces the same result as equation (6.1). Assuming the orientation of the rotation axis is given by ($\phi_0$,$\psi_0$,$\chi_0$), we obtain the final expression for the angular response of the tiltmeter:

$$\alpha' = \arcsin(\cos\gamma \cdot \sin(\epsilon + \psi_0) \cdot \sin(\chi_0 + \theta) + \sin\gamma \cdot \cos(\chi_0 + \theta)) \tag{6.3}$$

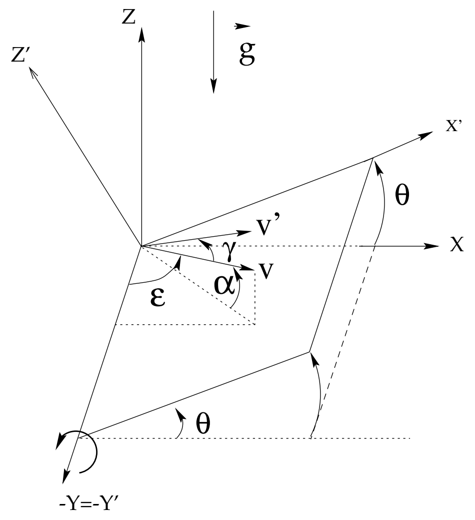


Figure 6.7: *Angular definitions when the rotation axis (Y') belongs to plane XY. $\theta$ is the angle moved by the structure, $\alpha$ is the angle measured by the tiltmeter and $\epsilon$ is the misalignment of the sensor. For pure longitudinal tilts, $\epsilon$ should be 90 degrees.*

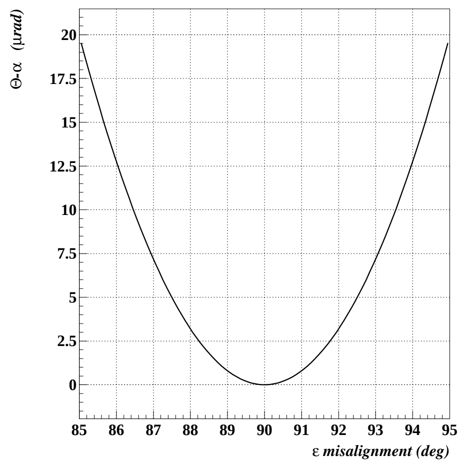


Figure 6.8: *Difference between the angle moved by the platform and angle measured by the sensor, as a function of the misalignment.*

### 6.4.3 Note on absolute values of the angle

During the manufacturing process, once the case of the sensor is built, it has to be placed inside the metal housing. As it is impossible to accommodate the case perfectly level, it will keep an offset called *tiltmeter bias*. Knowledge of the tiltmeter bias is important while computing absolute values of the angle.
As it is explained in the tiltmeter technical documentation [7], the bias can be obtained measuring the output of the sensor in two mirrored positions (rotation by 180 degrees the Z axis). Rough measurements of the bias ($B_i$) of the two AGI sensors were measured to be: $B_1 = (-458.1 \pm 23.1)$ $\mu$rad and $B_2 = (1.5 \pm 0.1)$ mrad. These values are certainly much higher than values reported by the manufacturer ($B \leq 100$ $\mu$rad) [8].
For the calibrations presented in this work, we have ignored the tiltmeter bias and have calculated the variation of the output voltage with respect to the position $V = 0$ mV. Polynomial coefficients do not change their value by this election.

## 6.5 The tiltmeter equation

As it was said before, tiltmeters are 1D sensors. The aim of our tests is to obtain calibrations of these devices. A calibration of a tiltmeter consists in finding the relation between the output voltage and the angle moved. Under a longitudinal tilt, tiltmeters from AGI and AOSI firms

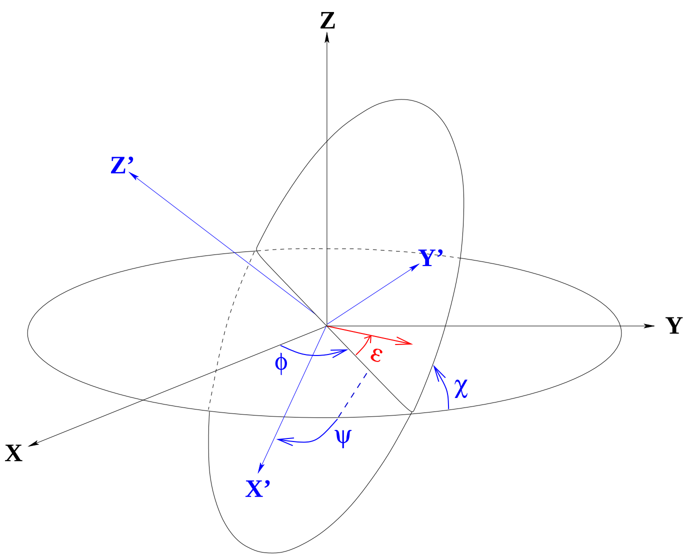


Figure 6.9: *Angular definitions for a rotation axis out of the XYZ plane. The new rotation axis X', can be conveniently defined as a function of Euler angles.*

have been measured. Each measurement has been repeated at least four times.
We started the operation (see figure 6.7) by finding the position corresponding to a zero value for the output voltage. From that point we tilted the sensors from -0.3 to +0.3 degrees recording the output voltage and the Heidenhain value (first AGI calibration) or the angle measured by the ALMY sensors (second AGI calibration and EZ calibration) at each step.
No wedges were used for the measurements. $\gamma$ is then equal to 0 in equations (6.1) or (6.2), and then:

$$\alpha' = \alpha = \arcsin(\sin\epsilon \cdot \sin\theta) \tag{6.4}$$

The angles $\alpha$ and $\theta$ coincide only for $\epsilon = \pi/2$.

### 6.5.1 No misalignment considered

One typical example of the sensor response (in Volts) as a function of the $\theta$ angle (in degrees) moved by the tripod is shown in figure 6.10 top. It corresponds to one of the calibrations for sensor number 1.
Data points were fitted (full line in figure 6.10 top) to

$$V = V_0 + k \cdot \alpha + k' \cdot \alpha^2 \tag{6.5}$$

with $\epsilon = \pi/2$ in equation (6.1)
We found

$$V_0 = \quad 1.0 \quad \text{mV}$$

$$\begin{aligned} k &= -3.9008 \quad \mathrm{V/deg} \\ k' &= 0.0296 \quad \mu\mathrm{V/deg}^2 \end{aligned}$$

The constant term $V_0$ corresponds to the output voltage obtained for an arbitrary zero defined in our setup. The linear term is the dominant one. Once the position of the electrodes on the platform is known, the sign of the slope indicates the sense of the tilt. The quadratic term is a correction to decrease the RMS of the residuals, increasing the precision.

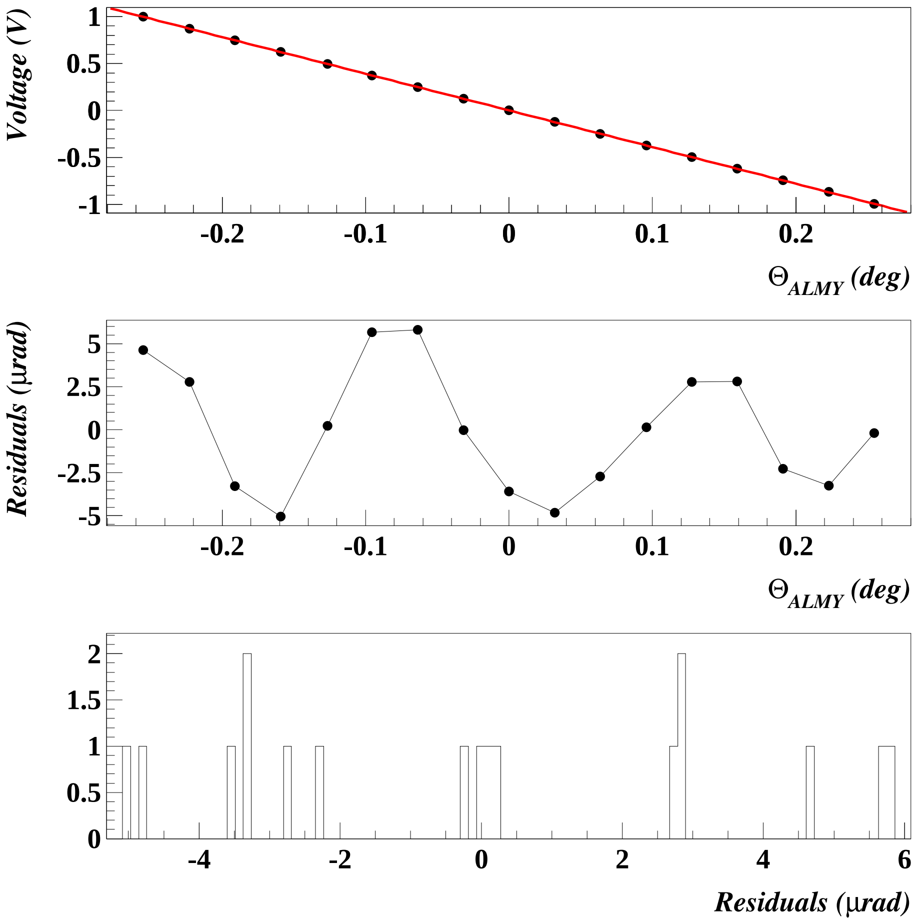


Figure 6.10: *From a longitudinal measurement: a) Output voltage as a function of the tilt fitted to a quadratic polynomial. b) The residuals from the fit as a function of the tilt. c) The distribution of the residuals.*

The spread of the residuals (in $\mu$rad) is shown in figure 6.10 middle and distributed in figure 6.10 bottom. It shows a RMS of 3.4 $\mu$rad.
The measurements were repeated four times. The stability of the several measurements is shown in figure 6.11. Mean values and standard deviations found for $V_0$,$k$ and $k'$ are:

$$V_0 = \quad (0.6 \pm 0.6) \quad \mathrm{mV}$$

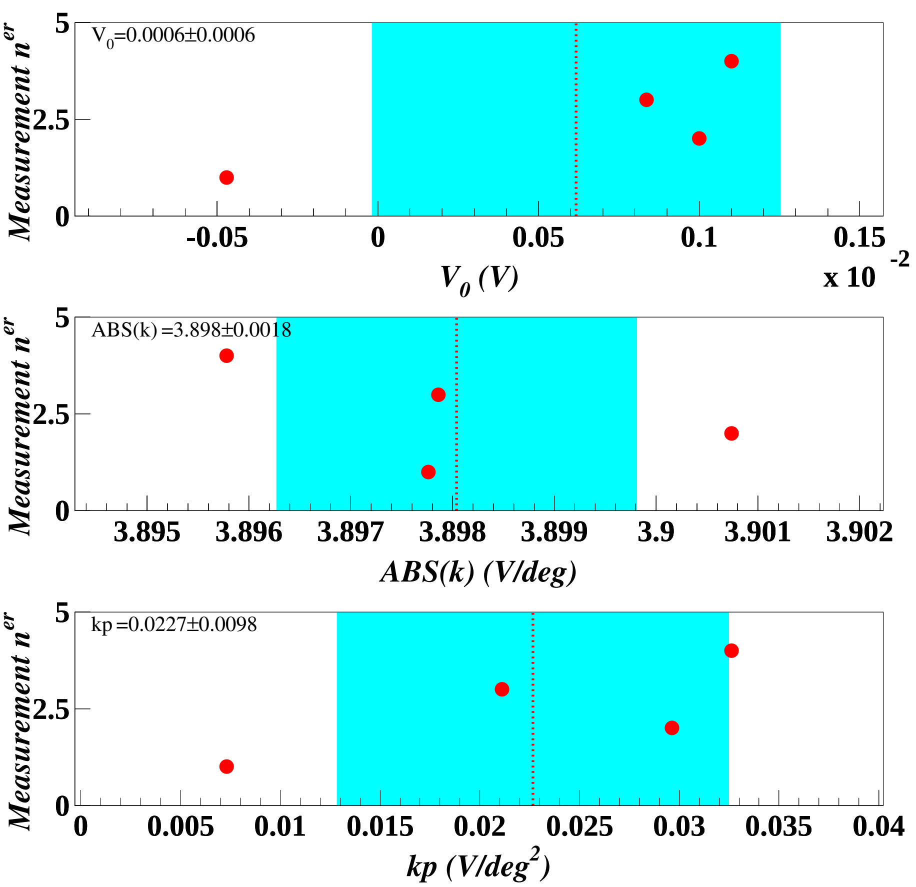


Figure 6.11: *For the four measurements carried out (see text): a) tiltmeter offset, b) linear factor and c) quadratic term. The global average is the dotted line and the shaded area is the global RMS.*

$$\begin{aligned} k &= \quad (-3.8980 \pm 0.0018) \quad \mathrm{V/deg} \\ k' &= \quad (0.0227 \pm 0.0098) \quad \mu\mathrm{V/deg}^2 \end{aligned} \tag{6.6}$$

The distribution of the residuals (in $\mu$rad) for the four measurements, given in figure 6.12, shows a RMS of 3.3 $\mu$rad. This corresponds to the measured resolution for sensor number 1.
The four measurements done for sensor number 2, employing a quadratic expression, give a RMS for the residuals of 6.4 $\mu$rad. Raising one order the degree of the polynomial, the RMS decreases to 4.3 $\mu$rad. This corresponds to a lower quality construction for sensor number 2.
The decision on the degree of the fitting polynomial is done employing an iterative method. Once average parameters of the polynomial are obtained, we consider them as the calibration parameters of the sensor. Then, each independent measurement is fitted using these parameters and the residuals are calculated. In case that the RMS of the residuals amounts more than 5 $\mu$rad, the polynomial degree is increased and the process repeats again. The process stops whenever residuals are smaller than 5 $\mu$rad or a minimum value is reached. According to it, we have calculated that sensor called AGI1 is accurately parametrized using a second order polynomial, while sensor AGI2 needs a cubic expression. In any case, we are looking for **linear**

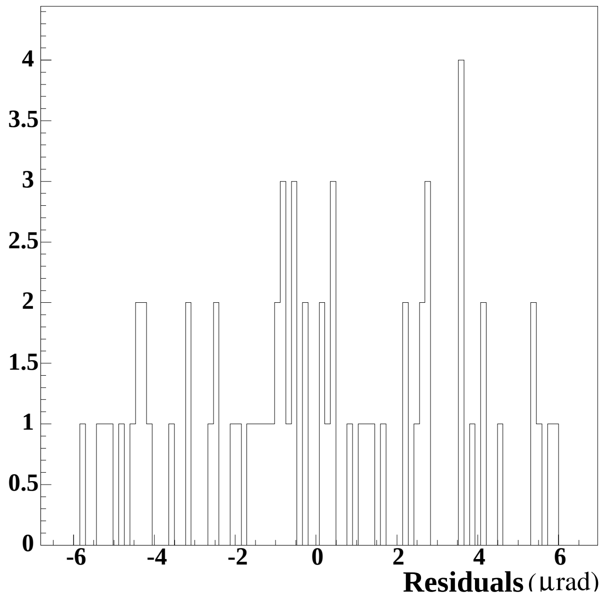


Figure 6.12: *Projection of the residuals of a quadratic fit for sensor 1 (four experiences) discarding the $\epsilon$ contribution to the output potential.*

tiltmeters in the range $\approx \pm 0.3$ arcdeg.

### 6.5.2 Considering misalignment

Up to here, $\epsilon$ was considered equal to $\pi/2$ in equation (6.1). We have repeated the analysis leaving $\epsilon$ free in the fits. The reproduction of the data is equally good in terms of the $\chi^2$ and the RMS of the residuals for the full set of fits.
For sensor number 1, the mean values found were

$$\begin{aligned} V_0 = & \quad (0.6 \pm 0.9) & \mathrm{V} \\ k = & \quad (-3.9151 \pm 0.0038) & \mathrm{V/deg} \\ k' = & \quad (0.0236 \pm 0.0045) & \mu\mathrm{V/deg}^2 \\ \epsilon = & \quad (84.7 \pm 0.6) & deg \end{aligned} \tag{6.7}$$

From the fitting point of view there is no difference between both descriptions of the data, with $\epsilon$ equal or not to $\pi/2$. The calculated misalignment makes the difference. For the maximum expected longitudinal tilt (0.3 deg.) the difference in the fitting parameters leads to an error in the determination of the real angle of about 20 $\mu$rad, which is out of the allowed error for the measurement of the $\phi$ angle in CMS. The alignment of the sensors with respect to the tilt axis is then a crucial issue. An unknown misorientation of a few degrees will avoid to obtain the needed precision.

### 6.5.3 Non-Unicity of the solution

The measurements presented in the former section have shown that the misalignment between the rotation axis and tiltsensor is a critical variable which may determine whether the angle measured by the tiltsensor is the angle moved by the structure. Employing equation (6.1) we have estimated that this misalignment between rotation axis and tiltmeter internal axis might be about 85 degrees. We may wonder whether this calculated value is meaningful or if it is just a mathematical solution of the problem. The complexity of equation (6.1) can lead us to inquiry whether there is more than one set of parameters that fulfill the equation.
We have recalculated the fitting parameters (6.7) for different *starting values* of the misalignment angle ($\epsilon_0$) needed in the fit. The result is shown in figure 6.13 for a set of measurements. We represent, as a function of $\epsilon_0$, the value of $V_0$, $k$, $\epsilon$ and the residuals of the quadratic fit. The left axis refers to the value of these magnitudes (filled circles). Each point summarizes 4 measurements. Therefore, in the right axis, we show the RMS of the values (empty circles). Consequences are clear: depending on the starting value of the misalignment angle we calculate different values of the scale factor $k$ and the misalignment $\epsilon$. Both variables, $k$ and $\epsilon$ are highly correlated. The calculated correlation coefficient for this measurement is -0.954.

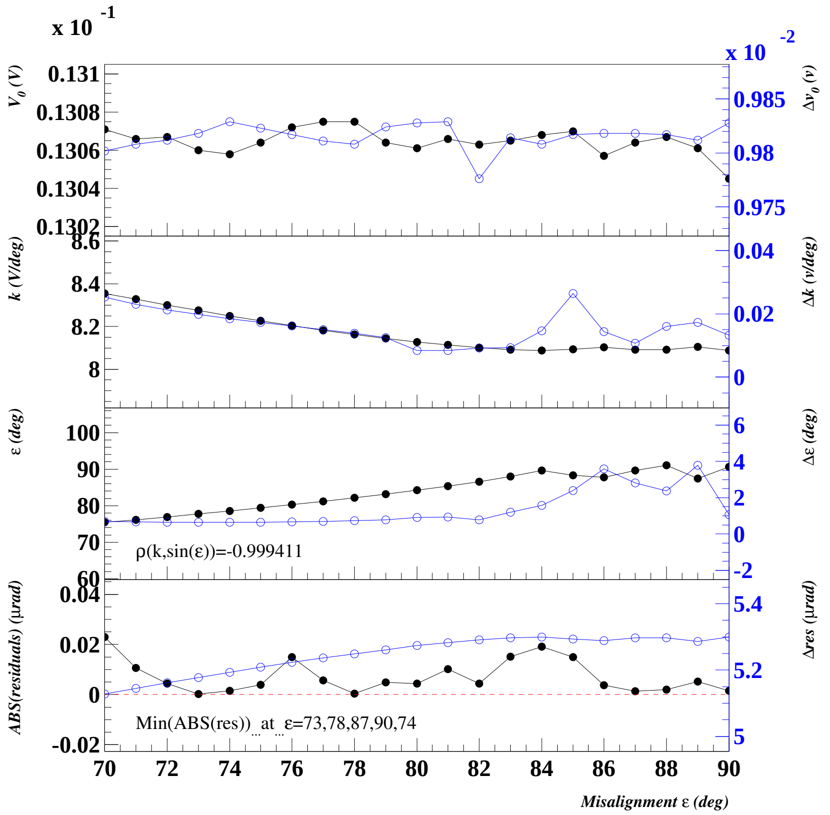


Figure 6.13: *Voltage at zero angle, scale factor, misalignment and residuals from fit to a quadratic polynomial, as a function of the initial value inferred for the misalignment. Left axis (filled circles) refers to average values of the magnitudes. Right axis refers (empty circles) to the RMS.*

The correlation can be understood expanding the value $\alpha$ into series of powers. In the interval

$[-0.3, 0.3]$ degrees, $\sin\theta = \theta$. Since $|sin\epsilon| < 1$, then:

$$\alpha = \arcsin(\sin\epsilon \cdot \sin\theta) \approx \sin\epsilon \cdot \theta \tag{6.8}$$

$$\arcsin\alpha \approx \sin\epsilon \cdot \theta \tag{6.9}$$

Therefore:

$$V \approx V_0 + k \cdot \sin\epsilon \cdot \theta + k' \cdot \sin^2\epsilon \cdot \theta^2 \tag{6.10}$$

Depending on the starting value of the parameters, we can find many pairs $(k, \epsilon)$ such that the above condition is fulfilled. Equation (6.10) shows why a fit to $k$ and $\epsilon$ independently will not lead to the real value of both magnitudes, *unless one of them be known in advance.* This equation clearly shows that a fit to the output of the sensor discarding the misalignment (or reciprocally, considering $\epsilon = \pi/2$) will underestimate the real value of the slope $k$ by a factor $\approx \sin\epsilon$. This statement can be verified using the set of parameters 6.7. The value of $k \cdot \sin\epsilon = -3.8984$ V/deg coincides with the fitted slope $k$ =-3.8980 assuming no misalignment (parameters set 6.6).
Theses facts show that, in order to obtain the calibration parameters of the sensor, either an external measurement of the misalignment or an independent measurement of the scale factor are needed. Fortunately, the manufacturer provides the scale factor (which we call $k_{true}$) for the sensors. We were informed that the calibration of the sensors is done in such a way that the uncertainty in the misalignment angle is less than 1 arcdeg [9]. Therefore, angle $\epsilon = 90 \pm 1$ arcdeg. The effect of this misalignment in the slope value is negligible: $\leq 1$ $\mu$rad in 0.3 arc deg.

### 6.5.4 Tiltmeter hysteresis

The hysteresis is the dependence of the output signal, after transients have decayed, upon the history of prior inputs and the direction of the current traverse. Hysteresis, for tiltmeters, comes mainly from two different sources: the sensor itself and the mechanics employed for calibration. Regarding the sensor, the viscosity of the liquid avoids a perfect symmetry in the response after a change in the tilt sense.
In figure 6.14 we represent, for AGI sensor number 2, the residuals of a parabolic fit, as a function of the angle moved. The measurement corresponds to a tilt from 0 to 0.3 deg, noted in the figure as "First travel", followed by a backwards tilt from 0.3 to -0.4 deg (second travel). It is clear that the residuals do not overlap, meaning that the drift of the bubble was not be reversible. The scan finishes after retrieving the starting point with a tilt from -0.4 up to 0 deg (third travel).
At this stage, there are two options. Either:

- One considers the effect on figure 6.14 is due to the hysteresis and takes it into account. Then the scans are split into travels. For instance, a scan as that explained above is broken into three individual scans and fitted *independently.* In this way, the dependence on the tilt history is broken. The parameters of the fitting functions are calculated as the average of the individual runs.

- the hysteresis is neglected and the multiple scan is studied as a whole. Then one fit is employed for the whole measurement.

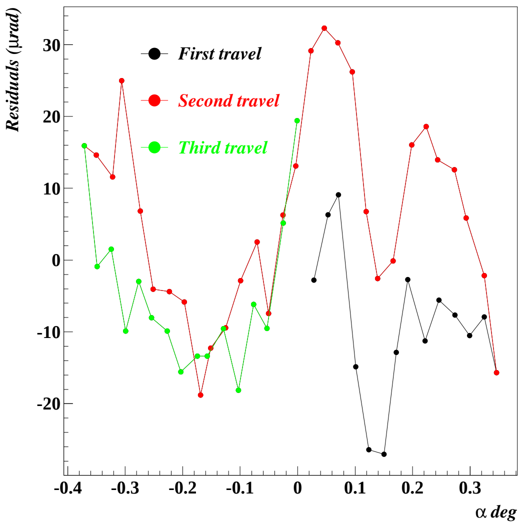


Figure 6.14: *Likely manifestation of a hysteresis effect of the tiltmeter plus platform hysteresis: residuals of three consecutive tilting sequences. Each travel is fitted independently of others.*

The best solution depends on the magnitude of the residuals which, as we will show, is directly related with the quality of the tiltmeter. A decision on these tiltmeter hysteresis will be done in section 6.6.1.

## 6.6 Longitudinal calibration of tiltmeters

In this section we show the results of the *calibration* of the several tiltmeters. Three different fitting functions are tested:

1) A polynomial in $\theta$, P($\theta$), discarding any misalignment on/off plane.

2) A polynomial in $\alpha$, P($\alpha$), having the misalignment $\epsilon$ into account. The starting value $\epsilon_0$ for $\epsilon$ being somewhat arbitrary.

3) A polynomial in $\alpha$, P(Euler), using the information of EULER angles.

$\theta$ and $\alpha$ were previously defined in section 6.4. As explained in section 6.3, AGI sensors were measured twice with different setups. The set of measurements CIEAGI1, CIEAGI2 refer to measurements done using the setup with the tripod. These measurements contain no change in tilt sense. AGI measurements without prefix “CIEand AOSI measurements employed transparent sensors to report the calibration angle. There are two changes of tilt sense in these measurements. Typically, the sequence was:

1) Tilt from 0 to 0.3 deg (first travel)

2) Tilt from 0.3 to -0.3 deg (second travel, first change of tilt sense).

3) Tilt from -0.3 to 0 deg (third travel, second change of tilt sense).

Those measurements containing tilt sense changes will be studied twice: one ignoring the tilt sense and the other splitting the several travels. This will help us to take a decision on the hysteresis.
Foreseeing that the hysteresis may depend on the tilt sense, we further classified the tilts with the suffix (+,-) attending to the sign of the slope output signal with tilt angle. Table 2 summarizes the notation and conditions for each measurement.

| Label | Description |
|---|---|
| CIEAGI[1.2] | Employed tripod<br>One travel<br>Negative slope |
| AGI[1, 2]- | Negative slope<br>Three travels |
| AGI[1, 2]+ | Positive slope<br>Three travels |
| AGI[1, 2] | Positive and negative combined. Considered as one travel |

Table 2: Measurement notation

### 6.6.1 Analysis of the calibrations

As explained during this chapter, tiltmeters measure an angle with respect to gravity. The misalignment of the device makes the angle measured to be different from the real angle moved by the structure to which the tiltmeter is coupled. A calibration of a tiltmeter is done by tilting the sensor a known quantity. The output voltage of the sensor is then fitted to a mathematical function.
Figure 6.15 and table 3 show the precision of the several fitting methods, in terms of RMS of the residuals, parametrized for the three different quadratic fits (P($\theta$),P($\alpha$),P(Euler)). Parameters $(k, k', \epsilon)$ were left free in the fits. Third and fifth numeric columns show the average fitted values for the misalignment. Repeated measurements of the same sensor are fitted independently. Therefore, the quantities are given as the average RMS and the dispersion with respect to the mean value. Measurements CIEAGIx achieve the best resolution. The second set of AGI measurements exhibit slightly worse angular resolution. The effect of hysteresis (difference between AGIx$\pm$ and AGIx measurements, where AGIx$\pm$ refers to any AGI1+,AGI1$-$,AGI2+,AG2$-$) is bellow 5 $\mu$rad.
Figure 6.15 clearly shows the poor precision obtained by AOSI sensors. Their performance is beyond our worse request (15 $\mu$rad). These sensors are rejected for alignment purposes.
Table 3 refers to independent calibrations of the sensors. It means that several measurements of the same sensor are fitted independently. The parameters obtained are therefore different from fit to fit. We can quantify how the spread in the average parameters affects the performance of the fit. In order to do this calculation we compute the average parameters $(\overline{k} \pm \sigma_k, \overline{k'} \pm \sigma_{k'})$ of the independent fits as done above. Then, these average parameters are fixed and employed

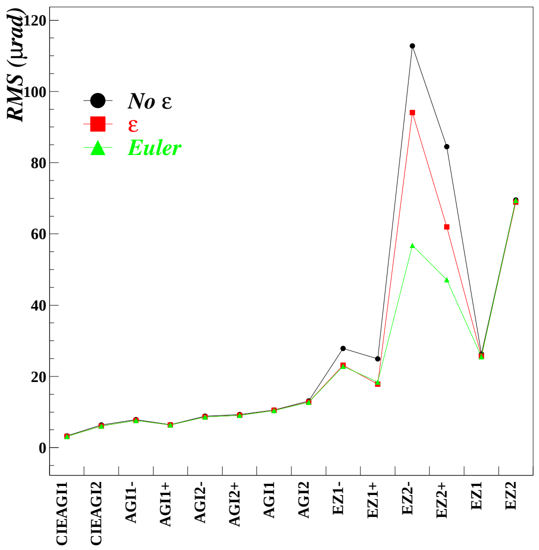


Figure 6.15: *Average RMS of the fit residuals. Each horizontal entry is the average of several measurements taken on the same sensor. Overimposing three different fitting strategies, namely: no misalignment, misalignment and Euler angles.*

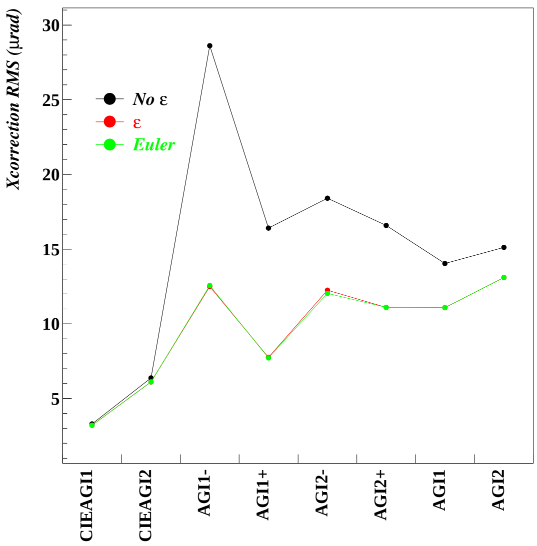


Figure 6.16: *Angular resolution computed using average tiltmeter parameters, parametrized for different fitting polynomial.*

to fit each measurement. The difference between the angle tilted by the structure ($\theta_{moved}$), input in the calibration, and the angle calculated from the measurement ($\theta_{calc} = \theta(\alpha)$) will measure the repeatability of the fit. The angle $\theta_{calc}$ is obtained solving equation (6.5) and having expression 6.1 into account.
The calculation is done for the three different fitting polynomial: no misalignment, misalignment and polynomial including Euler angles. Mean values of the differences result to be centered on zero, with RMS values as shown in table 4 and figure 6.16. As it happened with table 3, we also show the dispersion of the RMS values themselves.
Fortunately, the values shown in table 4 **do not** depend on the value of $\epsilon_0$. Therefore, even ignoring the true values of the scale factor and misalignment, the conclusions of this comparison of performance remain valid. The $\epsilon_0$ invariance is consequence of the correlation between $k$ and $\epsilon$, as stated in section 6.5.3. There, any value of the initial parameter $\epsilon_0$ led to a valid set of fit parameters (although just one can happen in reality). Thus, there is a huge number of parameters $(k, k', \epsilon)$ such that:

$$k_1 \sin\epsilon_1 = k_2 \sin\epsilon_2 = \quad \ldots \quad = k_{true} \sin\epsilon_{true} \tag{6.11}$$

$$k'_1 \sin^2\epsilon_1 = k'_2 \sin^2\epsilon_2 = \quad \ldots \quad = k'_{true} \sin^2\epsilon_{true} \tag{6.12}$$

| | P($\theta$) ($\mu$rad) | P($\alpha(\epsilon)$) ($\mu$rad) | $\epsilon$ (deg) | P(EULER) ($\mu$rad) | $\epsilon_{EULER}$ (deg) |
|---|---|---|---|---|---|
| CIEAGI1 | 3.3±0.4 | 3.2±0.4 | 84.7±0.6 | 3.2±0.4 | 84.5±0.4 |
| CIEAGI2 | 6.4±0.2 | 6.1±0.3 | 83.5±0.2 | 6.1±0.3 | 83.2±0.2 |
| AGI1- | 7.9±2.3 | 7.7±2.2 | 86.9±5.3 | 7.6±2.2 | 83.3±3.6 |
| AGI1+ | 6.5±2.1 | 6.3±2.2 | 83.4±2.0 | 6.3±2.2 | 83.6±1.5 |
| AGI2- | 8.9±3.9 | 8.6±4.1 | 86.1±3.4 | 8.6±4.1 | 86.2±2.5 |
| AGI2+ | 9.3±3.8 | 9.1±3.78 | 82.2±6.5 | 9.1±3.8 | 81.9±5.2 |
| AGI1 | 10.6±1.0 | 10.5±1.0 | 82.2±1.0 | 10.4±0.8 | 82.5±0.9 |
| AGI2 | 13.1±0.9 | 12.8±1.2 | 79.0±5.1 | 12.7±1.2 | 79.8±4.9 |
| EZ1- | 27.8±3.7 | 23.1±1.1 | 85.4±6.3 | 22.9±1.2 | 84.7±2.7 |
| EZ1+ | 25.0±3.2 | 17.8±4.0 | 86.3±2.5 | 18.4±2.8 | 86.6±0.4 |
| EZ2- | 112.8±80.4 | 94.1±47.3 | 70.2±5.9 | 56.8±38.4 | 73.1±10.1 |
| EZ2+ | 84.5±39.4 | 62.0±15.0 | 73.6±8.6 | 47.1±12.4 | 74.8±8.1 |
| EZ1 | 26.3±1.7 | 25.7±1.5 | 82.3±1.6 | 25.5±1.2 | 81.3±1.9 |
| EZ2 | 69.5±2.1 | 68.9±1.4 | 84.5±2.3 | 69.5±0.6 | 85.6±2.1 |

Table 3: Average fitting precision (expressed as average RMS of residuals ± standard deviation) for several *independent* calibrations performed on AGI (fit to a quadratic polynomial) and AOSI sensors (using a polynomial of $6^{th}$ degree). First column assumes no misalignment, second introduces a misalignment $\epsilon$, forth column uses Euler angles (see section 6.4).

where $(k_{true}, k'_{true}, \epsilon_{true})$ are the parameters happening in the calibration. If the above two conditions are verified, then:

$$\theta_{calculated} = \frac{-k\sin\epsilon \pm \sqrt{(k\sin\epsilon)^2 - 4k'\sin^2\epsilon}}{2k'\sin^2\epsilon} \tag{6.13}$$

as obtained from the second order equation (6.10) is invariant against the values $(k, k', \sin\epsilon)$ chosen. Paradoxically, this feature allows us to calculate the angle $\theta_{moved}$ moved by the structure to which the tiltmeters are attached but fails to report the magnitudes which are the aim of the tiltmeter calibration: $(k_{true}, k'_{true})$.

Knowledge of $\theta_{moved}$ is provided by the constraint imposed by the fit: a series of consecutive measurements taken under a common misalignment angle. However, in CMS the tilts will not happen along a sequence but will be instantaneous and along different axis.

One interesting result from table 4 is that the reconstruction of the angle moved by the structure is more accurate when misalignment is taken into account in the calculations. This is because the spreads $(\sigma_k, \sigma'_k)$ are smaller when the misalignment is considered. This makes the average parameters to represent more accurately the calibrations involving $\epsilon$ than those discarding it.

Comparison in table 4 of split measurements with roundtrip ones (see for instance AGI2+,- rows and AGI2 row) does not show a dramatic difference on performance. The sensors under study therefore *show a negligible hysteresis*. In general, hysteresis can be studied for each independent device using this method and discard those sensors showing a non zero value.

| | P($\theta$) $\mu$rad | P($\alpha(\epsilon)$) $\mu$rad | P(EULER) $\mu$rad |
|---|---|---|---|
| CIEAGI1 | 3.3±0.4 | 3.2±0.4 | 3.2±0.4 |
| CIEAGI2 | 6.4±0.3 | 6.1±0.3 | 6.1±0.3 |
| AGI1- | 28.6±9.3 | 12.5±4.8 | 12.6±4.9 |
| AGI1+ | 16.4±5.8 | 7.7±2.7 | 7.7±2.7 |
| AGI2- | 18.4±5.7 | 12.2±6.8 | 12.0±7.0 |
| AGI2+ | 16.6±7.2 | 11.1±4.4 | 11.1±4.4 |
| AGI1 | 14.0±5.0 | 11.1±1.6 | 11.1±1.6 |
| AGI2 | 15.1±1.1 | 13.1±0.8 | 13.1±0.8 |

Table 4: RMS of average differences $\theta_{moved} - \theta_{calculated}$ for the three different polynomial. Sensors from AOSI are not included.

## 6.7 Measuring transversal tilts

As already pointed out, during CMS operation, eventual "pure" transversal tilts may appear. Their range is expected to be small (± 0.3 deg).
According to the geometrical description given by formula 6.1 a tilt with $\epsilon = 0$ degrees would correspond to a "transversal" tilt. Since expression 6.1 is valid for both kind of tilts, a "transversal tilt" will be considered as a tilt with small $\epsilon$ from now on. If formula 6.1 is used with $\gamma = 0$ and $\epsilon = 0$ then $\alpha' = 0$, independently of the $\theta$ value. This means that when the sensor is perpendicular to the gravity then, tilts perfectly transversal to the sensor produce no change of the output voltage. This can be understood due to the symmetry of the bubble with respect to the electrodes. However, if the sensor is lifted by one of its extremes, then $\alpha'$ is nonzero and the response of the sensor can be studied. Figure 6.17 shows the expected voltage suppression (after using equation (6.1)) when tilting the sensors transversally in the range $\theta \in [-0.3, 0.3]$ deg for a $\gamma$ value of $\approx$ 2 deg. The curve is just a linear interpolation between points.

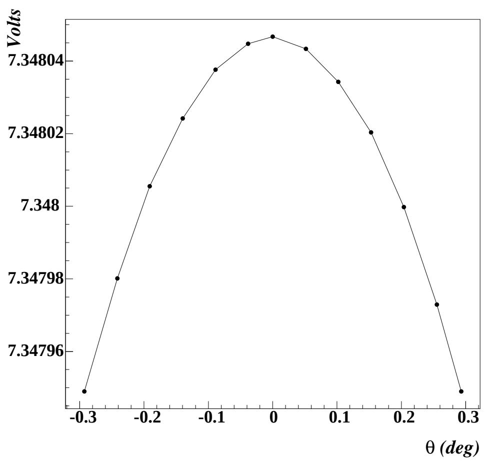


Figure 6.17: *Example of the expected reduction of the output voltage for pure transversal tilts (see text).*

We have tried to measure the sensor response under such tilts placing the sensors transversal to the tilt motion of the tripod. In order to get a non-zero signal, the sensors are lifted by means of a wedge under one of their extremes. The setup depicted in this figure corresponds to $\epsilon$=0 in figure 6.7.
For the test, we tilted the tripod in figure 6.18, from -0.3 deg to 0.3 deg. This angle now corresponds to a transversal tilt of the sensors in the same angular range. The measured voltage as a function of the transversal tilt angle is given in figure 6.19 for sensor number 1. As one can see, the shape is not looking like in figure 6.17, but rather reminds the behavior in figure 6.10a).

The indication seems clear: the longitudinal axis of the tiltmeter and the tilt axis of the tripod were not perfectly perpendicular ($\epsilon \neq 0$) and the small longitudinal component in the overall tilt is masking the "transversal contribution" to the output voltage. The magnitude of the output voltage is dominated by the effect of the wedge and the slope by a non zero value of $\epsilon$.

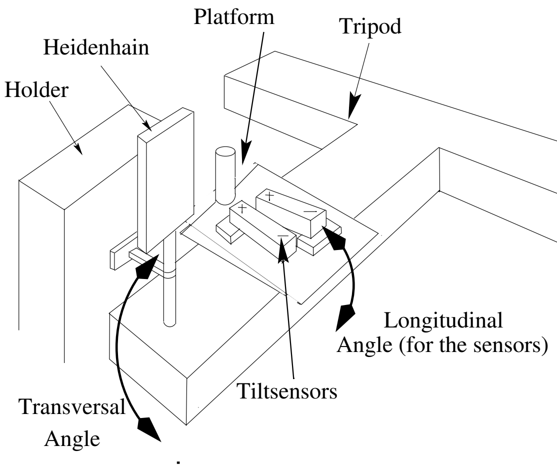


Figure 6.18: *3D view of the arrangement of the sensors during a transversal calibration. The sensors are lifted using wedges.*

To check above statement we have fitted the data in figure 6.19 to a linear expression for V using the manufacturer scale factor, leaving $\epsilon$ and $\gamma$ as free parameters (equation (6.1)).
The result of the fit (continuous line in figure 6.19) were $\epsilon = 1.69$ degrees and $\gamma = 1.83$ degrees. The quality of the fit is good and the RMS of the residuals amounts for 3.1 $\mu$rad.
Data in figure 6.19 is then compatible with a misorientation of about 1.7 deg with respect to the perpendicular. The value of $\gamma$ found in the fit is consistent with the wedge we put under the sensors. It was not measured in advance with precision and this is why it was left free in the fit.

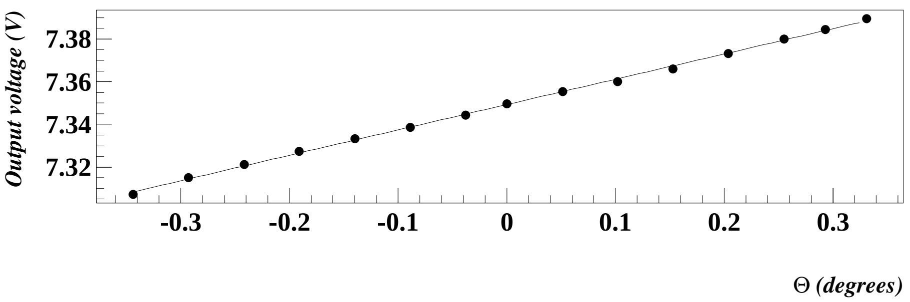


Figure 6.19: *Output response of one of the sensors as a function of the transversal tilt (see text).*

According to figure 6.17 the maximum expected suppression of the output voltage due to transversal tilts in the range $\pm 0.3$ deg is in the $1.4 \times 10^{-3}\%$ inducing in the present test a systematic error well smaller than 1 $\mu$rad. The simulated behavior coincides with the measurements of the manufacturer [9].

## 6.8 Dual tiltmeter arrangement

In CMS, the misalignment between the tiltmeters axis and the rotation direction will not be known. However, from the above experiences on longitudinal tilts, we have learned that it is crucial a correct positioning of the sensor with respect to the expected tilt axis. A misorientation of about 3 degrees would induce a transversal tilt that may account for up to 8 $\mu$rads. This is almost twice the measured intrinsic resolution of the sensors (4-5 $\mu$rad).
It is difficult to foresee the orientation of the tilt axis of large structures such as MABs. Instead, a monitoring of the magnitude of the misalignment angle between tiltmeter and rotation axis of the MAB releases the constraint on the littleness of the misorientation. In case the misalignment would exceed a certain limit, we might correct the tiltmeter output thus providing a reliable measurement of the $\phi$ angle. The usage of two tiltmeters arranged under an angle is used to calculate the misalignment between both axis. A simplification of the setup is shown in figure 6.20, where the several angles involved are depicted.
The operation of the device needs first of a combined calibration. It is worth to have each sensor characterized (knowledge of $k$ and $k'$) in advance. Thus, the number of variables decreases and fitted parameters become more reliable. The angle between both sensors does not need to be known: it is calculated from the combined calibration. The calibration of the device is similar to that of an individual tiltmeter. The platform basis, with both sensors on top, is tilted following the calibration procedure explained in section 6.5. Signals from both tiltmeters are independently fitted according to equation (6.5) (keeping $k$ and $k'$ fixed) and the misalignment angles $\epsilon_i^c$ and $\epsilon_i^c$ are calculated. Then, the angle $\delta = \epsilon_1^c - \epsilon_2^c$ is the angle between both tiltmeters. Provided both sensors are not removed from the common support, the calculation of the angle stands. When the dual tiltmeter is placed on a moving structure, the combined reading of both sensors is employed to calculate the orientation of the tilting axis.
Equation (6.5) is a second order equation in $\alpha' = \alpha$ (no wedges under the sensors are needed), which can be solved for $\alpha$. Let $\alpha_i$ be the physical root of the equation. Then, according to equation (6.1):

$$\alpha_1 = \arcsin(\sin\epsilon_1 \sin\theta) \tag{6.14}$$
$$\alpha_2 = \arcsin(\sin(\epsilon_1 - \delta)\sin\theta) = \tag{6.15}$$
$$= \arcsin(\sin\alpha_1 \cos\delta - \cos\epsilon_1 \sin\delta \sin\theta) \tag{6.16}$$

Manipulation of the last equation produces:

$$\cot\epsilon_1 = \cot\delta(1 - \frac{\sin\alpha_2}{\sin\alpha_1 \cos\delta}) \tag{6.17}$$

For an instantaneous movement, the misalignment $\epsilon_1$ between the tilting axis of the tiltmeter and the rotation axis is calculated, using the information of the angle measured by the tiltmeters and knowing the relative angle between both. Provided $\epsilon_1 \leq 3$ degrees the tiltmeter reading can be trusted. Otherwise, it has to be corrected by $\epsilon_1$ as calculated by 6.17.

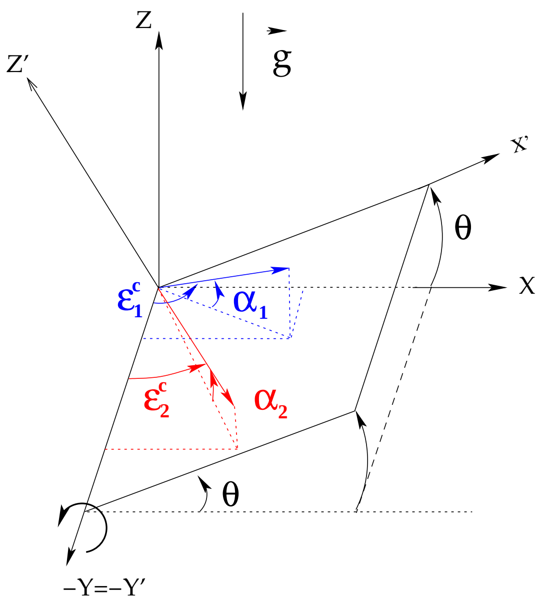


Figure 6.20: *Two sensors arranged under an angle* $\delta = \epsilon_1^c - \epsilon_2^c$ *will allow to reconstruct the misalignment* $\epsilon_1$ *between the tiltmeter and the rotation axis.*

When Euler angles are considered, the above equation remains valid just substituting $\epsilon_1$ by $\epsilon_1 + \psi$. It is clear that, with just a single measurement, values for $\epsilon_1$ and $\psi$ can not be calculated simultaneously. Case $\epsilon_1 + \psi$ exceeds the 3 degrees threshold we must correct by misalignment. Fortunately, the correction (see equation (6.2)) depends on $\epsilon_1 + \psi$.

### 6.8.1 Application case

We have applied the method defined above on real measurements done on two independent 1D AGI sensors. The sensors were screwed and arranged (by hand) perpendicular to each other. Sensors AGI1 and AGI2 were used for this test, using the setup with the tripod. Then, the tripod was tilted from -0.3 deg to 0.3 deg. The measurements were repeated 8 times, four with sensor AGI1 as sensor 1 in figure 6.20 and 4 with sensor AGI2.
In order to crosscheck the functioning of the method above, we calculate the moved angle $\theta_{calculated}$ and compare with the real angle moved $\theta_{moved}$. The value of $\theta_{calculated}$ is obtained from equation (6.14) once $\epsilon_1$ is calculated. The difference $\theta_{calculated} - \theta_{moved}$ is shown in figure 6.21 for AGI1. No Euler angles were included. Besides, the manufacturer calibration constants were employed to give credibility to the fitted misalignments. The figure shows that, in average, we can calculate the real angle tilted by the platform with an error of 4 $\mu$rad. Slightly better results are obtained by increasing the degree of the fitting polynomial.

## 6.9 Laser Level

Tiltmeters are small size devices. The information of the angle given by them is therefore limited to a small area around the sensors. In order to define the inclination of a big element one has to rely on the rigidity and stiffness of the structure. In CMS, we propose to measure the angle of

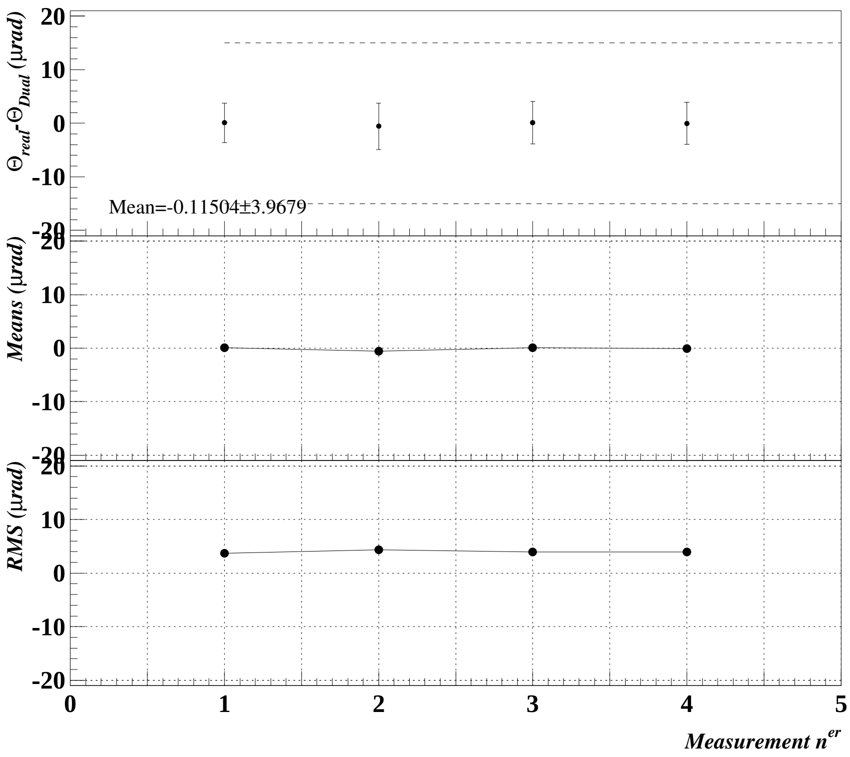


Figure 6.21: *Difference $\theta_{calculated} - \theta_{moved}$ for four measurements of sensor AGI1 (sensor 1) with AGI2 in perpendicular. The angle of $\theta_{calculated}$ was obtained using equation (6.14). Upper plot shows the mean value of the difference. Error bars are the RMS of the calculation. Middle plot is a zoom of the mean values. Bottom plot a zoom of the RMS.*

the MABs using Laser Levels. A Laser Level is a combination of two angle measuring systems. On one hand, a tiltmeter system measures the angle with respect to the gravity of the surface where it is located. On the other, a laser beam monitored by two ALMY sensors calculates the angle of the laser (with respect to a known reference), extending the measurement of the tiltmeters. In this section we will show how both measurements are coupled and why the Laser Level will be a tool for monitoring of deformations of the structure.

We have constructed and calibrated a first Laser Level unit prototype. The unit consists (see figure 6.22) in a stainless steel support with two built-in tilts to which a laser diode and a tiltmeter (AGI sensor number 1) were attached. The support is built in such a way that a tilt of the basis translates in a simultaneous tilt of the tiltmeter and laser. Away from the platform, two ALMY sensors endowed with special mechanical interface are inserted inside precise mounting sockets. These reference sockets are referenced in the space such that their coordinates are known in a common reference system. All this allows to measure the angle of the laser beam with respect to the horizontal.

The calibration of a laser level unit is the calibration of the angle that the beam makes with the horizontal. In this way, when the unit is attached to a given piece, the angle measured with the tiltmeter is extended, in a known direction, much beyond the very short tiltmeter base.

The calibration procedure is a two step process. First of all, the tiltmeter is levelled on both axis.

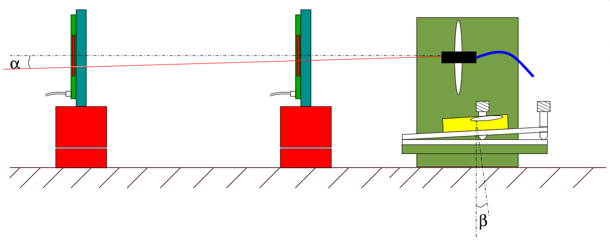


Figure 6.22: *Schematics view of the Laser Level operation. Two ALMY sensors endowed with a mechanical interface to a reference network measure the angle tilted by the tiltmeter, some meters away from the own measurement of the clinometer.*

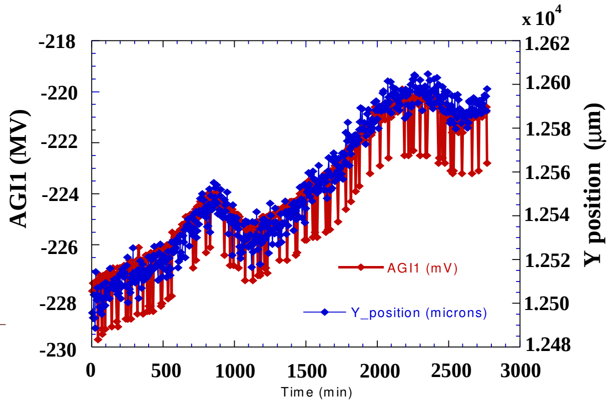


Figure 6.23: *The angle tilted by the Laser Level structure is measured simultaneously by tiltmeter and ALMY sensor. Lefts axis corresponds to output voltage given by the tiltmeter. Right axis is the position of the beam measured in the ALMY.*

The basis of the Laser Level is then fixed and remains untouched. In this position the output of the tiltmeter corresponds to a small angle $\beta$ (see figure 6.22). The laser beam is then moved as to pass through the center of the ALMY sensors. The angle of the beam $\alpha$ is measured in the reference network. In this way the laser beam is referenced with respect to the tiltmeter. When the angle measured by the ALMYs is $\alpha$, the tiltmeter basis will be perpendicular to gravity. The measurement of the tiltmeter is thus extended. Reversely, if the tiltmeter reading is $\beta$, the beam should pass through two known points of the sensors. If the positions reported by the ALMY sensors differ from the positions recorded on calibration, it would indicate a deformation of the structure.
We performed two calibrations of the device. The values found for $\alpha$ and $\beta$ in the first calibration were:

$$\begin{aligned} \alpha_0 = & \quad -750.7 \pm 1.4 \ \mu\text{rad} \\ \beta 0 = & \quad -39.3 \pm 0.6 \ \mu\text{rad} \end{aligned}$$

The system was then left measuring for 48 hours. After this time, the angles measured were:

$$\begin{aligned} \alpha_1 = & \quad -723.0 \pm 1.2 \ \mu\text{rad} \\ \beta 1 = & \quad -12.3 \pm 4.7 \ \mu\text{rad} \end{aligned}$$

When comparing the angles reported by tiltmeter and sensors, it is clear that there was a rotation of the device as a whole. This can be easily seen comparing:

$$\alpha_0 - \alpha_1 = \quad \beta_0 - \beta_1 \approx -27 \quad \mu\text{rad}$$

Furthermore, the motion detected by both, laser and tiltmeter is completely correlated, as can be seen in figure 6.23. This figure compares the tiltmeter response (left axis) and the vertical position measured by an ALMY sensor (right axis). The result shows that the reading of there was a motion and that it was a tilt, most likely due to temperature variations of the environment

## 6.10 Conclusions

In the current alignment scheme, the relative orientation between the Muon chambers and Central Tracker can not be measured accurately making use of the network of sensors linked by lasers. Their orientation, along the CMS $\phi$ coordinate, will be measured using tiltmeters. These devices allow precise angular positioning with respect to gravity.
Tiltmeters are 1D sensors. It means that they measure the tilt along a privileged direction (longitudinal). Unfortunately, the rotation axis will almost never be perpendicular to the preferred direction. In this chapter we have described the tilt operation from a geometrical point of view. We have identified the most important variable affecting the performance of this device: the angular misalignment with respect to the rotation axis. If the misalignment (or misorientation) of the tiltmeter with respect to this axis were bigger than 4 arc deg, then the angle reported by the tiltmeter and the real angle moved by the tiltmeter holder structure would be as different as 15 $\mu$rad, independently of the error contribution from the sensor itself.
We have calibrated a couple of electrolytic tiltsensors from two different manufacturers. We have shown that a proper calibration of these devices imposes stringent requirements on the setup. Precise calibrations demand a mechanical configuration where the misalignment can be controlled. Otherwise, the parameters obtained from calibrations are dependent on the misalignment estimation. Fortunately, the manufacturer provides calibrations of these devices under controlled misalignment conditions.
Although misalignment values were not known in our setup, we managed to extract some interesting conclusions from our data. We studied the individual resolution of each sensor and the repeatibility of the calibrations, both concepts determining the quality of the devices. We have chosen the tiltsensors from Applied Geomechanics as the most performant ones.
In CMS, tiltsensors will be mounted as part of a bigger structure called Laser Level. The Laser Level contains a tiltmeter (level) plus a laser whose relative orientation has been previously calibrated. The laser level unit is then attached to a structure called MAB (see chapter 2) which is itself mounted in the iron barrel yoke. Foreseeing that uncontrolled movements of the iron structure could perhaps occur, we propose to use two tiltsensors instead of one for accurate measurement of the $\phi$ angle. We have shown how the combined operation of two sensors determines the misalignment of an instantaneous tilt and managed to calculate: the relative angle of the sensors, their misalignment and the real angle moved by the structure.

# Bibliography


[1] The CMS Collaboration, *The Muon Project Technical Design Report* , CERN/LHCC 97-32.

[2] The CMS Collaboration, *The Tracker Project Technical Design Report* , CERN/LHCC 98-6.

[3] Applied Geomechanics Incorporated 1336 Brommer Street Santa Cruz, CA 95062 U.S.A. The model tested in this work belongs to the 756-Series Mid-Range Miniature Tilt Sensors.

[4] Advanced Orientation Systems Inc., 1901 E. Linden Ave. Unit 22. Linen NJ 07036. The models studied in this work belong to the EZ-TILT-3000 Series.

[5] Heidenhain Digital Length Gauge Systems
http://www.heidenhain.com

[6] Kennametal Inc. (NYSE: KMT), Latrobe, Pennsylvania, USA
http://www.kennametal.com

[7] Technical note available from:
http://www.geomechanics.com/pdf/bias.pdf

[8] See application note: *Using Tiltmeters as Precision Levels* , available from:
http://www.geomechanics.com/applications/

[9] Gary Holzhausen, President of Applied Geomechanics Incorporated, private communication

# Chapter 7

# CMS Link radiation endurance tests

## 7.1 Introduction

LHC will reach the nominal luminosity of $10^{34}$ cm$^{-2}$s$^{-1}$ from the fourth year onwards. A low luminosity start up will precede the high luminosity operation. About 0.5 $\times 10^5$ pb$^{-1}$ will be accumulated per calendar year at high luminosity [1]. For these working parameters, the number of interactions per second is $\sim 10^9$, creating an extremely hostile radiation environment.
Due to its proximity to the interaction point, tracker detectors (silicon microstrip and pixel detectors) will have to operate in a very harsh radiation environment. The irradiation level will cause an appreciable deterioration of the detector performance. It is even expected that some of the devices produced from standard detector grade silicon will not survive to the envisaged operational period of the experiments [2]. The very high cost for the silicon instrumented tracker has led to the request that the detectors should be fully operational for at least 10 years and hence it has to be guaranteed that they will have a sufficiently high radiation tolerance. Concerning the alignment components, the comparative smaller amount of sensors utilized makes feasible periodic substitutions at shutdowns, provided they can be accurately repositioned.
Some of the alignment devices will be located in spatial regions with very high particle fluences. In a recent review of the tracker alignment [3] either ALMY sensors or modified silicon modules (see section 2.2) are candidates to be encapsulated in the inner tracker. The same radiation endurance requested to the inner silicon detectors would be desirable for the ALMY sensors, implementing hydrogenated amorphous silicon as active semiconductor material. At $|\eta| = 3$, interleaved between the ECAL endcap and the endcaps of the tracker, there will be optical periscopes. In addition, laser sources and optical glasses will be placed very close to the outer muon spectrometer endcap.
The radiation tolerance of all these elements is of supreme interest and have led us to test the resistance of the most compromised link alignment components. This chapter deals with the behavior of glasses, coatings and glues under irradiation with *gamma-rays* from $^{60}$Co sources and with the observed change in performance of the amorphous silicon sensors when irradiated with *gamma-rays* and *neutrons* . In section 7.2, a description of the different radiation fields expected around the regions of interest for alignment is given. A decision on radiation hard optical glasses is done in section 7.3, also showing the performance of irradiated optical coatings. Glues joining optical pieces must be radiation tolerant, to avoid unwanted beam motion. Results on glues irradiation appear in section 7.4. We present, in section 7.5 a review of the radiation damage in crystalline and amorphous silicon. Finally, a detailed exposition of the radiation damage on

ALMY sensors is presented in the last section.

## 7.2 Radiation environment near alignment components

### Inner tracker environment

The proximity of the inner tracker ($22 < r < 52$ cm approx.) to the vertex imposes the hardest restrictions on radiation endurance. The radiation levels expected are adopted as reference values: if components survive the fluences and doses characteristic of the inner detector they will operate in any other region of the experiment with equal or better performance. Main figures follow [1]:

- Simulations show that the charged hadron flux is, to a good extent, independent of the $z$-coordinate and varies as $1/r^2$, where $r$ is the distance from the beam line. The former law also stands out of the tracker region. The charged hadron fluence is dominated by pions with protons and charged kaons each accounting for about 10%.
- The photon spectrum is dominated by photons below 10 MeV, with a lower peak at higher energy due to $\pi^0$ decays.
- The neutron fluence is lower than the charged hadron fluence in the barrel part. However, due to the intense albedo from the endcap ECAL, the neutron fluence at the last disks clearly exceeds the charged hadron fluence.

The energy spectrum of the different particles has been calculated for all the CMS detectors and will rarely exceed some 10 GeV.

### Outer tracker environment

Simulations of the outer tracker barrel environment show that the neutron fluence increases slightly at the last endcap disks whereas the charged hadron fluence and dose are essentially independent of the $z$-coordinate. The spectra become harder towards higher pseudorapidities. Thus, an extension of the barrel averages into the endcap is valid, except for the neutron fluences at the last disks.
While the fluence originating from the vertex is irreducible, a neutron moderator lining of the ECAL is shown to efficiently reduce the neutron albedo, which is particularly intense for the $PbWO_4$ crystals.
Energy of the different particles ranges from $10^{-1}$ to $10^4$ MeV, except for the photon spectrum dominated by energies below 10 MeV.

### Electromagnetic calorimeter environment

In the ECAL detector [4], covering up to $|\eta| = 3$, the secondaries from the pp collisions are an important component of the background, but neutron albedo and the energy deposition in hadronic and electromagnetic cascades are at least equally important. Most of the neutron flux, which is harmful to the inner detectors downstream is generated by hadronic interaction in the ECAL crystals. The maximum neutron fluence and maximum dose is reached at the

| Position | A1 | A2 | A3 | LB | A4 | A5,A6 |
|---|---|---|---|---|---|---|
| Source | [1] | [1] | [1] | [5] | [5] | [5] |
| z(cm) r(cm) | z=121 r=22 | z averaged r=35 | z=121 r=52 | z=121 r=100 | z=666 r=460 | z=666 r $\in$ [400,700] |
| Hadrons (E>100 keV) ($cm^{-2}$) | $1.6\ 10^{14}$ | $9\ 10^{13}$ | $4.7\ 10^{13}$ | $<5\ 10^{13}$ | $<5\ 10^{9}$ | $<5\ 10^{7}$ |
| Neutrons total ($cm^{-2}$) | $3.5\ 10^{13}$ | $8.5\ 10^{13}$ | $1.9\ 10^{13}$ | $<5\ 10^{14}$ | $<5\ 10^{11}$ | $<5\ 10^{10}$ |
| Absorbed dose (kGy) | 67 | 36 | 19 | <100 | $<10^{-3}$ | $<10^{-3}$ |

Table 1: *Rough estimation (after pag. 15 [1], color plots in [6]) of 10 years of hadron fluences, neutron fluences and absorbed dose for points of CMS near alignment elements. The row position refers to the locations defined in figure 7.1*

high-$\eta$ corner of the ECAL endcap, where the integrated fluence value exceeds $10^{15}$ $cm^{-2}$ with an absorbed dose about 0.1 MGy, after 10 years.
Energy of photons and charged hadrons keeps below 10 GeV and neutron energies below $10^{-1}$ GeV.

### Hadronic calorimeter environment

In the space regions in the $|\eta| = 3$ neighborhood the irradiation dose will be as high as 10 kGy/year at the LHC nominal luminosity of $10^{34}$ $cm^{-2}$ $s^{-1}$. The neutron fluence can be as high as $10^{14}$ $cm^{-2}$ per year, while for the charged hadron particles may reach the $10^{13}$ $cm^{-2}$ and year.

### Muon spectrometer environment

The muon system requires the most complicated shielding of all CMS subdetectors, since it gets background contributions from [5]:

- The pp collisions directly, neutron albedo and hadronic punchthrough in the main detector $|\eta| < 3$. Neutrons produced during nuclear evaporation have typical energies of 1 MeV, and those coming from intranuclear cascades have energies up to several hundred MeV.
- Leakages originated in the HF (important in the endcap muon system $|\eta| \in [3.0, 5.3]$).
- Machine background: beam losses in the LHC machine, due to beam-gas scattering, produce high energy muons with energies up to several TeV. Machine background will be the most important background during the low-luminosity phase [5].

A rough estimation of hadron fluences, neutron fluences and absorbed dose for places near alignment components is given in table 1. Label A1 refers to the position where periscopes, ALMY sensors, tiltmeters and distance monitors are placed. A2 will house either ALMY sensors

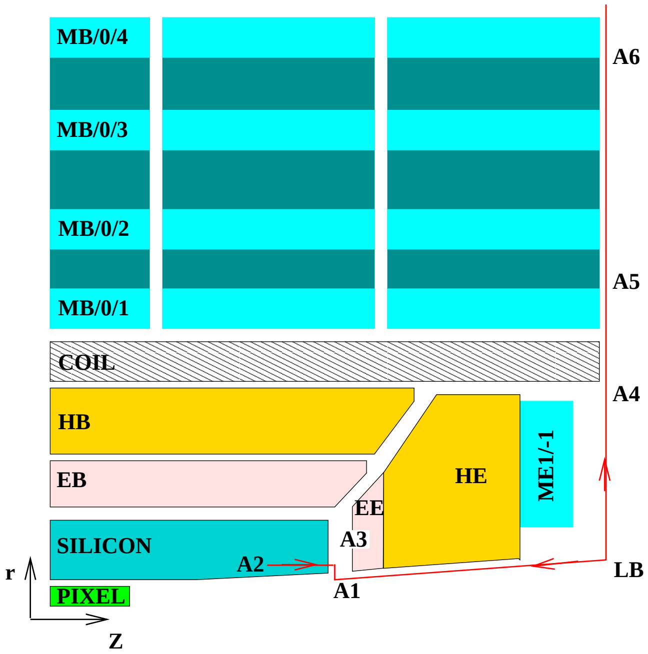


Figure 7.1: *Freehand drawing of a quarter of an active plane in CMS. Labelled positions address positions of alignment components. "Ax" refers to ALMY positions. "LB" stands for Laser Box. Radiation Levels at these points are given in table 1*

or silicon modules. A3 refers to the position of ALMY sensors in the Muon TDR Link alignment layout. Label LB locates the laser box position. Finally A4 to A6 show extra positions for ALMY sensors, distance monitors, tiltmeters and Link electronics.

In table 1, values for the neutron fluences are the least accurate since after the tracker TDR, the thickness of the barrel moderator has been reduced. As no update on radiation environment has been published[1], the values shown here are underestimations of the real values. Furthermore, following [6] a safety factor of 2 should be applied to all data to account for uncertainties in the simulations. The data in the table are ordered left to right in terms of increasing radial coordinate. The row "Position" locates the position of the different points in figure 7.1. The source where the data were obtained is shown in row "Source". All the values are approximated, and are intended to have an idea of the order of magnitude for each variable. Particle energy spectra: energy of neutrons below 100 MeV and energy of photons below 10 MeV.

## 7.3 The effect of irradiation on glasses

At the laser boxes (see figure 7.1), transparent rhomboid section prisms are glued to right angle prisms, to split and shift the incoming light ray (see figure 7.2). Each light source generates three laser beams. One beam gets inside the tracker and changes twice its direction by means of a periscope located in the tracker endcap. The periscope is made of an splitter and a mirror, both glued to a rigid bar of fused silica. The transmittance of these elements should remain

[1] Only reference [6] shows a re-calculation of data relative to the outer tracker

constant for proper operation of the alignment system.

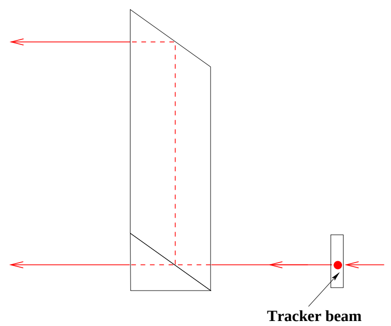


Figure 7.2: *Sketch of Laser Box optics. Two parallel rays travel to the muon barrel. A third beam is perpendicular to the paper.*

We have irradiated with gamma-rays (1.17 and 1.33 MeV), using $^{60}$Co sources, four different type of glasses: BK7, BK7-G18, fused silica and optical grade fused silica (synthetic quartz). The designations of glasses used in optics are based on their dispersions (variation of refraction index with wavelength) and further subdivided by composition. They have letter designations (e.g. BK7) and number designations (called "glass numbers", e.g. 517642 [7]). In particular:

- BK7 (borosilicate) from SCHOTT [8] is a very common material for optical components in the visible range. It is highly transparent from 350 nm.

- Fused Silica is synthetic molten quartz glass. Optical glasses made on fused silica present very good optical transmission characteristics in the UV range besides a high transmission up to the infrared. They have a very low coefficient of thermal expansion in combination with high temperature resistance, and high corrosion resistance.

The irradiation of the above optical glasses was done at the NAYADE facility of CIEMAT. The four glasses were irradiated up to a total dose of 100 kGy, equivalent to 10 years of use in the region of CMS of $|\eta| \approx 3$, at the nominal luminosity of LHC (see table 1).
As a result of the irradiation, the BK7 sample turned from transparent to absolutely black (see figure 7.8). The fused silica became grey. On the contrary, BK7-G18 and synthetic quartz did not degrade in excess their optical properties. As an example, we compare in figure 7.3 the transmittance and the reflectance spectrum of non irradiated and irradiated probes of synthetic quartz [9]. Upper curves correspond to transmittance curves, and they attach to the left scale. Reflectance spectra is shown in the right axis.
The observed darkening of BK7 and fused silica is a consequence of radiation-induced defects acting as optical absorption centers. These centers can be introduced by ionization or displacement mechanisms. Pre-existing defects may also become optically active after exposure to radiation.
The measurements (not shown) done in the UV range reveal a degradation in transmission of up to 15%, while no change ($< 0.5\%$) is observed in the IR.

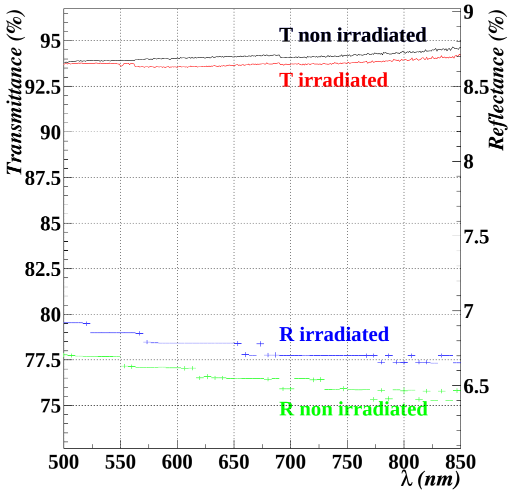


Figure 7.3: *Reflectance and transmittance of optical grade fused silica. Left scale refers to the transmittance and right scale to the reflectance. The degradation in transmission stays always below 0.5%. A slight increase in the reflection in agreement with the small lose in transparency is observed*

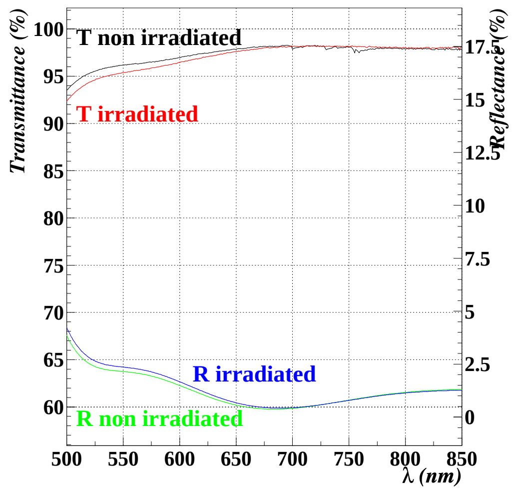


Figure 7.4: *Degradation of transmittance and reflectance of a plate of BK7-G18 with antireflection coating after 10 MRad. Left scale refers to the transmittance, right scale to the reflectance. Non irradiated reflectance and transmittance spectra are also shown.*

### 7.3.1 Gamma irradiation of coatings on glass

Antireflection (reflection) coatings are used to increase the transmittance (reflectance) of a material. As a rule of thumb, regarding the transmittance, a single layer antireflection coating (ARC) reduces reflectance of a film to zero, for a single wavelength[2]. A double layer ARC widens the wavelength range where the reflectance is minimum. The addition of an extra layer to the ARC greatly rises the number of possible groups of designs.

Those optical pieces that have to be operated in transparent mode may be coated by ARC. On the contrary, glasses to be used as mirrors are covered with reflecting coatings. We have irradiated with the same $^{60}$Co gamma source, antireflection and reflection coatings on BK7-G18. The dose was again 100 kGy.

The effect of the irradiation on a standard triple ARC is shown in figure 7.4. Left axis corresponds to the transmittance and right axis to the reflectance measurement. The difference between irradiated and fresh samples is negligible. No changes are observed in the reflection curves. From these plots it is clear that the degradation of BK7-G18 with ARC is even smaller than the degradation of the BK7-G18 without it (figure 7.3).

Concerning reflecting coatings, we show in figure 7.5 the reflection curves before and after

[2]The refraction index of the ARC n$_{film}$ = $\sqrt{n_{substrate}n_{medium}}$ is not achievable for all wavelengths.

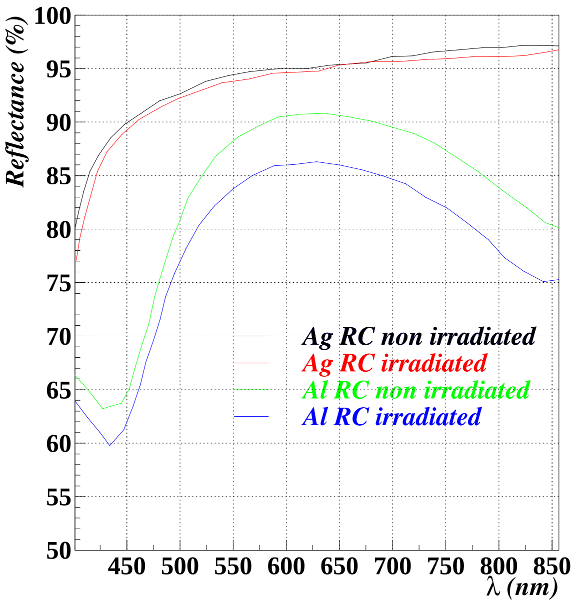


Figure 7.5: *Effect of irradiation on reflection coatings (RC). Upper curves correspond to Ag RC. Both at the bottom refer to the Al coating and its degradation after 100 kGy.*

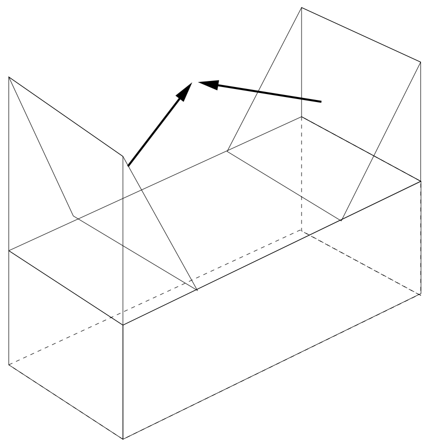

Figure 7.6: *Sketch of a retro-reflector. The arrows represent the normal to the inclined faces.*

irradiation (same 100 kGy dose) of a BK7-G18 glass layer covered with an aluminium coating on the front face. In this case, the reflection power results degraded by more than 5% in the visible. On the contrary, a coating of silver on the back face results almost insensitive to the irradiation as clearly seen in 7.5.

## 7.4 The effect of irradiation on glues

Some components of crucial optical elements as the laser box or the periscope are attached among them by gluing. The glue joining the components should not degrade, to avoid undesirable motions which would contribute to the beam instability. In order to test the glue radiation hardness we have constructed two retro-reflector like objects in BK7, each consisting on two right angle prisms glued to the two extremes of a rectangular prism, as shown in figure 7.6. We have used a coordinate measuring machine DEA[3] [10], having about 5 $\mu$m resolution in each of the 3 coordinates, to define the two inclined planes of the retro-reflector and calculate the angle that the two normals form in space (also drawn in figure 7.6). By construction, the angle will be close to $\pi/2$. One of the retro-reflectors was glued with LOCTITE 350 and the other with

[3] Manually operated, vertical bridge-type machine capable of making measurements in three axes. The machine is used to inspect various features of manufactured components to ensure quality and conformance relative to an engineering drawing

EPOTECNY NOA61.
The DEA machine works by contact: one pin (see photographs on figures 7.7 and 7.8) touches one of the inclined faces and takes 9 points over the whole surface. The normal to the plane is then calculated. Then, the pin moves to the second plane and repeats the operation. The procedure is repeated as to obtain 20 pairs of normals that are combined to each other as to obtain 400 independent measurements of the angle in the space between both normals. The results, for LOCTITE 350 and NOA61 respectively, can be seen in figures 7.9 and 7.10. Numerical values are given in table 2.

Figure 7.7: *Overall view of one of the retro-reflectors at the DEA machine table*

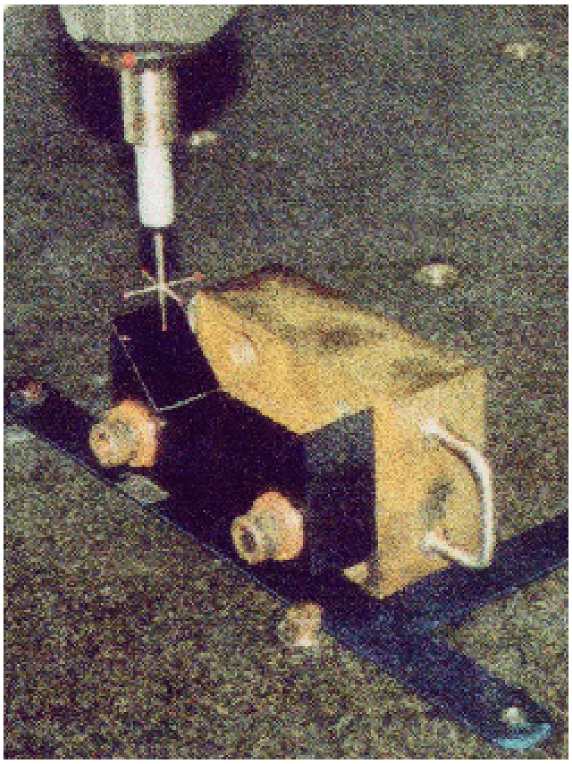

Figure 7.8: *Detail of the retro-reflector at the DEA machine table*

The difference in time between measurements, even for the same dose and the same object, was of several months, to avoid repetition of environmental conditions. The two first points in figures 7.9 and 7.10 and first two lines in table 2 correspond to measurements before any irradiation. Error bars in the figures are the RMS of the distributions of the reconstructed angles, also shown in table 2.
After the first 100 kGy of gamma-ray dose we observe a change of the angle distributions for both types of glues. In the case of LOCTITE the angle varies by 46 $\mu$rad and 56 $\mu$rad for NOA61. The change in angle corresponds to a slight twist of the right angle prisms on their base, that may correspond to a deformation of the thin glue layers.

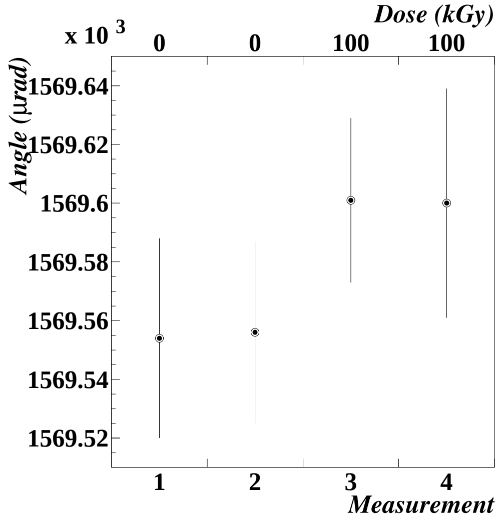


Figure 7.9: *The effect of the irradiation on the mechanical properties of LOCTITE. Bottom axis shows number of measurement. Upper axis summarizes the dose.*

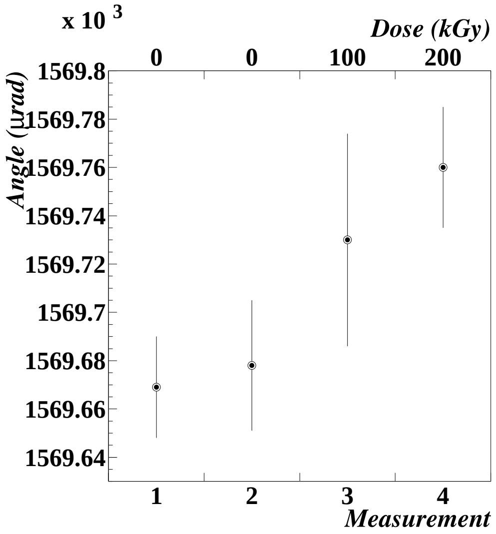


Figure 7.10: *The effect of the irradiation on the mechanical properties of EPOTECNY. Bottom axis shows number of measurement. Upper axis summarizes the dose.*

To confirm that the change is related to the irradiation, we have given a second 100 kGy gamma-ray dose to the object glued with NOA61 and then proceeded to a new measurement of the angles. The results are found at the fourth entry in figures 7.9 and 7.10 and in table 2. Mean values for LOCTITE 350 are compatible, while the mean value for the NOA61 object has moved by some 30 $\mu$rad in the same direction as before.

It is clear that we are observing motions of the glued prisms, but unfortunately, with an error that is comparable with the magnitude of the changes. More sophisticated measurements will be needed.

| LOCTITE 350 | | | EPOTECNY NOA61 | | |
|---|---|---|---|---|---|
| Dose (kGy) | Angle ($\mu$rad) | RMS ($\mu$rad) | Dose (kGy) | Angle ($\mu$rad) | RMS ($\mu$rad) |
| 0 | 1569554 | 34 | 0 | 1569669 | 21 |
| 0 | 1569556 | 31 | 0 | 1569678 | 27 |
| 100 | 1569601 | 28 | 100 | 1569730 | 44 |
| 100 | 1569600 | 39 | 200 | 1569760 | 25 |

Table 2: *Results from glue deformation due to the irradiation (see text)*

## 7.5 The effect of irradiation on silicon

As it has already been mentioned, either slightly modified silicon modules or ALMY sensors are planned to be used by the Tracker alignment system at the Link-Tracker interface. The radiation tolerance of silicon devices has become of supreme interest in present and foreseen high energy physics experiments. The development of radiation hard silicon detectors that can operate beyond the limits of present devices and that ensure guaranteed operation for the whole lifetime of the LHC experimental program led to the creation of the ROSE (Research and development On Silicon for future Experiments) collaboration [11]. A remarkable amount of systematic studies have been coordinated under the ROSE collaboration, defining detector layout and process technologies to test radiation hardness of the devices [2]. However, all the radiation hardness studies being carried out deal with crystalline silicon (c-Si), but not with amorphous silicon (a-Si). The difference between crystalline and amorphous structure is so important that the results obtained for the former can not be extrapolated for the latter.
The rest of this section will stress basic differences between the irradiation of c-Si and a-Si. We will present the most remarkable facts about the interaction and consequences of the interaction of radiation with these materials.

### 7.5.1 Irradiation of c-Si devices

The radiation endurance of silicon detectors is nowadays very well documented. A comprehensive study is found in references [2, 12]. Here we will highlight the most important effects of irradiation on c-Si.
The interaction of high energy particles with *crystalline semiconductor* devices usually produces three types of effects [13]:

- Displacement of atoms in the crystal lattice, removing atoms from their nominal positions: bulk damage.
- Creation of electron-hole pairs, used to detect the passage of high energy particles.
- Creation of local charged regions due to long term ionization effects. This effect is important for oxides and insulators coupled to semiconductor devices. It is a surface damage.

Among them, the main damage contribution is caused in the silicon bulk and is produced by displacements of atoms.
It is well known that any particle fluence can be reduced to an equivalent 1 MeV neutron fluence producing the same bulk damage in a specific semiconductor. This scaling rule is called the NIEL -Non Ionizing Energy Loss- hypothesis, and it assumes that the generation of bulk damage is due to non-ionizing energy loss. In practice, the displacement damage function $D(E)$ (equivalent expression for the NIEL value) is used. The damage functions of neutrons, electrons, pions and protons are shown in figure 7.11. According to this figure, the damage induced in silicon depends not only on the particle type, but also in its energy. The damage function for protons rises towards low energies and the pion damage has a local maximum in the $\Delta$-resonance region. An energy of 190 eV is needed for a neutron to displace an atom. The damage function of the neutron rises below that value, due to neutron capture for which the emitted gamma results in a recoil energy of about 1 keV. For spectra to be expected in the inner detectors of LHC, it does however not play a significant role.
The interaction of incident particles with the silicon layer leads to:

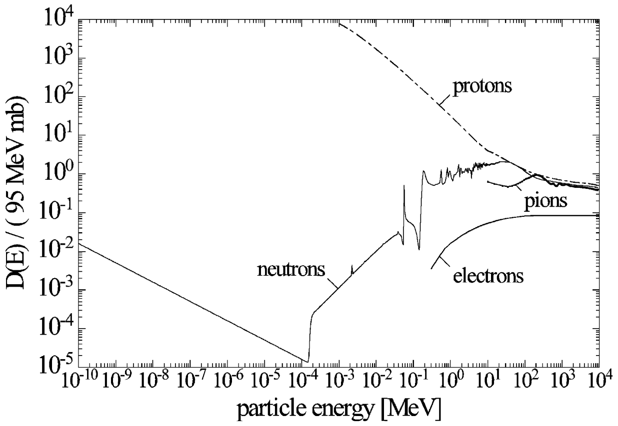


Figure 7.11: *Most reliable evaluation of the displacement damage functions for neutrons, protons, pions and electrons as recommended by the ROSE collaboration [2, 14].*

- Reverse current increase, proportional to the equivalent 1 MeV neutron fluence.
- Inversion of the conduction type (i.e. a starting $n$-type material becomes $p$-type). This inversion produces a dramatic change of the depletion voltage (needed to maintain a full sensitivity over the whole detector thickness). It can happen that the depletion voltage becomes larger than the operational voltage and the detector has to be operated in partial depletion.
- Creation of defects acting as trapping centers. This affects the charge collection efficiency, reducing the signal height and thus worsening the signal to noise ratio. For silicon detectors this is less problematic than the two above effects, since the operational voltage can be raised to guarantee a sufficiently high electric field throughout the detector thickness.

To avoid a strong raise of the noise (and an increase in power consumption and heat dissipation) the silicon detectors will be cooled. It will be needed not only during the operational beam periods, but also during stand-by periods, which should not exceed two weeks [2]. Operation at low temperatures and utilization of a process technology allowing high-voltage operation are conventional methods for guaranteeing the design criteria during 10 years of LHC operation. It has been found that a high oxygen doping concentration leads to an improved radiation hardness of the bulk material. With this new material the operation of pixel detectors at distances about 10 cm from the interaction vertex can now be assured [12].

### 7.5.2 Irradiation of a-Si:H

It was in 1977 when Staebler and Wronski measured that electrical and optical properties of a-Si:H were affected by photon irradiation [15]. They showed that the dark conductivity and photoconductivity of a-Si:H films were reduced by prolonged illumination with intense visible light and recovered by thermal annealing. Since this report, induced metastable changes in the properties of a-Si:H are referred to by the name Staebler-Wronski effect (SWE). The SWE is intimately related to the presence of metastable defects[4] in the middle gap. The explanation and modeling of the SWE was given by Stutzmann *et al.* in reference [16]. They assume that new metastable defects dangling bonds ($D^0$,$D^+$, $D^-$) are created by the fraction of nonradiative, direct tail-to-tail recombination transitions (noted as $A_t$ in figure 3.8). In undoped a-Si:H the defects are neutral $D^0$ singly occupied states. In n-doped a-Si:H the defect are predominantly negatively charged doubly occupied $D^-$ states while in $p$-type silicon the defects are $D^+$, unoccupied states. For a more detailed view of the SWE refer to section 3.4.

In the early work on a-Si:H there were studies of defect creation by charged particle bombardment. These studies can not be compared to the well structured and systematic studies existing for the c-Si. Furthermore, the tests were proposed to study particular details of the properties of a-Si:H with the radiation fluence. There is no modeling of the interaction of radiation with the a-Si:H and some contradictory results have been published. Clear evaluation of damage effects are not yet available. What seems to be clear is that the bombardment induces dangling bonds either by ionization (gamma rays) or atomic displacement (electrons, $\alpha$-particles, protons) and its effects are reversed by annealing [17]. Following subsections review the effect of neutron, gamma and proton irradiation on a-Si:H through the work referenced in [18]-[23].

#### Gamma irradiation of a-Si:H

In reference [18], *in* and *ip* type amorphous silicon are deposited on a substrate of Al on glass. On top of the intrinsic silicon, aluminium electrodes were also deposited. Film thickness of silicon was 1 $\mu$m and the deposition temperature 200°C. Gamma-ray fluences ranged from $10^{16}$ to $10^{17}$ photons/cm$^2$. After irradiation both samples became $p$-type. Measurements of the number of defects showed a remarkable increase of three orders of magnitude of $D^+$ states, produced by the processes $D^0 \rightarrow D^+ + e$ and $D^- \rightarrow D^+ + 2e$. The electrons contribute to increase the photoconductivity of the device as well as the dark conductivity.

Reference [19] establishes a parallelism between gamma radiation damage in a-Si:H and the SWE. The tested samples are glow-discharge a-Si:H deposited on a substrate at temperature 200 °C, structured as: Pd/undoped a-Si:H/P-doped a-Si:H/ITO/Corning 7059 glass. The total fluence was $10^{18}$ photons/cm$^2$. Measurements show a sublinear increase of the number of $D^0$ dangling bonds [5] with the fluence. The mobility-lifetime product (proportional to the photoconductivity) decreases, one order of magnitude, linearly with the density of neutral dangling bonds. After the $\gamma$ irradiation the samples were light soaked with an intense Ar ion laser at 488 nm. It was observed that the decrease of the photoconductivity is remarkably slower than for fresh samples. Our interpretation is that the irradiation leads to ionization, and the photoconductivity quench is induced by the reaction $D^+ + e^- \rightarrow D^0$.

#### Neutron irradiation of a-Si:H

Neutron irradiation of the $Si^{30}$ can induce a nuclear reaction known as neutron transmutation doping (NTD). NTD might be used as a doping method, by means of the following reaction

[4] Local minima of the energy of the semiconductor. Transitions to these levels can be stimulated by illumination.

[5] $D^0$ are the only defects which are detectable using the electron spin resonance -ESR- technique, employed by these authors.

$$Si^{30}_{14}(n,\gamma) \rightarrow Si^{31}_{14} \xrightarrow{\beta^-} P^{31}_{15}$$

where isotope $Si^{31}$ is unstable with half decay time of 2.63 h. Different authors succeeded [20] or failed [21] reproducing this phenomenon. Most recent reference [21] reports a five order of magnitude decrease of the dark conductivity and photoconductivity for radiation fluences between $10^{14}$ and $10^{18}$ neutrons cm$^{-2}$. a-Si:H samples were prepared by glow discharge at 250°C. The thickness of the sample was 400 nm, and quartz glass was employed as substrate. The photoconductivity was recovered after annealing at 190°C for 90 minutes.

### 7.5.3 Proton irradiation of a-Si:H

The radiation damage by 12 MeV protons at fluences between $10^{13}$ and $7\times10^{15}$ and annealing of a-Si:H are studied in reference [22]. Thin films of a-Si:H (from 0.7 to 2 $\mu$m thickness) were deposited by glow discharge on 8 $\mu$m Al foils. On top, semitransparent metal dots (Schottky diodes) of Pd or Cr 2 mm in diameter formed the top contacts. As a result of the irradiation, the short circuit current decreases by one order of magnitude and the optical absorption increases for $\lambda > 827$ nm (sub-band gap absorption). This reflects an increase in midgap state density. The relation between defect creation and proton fluence is sublinear. After a thermal anneal for 12 minutes at a temperature of 200°C the short-circuit current recovered to about 85% of its initial value.
Finally, $n$-type a-Si:H thin films deposited using plasma enhanced chemical vapor deposition on 7059 Corning glass were irradiated [23]. The temperature was 270 °C and the energy of the Helium ions was 2 MeV. The ion fluence ranged from $10^{11}$ to $10^{15}$ cm$^{-2}$. Large changes in the optical absorption for wavelengths between 730 and 1400 nm were observed. The steady-state photoconductivity showed decreases of almost five orders of magnitude for a fluence of $10^{15}$ cm$^{-2}$. The detailed study done by the authors reveals that the result of irradiation is an increase of the defect density, without increase of the disorder of the system (which is related with the slope of the valence band [24] -see also figure 3.8 left-). For temperatures greater than 175 °C the damage is completely annealed.

### 7.5.4 c-Si and a-Si comparison

In reference [17], c-Si diodes 255 $\mu$m thick are irradiated with a neutron fluence of $10^{13}$ cm$^{-2}$. The diode failed while a fluence of $4 \times 10^{14}$ cm$^{-2}$ on a 12 $\mu$m a-Si:H pin diode produced 20% change in signal, with an increase of a factor ten of the leakage current. Besides, effects on a-Si were fully annealed after 180 °C annealing. Hanak *et al* [25], using 1 MeV protons, concluded that a-Si:H diodes (solar cells) were 50 to 100 times more radiation resistant than c-Si and GaAs cells. On the other hand, [22] questions a-Si being more radiation resistant than c-Si.

## 7.6 The effect of irradiation on semitransparent amorphous-silicon sensors

Located within the tracker, 2D semitransparent amorphous silicon sensors are used to tag spatial positions of the beam light. Efficient reconstruction of the system is achieved only if the optical properties and performance of these sensors do not change with the irradiation.

We have irradiated [26] with gamma-rays and neutrons two different sensors: one having a single a-Si layer (Schottky sensor) and a second one constructed with 3 a-Si layers (*pin* sensor). The structure of the sensors was already discussed in detail in chapter 3. Once the gamma irradiation was completed, the two sensors underwent an irradiation with fast neutrons.
For all the tests presented here, the sensors were not powered during the irradiation. After each iteration we measured the optical properties of both samples, namely light deflection and transmittance. The response to uniform white light was recorded for the Schottky sample, since it was equipped with electronics.

### 7.6.1 The irradiation

As for the other optical elements, the gamma-ray irradiation was done at the NAYADE facility of CIEMAT using $^{60}$Co sources. The gammas were produced by $^{60}$Co sources delivering a total flux of 3 kGy/hour. The total dose was 100 kGy, which corresponds to the expected accumulated dose in c-Si after 10 years of CMS operation at the maximum luminosity ($10^{34}$ cm$^{-2}$s$^{-1}$). The irradiation was done in steps of 100 Gy and 10, 15, or 20 kGy. Photon energies from $^{60}$Co are 1.17 and 1.33 MeV. The Schottky sensor was equipped with front-end electronics, while the other sample was just the bare *pin* stack on glass.
The neutron irradiation made use of the fast neutron source based on the MGC-20 cyclotron [27] facility available at ATOMKI (Debrecen, Hungary). The neutrons were produced by p(18 MeV)+Be reactions. The fluence was $1.1 \times 10^{15}$ neutron cm$^{-2}$ (pessimistic estimation of the fluence expected after 10 years of CMS operation at the maximum luminosity). The mean energy of the broad spectrum source was 3.7 MeV with a typical flux of $1.6 \times 10^{9}$ cm$^{-2}$ s$^{-1}$. The spectral intensities and the angular distributions of this neutron source [28] were used to plan de irradiation. Neutron transport calculations were carried out by using MCNP-4B transport code [29] in order to prepare the geometry for irradiation. During the irradiation an aluminium disk (13 mm diameter and 0.76 mm thickness) was placed behind the sensors and the $^{27}$Al (n,$\alpha$) $^{24}$Na reaction was used as a fluence monitor. The irradiation was done in two exposure periods: first one with a fluence of ($1.1 \times 10^{14} \pm 12\%$) cm$^{-2}$, followed, a few months later, by a second dose of ($10^{15} \pm 37\%$) cm$^{-2}$ in three fractions.
The last three fractions could only be delivered in the target neighborhood (at about 70 mm sample-source distance) where the longitudinal and transverse gradients of the neutron field were rather high. For these fractions, the sources of the large uncertainty on the total neutron fluence are:

1) the uncertainties on the sample positioning during the three fractions $\approx$ 15%,
2) the flux heterogeneity $\approx$ 15%,
3) the fluctuations in the current density distribution of the incident proton beam $\approx$ 5%,
4) the uncertainties on the activity measurements $\approx$12%,
5) the uncertainties on the nuclear data used $\approx$10%
6) the uncertainty on the estimation of the neutron fluence below 0.3 MeV $\approx$25%.

The spectrum of the associated photons could not be measured directly and, therefore, precise calculations of the absorbed dose are not feasible. However, an additional dose of 5 kG $\pm$

37% was estimated from human muscle equivalent material using the so-called twin-chamber technique [30].

### 7.6.2 Experimental set-up for optical measurements

The experimental set-up for optical measurements consisted of a He-Ne (633 nm) laser, the sensor under test, located at a distance of about 0.6 m from the laser, in the light path, and a second position detector (a Schottky sensor) located 2.58 m downstream the first sensor. The second sensor reconstructs the light spot and measures the deflection angle originated by the first one, by measuring in advance, the position of the laser light spot in the absence of the first sensor.

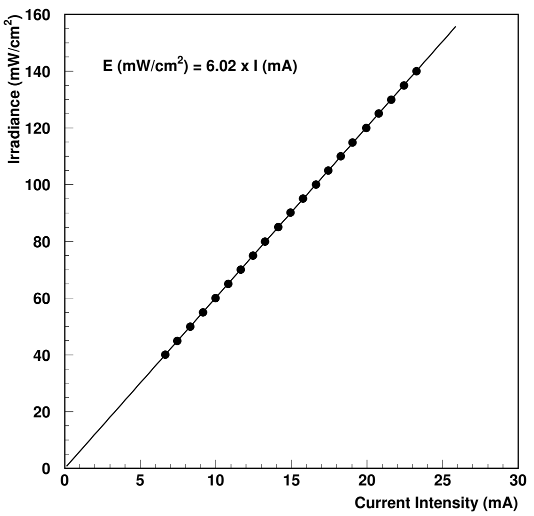


Figure 7.12: *Photocell calibration (see text).*

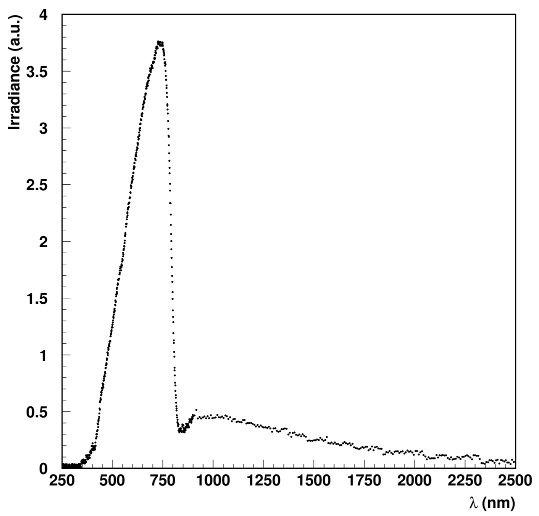


Figure 7.13: *Halogen lamp irradiance spectrum.*

In order to account for the whole active surface ($2 \times 2$ cm$^2$), the sensor under test is placed on two motorized platforms (one vertical and one horizontal) and data are taken over a $16 \times 16$ matrix of points (1 mm pitch). The motorized platforms have 2 $\mu$m resolution. The broad step employed reduces the scanning time and thus contributes to minimize any beam motion originated by a beam drift.
The transmittance to the HeNe wavelength is calculated as the ratio between the signal read in the second sensor when the first is in the light path and that in the absence of the first sensor. This method is very sensitive to any laser intensity instabilities and has a typical 10% uncertainty due to the HeNe laser fluctuations.
For the photoresponse test of the Schottky sensor, a white light from a halogen lamp mounted in the focus of a dichroic reflector and coupled to a diffuser was used to illuminate the whole surface. The monitoring of the halogen lamp was done with a photocell whose induced photocurrent

intensity had previously been calibrated. Figure 7.12 shows the irradiance of the lamp as a function of the measured current intensity in the photocell. Data points include measurement errors. The solid line represents a fit of the data points to the function:

$$E(\mathrm{mW/cm^2}) \quad = \quad (6.02 \pm 0.001) \times I(\mathrm{mA}) + (-0.03 \pm 0.08) \tag{7.1}$$

The white light spectrum, in terms of the irradiance as a function of the wavelengths emitted by the lamp, is shown in figure 7.13.

### 7.6.3 Results

**Beam deviation**

Keeping fixed the position of the laser, the sensor under test was scanned over its whole surface using the motorized platforms. The X and Y positions of the light spot were reconstructed on the farthest sensor. The difference with respect to the reference position (the reconstructed light spot in the absence of the sensor under study) was calculated and divided by the distance between both sensors. In this way, the X ($\theta_x$) and the Y ($\theta_y$) components of the deflected angle were measured for all the points.

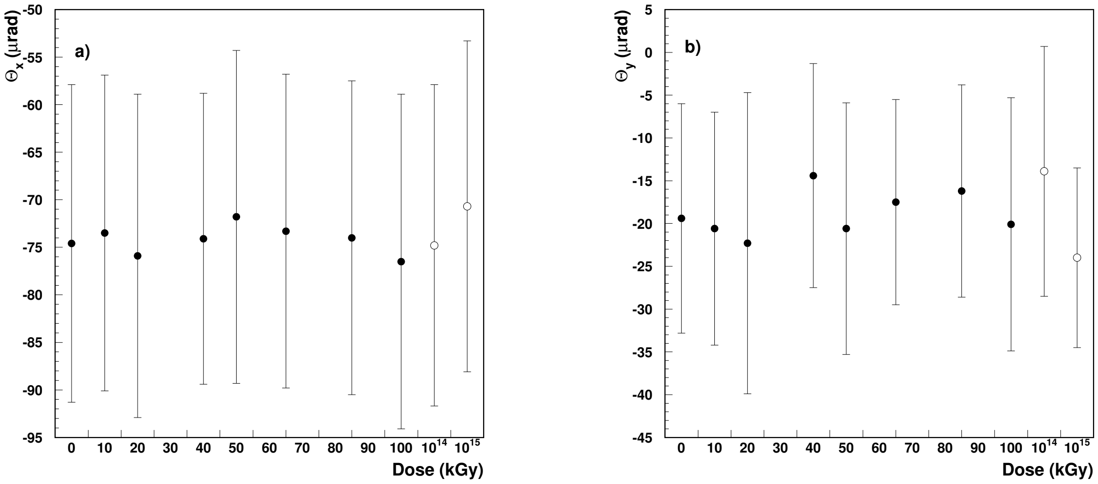


Figure 7.14: *For the Schottky sensor, mean X (left) and Y (right) values of the deflection angles as a function of the absorbed dose*

As seen in section 4.4, the distributions of the deflected angles do not have Gaussian shapes. Figures 7.14 and 7.15 show, as a function of the accumulated dose, the surface-averaged values of the deflection angles for the Schottky and the *pin* sensors, respectively. Angles are given in $\mu$rad. The last two points in the plots correspond to 100 kGy gamma-irradiation plus $10^{14}$ and $10^{15}$ neutrons/cm$^2$. The error bars represent the RMS of the angular distributions. Even within the large dispersion of the measurements (the measurements were done in a removable setup) there is no appreciable change along the irradiation.

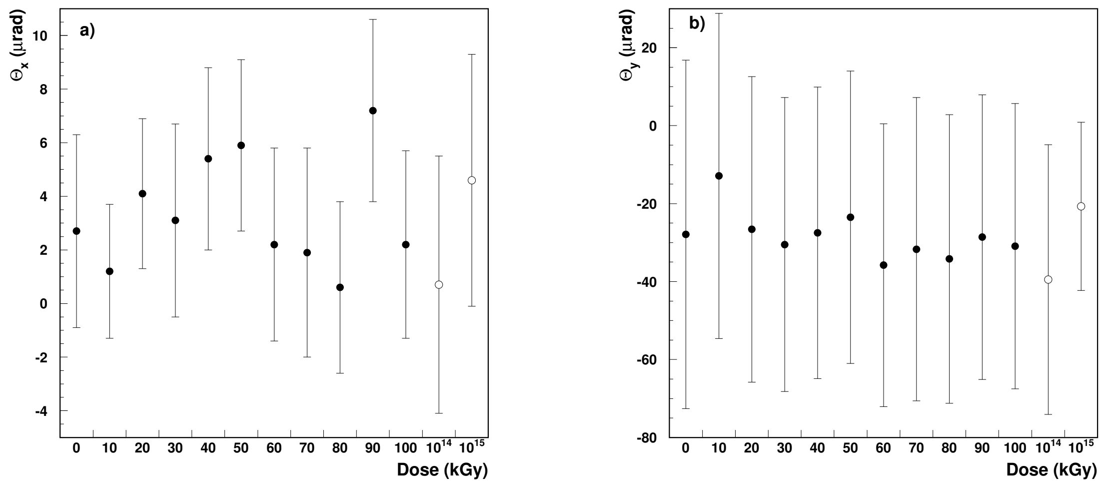


Figure 7.15: *For the* pin *sensor, mean X (left) and Y (right) values of the deflection angles as a function of the absorbed dose.*

### Transmittance

The transmittance at the HeNe wavelength as function of the absorbed dose is given in figure 7.16 left and right, for the Schottky and the *pin* sensors respectively. The transmittance was calculated at each point of the scanned surface and averaged, the error bars representing the RMS of the corresponding distributions. The last two points in the referenced figures correspond to 100 kGy photon irradiation plus $10^{14}$ and $10^{15}$ neutrons/cm$^{-2}$.
From figure 7.16 it can be concluded that, within the large fluctuations observed, a small (if any) degradation occurs (less than 10%) at the beginning of the irradiation with photons not evolving any further even after the complete irradiation exposure to photons and neutrons. The degradation in transmittance is not dramatic, as it will be shown in section 7.6.4. It is tempting to think that this degradation of the transmittance is related to a darkening of the glass and not to the creation of dangling bonds since, as shown in figures 4.39 and 4.40, the raise of dangling bonds density does not affect the transmittance.

### Electronics

The Schottky sensor was equipped with some nearby electronics located on its frame, consisting of multiplexers, resistors and capacitors.
The multiplexers were DG406 (16 to 1) from SILICONIX. All of them malfunctioned with gammas after an accumulated dose of 200 Gy.
However, resistors and capacitors survived after completion of the irradiation (photons plus neutrons). The resistors are surface-mounting devices (SMD), made of nicrom packaged in ceramics, with a resistance of 47 k$\Omega$. They act as bias resistors for the sensors. The capacitors are multilayer ceramics SMD. Their capacitance is 0.1 $\mu$F. They act as multiplexer bypass capacitors.
Prior to each irradiation the multiplexers were unwelded and removed from the front-end electronics of the Schottky sensor.

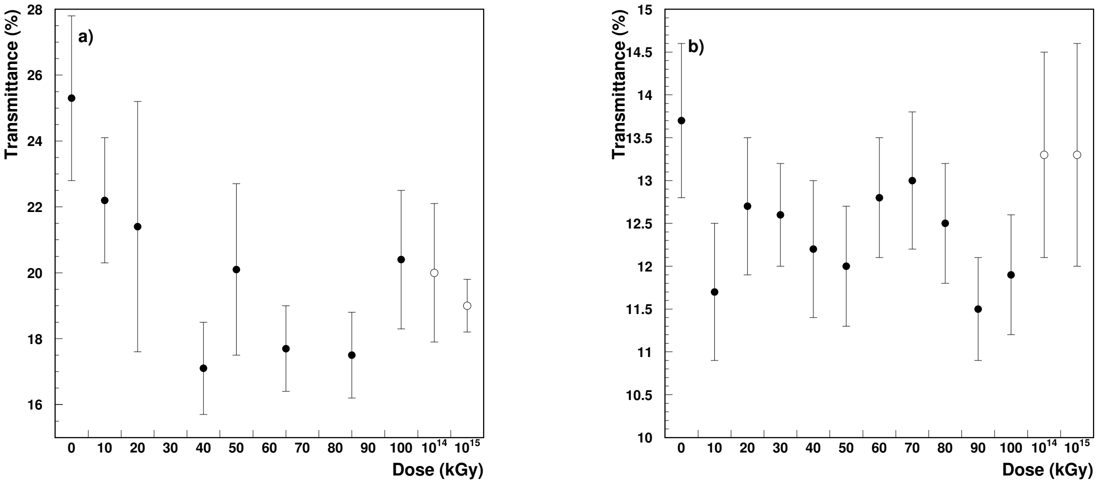


Figure 7.16: *Transmittances as a function of the calculated dose for Schottky sensor (left) and* pin *sensor.*

### Response

The response of the Schottky sensor was measured before starting the gamma irradiation and after a few steps, using the uniform white light mentioned above. These measurements were done illuminating the sensor through the glass substrate face and with an irradiance of 0.16 mW/cm$^2$. Measurements after each neutron irradiation step were done in the same experimental conditions. The time lapse between neutron irradiation and measurements was about 1 month and therefore some annealing processes most probably took place even at ambient temperature.

Since the laboratory was not completely dark, a first measurement was done with the uniform light source off. Then, the lamp was switched on, the irradiance was measured with the photocell and new data were taken. The response from every strip was recorded and the background subtracted. The values measured were uniform among the strips. Mean values are:

| | | |
|---|---|---|
| S(ADC counts) | $= 196.1 \pm 4.1$ | before irradiation |
| S(ADC counts) | $= 195.9 \pm 3.9$ | at 200 Gy (gammas) |
| S(ADC counts) | $= 174.6 \pm 4.6$ | at 10 kGy (gammas) |
| S(ADC counts) | $= 176.9 \pm 4.9$ | at 100 kGy (gammas) |
| S(ADC counts) | $= 140.4 \pm 8.0$ | at 100 kGy gammas and $10^{14}$ neutrons/cm$^2$ |
| S(ADC counts) | $= 121.9 \pm 7.2$ | at 100 kGy gammas and $1.1 \times 10^{15}$ neutrons/cm$^2$ |

As from 10 kGy photons, a degradation of about 10% is detected. The $10^{14}$ cm$^{-2}$ neutron irradiation adds a 20% additional decrease in the sensor response, and the further $10^{15}$ cm$^{-2}$ neutrons still decreases the signal by another extra 15%. In total, the signal after 100 kGy and $1.1 \times 10^{15}$ neutrons/cm$^2$ , represents about 60% of the initial one.

### 7.6.4 Comparison between irradiated and non irradiated Schottky sensors

For completeness we have compared the response and the transmittance, to uniform white light, of the irradiated sensor with the same magnitudes measured on two other Schottky, non-irradiated, sensors.

#### Response

The sensors were illuminated with the uniform white light on both faces. The irradiance was kept constant at 0.46 mW/cm$^2$, close to saturation, to increase the output current.

The comparison is shown in figure 7.17. The figure is divided in two parts: on the left hand the results after illumination of the sensitive face, on the right hand the measurements done illuminating the sensor through the glass substrate face. Labels A, G and D are arbitrary names for the three sensors. Letter D corresponds to the irradiated one. $D_{14}$ and $D_{15}$ correspond to the measurements after 100 kGy photons and $10^{14}$ and $10^{15}$ neutrons/cm$^2$, respectively.

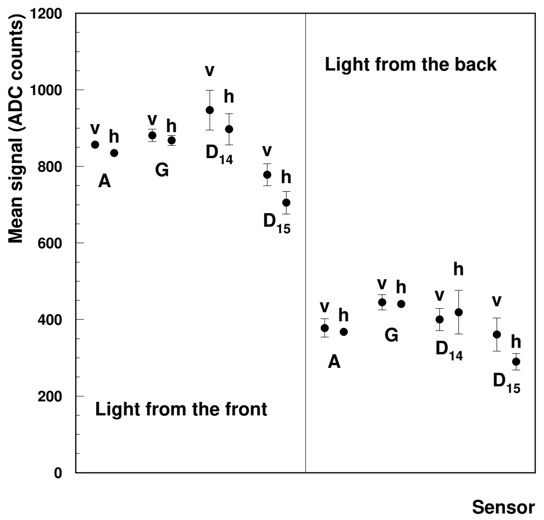


Figure 7.17: *Comparison of the responses of non-irradiated (A and G) and irradiated (D) Schottky sensors (see text).*

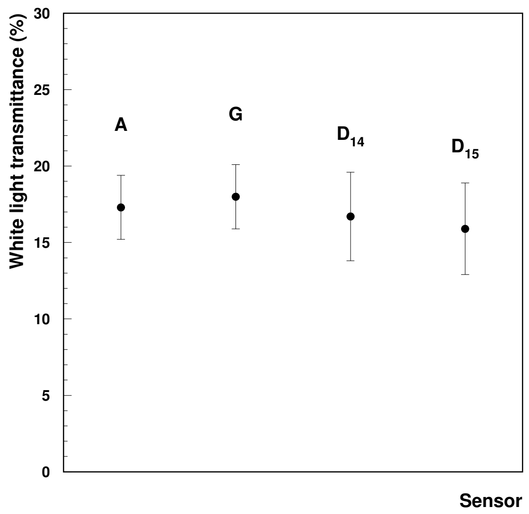


Figure 7.18: *Comparison of the transmittance of non-irradiated (A and G) and irradiated (D) Schottky sensors (see text).*

Data points are the average values of the signals read from the 64 vertical (v) and the 64 horizontal (h) strips. Error bars are the RMS of the corresponding distributions. Data show, in general, a good response uniformity among strips. Sensor D shows a clear response degradation after the $10^{15}$ neutrons/cm$^2$ irradiation step.

#### Transmittance

Using the white light source we have measured the transmittance of the irradiated and non irradiated Schottky sensors by installing the photocell in front of and behind the sensors. The intensity of the current in the photocell is measured in both positions and the ratio is taken as the transmittance of the sensors to the integrated white light spectrum shown in figure 7.13.
The comparison of results is given in figure 7.18. Within the errors (representing the RMS of various measurements) the transmittance values are compatible among them.
From the comparison of the response and transmittance of the irradiated sensor to those of two other (non irradiated) Schottky devices, it is concluded that, within the errors, their responses and transmittances to an uniform white light are not inconsistent. This fact evidences that the construction of sensors is not very uniform, but also, that the irradiation (up to doses applied) will not spoil sensor performance for the application foreseen.

## 7.7 Future actions

The irradiation tests presented were intended to validate the utilization of the tested components. During these tests, we did not monitor ALMY properties on-line, partly due to the absence of electronics able to survive the unprecedented doses expected for LHC. Our tests show that ALMY sensors are radiation tolerant, at least after room temperature annealing. We are planning new tests with electronics far away from the radiation source that will allow to study the damage development. Further irradiation tests will be carried out with protons at the 24 GeV/$c$ proton primary beam of the CERN-PS [31] and pions somewhere else.

# Bibliography


[1] The CMS Collaboration, *The Tracker Project. Technical Design report* CERN/LHCC 98-6, CMS TDR 5, 15 April 1998.

[2] G. Lindström, M. Moll, E. Fretwurst, *Radiation hardness of silicon detectors – a challenge from high-energy physics*, Nucl. Instr. and Meth. A 426 (1999) 1-15.

[3] A. Ostapchuk, S. Schael, *An alignment system for the CMS tracker* http://accms04.physik.rwth-aachen.de/~cms/alignment.html

[4] The CMS Collaboration. *The Electromagnetic Calorimeter Project. Technical Design Report*, CERN/LHCC 97-33.

[5] The CMS Collaboration, *The Muon Project. Technical Design Report*, CMS TDR 3, CERN/LHCC 97-32. 15 December 1997.

[6] The CMS collaboration, *Addendum to the CMS Tracker TDR*, CERN/LHCC 2000-016, CMS TDR 5, Addendum 1. 21 February 2000 http://cmsdoc.cern.ch/~marica/addendum.pdf

[7] Detailed description may be found in: http://hyperphysics.phy-astr.gsu.edu/hbase/geoopt/glass.html

[8] Schott Corporation, 3 Odell Plaza, Yonkers NY10701 http://www.schottglass.com

[9] Measurements done with a Perkin-Elmer Lambda 9 spectrophotometer at CIDA (Madrid, Spain).

[10] Digital Electronic Automation, Inc.

[11] Research and development On Silicon for future Experiments http://rd48.web.cern.ch

[12] Michael Moll, *Radiation Damage in Silicon Particle Detectors –microscopic defects and macroscopic properties –* , Universität Hamburg, Ph.D. Thesis, 1999. (http://sesam.desy.de/~moll/thesis/index.html)

[13] Victor A.J. VAN LINT, *The physics of radiation damage in particle detectors*, Nucl. Instr. Meth. A253 (1987) 453-459.

[14] Angela Vasilescu, Gunnar Lindström, *Notes on the fluence normalization based in the NIEL scaling hypothesis*, ROSE/TN/2000-02 June 2000.

[15] D.L. Staebler and C.R. Wronski, Appl Phys. Lett. 31, 292 (1977).

[16] M. Stutzmann, W.B. Jackson, and C.C. Tsai, *Light-induced metastable defects in hydrogenated amorphous silicon: A systematic study* , Phys. Rev. B 32, 1 23-46.

[17] Shafi Qureshi, *Hydrogenated amorphous silicon radiation detectors: material parameters; radiation hardness; charge collection*, January 1991, LBL-30292.

[18] O. Imagawa, K. Yasuda, A. Yoshida *Gamma-ray irradiation effect in amorphous hydrogenated silicon*, J. Appl. Phys. 66 (10), 15 November 1989.

[19] J. Shirafuji, S. Nagata, K. Shirakawa *$\gamma$-Irradiation Effect on Electronic Properties in Hydrogenated Amorphous Silicon*, Phys. Stat. Sol (a) 98, 311 (1986).

[20] H.Hamanaka *et al.*, Appl. Phys. Lett. 45 (1984) 786

[21] Wang Shulin *et al.*, *Study of neutron irradiated a-Si:H*, Chinese Phys. Lett. Vol. 7, No.9 (1990) 418

[22] R. Schwarz, J. Kolodzey, S. Aljishi and S. Wagner, *Radiation damage by 12 MeV protons and annealing of hydrogenated amorphous silicon*

[23] J. Scott Payson, James R. Wooyard, *Radiation resistance studies of amorphous silicon films*

[24] S. M. Sze *Physics of Semiconductor Devices*, Ed. John Wiley & Sons, Second Edition.

[25] J. J. Hanak, E. Chen and A. Myatt, *Nineteenth IEEE Photovoltaic Conf.*, (1987) New Orleans.

[26] J. Cárabe *et al. Results on photon and neutron irradiation of semitransparent amorphous-silicon sensors*, NIM A 455 (2000) 361-368.

[27] A. Fenyvesi et al., Z. Medizinische Physik 1 (1991) 1.

[28] M.A. Lone et al., Nucl. Instr. and Meth. A143 (1977) 331.

[29] J.F. Breismeisteir, *MNCP, A General Montecarlo N-particle code*, LA-12625-M, March 1997, Los Alamos National laboratory.

[30] .J. Boerse et al., British Journal of Radiology 54 (1981) 882.

[31] M. Glaser *et al.*, *New irradiation zones at the CERN-PS*, Nucl. Instr. and Methods A 426 (1997) 72-77.

# Chapter 8

# ISR Tests Results

## 8.1 Introduction

Position sensing detectors and tiltmeters are crucial elements for the proper functioning of the CMS alignment system. Their combined operation will allow to monitor the position of the different tracking detectors and will report their relative orientation in $\phi$. In the current CMS alignment baseline more than 100 transparent position sensors will be used to measure the position of the light spot arising from the laser sources. The $\phi$ orientation of MAB and tracker structures will be measured employing tiltmeters (minimum of 24 for Link and Tracker). The amount of sensors foreseen and the complexity of the system make wise to study the performance of a full-minimum arrangement that contains these relevant components. Such arrangement was set up in the ISR hall at CERN.
The real scale test was devised as a simplified version of one half of a CMS R-Z plane containing all the relevant elements for the position monitoring: a tracker zone, a one half of active plane of the Barrel system and two Endcap lines plus the connection between them and the Link lines.
The pursued goal after the ISR test is the estimation of the system performance and measurement accuracy. Prior to it, the calibration and validation of individual components at home institutes was performed. Calibration and characterization of transparent position sensors and tiltmeters has been thoroughly studied in former chapters. Here we will present the results from calibrations of the rest of Link System sensors. The overall performance and accuracy of of the system will be presented elsewhere [1].

## 8.2 The ISR preamble

In spring 1999, we performed a very preliminary approach to the ISR test. The idea behind this experience was to study the environmental conditions in the hall and perform a calibration of a first laser box (light source unit) prototype composed by a laser diode and a beam splitter cube sending two rays at 95 arc deg. The calculation of the angle was done employing transparent position sensors. Since relative positions between sensors must be known, we employed a network of surveyed points. Five concrete blocks were utilized to define the survey network. The positions of the blocks reproduced the CMS Link geometry near the laser beam at $\eta = 3$.
A survey network is made of a number of instrumented points whose coordinates are referred to a common 3D frame. Typical precisions obtained with these methods are in the 10-50 $\mu$m range, depending on the technique employed. On top of the concrete blocks, CERN standard

Figure 8.1: *Standard survey socket. This module allows insertion of units in a repeatible way (error ∼30 μm).*

Figure 8.2: *ALMY sensor −front and backside−. The center of the sensor is known better than 1 μm. The tail is inserted inside the hollow of the socket shown in figure 8.1.*

mechanical survey sockets were employed (see figure 8.1). The interface between the survey sockets and the position sensors required embedding the sensors within squared frame supports with tails (see figure 8.2). By using an optical technique called “fiducialization”, the geometrical center of the sensor 2D sheet can be known with an accuracy of 1 $\mu$m. The tail allows the ALMY sensor to be inserted within the survey sockets with a repeatibility of 20-30 $\mu$m.

Several stability measurements were performed, using two sensors in the farthest positions from the laser source (4 and 6 m, depending on the branch, as seen in figure 8.3). The environmental conditions, temperature, atmospheric pressure and relative humidity were controlled revealing quite stable conditions all along the tests period. The measurements done under these conditions show that the stability of the light spot on position sensors was better than 5 $\mu$m for measurement periods of up to 12 hours.

Some changes in the environmental conditions were consciously induced. Air flows degrades significantly the spatial resolution ($\sim$5 $\mu$m) but an homogeneous background light did not degrade the spatial position resolution.

Employing two ALMY sensors per branch, and taking the effect of the beam deflection into account, the angle between rays of a first laser box with two branches (see figure 8.3) was measured. The measured angle between rays was 95.0195 arc deg, the experimental accuracy was 14 $\mu$rad, the repeatibility of several measurements being about 4 $\mu$rad.

## 8.3 The ISR facility

The ISR tests started at the beginning of the spring 2000. The ISR test was divided into three working periods. Previously the hall was conditioned and the concrete blocks (supporting the network sockets and the instrumentation) placed at the experimental area.

The first period included the months of May and June 2000. By middle of May the installation of the different components of the Link System (see chapter 2) started, including the Data Acquisition System, laser sources, periscopes, tubes, proximity sensors, tiltmeters, temperature sensors and three fiducialized 2D ALMY sensors.

In May, a first calibration of the network, including coordinates of the Link and Barrel points plus distance measurements. The aim of this preliminary set-up was first to test the acquisition system, and second, to calibrate in-situ the Laser sources and periscope prototypes. These calibrations could not be afforded elsewhere, due to the space restrictions. Second and third periods dealt with global measurements of the system.

The calibrations carried out in the ISR hall took advantage of the precise definition of the survey network. The CMS $\phi$ direction was set vertically, benefiting of the more precise measurements provided by optical levelling. An aerial view of the hall and the network is shown in picture 8.4. Several rounds of survey and photogrammetric measurements were done along the test period with the aim of evaluating the stability of the network and prove some calibrations of components. The stability of the network for 5 months was of about 100 $\mu$m. The different measurements obtained for the points can be found in [2].

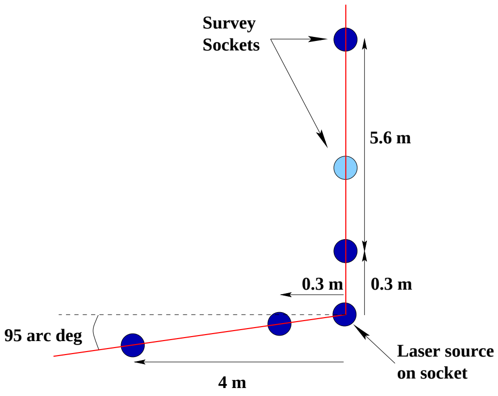


Figure 8.3: *The ISR setup during year 1999 (ISR preamble). Five reference points (shaded) are employed for the calibration of the angle between branches. The extra point was utilized for stability measurements.*

Figure 8.5 represents the symmetric $-Z/+Z$ sides of half of an alignment $\phi$ plane. Only the left side (-Z) was almost fully instrumented: the ME/1/1 transfer was skipped and the ME1/2 chamber was mimic with two sensors in line. On the other hand, a large plate was used as mock-up of the MABI. At $+Z$, two ALMYs fake the length of a MAB. Concerning the Link System, the set-up was integrated by 2D position sensors, laser sources, periscopes, distance measurement elements (tubes and proximity detectors), a laser level prototype, tiltmeters, temperature sensors and the data acquisition system. These elements were distributed over 10 system positions (shaded locations in figure 8.5) plus other 10 aiding points (empty boxes). The notation for each point is also shown in figure 8.5.

Three different laser sources, 780 nm nominal working wavelength, sitting at FI, FII and MABI2 (figure 8.5) were employed. The output power prior to the injection in the monomode fibers was 10 to 20 mW. Laser sources FI and FII were equipped with mechanical choppers, establishing thus an ordered sequence in the illumination of the sensors. Transparent position sensing detectors (ALMYs) were mounted using special mechanical frames plus supports at system sockets.

Periscopes in the alignment system of CMS are floating elements which lead the laser beam from $|\eta| = 3$ along the outer contour of the inner tracker (old Tracker alignment system layout). In the ISR test we had two periscope versions available, one of them built within specifications,

Figure 8.4: *Picture of the ISR hall taken during the setup of the Link System. Concrete blocks of different heights represent locations of CMS were alignment components will be utilized.*

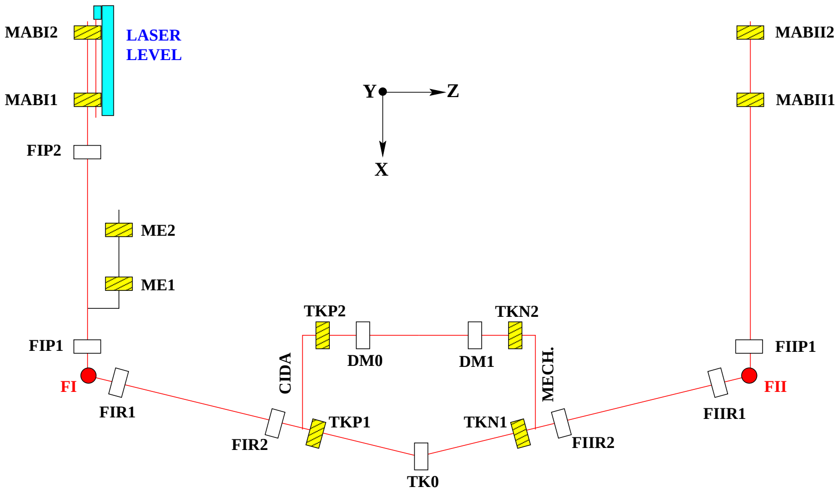


Figure 8.5: *Schematics view of the ISR laboratory Link test layout. Shaded boxes correspond to real system positions. Empty boxes are aiding points employed for the calibration of Link components. Each one of these points lay on top of weighted concrete blocks. Labels for each position are specified.*

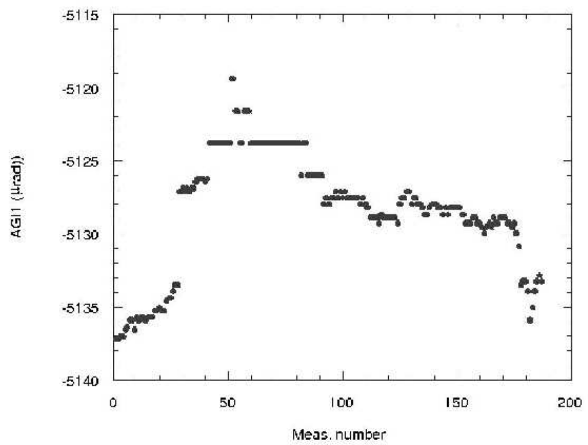


Figure 8.6: *Long term stability of an AGI sensor located in the Laser Level unit at the MAB.*

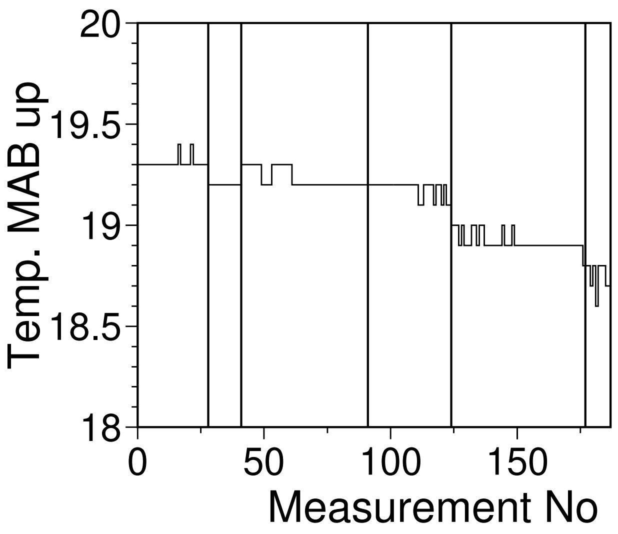


Figure 8.7: *Temperature stability during a 3 days period. Vertical lines separate different periods of time.*

called CIDA periscope, the other made of spare parts and called mechanical periscope. Their positions are marked in figure 8.5. A two dimensional AOSI tiltmeter was attached to CIDA periscope. Two 1D AOSI tiltmeters were coupled to the mechanical periscope.

The MAB structure was equipped with a Laser Level prototype made of a 1D AGI tiltmeter and a laser beam illuminating the rear side of ALMY sensors MABI2 and MABI1, in this order. A second AGI tiltmeter was left untouched near the left MAB structure. The AGI1 tiltmeter mounted as part of the Laser Level prototype showed a stable response over the whole data taking time (17 hours approximately). The output of the tiltmeter, already converted to angular units, can be seen in figure 8.6. The peak near measurement number 50 corresponds to a manipulation of the MAB structure.

Distance measuring sensors for short range measurements at the end of large monitored hollow tubes were employed for measurements of coordinates R and Z. Two different kinds of tubes were employed: a low cost aluminum tube, for the Z measurement and a much more expensive carbon fiber tube for R measurements. Both of them were equipped with temperature probes to enable gradient corrections. Distance measurements are aimed to obtain distances FIR1-FIR2 and FIP1-FIP2 independently. The short distance measuring sensors use targets either for contacting (if they are contact sensors) or to allow light to be reflected (if they are non-contact sensors).

The temperature environment at the ISR set-up was almost constant during all the measurements. Day/night temperature variations of about 1 degree were measured. Figure 8.7 shows the temperature as measured by a probe sitting in a MAB during three days time period.

The data acquisition system was serial based. ADAM modules allow the setup of a serial bus among devices that do not necessarily employ this protocol. ADAM modules are fast and space and cost saving. The whole data acquisition and synchronization for the Link system was done with a single PC, running LabView under Windows. The signals of the transparent position sensors were digitized by their electronic box and, by means of ADAM modules 4521, connected to a fast RS-485 bus. Signals from proximity sensors, tiltmeters and temperature sensors were digitalized and fed into modules 4017 and 4060. The conversion from RS-485 to RS-232 necessary to establish the communication with the serial port PC was done through ADAM-4520 modules.

## 8.4 Calibration of components

Prior to the utilization of the ISR setup as a validation method for the alignment system, its accurate referenced network was employed for optical calibrations of components that elsewhere could not be afforded. The elements calibrated with the help of the survey network were the laser boxes FI and FII and the two mechanical periscopes. We will give here a brief overview of the calibration procedure and a summary of the results.

### Laser Sources I and II

In the Link system, two parallel rays travel all the way up from the iron nose to the external muon chambers. A third laser beam follows the CMS geometry along $\eta = 3$ and reaches the Tracker.
By means of a beam splitter the first beam emerges at 95 degrees with the incoming beam. Afterwards, a modified rhomboid prism splits and shifts the transmitted beam into two parallel beams traveling close to the endcap and muon chambers.

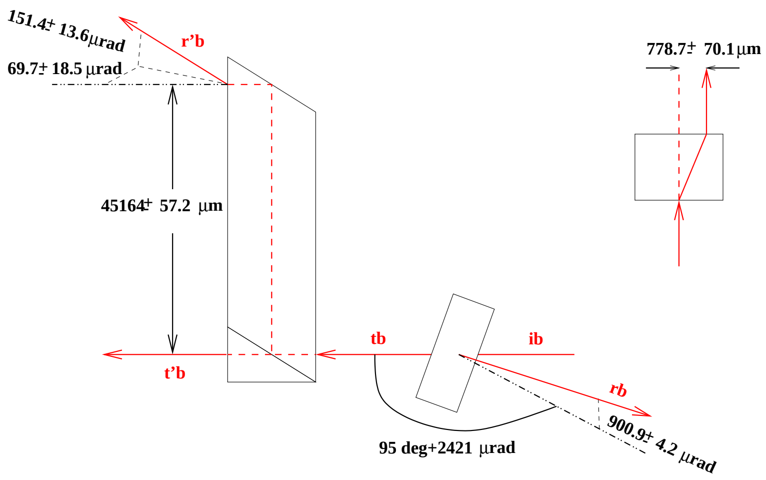


Figure 8.8: *Laser Box I calibration results. The lack of parallelism out of the plane between rays r'b and t'b is ≈ 69.7 μrad and 901 μrad between rays tb and rb. The right inset shows the shift out of the plane between the incoming and outcoming beams.*

The calibration of a laser box consists in the measurement of the parallelism and the exiting distances between rays and relative angle between branches. Later on, these data are employed for

| | Nominal | Measured | Max. required design uncertainty | Experimental reconstruction uncertainty |
|---|---|---|---|---|
| Splitter deviation out of the plane | 0 deg | (900±4.2) $\mu$rad | 25 $\mu$rad | 12.6 $\mu$rad |
| Splitter deviation in the plane | 95 deg | 95 deg +(2421.4±4.7) $\mu$rad | 50 $\mu$rad | 22.1 $\mu$rad |
| Rhomboid shift out of the plane | 0 $\mu$m | (778.7 ± 70.1) $\mu$m | 100 $\mu$m | 115.7 $\mu$m |
| Rhomboid shift in the plane | 4.5 cm | (45164.0±57.2) $\mu$m | 200 $\mu$m | 186 $\mu$m |
| Parallelism out of the plane | 0 deg | (69.7±18.5) $\mu$rad | 65 $\mu$rad | 32.9 $\mu$rad |
| Parallelism in the plane | 0 deg | (151.4±13.6) $\mu$rad | 130 $\mu$rad | 64.5 $\mu$rad |

Table 1: Laser Box I, design specifications and results from calibration measurements

the position reconstruction of the system. The light sensing elements employed for the calibrations were in line fiducialized and network referenced ALMY sensors, allowing the reconstruction of the laser beam directions. The fitted positions on the sensors are employed in the reconstruction software to calculate the several parameters. The results of the calibration for laser box I are interpreted graphically in figure 8.8 and shown in table 1. The aim of the calibration was to know the laser box parameters with an error below the design uncertainty. As we can see from the referred table, the experimental uncertainty falls within design specifications.
According to the ISR layout, the second laser box prototype, called laser box II, had just a splitter plate. For this reason, it just sends two beams. One going to the Tracker and the other directed to the MABII region (see figure 8.5). The measured vertical projection turned out to be 1881.9 ± 3.3 $\mu$rad (was 900.9 in laser box I). The horizontal projection amounted 1703.5 ± 4.7 $\mu$rad (~2421 $\mu$rad in laser box I).

## CIDA periscope

In the CMS Link alignment layout, periscopes allow to shift the laser beam coming from the laser box at $|\eta| = 3$ up to a constant R value.
The periscope calibration consists in the determination of the several angles and distances between incoming and outgoing beams, for a given orientation in space. The correlation between the reflected beam and the orientation of the periscope was also studied. All the calibrated variables uncertainties kept belong design specifications, as shown in table 2. The calibration parameters of the CIDA periscope are depicted in figure 8.9.

## Mechanical periscope

It has already been mentioned (section 8.3) that the second periscope prototype had been built with mechanical pieces fixed by screws. The stability and performance of this element is therefore expected to be worse than the optical periscope (employing a very rigid glass with splitter and

| | Nominal | Measured | Max. required design uncertainty | Experimental reconstruction uncertainty |
|---|---|---|---|---|
| Reflected beam $(\widehat{rb, r''b})_{out}$ | 0 deg | (295±9.2) $\mu$rad | 25 $\mu$rad | 22.0 $\mu$rad |
| Reflected beam $(\widehat{rb, r''b})_{in}$ | 87266.5 $\mu$rad | (87235.0±11.8) $\mu$rad | 50 $\mu$rad | 20.0 $\mu$rad |
| Transmitted beam $(\widehat{rb, t''b})_{out}$ | 0 $\mu$rad | (29.3 ± 9.8) $\mu$rad | No constraint | 24.6 $\mu$rad |
| Transmitted beam $(\widehat{rb, t''b})_{in}$ | 0 $\mu$rad | (21.1±5.3) $\mu$rad | No constraint | 21.2 $\mu$rad |
| r”b shift out of plane | 0 $\mu$m | (155.4±16.2) $\mu$m | No constraint | 63.3 $\mu$m |
| r”b shift in plane | 35.0 cm | (35.6630±0.015) cm | No constraint | 42.2 $\mu$m |
| t”b shift out of plane | 0 cm | (47.1±12.0) $\mu$m | 100 $\mu$m | 64.8 $\mu$m |
| t”b shift in plane | 5.7 mm | (5.80±0.02) $\mu$m | 200 $\mu$m | 42.9 $\mu$m |

Table 2: CIDA periscope, design specifications and results from calibration measurements

| | Nominal | Measured | Max. required design uncertainty | Experimental reconstruction uncertainty |
|---|---|---|---|---|
| Reflected beam $(\widehat{rb, r''b})_{out}$ | 0 deg | (1031.6±32.7) $\mu$rad | 25 $\mu$rad | 30.4 $\mu$rad |
| Reflected beam $(\widehat{rb, r''b})_{in}$ | 87000 $\mu$rad | (86416.0±54.5) $\mu$rad | 50 $\mu$rad | 21.9 $\mu$rad |
| Transmitted beam $(\widehat{rb, t''b})_{out}$ | 0 $\mu$rad | (211.8 ± 12.6) $\mu$rad | No constraint | 26.6 $\mu$rad |
| Transmitted beam $(\widehat{rb, t''b})_{in}$ | 0 $\mu$rad | (221.9±12.0) $\mu$rad | No constraint | 19.9 $\mu$rad |
| r”b shift out of plane | 0 $\mu$m | (4179.2±73.2) $\mu$rad | No constraint | 64.6 $\mu$rad |
| r”b shift in plane | 35.0 cm | (35.5760±0.057) cm | No constraint | 33.9 $\mu$m |
| t”b shift out of plane | 0 cm | (40.2±75.6) $\mu$m | 100 $\mu$m | 64.9 $\mu$m |
| t”b shift in plane | 500 $\mu$m | (437.7±12.4) $\mu$m | 200 $\mu$m | 34.2 $\mu$m |

Table 3: Mechanical periscope, design specifications and results from calibration measurements

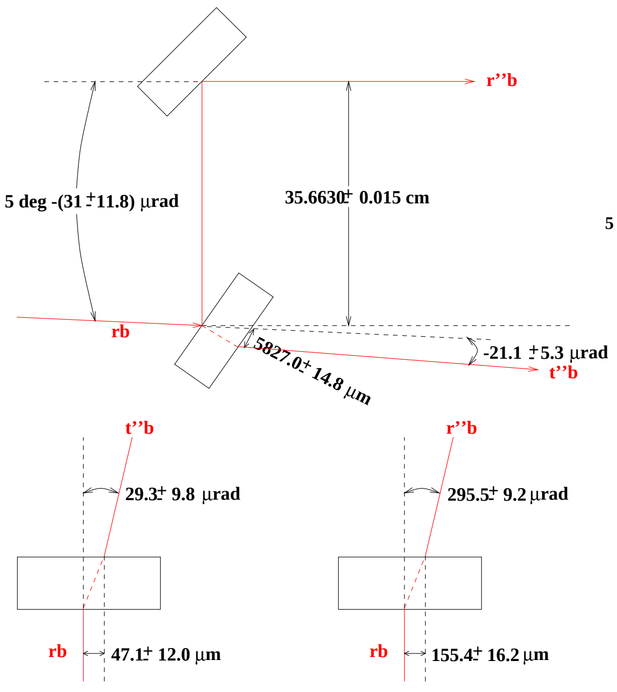


Figure 8.9: *Calibration results for CIDA periscope. The two bottom inserts show the displacement of the beam and the angles out of the plane.*

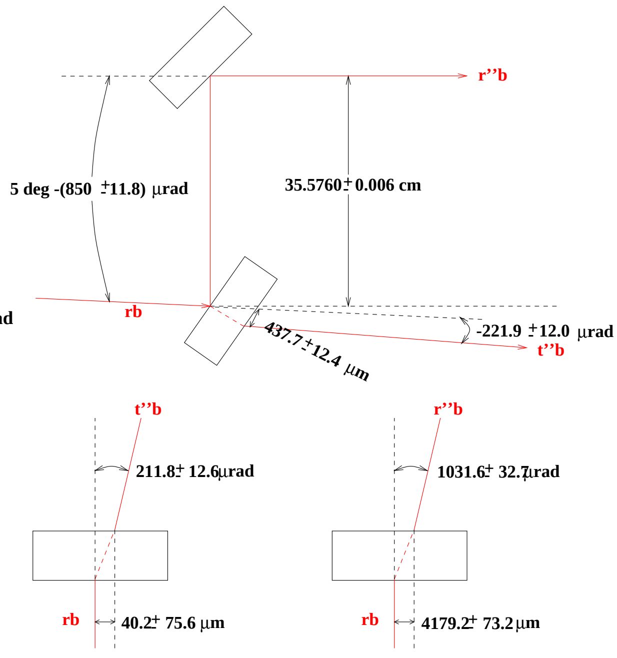


Figure 8.10: *Calibration of the mechanical periscope. Again, the two inserts at the bottom show the parameters that lay out of the plane of the sheet.*

mirror glued). For the calibration of the mechanical periscope we followed identical procedure as with CIDA periscope. The results of the calibration are interpreted graphically in figure 8.10 and explained in table 3, which also summarizes design constraints. It can be realized the worse quality of this prototype as compared to the CIDA periscope measured parameters.

### Distance measurements

In the current alignment concept, the laser boxes are floating objects. It means that their positions are not important provided that the laser beam falls within the active area of the sensors. However, the barrel and endcap alignment systems need to know $(R, Z)$ coordinates of their active elements, relative to the Link System. The Link system can measure the $Z$ coordinate of the source by measuring the position of the laser beam origin with respect to the Tracker. This measurement is obtained with *distance monitors*. In this section, we will present the calibration of such devices by means of the measurement of the $Z$ coordinate. As for this coordinate, another distance monitor will be employed for the measurement of the $R$ coordinate. In order to transfer the Tracker position to the muon and endcap chambers, the Tracker must provide the Link with rays of known orientations. This is a task of the Tracker internal alignment system, which has already been presented in chapter 2. An alignment disc structure instrumented with tiltmeters and position sensors, acting as the interface between Link and Tracker, will allow to measure the relative position of the alignment disc with respect to the Tracker coordinate system. Then, a long tube coupled to two short range proximity sensors will measure the distance between the periscope and a target attached to the laser box. The measurement of the $Z$ distance along the beam will be completed by calculating the offset between the laser beam origin and the target. This will be achieved reconstructing the two intersecting laser beam lines (at $\eta = 3$), since the opening angle between both is known.

Distance measurements use a large tube (made on aluminum or carbon fiber) plus short-range proximity sensors (see figure 8.11). We have employed two such kind of sensors, based on very different working principles. For the $Z$ measurement we used Heidenhain [3] contact gauge meters plus an aluminum tube. For the $R$ measurement we used optical triangulation sensors from OMRON [4] attached to a carbon fiber tube. In both cases, carbon fiber or aluminum, temperature probes located in several points will allow to correct the changes of the tubes with temperature.

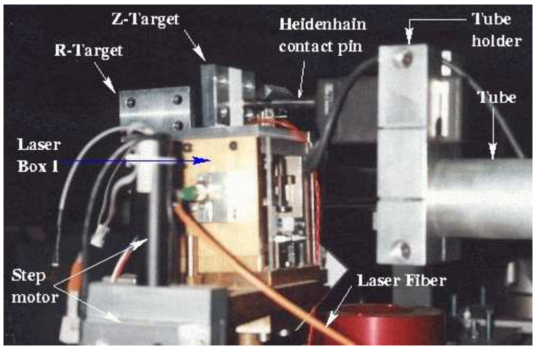


Figure 8.11: *Picture of the distance monitor between points FIR1 and F1 (figure 8.5). The view shows the left end of the monitor. A Heidenhain is sustained above the aluminum tube. The contact pin touches a target on top of the laser box.*

A calibration of a distance monitor determines the interdistance between proximity sensors. It only requires to know, with the required precision, the distance between two points. The calibration of two such monitors was carried out in the ISR setup taking advantage of the knowledge of the interdistance between sockets of the network. First of all, the distance between these two points was measured using the survey network. Then the tube with the two distance-meters coupled to its ends was inserted in between the targets. Then the distance between the targets minus the readings of the proximity sensors determines the offset between proximity sensors. One evaluation of the repeatibility of the measurement was calculated by repeated insertion and extraction of the distance monitor in the setup. The value obtained was 40.7 $\mu$m.

## 8.5 Conclusions

The complexity, the number of elements and the novel character of some of the CMS alignment system components demanded a combined real scale test that could demonstrate the viability of the CMS alignment concept. The setup of this test was done at the ISR hall at CERN, during the summer of 2000. Before this date, a very preliminary study of the hall conditions was carried out by the Link group to study the environmental conditions for the beam propagation. At that time (1999), a first calibration of a source (pre)prototype was also done.

The test of components needed for the Link subgroup still missed the calibration of some structural components (periscopes, laser boxes and distance monitors) which, due to space restrictions needed for optical calibrations, could not be afforded in the Link laboratory. In this sense, we have first employed the ISR setup as a calibration bench for these elements.

Fiducialized ALMY sensors working in transparent mode have been utilized for the calibrations.

Periscopes and laser boxes calibration results have been presented in this chapter. Besides, we have first studied the distance monitor feasibility and have calculated its resolution being below the requested 80 $\mu$m threshold. In this way, the totality of Link alignment components has been studied. After the calibrations, the ISR global test started. Results of the combined measurements are now out of the scope of this work, but will be presented very soon.

# Bibliography

[1] Amparo Lopez Virto, *Ph.D. thesis*, in preparation.

[2] J.N. Joux, Ch. Lasseur and K. Nummiaro, *CMS-ISR-Alignment Calibration Bench*, May $17^{th}$, 2000.
http//www.cern.ch/SurvExpDiffusion/cms.html

[3] Heidenhain Digital Length Gauge Systems
http://www.heidenhain.com

[4] Laser Displacement Sensor. Model Z4M-W100. OMRON Electronics
http://www.omron.com/about_omron/address.htm

# Chapter 9

# Summary and Conclusions

The LHC (Large Hadron Collider) will be the new research tool at CERN. It has been designed to produce proton-proton collisions with 7 TeV per beam, center of mass energy. Two high luminosity collision points are foreseen for two multipurpose experiments: CMS and ATLAS. Another two lower luminosity experiments LHCb and ALICE are also being constructed in the LHC ring. The work presented in this thesis has been developed for the CMS experiment being its alignment the application field.
CMS or Compact Muon Solenoid, is characterized for being a modular, highly compact detector. One of its key design features is a 4T solenoidal magnetic field which will curve charged particles in the transverse plane thus aiding the measurement of its momentum to a high accuracy. CMS is optimized to measure muons, which are important signatures from high energy hadronic events. In CMS, the muon momentum measurement will utilize the information of two subdetectors: the Central Tracker and the Muon chambers, for maximum accuracy. Compacity is ensured up to pseudorapidities of $|\eta| = 3$ for electromagnetic particles and up to $|\eta| = 5$ for hadronic particles.
With resolutions of order 100 $\mu$m per station, the maximum uncontrolled movements of the subdetectors should be comparable to their resolution. The main feature of CMS, its strong solenoidal magnetic field, will also be the most important source of instability for the placement of the subdetectors. After the magnet is switched on, the endcaps will shift by $\sim$1 cm towards the interaction vertex and the muon stations will move by 0.5 cm approximately. After the initial movements, operating conditions as temperature gradients and humidity will not guarantee the stability of the detector at the micrometer level. The magnitude and random character of these displacements lead to the necessity of an alignment system that monitors the changes. For the most important coordinate from the physics point of view, coordinate $\phi$, the alignment system should reconstruct the positions of the chambers within 75(200) $\mu$m for the inner(outer) endcap muon chambers and within 150-350 $\mu$m from the inner barrel chambers to the outer ones.
The alignment of big structures such as HEP detectors is usually accomplished by means of optomechanic systems which save space and are accurate enough. Compacity in CMS is obtained avoiding the maximum amount of dead regions in the detectors. This imposes severe constraints in the design of the alignment passages, since the system must adapt to the detector geometry and the lack of space. The most clear example of this is the layout of the Link system which runs around the external geometry of the subdetectors. A multipoint alignment based on sensors which intercept a single beam along distances of several meters seems to be the best solution from the integration point of view. The ALMY sensor allows this idea to be put into practice.

ALMY sensors are transparent digital position sensors fulfilling the above condition. The sensor is a multilayer device composed by a thin layer of hydrogenated amorphous silicon (a-Si:H) in between two layers of Indium Tin Oxide (ITO) on a glass substrate. Transparency is provided both by the transparency of the substrate and the transparency of the a-Si:H for thin layers of material. The ITO electrodes are segmented into strips, drawn perpendicularly in each layer. On top of the first layer of ITO, a thin layer of material isolates the device electrically. In general, a fraction of light incident on the device will be absorbed in the a-Si:H layer producing electron-hole pairs. Charges are then separated by the applied voltage and then collected by the electrodes. After that the current is converted to voltage, digitized and read out. The electronics in charge of this process depends on the ALMY sensor prototype.
ALMY sensors provide a two dimensional information of the position of the structures to which they are attached. This information is used to reconstruct the six degrees of freedom of each subdetector, considered as rigid bodies. The information provided by these position sensors is complemented by distance measurements among different subdetectors and precise measurements of the $\phi$ angle of the structures.

### ALMY sensors characterization

Early operation of ALMY sensors showed the existence of systematic effects both in the reconstruction of the spot position and in the transmission of the beam through the multilayer structure. The systematic effects arose as inhomogeneities in the reconstruction of the displacement of the light spot over the surface of the sensor (linearity) and, in transmission, as deviations of the beam position with respect to the undeflected beam. A sensor calibration consists in the calculation of both inhomogeneity patterns extended to the sensor surface.
More than 50 ALMY sensors have been calibrated. The sensors have been sorted into four sets. Sensors from sets III and IV had antireflection coatings to reduce the effect of multiple reflections.
We have studied and simulated the performance of three possible linearity algorithms. Then we chose the calculation of the residuals of the fit between reconstructed and moved positions as the best inhomogeneity estimator. The spatial resolution, averaged for all sensors within each group, is shown in table 4.4. It can be observed that the spatial resolution of these devices is better than 5 $\mu$m.
As it is shown in chapter 5, the interferences produced by multiple reflections in the several layers rule the operation of the sensor. With this idea in mind, the transmission of a Gaussian beam through the sensor was studied. We have found that the trends encountered in the deflection measurements (linear distribution plus oscillating pattern of the deflected angle as a function of the position of the spot on the sensor) can be explained as produced by the curvature of the substrate and the multiple reflections, respectively.
In any case, the bulk deflection (amounting about 100 $\mu$rad), coming from the curvature of the substrate had to be corrected to diminish the error contribution of the deflection. For those sensors without antireflection coating, the amplitude of oscillations made necessary a calibration matrix ($\sim 400 \times 400\ \mu\text{m}^2$ pitch). Deflection of sensors with antireflection coating can be accurately parametrized by using a second order polynomial, reducing thus greatly the volume of data collected per calibration.
Finally, we studied the Staebler Wronsky effect $-$ or reduction of the amorphous silicon photoresponse as a function of illumination time and laser power $-$ for four ALMY sensors. We found

a degradation of less than 2% in photoresponse for a period of time double of their operation in the LHC. This ensures a systematic contribution to the position error below 5 $\mu$m.

### ALMY simulation. Calculating transmittance and reflectance

Since the beginning of the ALMY operation, the question of the origin of the sensor inhomogeneities both in the detection of the light spot and in the beam deviation was studied. It was first assumed that the observed patterns could arise from inhomogeneities in the deposition process of a-Si:H. However, if the observed effect could be explained by the absorption of a-Si:H it should led to absorption variations much greater than the one measured experimentally. This argument pointed at interferences in the several layers of material as the reason for the observed *wavy* behavior. Chapter 5 was devoted to the study of the ALMY sensors from an interferential point of view.

In this study, each layer of the ALMY sensor is represented by a $2\times2$ matrix, called characteristic matrix, which becomes defined by the (complex) refraction index and thickness of the layer. The propagation of a monochromatic plane wave in absorbing media is calculated as the ordered product of the characteristic matrixes of each independent medium. By using this method, we have managed to reproduce accurately the transmittance (T) and reflectance (R) of an ALMY sensor.

The simulation is accomplished in several steps. First, T and R for separate layers of a-Si:H and ITO on glass are calculated. Then, calculated real and imaginary parts of the refraction indexes $-\,n$ and $k\,-$ are fitted to smooth and simple functions. These functions are fed into the whole ALMY simulation and utilized to reproduce its T and R curves. All calculations employ a $\chi^2$ algorithm, minimizing the difference between measured and calculated transmittance and/or reflectance.

An accurate description of the ALMY layers allowed us to try an optimization of the layers design. The aim of the optimization was to find a set of tolerant thicknesses ($\pm10$ nm) that lead to a maximum transmittance in a certain wavelength range ($\lambda \in [770, 780]$). The result of the optimization was a set of thicknesses for which transmittance keeps always above 79%.

### Measuring the $\phi$ angle in the alignment system of CMS

The aim of the CMS alignment system is to make the coordinate system of the Tracker available for the Muon and Endcap systems. After all the alignment iterations, the $(R, Z, \phi)$ active element positions will be known with respect to the interaction point. The $\phi$ coordinate is precisely measured using commercial tiltmeters (also known as inclinometers)

Tiltmeters are precision electrolytic levels, with typical resolutions of order $\mu$rad. They operate on the principle that a bubble, suspended in a liquid filled case, will always orient itself perpendicular to gravity. The sensor is operated by two excitation electrodes and the output voltage, proportional to the tilted angle, is provided by a pickup electrode. Tiltmeters have a preferred measuring direction, but it is not specified. If the sensor axis and the direction perpendicular to the rotation axis do not overlap, then the angle measured by the tiltmeter does not coincide with the angle rotated by the structure to which the tiltmeter is coupled. In our application, the misalignment can be 4 degrees, as much.

Two kinds of tiltsensors belonging to different firms were tested. We developed a geometrical description which allowed to calculate, in a calibration, the misalignment angle between rotation and internal axis. Besides, we showed that both scale factor (ratio of output voltage to tilt angle)

and misalignment can not be calculated simultaneously. The manufacturer is able to control the calibration misalignment angle to better than 1 deg, which translates into a negligible error to the scale factor. Even though both magnitudes could not be measured simultaneously, we have shown that the precision and resolution for each sensor can be calculated from measurements where the misalignment is fixed. We have rejected thus tiltmeters with the lower performance. Although we are looking for linear tiltmeters in the range $\pm 0.3$ deg we have found that, at least, a second order polynomial must be used to keep the resolution of the sensor below 5 $\mu$rad. Hysteresis of the output voltage versus tilted angle was found not to be important for the selected sensors.
We propose the utilization of two tiltmeters under a certain angle (in the plane) which relieves the constraint on the knowledge of the misalignment. Using these two sensors, it is possible to calculate the angle moved by the structure. A test of such a device showed that the angle moved could be reconstructed with 4 $\mu$rad error.
A first prototype of a Laser Level (being a composed object of tiltmeter and ALMY sensors) showed its feasibility as a tool for measuring angles of large structures (as the MABs), extending thus the local reach of the tiltmeter measurement.

### CMS Link radiation endurance tests

A thousand million of interactions per second lead to a very harsh radiation environment. Tracking detectors will undergo charged hadron fluxes, decreasing as $1/r^2$, photons and neutron albedo from the electromagnetic calorimeter which is reduced by lining of the ECAL. Forward detectors are more affected since the flux and energy of particles is higher. The muon system will receive hadronic leakages (overall the endcaps) and machine background which will be most important during the low luminosity phase.
Regarding alignment sensors and components, they will also be housed in a hard radiation environment. Optical glasses and mirrors have been irradiated to 10 years equivalent gamma-rays (100 kGy). Both BK7-G18 and optical grade fused silica (synthetic quartz) did not degrade their reflectance and transmittance performance. In fact, we found that a triple antireflection coating (to increase transmittance) or a silver reflection coating (to increase reflectance) on BK7-G18 further improved the radiation endurance of this material.
By constructing two retroreflector probes on BK7 we tested the radiation hardness of LOCTITE and EPOTECNY NOA61 as glues joining the optical pieces. The angle between the two right angle prisms of each retroreflector was measured mechanically. We observed changes in the stability of the glues after 100 and 200 kGy although the measurements could not be considered conclusive. New optical measurements will be carried out.
While radiation effects on c-Si are already well known and have been already parametrized, we have found that the effect of irradiation on a-Si has not been extensively treated in bibliography. It might well be because, up to know, the most extensive use of the a-Si:H has been its photovoltaic usage. It is tempting to relate the irradiation with the creation of defects in the band gap of a-Si:H. The created metastable defects would act as recombination centers and the photoconductivity would thus decrease. It is also clear from bibliography that further annealing of samples heal the produced effects.
Finally, and due to their relevance for the alignment system we irradiated a Schottky-type ALMY sensor and a *pin* type one (two different manufacturing techniques employed for these devices). The sensors were first irradiated with gammas from a $^{60}$Co source at CIEMAT, in steps of 0.1-20 kGy, up to a dose of 100 kGy. Neutron irradiation was accomplished in two steps ($1.1 \times 10^{14}$ and

$10^{15}$ n/cm$^2$). No change in deflection was observed after the combined exposure. A degradation about 10% in transmittance seems to appear after 10 kGy, but stabilizes after further exposure. Comparison of the signal response and transmittance with respect to that of fresh sensor does not lead to the conclusion of a degradation on performance, since the production of sensors shows an inhomogeneity comparable to the measured effect.

### ISR test results

Since the design phase of CMS, it has been clear that the performance of the experiment deeply relies on an alignment system monitoring the positions of the subdetectors among them. It has been already several years since we started studying individual components of the system. Regarding the Link group, calibrations of amorphous silicon position sensors and tiltmeters, among others, have been accomplished during this time. Due to the complexity and number of elements of the whole alignment system, a real scale test was devised in order to assemble and run the components of the alignment system altogether. This is the reason why, during June 2000, we proceeded with the first CMS real scale alignment test, also called ISR test.

As it name explains, the ISR test took place in the ISR hall at CERN. Once the rings were dismantled, a part of the hall was equipped with weighted concrete blocks, reproducing the CMS geometry. Each block represented positions of CMS where alignment sensors should be located. These blocks were all measured in a common reference system thanks to the CERN Survey Group. The alignment elements were endowed with special mechanics to interface the mechanics on the blocks.

Although the design goal of the ISR test was the validation of the alignment concept, it was used first by us to perform the calibration of periscopes, light boxes and distance monitors which, due to space restrictions, could not be performed elsewhere.

The calibration of the laser boxes, used the optical network defined by the survey measurements to calibrate the angles between reflected, transmitted and split beams of laser sources. The beams were measured using ALMY sensors in selected positions, providing the required experimental accuracy. One complete laser box prototype, containing two parallel beams along one direction and a third beam 95.7 arcdeg away, was measured. The laser box parameters were calculated with an uncertainty below the design tolerance.

The calibration of the periscopes also employed ALMY sensors, working in transparent mode, to measure the angles and distances between incoming and outgoing rays. Again two different prototypes were constructed. One was built within specifications at CIDA (Spain). The other was assembled using laboratory components. The results of the calibration of angles and distances (in space) between rays were obtained with an experimental accuracy better than design specifications.

Finally the distance monitor was also calibrated and the repeatibility of the design was checked. The precision and resolution obtained were below the 80 $\mu$m threshold requested.

The calibrations performed allowed the ISR test to be carried out later on. Results from the combined measurements are being analyzed and will be presented in a near future.

# Resumen en castellano de la memoria:

# Un sistema de alineamiento para el experimento CMS (Detector Solenoidal de Muones) del Gran Colisionador Hadrónico (LHC)

## Capítulo 1.– El LHC y el experimento CMS

El LHC o Gran Colisionador Hadrónico será el nuevo gran experimento del CERN (Laboratorio Europeo para la Investigación Nuclear). El LHC ha sido diseñado como el instrumento que permitirá acelerar haces de protones hasta una energía de 7 TeV por haz. Cuatro puntos de colisión serán instrumentados a lo largo del anillo del LHC. CMS y ATLAS serán experimentos de propósito general y alta tasa de interacción. ALICE y LHCb especializados en el estudio de colisiones de iones de plomo y estudio de la física del B respectivamente, serán experimentos con menor número de interacciones. El trabajo presentado en esta memoria ha sido realizado en el primero de estos experimento: CMS o $-$ Solenoide de Muones Compacto $-$.

El LHC se construye en la actualidad en el mismo túnel que LEP, el gran colisionador de electrones y positrones, que ha finalizado su exitosa operación en el año 2001. Para acelerar los protones hasta los 7 TeV, el LHC utilizará imanes superconductores de 8.36 T de intensidad. Como en el caso de LEP, la aceleración no se realizará en una sola etapa, sino que aprovechará la red de aceleradores del CERN.

Un total de $10^9$ interacciones por segundo unidos a la gran energía disponible en el centro de masas de la colisión, permitirá generar procesos físicos de muy baja probabilidad de ocurrencia. De entre ellos, la búsqueda del bosón de Higgs, cuyo acoplo a otras partículas les proporciona masa, será uno de los grandes protagonistas. La búsqueda del bosón de Higgs se realizará en distintos canales, según la masa que tenga esta partícula. Así, desde el límite superior de LEP hasta los aproximadamente 130 GeV, el bosón de Higgs podrá buscarse vía su desintegración en el canal $\gamma\gamma$. Entre 130-400 GeV la desintegración leptónica del Higgs a Z's virtuales (para masas del Higgs inferiores a 200 GeV) o reales permitiría observar esta partícula tras un año de operación a alta luminosidad. Si el bosón de Higgs propuesto por el modelo estándar no se encontrara, podría todavía buscarse dentro del marco teórico de la teoría conocida como Supersimetría (SUSY). Esta teoría predice compañeros supersimétricos de todas las partículas conocidas. El sector de Higgs en SUSY se extiende a cinco partículas. SUSY posee tambiénn candidatos para explicar la materia oscura del Universo. Además de la búsqueda del bosón de Higgs, el rango de energía del LHC permitirá desvelar si existen realmente sólo 3 generaciones de quarks y leptones, indagar si las partículas que hoy en día conocemos como elementales tienen estructura y comprobar si el estado de plasma de gluones y quarks existe, entre otros enigmas.

Para aprovechar el potencial de este colisionador, el experimento CMS utilizará un gran imán solenoidal (12.5 m de longitud, 5.9 m de diámetro) que generará un campo magnético axial de 4 T de intensidad. El campo magnético curvará las trazas de partículas cargadas, permitiendo así realizar una medida de su momento. En torno al vértice de interacción se suceden capas de detectores, cada uno de ellos especializados en la detección de un tipo de partículas. La disposición de estos detectores es tal que se evitan espacios muertos que apunten hacia el vértice. Alrededor del haz, los detectores se distribuyen con simetría cilíndrica, alrededor del vértice, y en forma de ruedas, a modo de tapas, en las partes frontal y trasera.

A una distancia radial de entre 4 y 20 cm, dos capas de módulos de píxeles de silicio cristalino proporcionarán información espacial sobre partículas cargadas y contribuirán a la identificación de la posición del vértice de interacción (ver figura 1.7). Cada módulo consta de una malla de píxeles cuadrados de 150 $\mu$m de lado, las cuales permitirán medir la traza de las partículas con una resolución de 15-20 $\mu$m. Las señales generadas serán amplificadas a pie de sensor, extraídas por cables y posteriormente transmitidas ópticamente. Debido al daño esperada por radiación, la capa más interna será reemplazada durante la segunda fase de operación del detector.

Entre los 20 y 210 cm se encuentra el sistema de trazas de Silicio dividido en zonas de barril interna y externa, y en la zona de los cierres (ver figura 1.8). La unidad básica del sistema es un módulo de Silicio (figura 1.9). En el barril interno los módulos se distribuyen en estructuras cilíndricas y están girados para compensar el ángulo de Lorentz. En el barril externo los módulos se distribuyen en barras y no se compensa el ángulo de Lorentz. Finalmente, en los cierres los módulos se distribuyen en paneles colocados alternativamente en ambas caras de las ruedas. Los módulos funcionarán a $-20°$C.

La medida de la energía de fotones y electrones se realiza en el calorímetro electromagnético, mediante la luz de centelleo producida en los cristales de óxido de plomo y volframio. En la zona del barril los cristales se agrupan en supermódulos (figura 1.11), en los cierres se disponen en una malla XY (figura 1.12). La luz de centelleo se amplifica en fotodetectores (APDs en el barril, VPTs en los cierres) leídos a 40 Mhz. Ya que el ángulo entre fotones (importante en la separación del fondo para el suceso H$\rightarrow \gamma\gamma$) es menor en los cierres que en el barril, se utilizará en los cierres un generador de cascadas o *preshower* que medirá el punto de impacto de los fotones con una resolución de 300 $\mu$m, típicamente.

Las partículas que interaccionan vía interacción fuerte depositarán su energía en el calorímetro hadrónico. El calorímetro consta de partes de barril y cierres. En ambos, se suceden planchas de cobre y plásticos centelleadores. Los plásticos emiten luz que es recogida por fibra y agrupada según su situación geográfica. Las señales se convierten a señales eléctricas mediantes HPDs. En las partes a muy bajo ángulo, un calorímetro de hierro y fibras de cuarzo completa la medida de la energía de jets. Los fotosensores utilizados en la parte más delantera son tubos fotomultiplicadores.

El sistema de muones utiliza cámaras de deriva para la medida de los muones en el barril

y cámaras multihilo en los cierres. Las cámaras de deriva miden el tiempo de deriva de la ionización producida por el paso de un muón. Celdas de deriva se agrupan en capas, siendo un conjunto de cuatro capas denominado supercapa. Cada cámara contiene 2 supercapas para la medida de la coordenada $\phi$ y una para la $Z$. Las cámaras proporcionales (CSC) contienen seis planos de tiras de cátodos cruzados por hilos ánodos. Cada CSC proporciona medida de dos coordenadas y puede operar en condiciones de alto campo magnético. Cada cámara del barril o de los cierres está recubierta por una o dos cámaras de paneles resistivos (RPC). Estas cámaras encierran un volumen de gas entre planchas resistivas, una de ellas dotada de tiras de electrodos. Su característica principal es una resolución espacial moderada complementada por una gran resolución temporal (inferior a 25 ns).
El Trigger de CMS es un trigger de primer nivel. Su función es la de determinar si un suceso seleccionado es aceptado o desechado, tras un periodo máximo de 128 cruces del haz. El sistema de Trigger evalúa 128 algoritmos, cada uno de ellos realizados sobre candidatos de electrones, muones o jets. Por lo tanto, sólo los sistemas de muones y calorímetros participan en el funcionamiento del Trigger. En general, cada subsistema selecciona sus candidatos y es un sistema global el que realiza las decisiones. Después de que el evento sea aceptado, la información se almacenada en cada subdetector es volcada.

## Capítulo 2.– El sistema de Alineamiento de CMS

El propósito del Sistema de alineamiento de CMS es el de definir un sistema de coordenadas donde se puedan conocer las posiciones de los elementos activos de cada subdetector. La precisión en el posicionamiento ha de ser comparable a la resolución de cada subdetector. Las fuentes que inducen la inestabilidad de los detectores son el campo magnético (que será capaz de desplazar las partes más internas del hierro hasta 1 cm), los gradientes de temperatura y la gravedad.
El alineamiento del Sistema de Trazas o *Tracker* se realizará en dos partes. Un sistema optomecánico alinea el subdetector al nivel de las 100 $\mu$m, y posteriormente un alineamiento software reconstruirá trazas para obtener una precisión de 10 $\mu$m. El primero se basa en haces láser que son medidos por los mismos detectores de silicio empleados para la medida de las partículas, con ligeras modificaciones que mejoren la transmisión de la luz. La utilización de sensores de posición transparentes de silicio amorfo (a-Si:H) es otra opción para la medida de la posición del haz láser dentro del *Tracker*. El alineamiento se realiza en ocho planos, a diferencia del resto de subsistemas que siguen una simetría de seis planos.
Los cierres utilizarán, cada uno, dos haces por cada cuarto de plano (ver figura 2.2). El alineamiento del barril interno y externo se realizará por rayos reflejados desde el rayo que atraviesa el Tracker de un extremo a otro de los cierres. Este rayo permitirá, además, el alineamiento relativo entre cierres. La salida del Sistema de Trazas es un conjunto de seis rayos de posiciones y orientaciones conocidas, necesarios para el Sistema de Relación. Para poder alinear con 10 $\mu$m de error, los módulos de silicio han de estar montados con 50 $\mu$m de precisión. La simulación global del sistema de alineamiento indica que los errores en el Tracker son los de mayor contribución al error total. Un error de 15 $\mu$m en la posición de los sensores que miden el haz que desde $|\eta| = 3$ entran al Tracker se convierten en 100 $\mu$m de incertidumbre en la posición de los MABs.
El sistema de alineamiento del Barril, se encarga de definir las cámaras de muones del barril como un sólido rígido. Cada cámara esta equipada de marcos con fuentes de luz. Las fuentes de luz son medidas por vídeo cámaras que miden las coordenadas $(R, \phi)$ directamente en las cuatro esquinas de la cámara, y la coordenada $Z$ en dos puntos de ella (ver figura 2.4). Las

vídeo cámaras se colocan en estructuras mecánicas (MABs, figura 2.5) que soportan además elementos del sistema de relación y del sistema de alineamiento de los cierres. Los MABs se encuentran intercalados entre las cámaras, de forma que definen una red de detectores y fuentes de luz que se observan. El conocimiento de la posición de los hilos de las celdas se obtiene por calibración de la posición de los hilos respecto a marcas fiduciales. La precisión requerida en el alineamiento de las cámaras internas es de unas 100 $\mu$m, aumentando hasta las 500 $\mu$m en las cámaras más externas.
El sistema de alineamiento de los cierres, mide las posiciones de sus elementos con respecto a los MABs más externos referenciados por el sistema de relación, el cual liga las coordenadas del MAB con las del detector central. La transferencia de las coordenadas $R\phi$ a las CSCs más externas, figura 2.6, se realiza mediante sensores de posición 2D transparentes (llamados COPS), colocados sobre soportes mecánicos. La medida de la coordenada $Z$ se realiza mediante sensores de proximidad ópticos acoplados a tubos de fibra de carbono, o mediante sensores de contacto en las cámaras ME1/3. Desde estos soportes, un haz láser radial intercepta dos sensores 2D colocados sobre cada CSC en las ruedas (figura 2.7), midiéndose así sus coordenadas $Z\phi$. La coordenada R de las cámaras internas requiere de nuevo la utilización de monitores de distancia. La precisión requerida para este sistema en la coordenada $\phi$ será de 150 $\mu$m, 400 $\mu$m en $R$ y casi 1 mm en la medida de $Z$.
Por último, el Sistema de Relación o Sistema de Ligadura se encarga de relacionar los anteriores subsistemas entre si, tomando el Sistema de Trazas como referencia. Para ello, se utilizan fuentes de luz flotantes situadas cada 60° en la coordenada $\phi$, cuya posición se calcula respecto a los sensores del sistema central. Las coordenadas $XY$ locales se miden con sensores 2D, el ángulo $\phi$ mediante inclinómetros y la coordenada Z mediante sensores de proximidad de corto rango acoplados a tubos de fibra de carbono o de aluminio. La fuente de luz manda dos haces a la zona del barril. Uno de ellos se utiliza para la medida de las cámaras ME1/2. El segundo haz generado por la fuente se subdivide para poder apuntar a un sensor de posición en la cámara ME1/1 (figura 2.11) y proseguir hacia los MABs. El haz dirigido al MAB (figura 2.10) es interceptado por otros dos sensores de posición que definirán la posición de los MABs respecto al rayo. La coordenada $R$ se medirá utilizando monitores de distancia como los de la coordenada $Z$ del sistema central. La comparación de la coordenada $\phi$ con el sistema central se hará utilizando inclinómetros.

## Capítulos 3 y 4.– Caracterización de sensores ALMY

Los sensores ALMY son sensores de posición transparentes. A diferencia de otros dispositivos como los CCDs, el sensor se construye sobre un substrato cristalino y emplea silicio amorfo como material fotoactivo, el cual, tiene la propiedad de ser transparente para láminas finas de material. Otra diferencia con respecto a los CCDs bidimensionales es que son los electrodos, y no la capa activa, los que están segmentados. Sobre el substrato cristalino (ver figura 3.12) se deposita una capa de $\sim$100 nm de óxido de Indio y Estaño (ITO) – electrodo – que se segmenta en 64 tiras mediante técnicas fotolitográficas. A continuación se deposita una capa de a-Si:H intrínseca (dispositivo *Schottky*) o tres capas (dispositivo *pin*) cuyo grosor oscila entre 100-1000 nm, según el diseño. Una segunda capa de ITO, se deposita encima del a-Si:H y se segmenta en 64 tiras perpendiculares a las anteriores. Finalmente, el dispositivo es protegido eléctricamente mediante una fina capa de aislante.
La segmentación en tiras de los electrodos produce un conjunto de 64 señales horizontales y 64

señales verticales, por lo cual la información 2D que ofrece el sensor está integrada a lo largo de cada electrodo. Para su operación hemos utilizado láseres con perfiles de intensidad Gaussianos. Aunque cada tira de electrodo tiene una anchura de 312.5 $\mu$m, la precisión que puede obtenerse es de 1 $\mu$m combinando la información de varios electrodos.

En un principio, los ALMYs fueron sensores comerciales. En la actualidad, el diseño del sensor está en las últimas fases de su desarrollo (al cual este trabajo contribuye). Los primeros prototipos de un sensor mucho más evolucionado que su predecesor comercial están siendo actualmente producidos en el *Institut für Physikalische Electronik* de la Universidad de Stuttgart.

Desde el punto de vista de su utilización en el sistema de alineamiento, un sensor de posición ALMY queda caracterizado por el estudio de linealidad (o bondad en la reconstrucción de la posición del haz de luz sobre el sensor) y el estudio de la transmisión del haz, ya que se trata de un sensor transparente. Las primeras pruebas con estos sensores mostraron la existencia de una falta de homogeneidad en la reconstrucción de la posición del haz sobre la superficie del sensor y en la reconstrucción de la posición del haz transmitido. Según comprobamos, estas inhomogeneidades eran estables y repetibles. No dependían del movimiento realizado, sino que estaban ligadas al sensor. La extensión del estudio al sensor completo produce patrones de inhomogeneidad que son diferentes para la linealidad y para la transmisión. Las calibraciones se realizaron barriendo la superficie activa del sensor con un haz láser, utilizando plataformas motorizadas.

Se presentan tres algoritmos posibles para el cálculo de la inhomogeneidad en la determinación de la posición. Una simulación geométrica del proceso de medida nos ha permitido seleccionar el algoritmo que mejor reproduce el patrón de inhomogeneidad original. La solución adoptada como estimador del patrón de linealidad ha sido el cálculo de los residuos del ajuste entre la posición reconstruída por el sensor y el movimiento realizado.

Debido a la transparencia del sensor, el mismo haz que es detectado por la capa de a-Si:H se propaga a través de las capas de material y prosigue su camino. La reconstrucción del haz en un sensor de posición situado detrás del sensor en estudio demostró que la propagación rectilínea del haz era afectada por la presencia del primer sensor. De igual manera que ocurrió con las medidas de linealidad, el efecto era repetible. Las distribuciones de la posición del haz desviado en el segundo sensor, interpretando toda la desviación introducida por el primer sensor como un ángulo de deflexión presentaron además dos tendencias claras. En primer lugar, el valor del ángulo deflectado no era constante, sino que variaba linealmente con la posición del haz sobre el primer sensor. En segundo lugar, superpuesto al comportamiento lineal, se observaba una oscilación.

La simulación óptica completa del funcionamiento del sensor (capítulo 5) señala las interferencias producidas por las múltiples reflexiones en las capas de material como el origen de los efectos de inhomogeneidad observados. Haciendo uso de esta información, la transmisión del haz a través del sensor ha sido simulada, simplificándola al caso de una sola lámina de material. La simulación señala la curvatura del substrato como la responsable del comportamiento lineal en la deflexión y las interferencias en las capas de material como responsables de las oscilaciones.

Cuatro conjuntos de sensores han sido estudiados en este trabajo. En total, hemos recogido la estadística de más de 50 sensores. Los sensores han sido cronológicamente clasificados. Además, cada conjunto, posee características definidas. Los conjuntos III y IV se corresponden con sensores que incorporan tratamiento antireflejante para eliminar el problema de las interferencias. En la tabla 4.4 se resumen las prestaciones, promediadas dentro de cada grupo, en linealidad para todos los sensores estudiados. La resolución espacial global es mejor que 5 $\mu$m para todos

ellos.
Aún para aquellos sensores con tratamiento antireflejante, el grosor y la falta de paralelismo del substrato conduce a valores del ángulo de deflexión del orden de la centena de $\mu$rad. En el caso de los sensores sin tratamiento, la deflexión ha de ser caracterizada mediante una matriz con una periodicidad de unas 400 $\mu$m. Para los sensores con tratamiento la deflexión geométrica puede caracterizarse con un polinomio de segundo grado que simplifica y reduce el volumen de datos por calibración de manera considerable. En cualquier caso, la deflexión puede conocerse con una repetibilidad inferior a los 5 $\mu$rad. La repetibilidad de las calibraciones nos condujo a estudiar la escalabilidad de las medidas de desviación del haz. Decimos que la deflexión escala con la distancia si el mismo valor de deflexión es obtenido, independientemente de la distancia entre sensores. Mediante la comparación de medidas con interdistancias de 1, 2 y 3 m observamos que sólo las dos últimas escalaban con la distancia. Una simulación interferencial del proceso de medida demuestra que a distancias inferiores a 1 m, la contribución de la componente interferencial al ángulo de deflexión es demasiado importante como para procurar escalabilidad.
Como se deduce de la figura 3.6, la absorción del a-Si:H es muy dependiente de la longitud de onda. Por ello, los valores de transmisión obtenidos fueron entre $\sim$15% para láseres de HeNe hasta el 80% empleando láseres de semiconductor.
La degradación de la respuesta del a-Si:H como consecuencia de la iluminación prolongada y potencia en la iluminación ha sido estudiada. Cuatro sensores (con tratamiento antireflejante) fueron iluminados durante 500 horas (el doble de tiempo que serán utilizados en CMS). El resultado fue una degradación inferior al 2%, acorde con la teoría del efecto Staebler Wronski. Esto equivale a un error en la determinación de la posición del haz inferior a 5 $\mu$m, en el área local del quemado.

## Capítulo 5.– Simulación de sensores ALMY. Calculando %R y %T

La utilización de detectores de Silicio para medir la trayectoria de partículas cargadas indujo la idea de la utilización de un dispositivo parecido para la medida de un haz de luz. Al igual que en los dispositivos de silicio, el objetivo fue diseñar un detector en el que la partícula que interacciona deposita poca energía y pasa a través. Este concepto, aplicado a la detección de fotones, condujo a construir un detector casi transparente a la longitud de onda de trabajo. El diseño de los detectores ALMY pasó así por varias etapas. En primer lugar, un diseño basado en c-Si fue utilizado. Sin embargo, debido a los problemas de inhomogeneidad en la detección y guiados por la mayor resistencia a la radiación esperada de un dispositivo hecho con un material amorfo, se decidió utilizar silicio amorfo hidrogenado (a-Si:H) como material activo. El rendimiento del sensor ALMY con silicio amorfo es mucho más homogéneo que el de su precursor cristalino. Sin embargo, desde el primer momento, aparecieron una serie de patrones en la reconstrucción de la posición del haz y en la desviación sufrida por éste al atravesar los distintos medios que indujeron a diversas interpretaciones. En un principio, el problema de los patrones fue atribuído a inhomogeneidades en el proceso de fabricación del a-Si:H. Sin embargo, si el efecto observado pudiera ser explicado por la absorción del a-Si:H, se deberían obtener variaciones de la absorción mucho mayores que las medidas. La interpretación de la inhomogeneidad de la respuesta del sensor en base a interferencias en las distintas capas de material fue entonces adoptada. Sin embargo, hasta la fecha, ningún análisis de la interacción de la luz dentro del sensor había sido realizado. En el capítulo 5 hemos demostrado que la

hipótesis interferencial como responsable del funcionamiento del sensor es la hipótesis correcta. Para ello, hemos simulado el proceso interferencial dentro de las distintas capas de material y hemos conseguido reproducir medidas de transmitancia y reflectancia de estos sensores.
El capítulo comienza con una introducción teórica que documenta las fórmulas utilizadas para el cálculo de la transmitancia y la reflectancia de ondas planas monocromáticas que se propagan en medios dispersivos (absorbentes). Como resultado más importante se demuestra que la propagación de la onda en un medio (delimitado por dos superficies paralelas) queda perfectamente especificada con el conocimiento de una matriz $2 \times 2$, denominada matriz característica que depende del índice de refracción complejo del material y del grosor de la capa. La propagación a través de una sucesión de medios se puede factorizar en el producto ordenado de matrices características de cada medio. Fórmulas para el cálculo de ambas magnitudes, considerando además un substrato finito, como es el caso de las medidas reales, se proporcionan al final de la introducción teórica. Esta formulación es mucho mas compacta y elegante que el cálculo clásico de reflexiones múltiples.
La formulación anterior es entonces utilizada para reproducir medidas de transmitancia y reflectancia hechas sobre un ALMY tipo Schottky. La simulación de estas magnitudes se realiza en varios pasos. En primer lugar, se reprodujeron medidas individuales de transmitancia y reflectancia de a-Si:H (figura 5.7) e ITO (figura 5.10) sobre substratos de vidrio. La técnica empleada fue una minimización $\chi^2$ en la cual se minimiza la diferencia entre el valor de transmitancia o reflectancia simulada y el valor medido. Ya que el índice de refracción depende de la longitud de onda, la minimización se realizó para cada valor de $\lambda$. Además se definieron una serie de condiciones sobre los valores de los índices, de forma que coincidieran con valores puntuales medidos experimentalmente. La transmitancia y reflectancia calculadas están muy cerca de las medidas experimentalmente. Como puede observarse en las figuras anteriores, la simulación permite obtener los valores de los índices que dan lugar a tales magnitudes. Estos índices fueron entonces ajustados a funciones simples y utilizados para la simulación global de la multicapa ALMY. El resultado del ejercicio se muestra en las figuras 5.13 para la transmitancia y 5.14 para la reflectancia. El acuerdo entre simulación y medida nos permite asegurar que es la interferencia en las capas del sensor la principal responsable de su funcionamiento.
Ya que lo índices de refracción calculados nos permiten reproducir de manera fidedigna las características del sensor y ya que estos índices dependen del proceso de producción pero no del grosor, se procedió a realizar una optimización geométrica del sensor. El objetivo de la simulación era encontrar un conjunto de grosores que tuvieran una tolerancia de $\pm 10$ nm y que condujesen a una transmitancia máxima sobre un rango amplio de longitudes de onda. Una vez calculados los grosores se comprueban si satisfacen la condición de tolerancia. Así, un conjunto de tres índices puede ser encontrado. La transmitancia correspondiente al valor nominal de los grosores y a los valores extremos se presenta en la figura 5.18.

## Capítulo 6.– Medida del ángulo $\phi$ en el sistema de Alineamiento de CMS

El alineamiento del detector CMS se realiza de forma modular. Cada subdetector se alinea internamente, de manera que pueda ser considerado localmente como un sólido rígido. En el caso del Sistema Central de Trazas, el sólido se refiere al sistema de referencia centrado en el vértice de interacción. La transferencia de las coordenadas del sistema central hasta el sistema de muones se realiza por medio del sistema de Relación o sistema *Link*. Este sistema hace uso de fuentes de luz que ligan el Sistema Central con el Sistema de Muones. La ligadura entre ambos sistemas se lleva a cabo mediante haces láser y sensores de posición (ALMYs) distribuídos a lo largo de la geometría interna del detector. La dimensión transversa del Sistema Central es pequeña para poder realizar medidas ópticas de ángulos con precisión del $\mu$rad. Por ello, se decidió utilizar un sistema de medida auxiliar del ángulo $\phi$ basadas en inclinómetros.

Un inclinómetro electrolítico es un sensor de nivel de precisión. Internamente, el sensor cuenta con una cápsula que encierra un líquido electrolítico y una burbuja. La operación del dispositivo se basa en que al inclinar la estructura, la burbuja siempre se nivela perpendicularmente a la gravedad. El dispositivo cuenta con dos electrodos de excitación y uno por el cual extrae la señal, que es proporcional a la fracción de área de los electrodos cubierta por la burbuja. Finalmente la cápsula se introduce dentro de una carcasa en la que se fija mediante un cemento especial. Idealmente, el voltaje de salida es lineal con el ángulo girado por el sensor.

El número y la forma de los inclinómetros disponibles en el mercado es muy variado. Se han estudiado las prestaciones de dos tipos de inclinómetros electrolíticos, pertenecientes a compañías diferentes. Los inclinómetros son dispositivos eminentemente unidimensionales. Miden de forma precisa la inclinación a lo largo de una dirección. Sin embargo, en la práctica es muy difícil alinear la dirección a lo largo de la cual el giro ocurre con la dirección privilegiada del sensor. Es por ello, que el ángulo medido por el sensor puede diferir del ángulo girado por la estructura. La magnitud de esta diferencia la hemos denominado *desalineamiento* , y queda definida en la figura 6.7 como el ángulo entre el eje de giro y el eje del sensor. La figura 6.8 muestra la diferencia entre el ángulo girado por la estructura a la cual está unido el inclinómetro y el ángulo que mediría un sensor ideal (sin ninguna contribución adicional al error), en función del desalineamiento. El error máximo de la medida limita el desalineamiento máximo que se puede permitir. La operación de inclinómetros en CMS requiere un desalineamiento inferior a 4 grados.

Si las prestaciones del sensor son sensibles al desalineamiento, es normal que una calibración de estos dispositivos precise del conocimiento de este ángulo. En nuestras medidas, aún sin conocer el ángulo real de desalineamiento en nuestras medidas hemos podido obtener una serie de conclusiones a partir de la formulación matemática desarrollada. Ello se debe a que, a lo largo de una medida, el cálculo del ángulo girado por la estructura no depende del desalineamiento sólo, sino que depende del producto del ángulo de desalineamiento y la constante de calibración que, afortunadamente, son constantes (ecuaciones 6.11 y 6.12). Así hemos extraído la precisión y la resolución para cada inclinómetro, desechando uno de los dos tipos de sensores medidos. Además hemos comprobado que la precisión de la medida aumenta al incluir la información del desalineamiento.

Durante la operación de CMS, los giros serán instantáneos y no tienen por qué realizarse con un desalineamiento constante. Por tanto, en una sola medida no es posible extraer el valor del ángulo girado y del desalineamiento. Utilizando dos inclinómetros que formen un ángulo entre ellos hemos demostrado que es posible obtener la información del ángulo movido en un giro instantáneo. El ángulo entre sensores puede ser medido, además, una vez que la constante de calibración del sensor sea conocida (proporcionada por el fabricante). Medidas realizadas con dos sensores unidimensionales en tal configuración han demostrado que se puede conocer el ángulo girado por la estructura mejor que 4 $\mu$rad, lo cual es suficiente para nuestras necesidades en CMS (figura 6.21).

Finalmente, hemos estudiado el posible efecto de histéresis de los sensores. La histéresis en un inclinómetro se manifiesta como un valor de la tensión de salida diferente en un movimiento angular de ida y vuelta. Se ha comprobado que, en las condiciones de medida, no hay histéresis ni mecánica ni eléctrica.

## Capítulo 7.– Tests de radiación en el sistema Link de CMS

Con una luminosidad nominal de $10^{34}$ cm$^{-2}$s$^{-1}$, el numero de interacciones por segundo esperadas en los dos detectores del LHC que operarán a alta luminosidad estará en torno a $10^9$. Con esta tasa de producción de sucesos, el flujo y la fluencia de neutrones, protones y fotones será el más agresivo de todos los experimentos colisionadores construídos hasta la fecha. De entre todos los detectores presentes en CMS, el sistema traceador central y sus tapas serán los más afectados por su proximidad al vértice de interacción. De hecho está previsto que la capa más interna ($R$ <10 cm) del sistema de píxeles de Silicio sea sustituída y reemplazada por una nueva ($R$ = 11.5 cm), durante la segunda fase de operación, a luminosidad alta. En principio, el resto de componentes del detector deberían mantenerse operativos durante al menos 10 años de operación de CMS.
Simulaciones del entorno de radiación en el detector CMS han sido llevadas a cabo por los distintos subdetectores. A continuación se exponen los principales conclusiones de estos estudios y el esperado efecto de la radiación sobre los subdetectores:

- En el sistema central de trazas el flujo de hadrones cargados será independiente de la coordenada $Z$ disminuyendo como $1/R^2$. Fotones con energías inferiores a 10 MeV predominarán. Una contribución menor, pero de mayor energía proviene de la desintegración de $\pi^0$s. Debido al *albedo* de las tapas del ECAL, la fluencia neutrónica en los últimos discos del *Tracker* excederá la fluencia hadrónica. En la zona del barril, la fluencia neutrónica será inferior a la fluencia hadrónica. Se ha calculado que un recubrimiento del ECAL a base de polietileno (rico en hidrógeno) es capaz de reducir el *albedo.*

  En virtud de la hipótesis NIEL, cualquier fluencia de un tipo de partículas determinado puede ser reducido a una fluencia equivalente de neutrones de 1 MeV que produzcan el mismo daño en el semiconductor. La figura 7.11 muestra la función de daño $D(E)$ (equivalente al valor NIEL) del Silicio. La energía necesaria para desplazar un átomo de silicio resulta ser unos 190 eV. Electrones (y fotones) apenas producen daño en el silicio. Sin embargo piones y protones producen mayor número de desplazamientos, siendo este último muy dependiente de la energía del protón incidente. Los efectos más importantes debido a la interacción de este fondo de partículas con los detectores de c-Si en el LHC serán: aumento de la corriente de retorno, inversión del tipo de conductor y, en menor medida, creación de centros de recombinación.

- En el calorímetro electromagnético, los secundarios de las colisiones $pp$, el albedo neutrónico y la deposición de energía de las cascadas son de igual importancia. Tanto la electrónica de lectura (a excepción de los APDs) como los cristales, podrán ser protegidos mediante material hidrogenado.

- En la región de $|\eta| = 3$ donde algunos componentes de alineamiento residirán, la dosis alcanzará 10 kGy/año, con una fluencia neutrónica de $10^{12}$ cm$^{-2}$ y año.

- El sistema de muones recibirá contribución directa de las colisiones $pp$, fugas desde el calorímetro hadrónico y fondo de la máquina que será la contribución más importante en la etapa de baja luminosidad.

En cuanto a los componentes del sistema de alineamiento hemos irradiado, hasta dosis y fluencias equivalentes a 10 años de LHC, vidrios, espejos, pegamentos y sensores transparentes de posición (ALMYs). Los tres primeros forman parte de la fuente de luz y de los periscopios.

Es importante que vidrios y espejos mantengan su transparencia y reflectancia y que el pegamento no degrade su forma a fin de mantener el ángulo relativo entre las estructuras unidas. Irradiación de 4 vidrios (BK7, BK7-G18, sílice fundida y sílice fundida de calidad óptica) con rayos gamma de la fuente de $^{60}$Co del CIEMAT muestra que tanto el BK7 como la sílice fundida se oscurecen como consecuencia de la irradiación. Los otros dos materiales apenas degradan sus prestaciones. Se ha comprobado además que los tratamientos antireflejantes (figura 7.4) o reflejantes (figura 7.5), según convengan, de las superficies disminuyen el daño por radiación.

Para comprobar la estabilidad de dos pegamentos distintos hemos construído dos retroreflectores con BK7 como material. Uno de ellos se ha pegado con LOCTITE, el otro con EPOTECNY NOA61. Como consecuencia del consabido ennegrecimiento del BK7 (ver figura 7.8), se eligió una medida por contacto para calcular el ángulo entre caras del retroreflector. Se realizaron dos medidas del ángulo relativo antes de la irradiación. A continuación ambos retroreflectores se irradiaron con 10 Mrad de gammas. El ángulo relativo se modificó por 46 $\mu$rad en el caso del LOCTITE (figura 7.9) y 56 en el caso del NOA61 (figura 7.10). Una segunda medida del LOCTITE (con varios meses de diferencia respecto a la primera) muestra la repetibilidad de la medida. A continuación una dosis extra de 100 kGy aplicada al otro retroreflector demuestra otro cambio en el ángulo relativo. Desafortunadamente, el error intrínseco del método no permite concluir claramente si lo que se observa es la imprecisión de la medida o un giro real. En el futuro se realizarán medidas de retroreflectores empleando BK7-G18 o sílice de calidad óptica y un método óptico para dilucidar esta cuestión.

Finalmente, y debido a su importancia para el correcto funcionamiento del sistema de alineamiento, se midió el efecto de rayos gammas y neutrones en las propiedades ópticas de los ALMYs. Un ALMY tipo Schottky y otro tipo *pin* , se sometieron a una primera irradiación de 10 Mrad de gammas procedentes de la fuente de $^{60}$Co. A continuaciòn se realizó la irradiación con neutrones en 2 pasos: una primera de $\sim 10^{14}$ n/cm$^2$ y otra segunda hasta $\sim 10^{15}$ n/cm$^2$. El ángulo de deflexión no se ve modificado como consecuencia de la radiación (figura 7.14 para el ALMY tipo Schottky, y figura 7.15 para el tipo *pin* ). La medida de la transmitancia, a la longitud de onda del HeNe, muestra una disminución uniforme de la señal inferior al 10% tras 10 kGy, estabilizándose la transmitancia en torno a este valor. Iluminando los sensores con luz blanca (monitorizada por una fotocélula) se midió la respuesta del sensor tipo Schottky, que era el único equipado con electrónica. Si bien las resistencias y los condensadores permanecieron intactos tras las diferentes fases de irradiación, se observo que los multiplexores (SILICONIX DG406) dejaron de funcionar a los 200 Gy, por lo cual se decidió proseguir las sucesivas irradiaciones sin estos componentes, que serían incluídos al final de cada irradiación. Tras 10 kGy de gammas se observa una degradación *uniforme* del 10% en la respuesta, que se incrementa en un 20% extra tras $10^{14}$ n/cm$^2$ y en otro 15% al final de los $10^{15}$ n/cm$^2$. Al comparar la fotorespuesta y la transmitancia de los sensores irradiados con sensores nuevos se observa que la degradación no es relevante, ya que queda absorbida por la no uniformidad existente entre sensores fabricados. En la figura 7.17 se observa la fotorespuesta por la cara delantera y trasera del sensor D (irradiado) con aquella de los sensores A y G (nuevos). En la figura 7.18 observamos la comparación de trasnmitancias entre los mismos sensores. Así pues, la degradación aunque relevante con respecto a las prestaciones iniciales, queda enmascarada por la inhomogeneidad en la fabricación. Para resolver el problema de los multiplexores se ha realizado un primer prototipo de sensor (figura 4.38) en el cual el multiplexado ocurre lejos de la zona conflictiva. Por ello y ya que la degradación ocurre de manera global en el sensor, podemos asegurar que los ALMYs seguirán operativos tras 10 años de utilización en CMS.

## Capítulo 8.– Resultados de los test ISR

Desde el principio del diseño del experimento CMS ha sido claro que las prestaciones de CMS como experimento de Física de partículas demandaban un sistema de alineamiento eficaz y redundante. El sistema de alineamiento de CMS ha pasado por varias etapas, y ha sido sometido a varias redefiniciones de elementos e incluso de subsistemas, como es el caso del sistema *Link*. En los capítulos anteriores hemos resumido el estudio de sensores de posición transparentes de silicio amorfo y de inclinómetros para el alineamiento. Al igual que el sistema Link, el resto de subsistemas ha ido desarrollando y estudiando sus propias soluciones para cada subdetector. Una vez que el desarrollo y el estado de los componentes alcanzó una estabilidad era tarea obligada una prueba conjunta, a escala real, de todos los subsistemas como ejercicio para lo que será el sistema de alineamiento final en CMS. La prueba se realizó durante el verano del año 2000, en el *hall* de los ISR (CERN).

Dado que el experimento CMS se encuentra en fase de construcción, la geometría de CMS fue reproducida por medio de grandes bloques de cemento que representaban posiciones en CMS. Los bloques de cemento se equiparon con mecánica de interfase donde poder colocar cada uno de los instrumentos de los subsistemas. Algunos de los elementos tuvieron que ser adaptados mecánicamente para poder ser utilizados en esta configuración, como es el caso de los sensores ALMYs (figura 8.2). El equipo de topografía del CERN se ocupó de la referenciación de cada uno de los bloques. La referenciación consistió en la definición de las posiciones de puntos escogidos en los bloques con respecto a un sistema de referencia común. Utilizando técnicas fotogramétricas y topográficas estándar, la posición de estos puntos puede conocerse con un error que oscila entre las 10 y 50 $\mu$m. El fin último del test ISR será recuperar, mediante las medidas combinadas de los subsistemas, las posiciones de estos puntos con una precisión comparable a la de la referenciación.

Previo a la realización de este test global, las calibraciones y el estudio de inclinómetros y sensores de posición fue llevado a cabo. Además, se construyeron prototipos de fuentes de luz, periscopios y sensores para la medida de distancias. Los diferentes prototipos fueron realizados siguiendo un control y estudio de sus dimensiones, componentes y disposición que aseguraran un correcto funcionamiento en la calibración. Las necesidades de espacio demandadas por las calibraciones ópticas de los periscopios y fuentes, nos llevo a utilizar primeramente la facilidad de los ISR como banco de calibración, previo a la realización del test global. En este capítulo, se resumen los resultados de estas calibraciones.

Ya en 1999, se realizó una primera iteración en una versión reducida de este dispositivo experimental, que tuvo como objeto el estudio de las condiciones ambientales (presión, humedad, temperatura) para la estabilidad en la propagación de los haces. Aprovechando las buenas condiciones de estabilidad y de propagación, se realizó una calibración de un prototipo de fuente de luz.

En el año 2000, y con la versión completa de la sala (figura 8.5), dos prototipos de fuente de luz fueron calibrados. Uno de ellos genera los tres haces (dos paralelos y uno a 95.7 grados con respecto a los anteriores). El otro prototipo extraía dos haces a 95.7 grados. La calibración consiste en medir las distancias y ángulos entre haces, en un sistema de referencia tridimensional.

Para la calibración se utilizaron sensores ALMYs referenciados dispuestos en línea midiendo la posición de los distintos haces. El resultado de la calibración del prototipo completo se muestra en la figura 8.8 y en la tabla 8.1. Como se observa en la tabla, la calibración se realizó con un error que se encuentra dentro de la incertidumbre de la medida, lo que prueba la fiabilidad de la construcción.

Dos prototipos distintos de periscopio fueron calibrados también. El primero de ellos, construído en el CIDA (España) en base a estrictos requisitos de estabilidad y precisión de montaje y que empleaba materiales resistentes a radiación. El segundo, construído con material disponible en el laboratorio. De nuevo, la calibración de los periscopios requiere calcular las distancias y ángulos entre rayos en el espacio, utilizando sensores transparentes en cada haz. Los resultados de las calibraciones se muestran en la figura 8.9 y tabla 2 para el periscopio CIDA y en la figura 8.10 y tabla 3 para el segundo prototipo. Por comparación con los parámetros medidos para el periscopio CIDA, se observa que en este caso existe una mayor dispersión con respecto a los valores nominales, posiblemente influenciados por la peor estabilidad y control del diseño. La calibración de estos prototipos permitió la realización de la medida conjunta de los subsistemas del barril, cierres y link, objetivo final de los test ISR. El resultado de estas medidas se analiza en la actualidad.

# Agradecimientos/Acknowledgements

El trabajo que se recoge en esta memoria ha sido desarrollado durante 5 años, casi un 18% de mi vida. Todo este tiempo ha sido una oportunidad única en la que he podido aprender de personas que llevan en ésto mucho más que mi escaso 18%.

En primer lugar, he de expresar mi gratitud al Instituto de Estudios de la Energía del CIEMAT *(Centro de Investigaciones Energéticas Medioambientales y Tecnológicas)*, que en este año 2001 cumple 50 años de existencia, donde he podido desarrollar este trabajo. Dentro del CIEMAT he sido acogido en el Departamento de Fusión y Partículas Elementales, cuyo director es el *Dr. Manuel Aguilar Benitez.* El *Dr. Marcos Cerrada Canales*, jefe del grupo de Partículas Elementales, posibilitó mi integración en el equipo. Gracias a ambos por confiar en mi trabajo hasta el final.

En el día a día he tenido la fortuna de trabajar bajo la supervisión de *Dr. Antonio Ferrando García.* Mi gratitud por su confianza, su respeto, sus aportaciones profesionales y personales.

Aunque esta tesis ha sido realizada casi íntegramente en el Grupo de Partículas del CIEMAT, soy alumno de Tercer Ciclo del Departamento de Física Moderna de la Universidad de Cantabria. La *Profesora Teresa Rodrigo Anoro*, jefa del Proyecto de Alineamiento, ha sido un ejemplo de tenacidad y rigurosidad. El *Profesor Alberto Ruiz Gimeno* posibilitó mi entrada en el grupo de Altas Energías de Santander. Agradezco su tutoría y apoyo en los primeros meses. Espero que esta memoria de tesis sirva como prueba de gratitud hacia ambos.

*Carlos Fernández Figueroa* me he aportado coherencia, método y curiosidad científica. Gracias a su ayuda he progresado en mi trabajo, es para mi un ejemplo a seguir y un amigo.

Si hay algo que caracteriza a la división de electrónica y automática del CIEMAT es su profesionalidad. Trabajar con *Antonio Molinero Vela* es disfrutar aprendiendo y trabajando. Gracias por tu empeño y tu consejo. La obtención de los datos que aparecen en este trabajo no habría sido posible sin los programas de adquisición escritos por *Juan Carlos Oller.* La experiencia y paciencia de *Javier Chércoles* me permitieron llevar a cabo la mayoría de las medidas realizadas.

I thank *Prof. Dr. Volker Soergel* for inviting me to join the ALMY Project at the Max-Planck Institute (MPI) of Munich. I am indebt to *Prof. Dr. Stefan Schael* for his guidance, the quantity and quality of the work done in common. I would also like to thank the support and encouragement from the rest of the Muon Working Group at MPI: *Hubert Kroha, Andreas Manz, Andrei Ostapchouk, Robert Richter, Sofia Choridou and Sandra Horvat.*

La gran mayoría de las medidas presentadas en esta memoria han sido realizadas *con nocturnidad* (y casi siempre durante el fin de semana) en colaboración con *Noelia García González.* Su contribución a este trabajo abarca desde la primera medida de los sensores ALMY hasta el último test en los ISR. De la misma manera, durante los últimos años he colaborado intensamente con *Amparo López Virto.* Gracias a las dos por proporcionarme medidas, por vuestro tiempo y por vuestra paciencia.

Durante las pruebas de caracterización de los sensores ALMY y el estudio de los *tiltmeters* mi trabajo se enriqueció con la participación del *Dr. Ivan Vila Álvarez*, el diseño mecánico de *Enrique Calvo Alamillo* y las correcciones de los *Dres. Pedro Arce Dubois* y *Francisco Matorras Weining.*

En el CIEMAT he compartido despacho con las *Dras. Isabel Josa Mutuberría, Begoña de la Cruz Martínez* y los *Dres. Juan Alcaraz Maestre* y *Nicanor Colino Arriero.* Muchas gracias por proporcionarme un ambiente de trabajo tan amigable y cómodo. De nuevo agradezco al *Dr. Nicanor Colino Arriero* y a los *Dres. Jesús Salicio Díez* y *Javier Rodríguez Calonge* por su inestimable ayuda informática. Jesús Salicio Díez fue clave para poder entender del funcionamiento de los *tiltmeters.*

El trabajo cotidiano en el CIEMAT ha sido facilitado por los Dres./Dras. *Pedro Ladrón de*

*Guevara, Javier Berdugo Pérez, Carlos Mañá Barrera, Eusebio Sánchez Álvaro, Jorge Casaus Armentano, MaryCruz Fouz Iglesias, María Chamizo Llatas, David Fernández Álvarez, Carmen Palomares Espiga y Miguel Ángel Falagán Bobillo.* Quiero hacer extensible este agradecimiento también al resto de compañeros de la Universidad de Cantabria: los Dres.*Jesús Marco de Lucas, Celso Martínez Rivero, José María López, Isidro González Caballero*, *Rafael Marco de Lucas, Martín López Fernández* y *Fernando Gómez Casademunt.*

Los *Dres. Julio Cárabe y José Javier Gandía*, han contribuído a rellenar el *gap* que tenía en el campo de los semiconductores y los dispositivos multicapa de silicio amorfo.

*Carlos Burgos Lázaro* guió mi formación en el estudio de los inclinómetros durante los primeros seis meses en el CIEMAT.

La colaboración con el personal del CIDA ha sido siempre muy provechosa y cordial. Tanto la *Dra. Gloria Pérez* como *Inés Génova* me han proporcionado medidas y bibliografía para la simulación de los sensores ALMY.

A *Laurent Brunel* me une un fuerte lazo de amistad y reconocimiento hacia su trabajo en el sistema de Alineamiento del Barril. Con el *Dr. Jorge Mocholí Moncholí* he compartido tardes de trabajo y ocio en el CIEMAT y en el CERN.

En el CIEMAT, el condimento más sabroso a las comidas se las han puesto mis compañeros, el *profesor Manuel Daniel Leal*, *José Risco Sanchez* a quien trunqué una prometedora carrera deportiva después de dos años de trabajo conjunto. *Juan José Martínez Morales* (con la broma perfecta en cada situación) y José Alarcón (de temer en el discurso rimado). También compartí muy buenos momentos de comida con el *Dr. Luciano Romero Barajas, Miguel Ángel Ariza, Juan Carlos Puras Sanchez, Luis Galicia, Carlos Blanco y José Luis Ramírez.*

*Concepción Braña*, me ha salvado en mis olvidos y desconocimientos burocráticos.

A los jef@s e investigador@s del mañana. Con ellos he reído, me he relajado y sobre todo he contribuído a aligerarles el peso de su nevera: *Ángela*, y sus dotes de repostería. *Carlos Delgado* y su sonrisa. *Jesús Puerta Pelayo* con 20 dedos sobre el teclado. *Elisa Lanciotti* alias bombones y flores. *Elena Zorzo*, con su alegría y finalmente *Carlos Díaz* crack del futbito.

Los seis meses que pasé en el Instituto Max Planck de Munich, fueron muy intensos profesional y personalmente. Mis amigos *Dimitri Pugachov, Juan Cortina, Carmen Pardo y José Carlos González* me hicieron sentir como en casa. Mis amigos de Gijón y Santander han soportado mis largas ausencias y mis cortas estancias.

Cómo agradecer lo que mis padres, mi hermana y mi novia han contribuído a esta tesis. El suyo ha sido el sacrificio más encubierto y la colaboración más notoria. Han empeñado una buena parte de su tiempo en este proyecto. Mi abuela Fé, tanto y tan bien nos cuidó. Mis padres, a quienes debo lo que soy y a donde llegue. Mi hermana, es un apoyo clave por proporcionarme estabilidad y rumbo. Y finalmente Lourdes, que sin saber nada de alineamiento lo ha padecido fin de semana a fin de semana.

Madrid, Julio de 2001

# Subject Index